Mixed finite element approximation of porous media flows

In view of:

Streamline computation through fractured porous media;
goal–oriented estimation of Darcy's equations;
and the travel time functional.

Fran Rourke

Thesis submitted to

University of Nottingham

in partial fulfilment for the award of the degree of

Doctor of Philosophy

in *Mathematics*

Supervised by

Prof. Paul Houston & Dr. Kristoffer G. van der Zee

May 2023

Abstract

The reliable simulation of flow in fractured porous media is a key aspect in the decision making process of stakeholders within politics and the geosciences, for example when assessing the suitability of burial sites for storage of high–level radioactive waste. This thesis aims to tackle the challenge that is the accurate simulation of these flows and does so via three computational developments. That is, suitable models for porous media flow with fractures; obtaining rigorous and reliable estimates of errors generated through these models; and the accurate simulation of the times–of–flight for particles transported by groundwater within the porous medium. Firstly, an expansion procedure for fractures in porous media is developed so that physical fluid laws are still retained when tracking particles across fracture–bulk interfaces. Moreover, the second contribution of this work is the utilisation of the dual–weighted–residual method to define suitable elementwise indicators for generic quantities of interest. The third contribution of this thesis is the attainment of accurate simulations of travel times for particles in porous media, achieved through linearising the functional representing the time–of–flight; in practice, numerical examples, including one inspired by the Sellafield site in Cumbria, UK, validate the performance of the proposed error estimator, and hence are useful in the safety assessment of storage facilities intended for radioactive waste.

Acknowledgements

Firstly, I wish to thank my supervisors Paul Houston and Kris van der Zee for their continued support and encouragement throughout my PhD. At every hurdle and roadblock it was obvious you both had full confidence in my ability to pull through and produce work to be proud of; for that, I am so very appreciative and could not have asked for a better, or more suited, pair of supervisors. Thank you Kris for our regular trips to coffee shops in Beeston during my final year, our discussions were both very helpful and interesting, and ensured I was actually on track to complete my PhD.

I would like also to acknowledge the School of Mathematical Sciences, the University of Nottingham, and the EPSRC for funding this work.

Finally, my partner Helena Holmes, for whom none of this would have been remotely possible without. For the unparalleled care and patience you have shown me during these last four years, I am so very grateful; thank you for having me be a part of your life. Our relationship has only ever known my PhD; I am so very excited to see what our future holds beyond it.

Contents

Chapter 1

Introduction

1.1 Motivation, objectives, and thesis contributions

Within many geophysical engineering applications, the accurate simulation of fluid flow within fractured porous media poses significant challenge. For example, in the safe long term storage of both CO_2 [77, 111, 119] and high–level radioactive waste [121], the reliable simulation of flows within these contexts typically contributes to decision making and risk assessment. Indeed, in the post–closure safety assessment of burial sites for radioactive waste, the precise computation of flow paths, and travel time for leaked solutes to reach the surface, is imperative when assessing the suitability of the sites.

The accurate tracing of streamlines, necessary to track particles in porous media flow, is a challenge in the presence of fractures. In the event a particle enters a fracture within the domain, the retainment of physical laws is required for a sensible simulation; especially within a finite element (FE) setting where the fractures are typically considered as lower dimensional objects. Such dimensionality assumption is paramount when considering real–life applications, where typically fractures are intersecting and occupy much of the domain in great quantities. Indeed, there is an ever growing need for high–fidelity simulations of flow within porous media, even when not considering fractures in the domain. Such accurate computations lend well for physical applications in the post–closure safety assessment of burial sites. Furthermore, the computation of travel times of particles in porous media flow, representing leaked radioactive solutes, requires extension and utilisation of existing tools within a FE setting. Having these tools at hand will more easily inform decisions

of key stakeholders, especially in regards to applications such as those involving high–level radioactive waste.

The objective of this thesis is to present three computational developments that enable more accurate simulations of flow in fractured porous media. First, a modelling approach will be presented for flows in fractured and non–fractured porous media. Then, rigorous estimates of the errors in the obtained numerical approximations are derived and analysed. Lastly, highly accurate computations of travel times of particles in porous media are obtained.

Porous media flow, within this thesis, will be modelled using Darcy's equations: a mixed system of partial differential equations (PDEs) combining conservation of mass, Darcy's law, and boundary conditions. Therefore, the natural choice of numerical approximation will be a mixed finite element method (MFEM) employing Raviart–Thomas (RT) and Brezzi–Douglas–Marini (BDM) elements; such methods obtain approximations of the Darcy velocity and pressure simultaneously. Well–posedness, stability, and convergence are well known for such a model and are presented within this work for both the continuous and discrete systems described within. An extension of Darcy's equations, and their analysis, is also presented for application to flow in porous media incorporating networks of (possibly) intersecting fractures; pooling together a few models found within the literature, along with their anaylses, as succinctly as possible.

The first main contribution of this thesis is the development of a finite element interpolant within fractures, in order to trace streamlines across fracture–bulk interfaces, while retaining physical laws. We define an interpolant for the velocity within the fracture, which has been expanded employing the procedure developed by Hægland, et al. [63, 66, 64], in a post–processed fashion, and show that conservation of mass and Darcy's law may still be weakly satisfied when streamline tracing. Since fractures in the domain are of a dimension one lower than the surrounding bulk material, there is no transversal flow information across the fracture widths themselves, hence the need for such a procedure.

The second main contribution relates to obtaining estimates in the errors of the computed numerical approximations. Indeed, in order to obtain accurate simulations of porous media flow, we present and apply the dual–weighted–residual (DWR) method in the context of Darcy's equations for generic quantities of interest. We aim to define elementwise indicators, derived from estimates in the DWR method, to develop and utilise the adaptive tools required to obtain efficient simulations of flow in porous media. We define elementwise indicators via integration–by–parts of the DWR estimate, but also present a couple of alternative decompositions that may be employed instead. Through the use of numerical examples, we investigate a property known as sharpness for the defined indicators; a prop-

erty paramount in applications, in order to gauge how reliable the simulations may actually be. We also test the reliability of the proposed error estimate itself, for quantities of interest of Darcy's equations. Our experiments reveal that when the MFEM employs RT elements, the proposed indicators are not sharp; meanwhile, a BDM implementation remains efficient. However, in both cases, the proposed DWR error estimate reliably predicts the error in approximations of linear quantities of interest.

The third main contribution is the attainment of accurate simulations of travel times of particles in porous media. In particular, the linearisation[1] of the functional employed to compute travel times. A key component in the application of the DWR method, when travel time is the quantity of interest, is the Gâteaux derivative of this functional. Here, we derive an exact expression for the derivative, based on employing a backwards–in–time initial–value–problem (IVP), considered to be dual, or adjoint, to the trajectory of the leaked solute. In doing so, the adaptive tools defined earlier may be utilised to obtain accurate simulations of the travel time for flows in porous media. Indeed, we showcase a few numerical examples in order to judge how reliable the proposed estimate is for the travel time functional. Of particular note is the final experiment of the thesis, in which real–life units found at the Sellafield site (located in Cumbria, in the United Kingdom) inspire the defined domain, in order to assess how well the estimate, through adaptive mesh refinement, performs in a physically motivated example. We show that it is indeed still the case that the error estimate performs very well, in this example.

1.2 Related work

Portions of the following literature are from [73], by the same author.

Models for porous media and fractured flow

Groundwater flow, governed by Darcy's equations, represents a viable simplified model for the fluid flow [96, 42] and will be exploited within this thesis. It is assumed that whilst the surrounding rocks may not be saturated while the repository is being built, they will eventually become saturated in its operational lifetime; thus, it is sufficient that in a post–closure assessment we can consider saturated conditions, and therefore use the time independent Darcy's equations as our model, rather than the usual Richards equations for capillary flow [43, p. 3]. Of course, within this context and in many others, there are more sophisticated models, cf. [109, 133, 113, 94, 27, 104, 61, 47, 99, 24] and the references cited

[1] This contribution, found in Chapter 7 in this thesis, is taken from the published work [73] whose contribution was obtained during, and for, the study of this PhD.

therein, where large–scale structures and complex topographical features, such as fracture networks or vugs and caves, are considered as parts of the domain. The solution–based *a posteriori* error estimation for these more sophisticated models may be found in, for example, the articles [41, 39, 40, 132, 71, 125, 97] and the references cited therein.

In the past few decades, homogenisation methods were used to obtain double continuum, or dual porosity models, and these were typically used to model the flow in fractured porous media [10]. However, as concurred by [84, 55], these models have their limitations. For example, a dual porosity model is not adequate for disconnected networks of fractures, nor is it typically good at handling an amount of fractures deemed too small, or too large. In these cases, it is better to represent the fractures explicitly with discrete–fracture–matrix (DFM) models instead. The strategy posed within DFM models is to average the governing equations across the fracture apertures. Assuming they are partially filled with debris, Darcy's law and conservation of mass hold also within the fractures; by averaging the equations a reduced model is obtained, coupled to the bulk Darcy flow with some interface conditions. In the earlier work [3], a model was presented assuming that the permeability within a single, non–immersed, fracture was much higher than in the bulk. This lead to the assumption of pressure continuity across the fracture. This model was later generalised in [94, 53, 6] to allow for the low permeability case, where such interface conditions were derived and pressure continuity was no longer required. Extensions to two–phase flows were later established in [59, 78], as well as coupling transport to the fluid flow in [4, 88], and the references therein. For networks of fractures, which may intersect, and may be fully–immersed, we refer to [54, 55]. Moreover, the conditions imposed in [55] at the intersection of fractures can be generalised further, as in [54, 46]. Furthermore, in the case where a network of fractures has permeability much higher than the surrounding porous rock, flow in the bulk domain can simply be ignored and only that within the fractures is considered; these models, typically referred to as discrete–fracture–network (DFN) models can be found in, for example, [58], and the references therein. However, we proceed with DFM models in mind. We mention also that models exist for which Darcy's law does not hold in the fractures, for example in [57], and that curved fractures may be considered [100, 34].

Utilising any of the above models for flow in fractured and non–fractured porous media relies on empirical data to generate information concerning the models. Indeed, the coefficients of material parameters, forcing terms, and the geometries of the domain are assumed known in applications. In reality, there is uncertainty associated with this information that is not addressed in a deterministic implementation; uncertainty in the model of course leads to uncertainty in solutions, streamlines, and quantities involving those solutions. Such

uncertainty and how to address it is beyond the scope of this thesis. We refer mainly to the work [43], and the references cited therein; here, uncertainty is addressed and developments for travel times in a random setting are made.

Darcy approximation and error estimation

Control of the discretisation error generated by the numerical approximation of partial differential equations (PDEs) has witnessed significant advances due to contributions in *a posteriori* error analysis and the use of adaptive mesh refinement techniques. Such algorithms aim to save computational resources by refining only a certain subset of elements, making up part of the underlying mesh, that contribute most to the error in some sense. In particular, we refer to the early works [1, 11, 12], and the references cited therein.

The original solution–based *a posteriori* error analysis for Darcy's equations, employing Raviart–Thomas elements, was undertaken by Braess and Verfürth in [28]; we also refer to [15, 14] which consider augmented, stabilised versions of Darcy's equations, whose original L^2–bound analysis was given in the article [88]. Moreover, there is a vast literature for the *a posteriori* error analysis for Darcy's equations in a variety of contexts. For example, [23, 107] presents the analysis for time–dependent Darcy flow; [48] uses the finite volume method for two–phase Darcy flow; and [13] uses an augmented discontinuous Galerkin method. For the (residual) norm–based *a posteriori* error analysis for Darcy's equations, and mixed finite element methods in general, we refer to the articles [127, 128] by Vohralík, and the references cited therein. In [126], similar to [36], residual–based *a posteriori* error bounds are derived by considering a Helmholtz decomposition in order to overcome the need for a saturation assumption previously assumed by [28]. Moreover, in [5] an enhanced velocity mixed finite element method is used instead.

Typically, in applications we are not concerned with pointwise accuracy of the numerical solution of PDEs themselves, but rather quantities involving the solution (which we will refer to as being goal quantities, or quantities of interest); in this setting goal–oriented techniques are employed to bound the error in the given quantity of interest. Work in this area was first pioneered by [17, 18] and [62], which established the general framework [106, 114] of the dual, or adjoint, weighted–residual method (DWR). When the quantity of interest is represented by a nonlinear functional, a linearisation about the numerical solution is employed in order for the problem to become tractable and computable; hence, the nonlinear functional must be differentiated. Solving a discrete version of this linearised adjoint problem allows for an estimate of the discretisation error induced by the quantity of interest, which may be decomposed further to drive adaptive refinement algorithms.

Unweighted, residual–based estimates can be derived based on employing certain stability estimates [50], but this results in meshes independent of the choice of the quantity of interest. The DWR approach has been applied to a vast number of different applications including the Poisson problem [17], nonlinear hyperbolic conservation laws [70], fluid–structure interaction problems [124], application to Boltzmann-type equations [72], as well as criticality problems in neutron transport applications [67].

An energy norm based approach can also be found in [33], where adaptive mesh refinement is employed to accurately compute streamlines via a streamfunction approach. More generally, the goal–oriented error estimation for linear functionals of Darcy's equations can be found in [101] which employs equilibrated–flux techniques in order to achieve a guaranteed bound. Furthermore, [92] extends this work to bound higher–order terms to demonstrate that the *a posteriori* bounds are asymptotically exact, as well as taking into account the error induced by inexact solvers.

For a set of slightly different homogenised problems, [35] presents the goal–oriented error estimation for general quantities of interest. We also point out the existing literature for goal–adaptivity in the context of contaminant transport, presented in the articles [20, 87], but which differs slightly from the work presented here. For the numerical experiments presented in Section 6.6, for example, following [25], we employ a mixed finite element method using the Brezzi–Douglas–Marini (BDM) elements. These elements, introduced originally in [31], define approximation spaces that have $H(\mathrm{div})$–conformity; continuity of the normal traces of velocity fields across element interfaces is thus guaranteed, and this is a characteristic vital for streamline computations. As noted, for example, in [44], there are problems associated with using the standard, nodal-based elements; most importantly is the attainment of nonphysical streamlines, as well as there being a lack of mass conservation at an elemental level. These problems are eradicated when a mixed formulation is used instead, where the velocity and pressure solutions are computed simultaneously.

Approximation of fractured porous media

The well–posedness of the aforementioned DFM models for flow in fractured porous media has been fully established. Indeed, the problem in mixed form in the original work [94] was proved to be well–posed within the same article, and this was partially extended to cover the case of an immersed fracture in [6]. By partially, we mean that in the latter, the problem was written in a second–order form, only requiring the pressure as a solution. For networks of fractures in mixed form, well–posedness was proved in [54], assuming that the pressure was imposed on part of the fracture boundary. In [55] this proof was extended to

cover well–posedness for a network of fractures, fully immersed in the domain.

As described in the unifying work [27], there are a few distinct features that are attractive in a numerical method, when attempting to approximate the fractured porous media problem; these features meet the criteria of being both robust and flexible. The attributes such a numerical method should possess are the following: mass conservation, grid flexibility, robustness in physically relevant limits, and are provably stable and convergent.

The notion of a mass conservative numerical scheme is paramount when the flow field is paired with transport. Indeed, transport schemes are typically very sensitive when non–conservative flow fields are used [89]. The two main methods which can ensure such mass conservation are finite volume methods (FVM) and mixed finite element methods (MFEM). Finite volume methods applied to fractured porous media, [6, 29, 83, 84, 117], are particularly useful in keeping condition numbers low and thereby reduce computational cost; for example, in [27], hybrid cells for fractures are added between the bulk matrix cells, and the small cells formed at the fracture intersections are excluded with the use of transformations. While formally consistent, these methods lack convergence analyses and typically require the computational grid to conform to the fracture network. However some work, in [122], has been undertaken to use a FVM with non–matching grids. Moreover, MFEM are great at imposing mass conservation locally since the flux, i.e., the Darcy velocity, is defined as a separate variable within the scheme. Moreover, these methods sit nicely within the readily available tools from functional analysis, which can be utilised to prove convergence and stability results [25, 30]. Combining the two methods is also an option, as done, for example, in [102], when considering transport in heterogeneous and fractured porous media; a MFEM is used for the flow problem, while a node–centered FVM is used for transport.

Furthermore, there is the issue of grid flexibility; indeed, generating a good quality computational grid for realistic fracture networks is very difficult. In an actual oil reservoir, for example, several thousands of fractures can be found, which can be fairly close together and intersecting [55]. There is an obvious need to accommodate networks like these in the choice of numerical method, for purposes in application. A computational grid which conforms to the network of fractures is often characterised by elements that are extremely small in size, and thanks to high aspect ratios and small angles, are often of a poor quality. In [93], it is suggested to locally modify the positions and geometry of fractures in order to keep an existing computational grid, and this can be done since the fractures are, in most cases, affected by some level of uncertainty anyway [21]. However, it is more preferred to avoid this geometric conformity in the first place. In the extended finite element method (XFEM), [45, 75, 54, 118], the surroundings of the fracture network are meshed independently from

the fractures themselves; the grids posed on the fractures are then added after the underlying grid, or mesh, is established. Thus, in the XFEM setting, fractures are able to cross through the domain and cut through elements in the underlying computational mesh. There are also some methods which allow for a partial nonconformity, in that the fracture network still aligns with the mesh on the bulk domain, but is in itself meshed independently, see for example [27, 56, 52]. Using XFEM has its advantages, but the elements that are cut may become arbitrarily small and special constructions are often required to retain stability. One could consider also the embedded finite element method (EFEM) [32, 88], the embedded DFM (EDFM) [90, 110] and the projection–based EDFM (pEDFM) [135, 80, 88] as alternative choices. In each of these, fractures are allowed to cut elements arbitrarily. While EFEM and EDFM can only handle the case of highly permeable fractures, pEDFM is able to handle low permeabilities as well; this latter method also has the fractures meshed independently of the underlying bulk grid.

There are still some alternative numerical methods that could be chosen to approximate flow in fractured porous media. For example in the works [55, 8, 54], the mimetic finite difference method (MFD) is employed for networks of fractures. MFD is known to be robust, even with highly distorted computational grids, and is related to the virtual element method (VEM) [19, 129, 47], which can be regarded as its evolution. These methods are both known to preserve the quality of the solution for very general grids, employing either polygonal or polyhedral elements that may be highly anisotropic. Discontinuous Galerkin methods (dG) have also been utilised for this problem in [47, 7]; while still expecting the computational grid to conform to fractures, each of these three methods are still very adaptable. Lastly, we mention the use of mortar methods. Introduced in [22], both non–matching grids and intersections of fractures can be handled in a very natural way [56, 9, 112]. The work undertaken in [27] sees the development of a MFEM utilising the mortar method framework, using fluxes as the mortar variable instead of the usual pressure. Moreover, being formulated hierarchically, a unified treatment of the porous rock, fractures, and intersections, in arbitrary dimensions, is obtained. This method is also robust with respect to the apertures of the fractures, allowing the limiting case of them vanishing and the fractures collapsing.

There has been some work undertaken regarding the *a posteriori* error estimation for flows in fractured porous media. In the articles [39, 40, 71, 125, 98] we see the derivation of adaptive routines and residual–based estimates for the solutions of the usual DFM models. In [125], it is the mixed–dimensional framework from [26, 27] that is utilised to derived such error bounds.

Streamline tracing and travel time

The time–of–flight for a non–sorbing solute to reach the surface, or boundary, of the domain is a key quantity when considering the post–closure safety assessment of facilities intended for use as deep geological storage of high–level radioactive waste [42, 105, 103, 96]. This time taken is represented, in this work, by the (nonlinear) travel time functional. Previously, work undertaken in [42] employed goal–oriented *a posteriori* error estimation for this functional, relying on a finite–difference approximation of its Gâteaux derivative. Indeed, time–of–flight calculations typically go hand–in–hand with streamline computations, cf. below.

Numerical streamline tracing within this work can be evaluated exactly under a lowest order approximation; indeed, following standard techniques outlined in [43, 82]. In the case of higher–order approximations, streamline computations become non–trivial and other techniques, such as time-stepping methods, must be employed instead. It has been shown however, that for divergence–free flows, the streamlines may be evaluated via a streamfunction approach to a high accuracy, for both low and high-order implementations [95, 81]. Outside of a finite element approximation, methods for streamline tracing are more sought after; indeed, in the finite volume setting, the velocity inside of grid cells may be unknown and methods for such tracing must be developed, as in [133, 65]. Moreover, application to fully unstructured grids may be found in [108] as well as tracing independent of the underlying mesh in [16] and for irregular geometries in [85], and, of course, the many references found therein. Lastly, the numerical streamline tracing in three spatial dimensions was pursued in [91], utilising a finite element method.

For extension of numerical streamline tracing to incorporate fractures in the porous media, we largely refer to the collection of works in [63] and the references cited therein, in which a finite volume method is used to obtain the numerical approximations of the fluid flow. Moreover, we also refer to the more recent work by [38] whose streamline approach is based on a boundary layer method. Furthermore, within, for example, [130, 134, 79, 2] and the many references stated therein, further developments in streamline tracing for fractured media are achieved for application to realistic, physical problems, such as water breakthrough, barrier–fracturing and the effects of number and position of fractures on time–of–flight calculations. There is also the early work by [76] in which flow at fracture junctions is discussed.

1.3 Thesis overview

Chapter 2: Preliminaries

Within this chapter, we present some preliminary results relating to traces, function spaces, and well–posedness of variational, or weak, problems of saddle–point type, in an abstract setting. These are to be used throughout the thesis.

Chapter 3: Darcy's equations and discretisation

Within this chapter, the analysis of Darcy's equations and their numerical approximation by the MFEM utilising RT and BDM elements can be found. Continuous and discrete well–posedness, discrete stability, and convergence of approximations are presented and proved, employing results from Chapter 2.

Chapter 4: Flow in fractured porous media

Similar to Chapter 3, we present here the model and analysis for flow in fractured porous media, proving the same results in this different setting.

Chapter 5: Streamlines through fracture porous media

Within this chapter, we employ the expansion procedure of one dimensional fractures in order to trace streamlines through them. An interpolant of the velocity field, post–processed using the existing Darcy velocities in the bulk and on the fractures, is defined in the continuous and discrete setting so that Darcy's law and conservation of mass are still weakly satisfied within the expanded fracture.

Chapter 6: Goal–oriented adaptivity for Darcy's equations

The dual–weighted–residual (DWR) method is presented within this chapter in an abstract setting, and is further contextualised in application to Darcy's equations. The definition of the elementwise indicators is given, and these are used in numerical experiments whose aim is to test the sharpness of the defined indicators as well as the reliability of the proposed error estimate for quantities of interest represented by generic linear functionals.

Chapter 7: The travel time functional

This chapter contains everything related to the travel time functional. We see how streamlines are computed in porous media, in the discrete setting (with no fractures) and define the travel time functional. The main result is presented and proved, deriving an expression for

the derivative of the travel time functional, which is employed in the DWR method in order to estimate the error in approximate travel time in a handful of examples. This chapter concludes with the Sellafield inspired example.

Chapter 8: Conclusions

To conclude this thesis, we summarise the work presented within each of the above chapters and draw some conclusions based on the insights gained throughout. Some details and discussion are given in view of possible extensions of this work.

Chapter 2

Preliminaries

Within this chapter, we first discuss the notion of the trace of both scalar and vector–valued functions and define some function spaces that will be used throughout the thesis. Furthermore, we present an abstract problem of saddle–point type, a form typical of variational, or weak, formulations of systems of elliptic PDEs; for example Darcy's equations. We address well–posedness of this problem and its discrete counterpart, concluding with a statement of quasi–optimality, a result which can be utilised to prove convergence results for the solutions and their approximations.

2.1 Traces and function spaces

The start of this chapter aims to establish some useful notation and function spaces that will be used throughout the rest of this thesis. Firstly, $\Omega \subset \mathbb{R}^d$, $d = 2, 3$, will denote an open and bounded domain with a Lipschitz, or polygonal, boundary $\partial\Omega$. We will fix the spatial dimension $d = 2$ later. Furthermore, the space of square–integrable functions on Ω is denoted, as usual, by $L^2(\Omega)$; the usual notation $H^m(\Omega)$ for the associated Sobolev spaces, with $m \geq 0$ an integer, will be used. The analogous vector–valued spaces in $\mathbb{R}^d$ will be denoted here by $[L^2(\Omega)]^d$ and $[H^m(\Omega)]^d$, respectively.

A concept most vital in both functional analysis and in numerical approximation schemes such as the finite element method, is the notion of the restriction, or trace, of a function at the boundary of the domain. Indeed, although continuous functions are well–defined here, the same may not be said for functions in Sobolev spaces. However, it is well known in functional analysis that this notion of trace can be extended to less regular functions, in

particular those in $H^1(\Omega)$; if the boundary of the domain is deemed *smooth enough*, for example being Lipschitz continuous, then we may define

$$v|_{\partial\Omega} := T[v],$$

where $T : H^1(\Omega) \to L^2(\partial\Omega)$ is the so–called trace–operator. This operator extends the notion of trace such that for $v \in C^0(\overline{\Omega})$, the trace $T[v]$ coincides with its actual, well–defined, restriction to the boundary. Moreover, the span of all the traces of $H^1(\Omega)$ functions is a proper dense subspace of $L^2(\partial\Omega)$, usually denoted as the fractional Sobolev space $H^{\frac{1}{2}}(\partial\Omega)$; the (algebraic) dual of this space is represented by the notation $H^{-\frac{1}{2}}(\partial\Omega)$.

A common occurrence in, for example, solving Poisson's equation [86, p. 72], is a function space defined according to this trace operator, and is given below as Definition 2.1.

Definition 2.1. $H_0^1(\Omega) := \{v \in H^1(\Omega) : v|_{\partial\Omega} = 0\}$.

Vector–valued functions play a key role within this work. In particular, we are interested in those square–integrable functions whose divergence is also square–integrable; these are defined in Definition 2.2 below.

Definition 2.2. $H(\mathrm{div}, \Omega) := \{\mathbf{v} \in [L^2(\Omega)]^d : \nabla \cdot \mathbf{v} \in L^2(\Omega)\}$.

This Hilbert space is equipped with the norm

$$\|\mathbf{v}\|^2_{H(\mathrm{div},\Omega)} := \|\mathbf{v}\|^2_{[L^2(\Omega)]^d} + \|\nabla \cdot \mathbf{v}\|^2_{L^2(\Omega)}.$$

Moreover, the normal–trace of a function in $H(\mathrm{div}, \Omega)$ is especially important and not immediately defined. That is, if $\mathbf{n} = \mathbf{n}(\mathbf{x})$ denotes the unit outward normal to the boundary $\partial\Omega$, the quantity $(\mathbf{v} \cdot \mathbf{n})|_{\partial\Omega}$ may not be well–defined. The technical details will be omitted, but [25, p. 49] ensures that it is possible to define this normal-trace in the space $H^{-\frac{1}{2}}(\partial\Omega)$; i.e., the normal–trace is well–defined as an action, or functional, acting on $H^{\frac{1}{2}}(\partial\Omega)$. This idea is realised in the following Green's formula[1]. Denoting $\langle\cdot,\cdot\rangle_{\partial\Omega}$ as the duality pairing between $H^{-\frac{1}{2}}(\partial\Omega)$ and $H^{\frac{1}{2}}(\partial\Omega)$, we thus have Proposition 2.3 below.

Proposition 2.3. *For* $\mathbf{v} \in H(\mathrm{div}, \Omega)$ *we have*

$$\langle \mathbf{v} \cdot \mathbf{n}, \psi \rangle_{\partial\Omega} = \int_\Omega \psi \nabla \cdot \mathbf{v} + \int_\Omega \mathbf{v} \cdot \nabla\psi,$$

for all $\psi \in H^1(\Omega)$.

Employing Proposition 2.3, one can show that the trace operator

$$T^d : \mathbf{v} \in H(\mathrm{div}, \Omega) \to (\mathbf{v} \cdot \mathbf{n})|_{\partial\Omega} \in H^{-\frac{1}{2}}(\partial\Omega)$$

[1] Commonly referred to as a form of integration–by–parts.

is surjective. This notion of trace allows for the definition of essential function spaces, whose use will become apparent when Darcy's equations are discussed in Chapter 3. To this end, suppose the boundary $\partial\Omega$ is partitioned into so–called Dirichlet and Neumann parts, i.e. $\partial\Omega = \partial\Omega^D \cup \partial\Omega^N$ such that their intersection is empty. We may now define the following function spaces.

Definition 2.4. $H^1_{0,D}(\Omega) := \{v \in H^1(\Omega) : v|_{\partial\Omega^D} = 0\}$.

Definition 2.5. $H_{0,N}(\mathrm{div},\Omega) := \{\mathbf{v} \in H(\mathrm{div},\Omega) : \langle \mathbf{v}\cdot\mathbf{n}, \psi\rangle_{\partial\Omega} = 0,\ \forall \psi \in H^1_{0,D}(\Omega)\}$.

Essentially, the space $H_{0,N}(\mathrm{div},\Omega)$ has those functions in $H(\mathrm{div},\Omega)$ whose normal–trace vanishes on $\partial\Omega^N$. However, according to [25, p. 50], *pathological properties* of the spaces $H^{\frac{1}{2}}(\partial\Omega^D)$ and $H^{-\frac{1}{2}}(\partial\Omega^N)$ disallows such a simple definition; however, remaining mathematically rigorous, Definition 2.5 will do and practically means the same thing.

With, momentarily, $d = 2$, it will be useful at this point to mention how the space $H_{0,N}(\mathrm{div},\Omega)$ interacts with respect to meshes, triangulations, or general partitions of the domain Ω; this behaviour will ultimately point to the most suitable choice of approximation spaces for the finite element implementation discussed in Section 3.3 for Darcy's equations. Paramount to the definitions of these approximation spaces is that if $\mathscr{T}_h$ is a partition[2] of $\overline{\Omega}$ into non–overlapping elements κ then functions in $H_{0,N}(\mathrm{div},\Omega)$ can be discontinuous across element interfaces, but their normal–traces across the interfaces are always weakly continuous. This is demonstrated in Proposition 2.6.

Proposition 2.6. *Define the broken Sobolev space*

$$Y(\Omega) := \{\mathbf{v} \in [L^2(\Omega)]^2 : \mathbf{v}|_\kappa \in H(\mathrm{div},\kappa),\ \forall \kappa \in \mathscr{T}_h\} \equiv \prod_{\kappa\in\mathscr{T}_h} H(\mathrm{div},\kappa).$$

Then,

$$H_{0,N}(\mathrm{div},\Omega) = \{\mathbf{v} \in Y(\Omega) : \sum_{\kappa\in\mathscr{T}_h} \langle \mathbf{v}\cdot\mathbf{n}_\kappa, \psi\rangle_{\partial\kappa} = 0,\ \forall \psi \in H^1_{0,D}(\Omega)\},$$

where $\mathbf{n}_\kappa$ *is the unit outward normal vector on the element boundary* $\partial\kappa$.

Proof. See [43, pp. 30–31], for example. □

2.2 Variational formulation and uniqueness of solution

With the notation and ideas described in Section 2.1 we can now proceed onto discussing the PDE problems of interest, which in the finite element method framework are usually transformed into a variational formulation first. For the sake of presentation, we will first

[2]These partitions will always be shape–regular triangulations in this thesis.

consider a class of abstract variational problems known as being of saddle–point type. The uniqueness and existence of solutions to such problems will be covered in a general manner, which will then be applied directly to Darcy's equations in Section 3.

To this end, let V and Q be Hilbert spaces equipped with the norms $\|\cdot\|_V$ and $\|\cdot\|_Q$, respectively. Denote their dual spaces by V^* and Q^*, respectively as well. Given the continuous bilinear forms $a(\cdot,\cdot) : V \times V \to \mathbb{R}$ and $b(\cdot,\cdot) : V \times Q \to \mathbb{R}$, and the continuous linear functionals $G \in V^*$ and $F \in Q^*$, the abstract saddle–point problem is to:

Find $(u, p) \in V \times Q$ such that

$$a(u, v) + b(v, p) = \langle G, v\rangle_{V^*,V} \quad \forall v \in V, \tag{2.1}$$

$$b(u, q) = \langle F, q\rangle_{Q^*,Q} \quad \forall q \in Q. \tag{2.2}$$

We denote the continuity constants for $a(\cdot,\cdot)$ and $b(\cdot,\cdot)$ by $\|a\|$ and $\|b\|$, respectively, i.e., we have

$$|a(v, w)| \le \|a\|\|v\|_V\|w\|_V \quad \forall (v, w) \in V \times V,$$
$$|b(v, q)| \le \|b\|\|v\|_V\|q\|_Q \quad \forall (v, q) \in V \times Q.$$

Moreover, the unique solvability of the saddle-point problem (2.1, 2.2) is given by Theorem 2.7; we omit the proof, which can be found in most textbooks on the topic, for example in [25, p. 223].

Theorem 2.7. *Under the foregoing notation, let $\langle\cdot,\cdot\rangle_{Q^*,Q}$ denote the duality pairing between Q^* and Q. Associate to the bilinear form $b(\cdot,\cdot)$ the continuous linear operator $\mathfrak{B} : V \to Q^*$ defined to be such that*

$$\langle \mathfrak{B}v, q\rangle_{Q^*,Q} = b(v, q) \quad \forall v \in V \ \forall q \in Q.$$

Then, if the following two conditions are each satisfied, the saddle–point problem (2.1, 2.2) has a unique solution $(u, p) \in V \times Q$.

- *The image, or range, of $\mathfrak{B}$ is equal to Q^*, i.e. $\mathfrak{B}$ is surjective.*
- *The bilinear form $a(\cdot,\cdot)$ is coercive on the kernel of $\mathfrak{B}$, i.e. there is a constant $\alpha > 0$ such that*

$$a(v, v) \ge \alpha\|v\|_V^2 \quad \forall v \in \mathrm{Ker}(\mathfrak{B}). \tag{2.3}$$

The first condition in Theorem 2.7 is equivalent to the well–known inf–sup condition on the bilinear form $b(\cdot,\cdot)$, commonly referred to as the Banach–Nécas–Babŭska compatibility condition, which says that

$$\inf_{q\in Q}\sup_{v\in V}\frac{b(v, q)}{\|v\|_V\|q\|_Q} =: \beta > 0.$$

It should be noted also, that Theorem 2.7 provides sufficient, but not necessary, conditions for the uniqueness and existence of a solution to (2.1, 2.2). The surjectivity of $\mathfrak{B}$ is necessary, but the coercivity of $a(\cdot,\cdot)$ on the kernel of $\mathfrak{B}$ is actually too strong; an inf–sup statement on the bilinear form $a(\cdot,\cdot)$ provides the necessary condition for well–posedness of this saddle–point problem, [25, p. 226], however, in our application within this thesis, the condition (2.3) is good enough. It is the continuity of the bilinear forms and the linear functionals, which we assume to be true, along with the conditions stated in Theorem 2.7 which imply the well–posedness of the problem.

2.3 Discrete well–posedness and approximation

Suppose $V_h \subset V$ and $Q_h \subset Q$ are finite–dimensional subspaces in which approximations of (u,p), solving (2.1, 2.2), are sought. For example, a mixed finite element method; these methods are simply the Galerkin method, which defines the following discrete problem:

Find $(u_h, p_h) \in V_h \times Q_h$ such that

$$a(u_h, v_h) + b(v_h, p_h) = \langle G, v_h\rangle_{V^*,V} \quad \forall v_h \in V_h, \tag{2.4}$$

$$b(u_h, q_h) = \langle F, q_h\rangle_{Q^*,Q} \quad \forall q_h \in Q_h. \tag{2.5}$$

Applying Theorem 2.7 to the problem (2.4, 2.5) of course requires a discrete notion of the associated operator $\mathfrak{B}$, which we will denote with $\mathfrak{B}_h$.

Following the theory outlined in [25, Chapter 5]. The discrete operator $\mathfrak{B}_h$ will be the restriction $\mathfrak{B}_{V_h,Q_h^*}$, i.e., $\mathfrak{B} : V_h \to Q_h^*$; the adjoint operator $\mathfrak{B}_h^*$ will be the restriction $\mathfrak{B}^*_{Q_h,V_h^*}$. Each of these operators are defined as the following compositions

$$\mathfrak{B}_h := \pi_{Q_h^*}\mathfrak{B}E_{V_h},$$
$$\mathfrak{B}_h^* := \pi_{V_h^*}\mathfrak{B}E_{Q_h},$$

where E_{V_h} is the extension operator from V_h to V, and $\pi_{Q_h^*}$ is the projection operator from Q^* to Q_h^*.

Written explicitly, Theorem 2.7 becomes, for the discrete problem (2.4, 2.5), the satisfaction of the two following properties.

- The image of $\mathfrak{B}_h$ is equal to Q_h^*.
- The bilinear form $a(\cdot,\cdot)$ is coercive on

$$\mathrm{Ker}(\mathfrak{B}_h) := \{v_h \in V_h : b(v_h, q_h) = 0,\ \forall q_h \in Q_h\},$$

i.e. there is a constant $\alpha_h > 0$ such that

$$a(v_h, v_h) \geq \alpha_h \|v_h\|_V^2 \quad \forall v_h \in \mathrm{Ker}(\mathfrak{B}_h).$$

As usual, the first property is equivalent to the discrete inf–sup condition

$$\inf_{q_h \in Q_h} \sup_{v_h \in V_h} \frac{b(v_h, q_h)}{\|v_h\|_V \|q_h\|_Q} =: \beta_h > 0, \tag{2.6}$$

However, it is not clear from (2.6) being satisfied whether or not the constant β_h depends on h, which may, for example, represent the mesh size parameter in a finite element setting. To be more careful, we say that the discrete inf–sup condition is satisfied if we have (2.6) *and* the constant is bounded below by some $\beta_* > 0$ as $h \to 0$, although this detail is not required to establish well–posedness. Indeed, it is in convergence analysis that this plays a role, and while we may still be able to obtain convergence estimates in the case that β_h depends on h, these will not be optimal [25, p. 268]; the same is true of the coercivity constant α_h, so it is useful to think of a different constant C_a such that $\alpha_h \geq C_a > 0$, independent of h, when considering the discrete setting. A sufficient condition for the existence of C_a is the inclusion of kernels $\mathrm{Ker}(\mathfrak{B}_h) \subset \mathrm{Ker}(\mathfrak{B})$ since here we have $\alpha_h = \alpha =: C_a$.

Indeed, we can view Theorem 2.7 as a fairly general version of (discrete) well–posedness neglecting the possible h–dependence of the coercivity and inf–sup constants discussed above. However, the situation $\beta_h \to 0$ may come to mind if left unaddressed. We refer the reader to the discussion in [25, pp. 301–302] for more details. To rid this dependence on h of the discrete inf–sup constant β_h, [25, pp. 303–305] has some additional considerations. For example, the existence of operators $\Pi_h : V \to V_h$ such that there exist a constant $C_\Pi > 0$ such that

$$\|\Pi_h v\|_V \leq C_\Pi \|v\|_V \quad \forall v \in V$$

gives the discrete inf–sup constant $\beta_h = \beta / C_\Pi$, independent of h and where β is an inf–sup constant for the continuous problem. These extra intricacies are taken into account in Section 3.4 when discussing the well–posedness and convergence for the mixed finite element approximation of Darcy's equations.

We note that within this setting, conformity (i.e. $V_h \subset V$ and $Q_h \subset Q$) transfers the continuity of the bilinear forms $a(\cdot, \cdot)$ and $b(\cdot, \cdot)$ directly from their continuous spaces to the discrete ones, with the same continuity constants $\|a\|$ and $\|b\|$, respectively.

Furthermore, this discussion ultimately leads to the following quasi–optimality result, which may be regarded as an extension of the well–known Céa's lemma for mixed systems giving rise to this form of saddle–point problem.

Theorem 2.8. *Let $(u, p) \in V \times Q$ be the solution of the problem (2.1, 2.2), and $(u_h, p_h) \in V_h \times Q_h$ be the solution of the discrete problem (2.4, 2.5); assume each of these problems are well–posed according to Theorem 2.7. Letting β_* be an inf–sup constant for the discrete pair (V_h, Q_h) and C_a the coercivity constant for $a(\cdot, \cdot)$ on $\mathrm{Ker}(\mathfrak{B}_h)$, one has the following estimate, with a constant C depending on $\|a\|$, $\|b\|$, β_*, and C_a, but independent of h:*

$$\|u - u_h\|_V + \|p - p_h\|_Q \leq C \left(\inf_{v_h \in V_h} \|u - v_h\|_V + \inf_{q_h \in Q_h} \|p - q_h\|_Q \right).$$

Moreover, when we have the inclusion of the kernels $\mathrm{Ker}(\mathfrak{B}_h) \subset \mathrm{Ker}(\mathfrak{B})$, we have

$$\|u - u_h\|_V \leq C \inf_{v_h \in V_h} \|u - v_h\|_V.$$

Proof. See [25, Theorem 5.2.5], for example. □

Theorem 2.8 indeed states that if both the continuous and discrete problems are well–posed, with the discrete constants independent of h, then we have an almost best approximation result in the form of a mixed, quasi-optimality estimate. Within the contexts of the chosen function spaces and their discrete counter parts (e.g., finite element approximations), interpolation estimates alongside this theorem give rise to *a priori* error estimates for the given problem; these estimates give insight into the expected rate of convergence, under, for example, uniform mesh refinement, of the approximate solutions obtained through solving the discrete problem.

Chapter 3

Darcy's equations and discretisation

Within this chapter, Darcy's equations and their approximation via a mixed finite element method will be presented. Well–posedness results in both the continuous and discrete settings will be given, in particular for both choices of arbitrary order Raviart–Thomas (RT) and Brezzi–Douglas–Marini (BDM) approximation spaces. Convergence of the discrete solutions will be addressed, combining interpolation results with the quasi–optimality result given previously in Theorem 2.8.

3.1 The governing equations

We denote, as standard in this thesis, $\Omega \subset \mathbb{R}^d$ $(d = 2, 3)$ as an open and bounded domain with Lipschitz, or polygonal, boundary $\partial\Omega$. We assume the boundary is partitioned as $\partial\Omega = \partial\Omega^D \cup \partial\Omega^N$. Darcy's equations are used to model the flow of saturated groundwater and are given by the following system of first–order PDEs, where we aim to seek the Darcy velocity $\mathbf{u} : \overline{\Omega} \to \mathbb{R}^d$ and the hydraulic head, or pressure, $p : \overline{\Omega} \to \mathbb{R}$ such that:

$$\mathbf{K}^{-1}\mathbf{u} + \nabla p = \mathbf{0} \quad \text{in } \Omega, \tag{3.1}$$

$$\nabla \cdot \mathbf{u} = f \quad \text{in } \Omega, \tag{3.2}$$

$$p = g_D \text{ on } \partial\Omega^D, \tag{3.3}$$

$$\mathbf{u} \cdot \mathbf{n} = 0 \quad \text{on } \partial\Omega^N. \tag{3.4}$$

The equation (3.1) is referred to as Darcy's law, while (3.2) is the equation for conservation of mass[1].

We briefly discuss the other terms appearing in (3.1) – (3.4). We denote with $\mathbf{n} = \mathbf{n}(\mathbf{x})$ the unit outward normal vector to $\partial\Omega$. The matrix $\mathbf{K} = \mathbf{K}(\mathbf{x}) \in \mathbb{R}^{d\times d}$ is the hydraulic conductivity of the domain, representing (indeed, depending on) the permeability of the porous material making up the domain[2]. We assume that $\mathbf{K}$ satisfies the following property: *the smallest eigenvalue of* $\mathbf{K}$ *is bounded uniformly away from zero, and the largest eigenvalue is uniformly bounded, both with respect to* $\mathbf{x}$; i.e. there exist $\lambda_- > 0$ and $\lambda_+ \geq \lambda_-$ such that

$$\lambda_-|\mathbf{z}|^2 \leq \mathbf{z}^\top \mathbf{K}\mathbf{z} \leq \lambda_+|\mathbf{z}|^2 \ \forall \mathbf{x} \in \Omega \ \forall \mathbf{z} \in \mathbb{R}^d. \tag{3.5}$$

In particular, (3.5) implies that $\mathbf{K}$ is invertible.

Lastly, the problem data satisfies $f \in L^2(\Omega)$ and $g_D \in H^{\frac{1}{2}}(\partial\Omega^D)$; f representing any sources or sinks in the domain, and g_D being the Dirichlet boundary condition for the pressure.

Recall from Section 2.1 the following function spaces.

$$\begin{aligned} H(\mathrm{div},\Omega) &:= \{\mathbf{v} \in [L^2(\Omega)]^d : \nabla\cdot\mathbf{v} \in L^2(\Omega)\}, \\ H^1_{0,D}(\Omega) &:= \{\psi \in H^1(\Omega) : \psi|_{\partial\Omega^D} = 0\}, \\ H_{0,N}(\mathrm{div},\Omega) &:= \{\mathbf{v} \in H(\mathrm{div},\Omega) : \langle \mathbf{v}\cdot\mathbf{n}, \psi\rangle_{\partial\Omega} = 0 \ \ \forall \psi \in H^1_{0,D}(\Omega)\}. \end{aligned}$$

For ease of notation we set, moving forward, $\mathbf{V} = H_{0,N}(\mathrm{div},\Omega)$ and $Q = L^2(\Omega)$. To arrive at a weak, or variational formulation of Darcy's equations, we begin by multiplying (3.1) by a test function $\mathbf{v} \in H_{0,N}(\mathrm{div},\Omega)$ and (3.2) by a test function $q \in L^2(\Omega)$ and integrate each over Ω; next, we apply Proposition 2.3 to the former equation, arriving at a form fitting the abstract saddle–point type problem (2.1, 2.2). To this end, define the bilinear forms

$$a(\mathbf{v},\mathbf{w}) := \int_\Omega \mathbf{K}^{-1}\mathbf{v}\cdot\mathbf{w}, \quad b(\mathbf{v},q) := -\int_\Omega q\nabla\cdot\mathbf{v}, \tag{3.6}$$

and the linear functionals

$$G(\mathbf{v}) := -\langle \mathbf{v}\cdot\mathbf{n}, g_D\rangle_{\partial\Omega}, \quad F(q) := -\int_\Omega fq. \tag{3.7}$$

With these, the **continuous problem** is to:

Find $(\mathbf{u},p) \in \mathbf{V}\times Q$ such that

$$a(\mathbf{u},\mathbf{v}) + b(\mathbf{v},p) = G(\mathbf{v}) \equiv \langle G,\mathbf{v}\rangle_{\mathbf{V}^*,\mathbf{V}} \ \ \forall \mathbf{v} \in \mathbf{V}, \tag{3.8}$$

$$b(\mathbf{u},q) = F(q) \equiv \langle F,q\rangle_{Q^*,Q} \quad \forall q \in Q. \tag{3.9}$$

[1]The homogeneous boundary condition $\mathbf{u}\cdot\mathbf{n} = 0$ may be replaced by an inhomogeneous condition with little extra work regarding the well–posedness of the system, see, for example [25, p. 404].

[2]The hydraulic conductivity is given by $\mathbf{K} := (\rho g/\mu)\mathbf{k}$, where ρ is density of water, g is acceleration due to gravity, and μ is the kinematic velocity of water.

3.2 Well–posedness of the continuous problem

We notice, in this setting, that the induced operator $\mathfrak{B}$, appearing in Theorem 2.7 is nothing more than the (weak) divergence operator[3] from $H_{0,N}(\mathrm{div},\Omega)$ onto $L^2(\Omega)$ (identifying Q^* with Q, in this case), which we will show to be surjective. Furthermore, we will verify that the bilinear form $a(\cdot,\cdot)$ is coercive on the kernel of $\mathfrak{B}$ and thus, according to Theorem 2.7, a unique solution $(\mathbf{u},p)$ to Darcy's equations indeed exists; see also [43, pp. 25–29] or [25, pp. 401–405], for example, for similar details and proofs.

The unique solvability of (3.8, 3.9) is given thanks to the following three lemmas.

Lemma 3.1. *Under the foregoing notation, the bilinear forms $a(\cdot,\cdot)$ and $b(\cdot,\cdot)$ are continuous on $\mathbf{V}\times\mathbf{V}$ and $\mathbf{V}\times Q$, respectively.*

Proof. We start with $b(\cdot,\cdot)$. Let $\mathbf{v}\in\mathbf{V}$ and $q\in Q$. Then,

$$|b(\mathbf{v},q)| = \left|\int_\Omega q\nabla\cdot\mathbf{v}\right| \leq ||q||_{L^2(\Omega)}||\nabla\cdot\mathbf{v}||_{L^2(\Omega)} \leq ||q||_{L^2(\Omega)}||\mathbf{v}||_{H(\mathrm{div},\Omega)},$$

where the first inequality follows by the Cauchy–Schwarz inequality (C.S.) and the second by definition of the $H(\mathrm{div},\Omega)$ norm. Thus, $b(\cdot,\cdot)$ is continuous with constant $\|b\|=1$.

We now proceed with $a(\cdot,\cdot)$. Let $\mathbf{v},\mathbf{w}\in\mathbf{V}$. Then,

$$|a(\mathbf{v},\mathbf{w})| = \left|\int_\Omega \mathbf{K}^{-1}\mathbf{v}\cdot\mathbf{w}\right| \leq ||\mathbf{K}^{-1}\mathbf{v}||_{[L^2(\Omega)]^d}||\mathbf{w}||_{[L^2(\Omega)]^d},$$

again, using C.S. Setting $\mathbf{z}=\mathbf{K}^{-1}\mathbf{v}$ in (3.5) we see that

$$\lambda_-|\mathbf{K}^{-1}\mathbf{v}|^2 \leq (\mathbf{K}^{-1}\mathbf{v})^T\mathbf{K}(\mathbf{K}^{-1}\mathbf{v}) = (\mathbf{K}^{-1}\mathbf{v})^T\mathbf{v} = \mathbf{K}^{-1}\mathbf{v}\cdot\mathbf{v}.$$

Therefore,

$$||\mathbf{K}^{-1}\mathbf{v}||^2_{[L^2(\Omega)]^d} = \int_\Omega |\mathbf{K}^{-1}\mathbf{v}|^2 \leq \frac{1}{\lambda_-}\int_\Omega \mathbf{K}^{-1}\mathbf{v}\cdot\mathbf{v} \leq \frac{1}{\lambda_-}||\mathbf{K}^{-1}\mathbf{v}||_{[L^2(\Omega)]^d}||\mathbf{v}||_{[L^2(\Omega)]^d},$$

where the last inequality follows again by C.S; this then tells us that

$$||\mathbf{K}^{-1}\mathbf{v}||_{[L^2(\Omega)]^d} \leq \frac{1}{\lambda_-}||\mathbf{v}||_{[L^2(\Omega)]^d}.$$

Lastly, we acquire

$$\begin{aligned}|a(\mathbf{v},\mathbf{w})| &\leq ||\mathbf{K}^{-1}\mathbf{v}||_{[L^2(\Omega)]^d}||\mathbf{w}||_{[L^2(\Omega)]^d}\\ &\leq \frac{1}{\lambda_-}||\mathbf{v}||_{[L^2(\Omega)]^d}||\mathbf{w}||_{[L^2(\Omega)]^d}\\ &\leq \frac{1}{\lambda_-}||\mathbf{v}||_{H(\mathrm{div},\Omega)}||\mathbf{w}||_{H(\mathrm{div},\Omega)},\end{aligned}$$

showing that $a(\cdot,\cdot)$ is continuous with constant $\|a\| = 1/\lambda_-$. □

[3] In particular, $\mathfrak{B}\mathbf{v} = -\mathrm{div}\ \mathbf{v}$; the notation $\nabla\cdot\mathbf{v}$ will also be used throughout, interchangeably, to denote divergence.

Lemma 3.2. *Under the foregoing notation, the bilinear form $a(\cdot,\cdot)$ is coercive on*

$$Ker(\mathfrak{B}) = \{\mathbf{w} \in \mathbf{V} : b(\mathbf{w}, q) = 0 \ \ \forall q \in Q\}.$$

Proof. The condition (3.5) is equivalent to

$$\frac{1}{\lambda_+}|\mathbf{z}|^2 \leq \mathbf{z}^T\mathbf{K}^{-1}\mathbf{z} \leq \frac{1}{\lambda_-}|\mathbf{z}|^2 \ \forall \mathbf{x} \in \Omega \ \forall \mathbf{z} \in \mathbb{R}^d. \tag{3.10}$$

Let $\mathbf{v} \in \mathrm{Ker}(\mathfrak{B})$. Then, (3.10) with $\mathbf{z} = \mathbf{v}$ tells us that

$$a(\mathbf{v},\mathbf{v}) = \int_\Omega \mathbf{K}^{-1}\mathbf{v}\cdot\mathbf{v} = \int_\Omega \mathbf{v}^T\mathbf{K}^{-1}\mathbf{v} \geq \frac{1}{\lambda_+}\int_\Omega |\mathbf{v}|^2 = \frac{1}{\lambda_+}||\mathbf{v}||^2_{[L^2(\Omega)]^d}.$$

Furthermore, since $\mathbf{v} \in \mathrm{Ker}(\mathfrak{B})$ then $||\nabla\cdot\mathbf{v}||^2_{L^2(\Omega)} = -b(\mathbf{v}, \nabla\cdot\mathbf{v}) = 0$, so that

$$a(\mathbf{v},\mathbf{v}) \geq \frac{1}{\lambda_+}||\mathbf{v}||^2_{[L^2(\Omega)]^d} = \frac{1}{\lambda_+}\left(||\mathbf{v}||^2_{[L^2(\Omega)]^d} + ||\nabla\cdot\mathbf{v}||^2_{L^2(\Omega)}\right) = \frac{1}{\lambda_+}||\mathbf{v}||^2_{H(\mathrm{div},\Omega)}.$$

Thus, $a(\cdot,\cdot)$ is coercive on $\mathrm{Ker}(\mathfrak{B})$ with constant $\alpha = 1/\lambda_+$. □

Lemma 3.3. *Under the foregoing notation, the divergence operator*

$$\mathfrak{B} : \mathbf{V} \to Q, \quad \mathbf{v} \mapsto -\nabla\cdot\mathbf{v},$$

is surjective.

Proof. Let $q \in Q = L^2(\Omega)$. The Lax–Milgram Theorem, or Lemma, guarantees the unique existence of a $\Phi \in H^1(\Omega)$ satisfying the well–known Poisson–type problem

$$\begin{aligned} -\Delta\Phi &= q \ \ \forall \mathbf{x} \in \Omega, \\ \Phi &= 0 \ \ \forall \mathbf{x} \in \partial\Omega^D, \\ \nabla\Phi\cdot\mathbf{n} &= 0 \ \ \forall \mathbf{x} \in \partial\Omega^N. \end{aligned}$$

Consider $\mathbf{v} := \nabla\Phi$. Then, $(\mathbf{v}\cdot\mathbf{n})|_{\partial\Omega^N} = (\nabla\Phi\cdot\mathbf{n})|_{\partial\Omega^N} = 0$ and $-\nabla\cdot\mathbf{v} = -\Delta\Phi = q \in L^2(\Omega)$; therefore, $\mathbf{v} \in H_{0,N}(\mathrm{div},\Omega)$. Thus, for $q \in Q$ there is a $\mathbf{v} \in \mathbf{V} = H_{0,N}(\mathrm{div},\Omega)$ such that $\mathfrak{B}\mathbf{v} = q$, i.e., $\mathfrak{B}$ is surjective. □

To conclude this section we collect these results into the following theorem for well–posedness of Darcy's equations.

Theorem 3.4. *Under the foregoing notation, the saddle–point problem (3.8, 3.9) has a unique solution $(\mathbf{u}, p) \in \mathbf{V} \times Q$.*

Proof. The continuity of the linear functionals F and G, defined by (3.7) is trivial, and is obtained by applying C.S. and trace inequalities. Moreover, the bilinear forms $a(\cdot,\cdot)$ and

$b(\cdot,\cdot)$ are continuous according to Lemma 3.1 on their respective spaces. The coercivity of $a(\cdot,\cdot)$ on $\mathrm{Ker}(\mathfrak{B})$ is given by Lemma 3.2, and this, in conjunction with the surjectivity[4] of $\mathfrak{B}$, given by Lemma 3.3, satisfy the criteria of Theorem 2.7, guaranteeing the existence and uniqueness of a solution to (3.8, 3.9). □

3.3 Mixed finite element approximations

3.3.1 Polynomial spaces

Within this section we set $d = 2$ and only consider two–dimensional approximations to the solutions of our governing equations. Within the work of this thesis, just one main type of numerical approximation for the pressure p is considered, while we look at two different types of approximation for the Darcy velocity $\mathbf{u}$. These approximations are chosen with well–posedness and stability of solution in mind, ultimately leading to a convergence result at the end of this chapter. The numerical approximation of choice is that of finite element type; here, we work on triangular meshes of the domain only, employing a mixed finite element method in order to solve for the discrete pressure and Darcy velocity simultaneously, in order to preserve local mass conservation properties.

Carrying forward the notations established so far in this chapter, in order for us to build the necessary finite dimensional subspaces $\mathbf{V}_h \subset \mathbf{V}$ and $Q_h \subset Q$ (with $\mathbf{V} = H_{0,N}(\mathrm{div}, \Omega)$ and $Q = L^2(\Omega)$) we firstly consider the local approximation spaces on triangular elements. To this end, suppose we have a shape–regular triangulation $\mathscr{T}_h$ of $\overline{\Omega}$ and a single triangular element $\kappa \in \mathscr{T}_h$. For $i = 1, 2, 3$, denote by $\mathcal{E}_i$ the three edges of the triangle κ and consider the following function spaces given by Definitions 3.5, 3.6, and 3.7.

Definition 3.5. *For $k \geq 0$ an integer, define*

$$R_k(\partial\kappa) := \{\phi \in L^2(\kappa) : \phi|_{\mathcal{E}_i} \in \mathbb{P}_k(\mathcal{E}_i)\ \forall i = 1, 2, 3\},$$

where $\mathbb{P}_k$ denotes the usual space of polynomials of degree at most k.

Definition 3.6. *For $k \geq 1$ an integer, define*

$$BDM_k(\kappa) := \{\mathbf{v}_h \in [\mathbb{P}_k(\kappa)]^2 : \mathbf{v}_h \cdot \mathbf{n}_\kappa \in R_k(\partial\kappa)\},$$

where $\mathbf{n}_\kappa$ is the unit outward normal vector to $\partial\kappa$. Moreover, the dimension of this space is given by $dim(BDM_k(\kappa)) = (k+1)(k+2)$.

Definition 3.7. *For $k \geq 0$ an integer, define*

$$RT_k(\kappa) := \{\mathbf{v}_h \in ([\mathbb{P}_k(\kappa)]^2 + \mathbf{x}\mathbb{P}_k(\kappa)) : \mathbf{v}_h \cdot \mathbf{n}_\kappa \in R_k(\partial\kappa)\},$$

[4] We note that the continuity of $\mathfrak{B}$ is automatically guaranteed since $b(\cdot,\cdot)$ is continuous.

where $\mathbf{n}_\kappa$ *is the unit outward normal vector to* $\partial\kappa$*. Moreover, the dimension of this space is given by* $dim(RT_k(\kappa)) = (k+1)(k+3)$.

Definition 3.6 describes the Brezzi–Douglas–Marini element (BDM), first introduced in [31], while Definition 3.7 is the Raviart–Thomas element (RT) [115]. The RT and BDM elements are related by the following sequence of inclusions:

$$RT_0(\kappa) \subset BDM_1(\kappa) \subset RT_1(\kappa) \subset \dots BDM_k(\kappa) \subset RT_k(\kappa) \subset BDM_{k+1}(\kappa) \subset \dots$$

3.3.2 Degrees of freedom

Thanks to Proposition 2.6, we know that in order to construct finite–dimensional spaces $\mathbf{V}_h$, defined on $\mathscr{T}_h$, that are globally $H(\mathrm{div}, \Omega)$–conforming, we need only guarantee that functions $\mathbf{v}_h \in \mathbf{V}_h$ are in the local spaces $H(\mathrm{div}, \kappa)$ and that their normal–traces are continuous across all element interfaces in the triangulation. The former condition is clearly satisfied in either the BDM or RT setting. In light of the latter, suitable degrees of freedom must be defined for the spaces $BDM_k(\kappa)$ and $RT_k(\kappa)$; in the following, Propositions 3.9 and 3.10 help to ensure that such construction of suitable degrees of freedom is possible[5].

First, however, it will be useful to define the following family of polynomial spaces, referred to often as the first–kind Nédélec family [51, p. 176].

Definition 3.8. *For* $k \geq 0$ *an integer, let* $\mathbb{P}_k^h$ *denote the space of homogeneous polynomials of degree* k*. Then, define*

$$\mathcal{N}_k(\kappa) := [\mathbb{P}_k(\kappa)]^2 \oplus [\mathbb{S}_{k+1}(\kappa)]^2,$$

with

$$[\mathbb{S}_{k+1}(\kappa)]^2 := \{\mathbf{q} \in [\mathbb{P}(\kappa)_{k+1}^h]^2 : \mathbf{q}(\mathbf{x}) \cdot \mathbf{x} = 0\}.$$

Proposition 3.9. *For* $k \geq 1$ *an integer, and for any* $\mathbf{v}_h \in BDM_k(\kappa)$*, the following relations together imply* $\mathbf{v}_h = \mathbf{0}$*:*

$$\begin{cases} \int_{\partial\kappa} (\mathbf{v}_h \cdot \mathbf{n}_\kappa) p_k = 0 & \forall p_k \in R_k(\partial\kappa), \\ \int_\kappa \mathbf{v}_h \cdot \mathbf{w}_{k-2} = 0 & \forall \mathbf{w}_{k-2} \in \mathcal{N}_{k-2}(\kappa). \end{cases}$$

Proposition 3.10. *For* $k \geq 0$ *an integer, and for any* $\mathbf{v}_h \in RT_k(\kappa)$*, the following relations together imply* $\mathbf{v}_h = \mathbf{0}$*:*

$$\begin{cases} \int_{\partial\kappa} (\mathbf{v}_h \cdot \mathbf{n}_\kappa) p_k = 0 & \forall p_k \in R_k(\partial\kappa), \\ \int_\kappa \mathbf{v}_h \cdot \mathbf{p}_{k-1} = 0 & \forall \mathbf{p}_{k-1} \in [\mathbb{P}_{k-1}(\kappa)]^2. \end{cases}$$

[5] These propositions describe the unisolvency property for the defined degrees of freedom. Moreover, [25, p. 86] confirms that these sets are each linearly independent and therefore may be used to define the BDM_k and RT_k finite elements.

The expressions for the degrees of freedom are defined explicitly by choosing particular bases[6] for the spaces $R_k(\partial\kappa)$, $\mathcal{N}_{k-2}(\kappa)$, and $[\mathbb{P}_{k-1}(\kappa)]^2$. To this end, fixing k, we let $\{\phi_i^{(j)}\}_{i=1}^{n_j}$ be a basis for $\mathbb{P}_k(\mathcal{E}_j)$, $j = 1, 2, 3$, $\{\boldsymbol{\psi}_i\}_{i=1}^{n_{ned}}$ a basis for $\mathcal{N}_{k-2}(\kappa)$, and $\{\mathbf{q}_i\}_{i=1}^{n_p}$ a basis for $[\mathbb{P}_{k-1}(\kappa)]^2$. The values of n_j, n_{ned}, and n_p correspond to the dimensions of their respective spaces. With these bases in place, the degrees of freedom for the spaces $BDM_k(\kappa)$ and $RT_k(\kappa)$ are defined below, respectively.

Definition 3.11. *For $k \geq 1$ an integer, we denote by Σ_{BDM}^k the collection of the following linear functionals acting on $BDM_k(\kappa)$:*

$$\sigma_i^{\mathcal{E}_j}(\mathbf{v}_h) = \int_{\mathcal{E}_j} (\mathbf{v}_h \cdot \mathbf{n}_{\mathcal{E}_j})\phi_i^{(j)} \;\; \forall i = 1, \ldots, n_j, \;\; \forall j = 1, 2, 3,$$
$$\sigma_i^{ned}(\mathbf{v}_h) = \int_{\kappa} \mathbf{v}_h \cdot \boldsymbol{\psi}_i \;\; \forall i = 1, \ldots, n_{ned} \;\; (k \geq 2).$$

Definition 3.12. *For $k \geq 0$ an integer, we denote by Σ_{RT}^k the collection of the following linear functionals acting on $RT_k(\kappa)$:*

$$\sigma_i^{\mathcal{E}_j}(\mathbf{v}_h) = \int_{\mathcal{E}_j} (\mathbf{v}_h \cdot \mathbf{n}_{\mathcal{E}_j})\phi_i^{(j)} \;\; \forall i = 1, \ldots, n_j, \;\; \forall j = 1, 2, 3,$$
$$\sigma_i^{p}(\mathbf{v}_h) = \int_{\kappa} \mathbf{v}_h \cdot \mathbf{q}_i, \;\; \forall i = 1, \ldots, n_p \;\; (k \geq 1).$$

These degrees of freedom ensure that the continuity of normal–trace at element interfaces is enforced and thus will give rise (in Section 3.3.4) to approximation spaces $\mathbf{V}_h \subset \mathbf{V} = H_{0,N}(\mathrm{div}, \Omega)$. We refer the interested reader to [25, pp. 84–91] for more details.

3.3.3 Local interpolation operators

With the degrees of freedom previously described, the next logical step is to define a local interpolation operator

$$\rho_\kappa : H(\mathrm{div}, \kappa) \to \mathcal{M}_k(\kappa),$$

where $\mathcal{M}_k(\kappa)$ denotes either $BDM_k(\kappa)$ or $RT_k(\kappa)$. Such construction is unfortunately not possible due to the computation of quantities such as $\int_{\partial\kappa}(\mathbf{v} \cdot \mathbf{n}_\kappa)p_k$ for $\mathbf{v} \in H(\mathrm{div}, \kappa)$ and $p_k \in R_k(\partial\kappa)$; this expression only makes sense if $p_k \in H^{\frac{1}{2}}(\partial\kappa)$ as the normal–trace of $\mathbf{v}$ is defined only in $H^{-\frac{1}{2}}(\partial\kappa)$. In general, such an assumption is not true for functions $p_k \in R_k(\partial\kappa)$. However, if $\mathbf{v}$ is assumed slightly smoother, namely belonging in the space

$$W(\kappa) := H(\mathrm{div}, \kappa) \cap [L^s(\kappa)]^2, \tag{3.11}$$

[6] Often, the basis for $R_k(\partial\kappa)$ is selected so that the degrees of freedoms correspond to the average normal–trace over element edges (weighted by a polynomial); cf. [51, p. 164].

for some fixed $s > 2$, then the construction of an interpolation operator

$$\rho_\kappa : W(\kappa) \to \mathcal{M}_k(\kappa)$$

is indeed possible [25, p. 103], and shown below for both $BDM_k(\kappa)$ and $RT_k(\kappa)$, respectively.

Definition 3.13. *The local interpolation operator $\rho_\kappa : W(\kappa) \to BDM_k(\kappa)$ is defined to be such that, for $\mathbf{v} \in W(\kappa)$,*

$$\begin{cases} \int_{\partial\kappa}(\mathbf{v} - \rho_\kappa\mathbf{v}) \cdot \mathbf{n}_\kappa p_k = 0 & \forall p_k \in R_k(\partial\kappa), \\ \int_\kappa (\mathbf{v} - \rho_\kappa\mathbf{v}) \cdot \mathbf{w}_{k-2} = 0 & \forall \mathbf{w}_{k-2} \in \mathcal{N}_{k-2}(\kappa),\ (k \geq 2). \end{cases}$$

The interpolation operator for $BDM_k(\kappa)$ may also be built *piece–by–piece* using Whitney, edge, and bubble interpolants, as in [120, Section 3.1.3]. We refer also to [51, Chapter 16] for other constructions of both the BDM and RT interpolation operators.

Definition 3.14. *The local interpolation operator $\rho_\kappa : W(\kappa) \to RT_k(\kappa)$ is defined to be such that, for $\mathbf{v} \in W(\kappa)$,*

$$\begin{cases} \int_{\partial\kappa}(\mathbf{v} - \rho_\kappa\mathbf{v}) \cdot \mathbf{n}_\kappa p_k = 0 & \forall p_k \in R_k(\partial\kappa), \\ \int_\kappa (\mathbf{v} - \rho_\kappa\mathbf{v}) \cdot \mathbf{p}_{k-1} = 0 & \forall \mathbf{p}_{k-1} \in [\mathbb{P}_{k-1}(\kappa)]^2,\ (k \geq 1). \end{cases}$$

Error estimates for these local element–wise interpolation operators can be found in [25, p. 107]; for the divergence $\nabla \cdot (\mathbf{v} - \rho_\kappa\mathbf{v})$, there is also the error estimate [25, p. 108].

Of most importance are the spaces which consist of the divergences of functions from $\mathcal{M}_k(\kappa)$. We simply have, according to [25, p. 107] that

$$\begin{aligned} \operatorname{div}(BDM_k(\kappa)) &= \mathbb{P}_{k-1}(\kappa), \\ \operatorname{div}(RT_k(\kappa)) &= \mathbb{P}_k(\kappa). \end{aligned}$$

For convenience, denote these spaces by $D_k(\kappa) \equiv \operatorname{div}(\mathcal{M}_k(\kappa))$. Consequently, if we denote by π_k the $L^2(\kappa)$–projection onto $D_k(\kappa)$, we have the following commuting properties.

$$\begin{aligned} W(\kappa) &\to^{\operatorname{div}} L^2(\kappa) \to^{\pi_k} D_k(\kappa), \\ W(\kappa) &\to^{\rho_\kappa} \mathcal{M}_k(\kappa) \to^{\operatorname{div}} D_k(\kappa). \end{aligned}$$

Having defined the local spaces and interpolation operators, the construction of global analogues for these is now possible and thus we are able to define the approximation spaces that will be used in our mixed finite element setting.

3.3.4 Global approximations and interpolation

Recall that we let $\mathscr{T}_h$ be a shape–regular triangulation of $\overline{\Omega}$. Under the foregoing notation of this chapter, we define the following global approximation spaces.

Definition 3.15. $\mathcal{M}_k(\Omega, \mathscr{T}_h) := \{\mathbf{v}_h \in H(\mathrm{div}, \Omega) : \mathbf{v}|_\kappa \in \mathcal{M}_k(\kappa)\ \forall \kappa \in \mathscr{T}_h\}$.

Definition 3.16. $\mathcal{L}^0(D_k, \mathscr{T}_h) := \{q_h \in L^2(\Omega) : q_h|_\kappa \in D_k(\kappa)\ \forall \kappa \in \mathscr{T}_h\}$.

Firstly, we note that we clearly have the inclusion

$$\mathrm{div}(\mathcal{M}_k(\Omega, \mathscr{T}_h)) \subset \mathcal{L}^0(D_k, \mathscr{T}_h).$$

Moreover, similar to (3.11), we define

$$\mathbf{W}(\Omega) := H(\mathrm{div}, \Omega) \cap [L^s(\Omega)]^2,$$

for some fixed $s > 2$. Then, using the local interpolation operators defined in Definitions 3.13 and 3.14 we can construct the global interpolation operator

$$\Pi_h : \mathbf{W}(\Omega) \to \mathcal{M}_k(\Omega, \mathscr{T}_h), \tag{3.12}$$

which is defined so that, for $\mathbf{v} \in \mathbf{W}(\Omega)$, we have

$$(\Pi_h \mathbf{v})|_\kappa := \rho_\kappa(\mathbf{v}|_\kappa) \quad \forall \kappa \in \mathscr{T}_h. \tag{3.13}$$

Denoting by P_h the $L^2(\Omega)$–projection onto $\mathcal{L}^0(D_k, \mathscr{T}_h)$, we have the commuting properties

$$\mathbf{W}(\Omega) \to^{\mathrm{div}} L^2(\Omega) \to^{P_h} \mathcal{L}^0(D_k, \mathscr{T}_h), \tag{3.14}$$

$$\mathbf{W}(\Omega) \to^{\Pi_h} \mathcal{M}_k(\Omega, \mathscr{T}_h) \to^{\mathrm{div}} \mathcal{L}^0(D_k, \mathscr{T}_h). \tag{3.15}$$

In particular, [25, p. 110] guarantees the surjectivity property

$$\mathrm{div}(\mathcal{M}_k(\Omega, \mathscr{T}_h)) = \mathcal{L}^0(D_k, \mathscr{T}_h), \tag{3.16}$$

which we shall not prove, in general.

A key component in deriving an *a priori* convergence result for the approximation of Darcy's equations are error estimates for the global interpolation operators, stated below in Proposition 3.17. These, paired with the quasi–optimality result given by Theorem 2.8 directly deduce the convergence of the underlying MFEM.

Proposition 3.17. *Under the foregoing notation, there exists a constant $c > 0$ independent of h, such that for $\mathbf{v} \in \mathbf{W}(\Omega)$ and Π_h defined by (3.13),*

$$\|\mathbf{v} - \Pi_h \mathbf{v}\|_{[L^2(\Omega)]^2} \leq c h^m |\mathbf{v}|_{[H^m(\Omega)]^2},$$

for $1 \leq m \leq k+1$. *We also have*

$$\|\nabla \cdot (\mathbf{v} - \Pi_h \mathbf{v})\|_{L^2(\Omega)} \leq ch^s |\nabla \cdot \mathbf{v}|_{H^s(\Omega)},$$

where $s \leq k$ *for* $\mathcal{M}_k = BDM_k$ *and* $s \leq k+1$ *for* $\mathcal{M}_k = RT_k$.

Proof. See [25, pp. 103–110], for example. □

Furthermore, an error estimate for the $L^2(\Omega)$–projection operator P_h is given below in Proposition 3.18.

Proposition 3.18. *Under the foregoing notation, there exists a constant* $c > 0$ *independent of* h, *such that for* $q \in L^2(\Omega)$ *and* P_h *the* $L^2(\Omega)$*–projection onto* $\mathcal{L}^0(D_k, \mathscr{T}_h) = \operatorname{div}(\mathcal{M}_k(\Omega, \mathscr{T}_h))$,

$$\|q - P_h q\|_{L^2(\Omega)} \leq ch^{\psi(k)} |q|_{H^{\psi(k)}(\Omega)},$$

where $\psi(k) = k$ *for* $\mathcal{M}_k = BDM_k$ *and* $\psi(k) = k+1$ *for* $\mathcal{M}_k = RT_k$.

Proof. See [68, p. 29], for example. □

3.4 Well–posedness of the discrete problem

Having defined local and global approximation spaces, as well as stating a few error estimates for the global interpolation operators, we are now in a position to be able to state the discrete problem, corresponding to a mixed finite element approximation of the continuous Darcy problem (3.8, 3.9). To this end, define the finite element spaces $\mathbf{V}_h \subset \mathbf{V} = H_{0,N}(\operatorname{div}, \Omega)$ and $Q_h \subset Q = L^2(\Omega)$ as

$$\mathbf{V}_h := \{\mathbf{v}_h \in \mathcal{M}_k(\Omega, \mathscr{T}_h) : (\mathbf{v}_h \cdot \mathbf{n})|_{\partial\Omega^N} = 0\}, \tag{3.17}$$

$$Q_h := \mathcal{L}^0(D_k, \mathscr{T}_h), \tag{3.18}$$

according to the definitions given in Section 3.3.4.

Then, the **discrete problem** is to:

Find $(\mathbf{u}_h, p_h) \in \mathbf{V}_h \times Q_h$ such that

$$a(\mathbf{u}_h, \mathbf{v}_h) + b(\mathbf{v}_h, p_h) = G(\mathbf{v}_h) \;\; \forall \mathbf{v}_h \in \mathbf{V}_h, \tag{3.19}$$

$$b(\mathbf{u}_h, q_h) \qquad\qquad = F(q_h) \;\; \forall q_h \in Q_h, \tag{3.20}$$

with the bilinear forms and linear functionals precisely the same as those in Section 3.2.

To establish well–posedness of (3.19, 3.20), we refer to Theorem 2.7 and the subsequent discussion concerning the discrete problem in Section 2.3. Moving forward, we will explicitly

check the criteria in Theorem 2.7 for the lowest–order approximation spaces before relating and extending this result to higher–order approximations. Following this, stability concerns due to a possible h–dependence in the discrete inf–sup condition will be commented on, ensuring we can apply Theorem 2.8 in order to derive convergence estimates for this problem.

We firstly re–iterate that the continuity of the bilinear forms and the linear functionals on the spaces $\mathbf{V}$ and Q naturally follows on the discrete subspaces $\mathbf{V}_h$ and Q_h. Therefore, we proceed by only verifying the two main conditions in Theorem 2.7 in order to establish well–posedness.

To this end, recall the induced operator $\mathfrak{B} = -\text{div}$ for this problem. A well–known consequence of Banach's closed range theorem states that since the image of the discrete adjoint operator $\mathfrak{B}_h^*$ is trivially closed in $\mathbf{V}_h^*$ (since it is finite dimensional), the surjectivity of $\mathfrak{B}_h$ is equivalent to the injectivity of $\mathfrak{B}_h^*$ [25, p. 214]. This fact is exploited in the following theorem, in which we prove for the lowest–order approximation spaces that (3.19, 3.20) has a unique solution.

Theorem 3.19. *Let $\mathbf{V}_h$ and Q_h be such that $\mathcal{M}_k(\kappa) \equiv RT_0(\kappa)$ or $BDM_1(\kappa)$, so that $D_k(\kappa) = \mathbb{P}_0(\kappa)$. Then, (3.19, 3.20) has a unique solution.*

Proof. We first show that $\mathfrak{B}_h^* : Q_h \to \mathbf{V}_h^*$ is injective; here, the kernel of $\mathfrak{B}_h^*$ is given by

$$\text{Ker}(\mathfrak{B}_h^*) = \{q_h \in Q_h : b(\mathbf{v}_h, q_h) = 0 \ \forall \mathbf{v}_h \in \mathbf{V}_h\}.$$

Let $q_h \in \text{Ker}(\mathfrak{B}_h^*)$. Then, for all $\mathbf{v}_h \in \mathbf{V}_h$ we have

$$\begin{aligned} b(\mathbf{v}_h, q_h) = -\int_\Omega q_h \nabla \cdot \mathbf{v}_h &= \sum_{\kappa \in \mathscr{T}_h} \left(-\int_\kappa q_h \nabla \cdot \mathbf{v}_h \right) \\ &= \sum_{\kappa \in \mathscr{T}_h} \left(\int_\kappa \mathbf{v}_h \cdot \nabla q_h - \langle \mathbf{v}_h \cdot \mathbf{n}_\kappa, q_h \rangle_{\partial\kappa} \right) \\ &= -\sum_{\kappa \in \mathscr{T}_h} \langle \mathbf{v}_h \cdot \mathbf{n}_\kappa, q_h \rangle_{\partial\kappa}, \end{aligned}$$

via Proposition 2.3 and since $q_h \in Q_h = \mathcal{L}^0(D_k, \mathscr{T}_h)$ implies $\nabla(q_h|_\kappa) = 0$ on all elements $\kappa \in \mathscr{T}_h$. Denote by $\mathcal{E}_{\text{int}}$ the set of interior edges of the triangulation so that the summation can be taken over the element edges instead as

$$-\sum_{\kappa \in \mathscr{T}_h} \langle \mathbf{v}_h \cdot \mathbf{n}_\kappa, q_h \rangle_{\partial\kappa} = -\sum_{\mathcal{E} \in \mathcal{E}_{\text{int}}} \frac{1}{2} \langle \mathbf{v}_h \cdot \mathbf{n}_\mathcal{E}, [\![q_h]\!] \rangle_\mathcal{E} - \sum_{\mathcal{E} \subset \partial\Omega^D} \langle \mathbf{v}_h \cdot \mathbf{n}_\mathcal{E}, q_h \rangle_\mathcal{E} = 0, \tag{3.21}$$

where $[\![q_h]\!]$ denotes the jump in q_h across the interior edges. For $\mathbf{V}_h$ with $\mathcal{M}_k = RT_0$ there is a degree of freedom on each of the edges for the normal component $\mathbf{v}_h \cdot \mathbf{n}_\mathcal{E}$. Since (3.21)

is true for every $\mathbf{v}_h \in \mathbf{V}_h$, it is true for $\mathbf{v}_h$ such that

$$(\mathbf{v}_h \cdot \mathbf{n}_\mathcal{E})|_\mathcal{E} = \begin{cases} [\![q_h]\!] & \text{for } \mathcal{E} \in \mathcal{E}_{\text{int}}, \\ q_h & \text{for } \mathcal{E} \subset D, \end{cases}$$

recalling that there are no degrees of freedom on the edges contained in $\partial\Omega^N$. Here, we can see that

$$\sum_{\mathcal{E}\in\mathcal{E}_{\text{int}}} \frac{1}{2} \int_\mathcal{E} [\![q_h]\!]^2 + \sum_{\mathcal{E}\subset D} \int_\mathcal{E} q_h^2 = 0.$$

Since each sum is made up of strictly non–negative contributions, it must be true that each of the integrals vanish:

$$\int_\mathcal{E} [\![q_h]\!]^2 = 0, \quad \forall \mathcal{E} \in \mathcal{E}_{\text{int}},$$

and

$$\int_\mathcal{E} q_h^2 = 0, \quad \forall \mathcal{E} \subset D.$$

This implies that $[\![q_h]\!] = 0$ across all of the interior edges and $q_h = 0$ on the boundary edges in $\partial\Omega^D$. Furthermore, so long as $\partial\Omega^D$ is not empty, there will always be at least one edge in the triangulation where $q_h = 0$; since q_h is piecewise constant and the interior jumps are all zero, this can only mean that $q_h = 0$ everywhere.

Therefore, $\text{Ker}(\mathfrak{B}_h^*) = \{0\}$, and $\mathfrak{B}_h : V_h \to Q_h^*$ is surjective. Since $\mathfrak{B}_h(\mathbf{V}_h) \subset Q_h^*$ holds for both choices of $\mathcal{M}_k$ (and since for either velocity space the scalar space Q_h is the same), the inclusion $RT_0(\Omega, \mathscr{T}_h) \subset BDM_1(\Omega, \mathscr{T}_h)$ means $\mathfrak{B}_h : \mathbf{V}_h \to Q_h^*$, where $\mathbf{V}_h$ has $\mathcal{M}_k(\kappa) = BDM_1(\kappa)$, is also surjective.

To show that the bilinear form $a(\cdot,\cdot)$ is coercive on the kernel of $\mathfrak{B}_h$ we show the inclusion

$$\text{Ker}(\mathfrak{B}_h) \subset \text{Ker}(\mathfrak{B}).$$

Here, the coercivity on the latter, proved in Lemma 3.2, will simply transfer to the former. To this end, let $\mathbf{v}_h \in \text{Ker}(\mathfrak{B}_h)$. Then, for all $q_h \in Q_h$ we have

$$b(\mathbf{v}_h, q_h) = -\int_\Omega q_h \nabla \cdot \mathbf{v}_h = 0.$$

From (3.16) we have that $\text{div}(\mathcal{M}_k(\Omega, \mathscr{T}_h)) = \mathcal{L}^0(D_k, \mathscr{T}_h) = Q_h$; since $\mathbf{V}_h \subset \mathcal{M}_k(\Omega, \mathscr{T}_h)$ and since images preserve subsets, we deduce that $\text{div}(\mathbf{V}_h) \subset Q_h$. Therefore, there is a $q_h \in Q_h$ such that $\nabla \cdot \mathbf{v}_h = q_h$. Consequently,

$$\int_\Omega |\nabla \cdot \mathbf{v}_h|^2 = 0,$$

thus $\nabla \cdot \mathbf{v}_h = 0$ and $\mathbf{v}_h \in \text{Ker}(\mathfrak{B})$. Therefore, $\text{Ker}(\mathfrak{B}_h) \subset \text{Ker}(\mathfrak{B})$. □

3.4.1 Arbitrary order spaces and discrete inf–sup

An extension of the discussion started in Section 2.3 is the following proposition. The aim of such result is the attainment of a discrete inf–sup constant, in this case β_0, which is independent of the mesh size parameter h. We refer the reader back to Section 2.3 where the importance of such condition is highlighted.

Proposition 3.20. *Assume that we are given a Banach space $W \hookrightarrow V$ with norm $\|\cdot\|_W$. Suppose that*

$$\sup_{w\in W} \frac{b(w,q_h)}{\|w\|_W} \geq \beta_W \|q_h\|_Q \ \ \forall q_h \in Q_h,$$

and assume that there exists a family of uniformly continuous operators Π_h from W into V satisfying

$$\begin{cases} b(\Pi_h w - w, q_h) = 0 & \forall w \in W \ \forall q_h \in Q_h, \\ \|\Pi_h w\|_V \leq C_W \|w\|_W, \end{cases}$$

with C_W independent of h. Then, we have

$$\sup_{v_h\in V_h} \frac{b(v_h,q_h)}{\|v_h\|_V} \geq \ \beta_0 \|q_h\|_Q \ \ \forall q_h \in Q_h,$$

with $\beta_0 = \beta_W / C_W$.

Proof. See [25, pp. 304–305], for example. □

Indeed, with Π_h defined as the global interpolation operator from (3.12), we have

$$b(\mathbf{v} - \Pi_h \mathbf{v}, q_h) = \int_\Omega (\text{div } \mathbf{v} - \text{div } \Pi_h \mathbf{v}) q_h = 0 \ \ \forall q_h \in Q_h$$

as a consequence of the commuting properties (3.14) and

$$\|\Pi_h \mathbf{v}\|_{\mathbf{V}} \leq c \|\mathbf{v}\|_{\mathbf{W}(\Omega)}$$

since the operators Π_h are uniformly bounded from $\mathbf{W}(\Omega)$ to $\mathbf{V}_h$ [25, p. 406].

Applying Proposition 3.20 we obtain a discrete inf–sup condition for all possible approximation spaces $\mathbf{V}_h$, defined according to (3.17), independent of h[7].

The property (3.16) automatically implies that in this setting we have

$$\text{div } \mathbf{V}_h = Q_h,$$

for $\mathcal{M}_k$ as either BDM_k or RT_k for any k. Indeed, this must then mean that the discrete operator $\mathfrak{B}_h$ is just the restriction of $\mathfrak{B}$, the divergence operator, to the discrete space

[7] We note that the first condition stated in Proposition 3.20 is satisfied since $\mathfrak{B}$ has continuous lifting from Q to $\mathbf{W}(\Omega)$; indeed, the $\mathbf{v}$ obtained in the auxiliary problem is in the space $\mathbf{W}(\Omega)$ and $\|\mathbf{v}\|_{\mathbf{W}(\Omega)} \leq c\|q\|_Q$ [25, pg. 404].

$\mathbf{V}_h$; this immediately implies that $\mathrm{Ker}(\mathfrak{B}_h) \subset \mathrm{Ker}(\mathfrak{B})$ and coercivity of the bilinear form $a(\cdot,\cdot)$ transfers from the continuous setting to the discrete. In particular, this, along with the satisfaction of Proposition 3.20 means that both the discrete coercivity and inf–sup constants are independent of h and therefore we may apply the quasi–optimality result given by Theorem 2.8.

To conclude, we state optimal *a priori* error estimates for the finite element approximations in the $L^2(\Omega)$ norm, stated below in Theorem 3.21.

Theorem 3.21. *Under the foregoing notations, let $(\mathbf{u}, p) \in \mathbf{V} \times Q$ be the solutions of the continuous problem (3.8, 3.9), and let $(\mathbf{u}_h, p_h) \in \mathbf{V}_h \times Q_h$ be the solutions of the discrete problem (3.19, 3.20). Then, there exists a constant $c > 0$, independent of h, whose value may change in each bound, such that the following hold:*

$$\|\mathbf{u} - \mathbf{u}_h\|_{[L^2(\Omega)]^2} \leq ch^s \|\mathbf{u}\|_{[H^s(\Omega)]^2},$$

for $s \leq k+1$, and

$$\|p - p_h\|_{L^2(\Omega)} \leq ch^s (\|\mathbf{u}\|_{[H^s(\Omega)]^2} + \|p\|_{H^s(\Omega)}),$$
$$\|\nabla \cdot (\mathbf{u} - \mathbf{u}_h)\|_{L^2(\Omega)} \leq ch^s \|\nabla \cdot \mathbf{u}\|_{H^s(\Omega)},$$

for $s \leq k+1$ if $\mathcal{M}_k$ is RT_k, and for $s \leq k$ is $\mathcal{M}_k$ is BDM_k.

Proof. This result is obtained by employing the quasi–optimality result given by Theorem 2.8 and the interpolation estimates given by Propositions 3.17 and 3.18. □

Chapter 4

Flow in fractured porous media

This chapter aims to introduce the reader to the model, and subsequent mixed finite element approximation, for flow in fractured porous media; the structure of this chapter, in more detail, is as follows.

First, we present the definitions and notations needed to fully describe the governing equations of the model; moreover, once the functional analysis setting for this problem is established, some details concerning traces of functions on fractures is given. Following this, a weak formulation of the equations is derived and we are able to discuss its well–posedness. For ease of presentation, we consider and prove well–posedness only for the simplified case where a single, non–immersed, fracture partitions the domain in two, following [94]. Furthermore, the mixed finite element method to be utilised is then presented with a variety of possible approximation spaces, including the use of Raviart–Thomas (RT) and Brezzi–Douglas–Marini (BDM) elements in the bulk portions of the porous media. Such approximation is such that the fracture network respects the underlying computational mesh, i.e. it is made up of element edges. For ease of presentation, interpolation results and discrete well–posedness are presented only for a lowest order RT approximation, as is standard in the literature. We conclude with an *a priori* convergence result for this type of approximation.

4.1 Fractures as manifolds

We proceed with some notations concerning the domain setting of this problem. To this end, let $\Omega \subset \mathbb{R}^d$, $d = 2, 3$, be an open and bounded domain representing the fractured porous medium. Assume that Ω has a Lipschitz, or polygonal, boundary $\partial\Omega$, partitioned into the

non–empty sets $\partial\Omega^N$ and $\partial\Omega^D$. The unit outward normal vector to $\partial\Omega$ is denoted, as usual, by $\mathbf{n}$.

Fractures in the domain are to be described as a collection of co-dimensional planar manifolds, which, in the two dimensional setting, are simply lines. We denote by $\Gamma \subset \Omega$ a network formed by the union of $N_\Gamma \in \mathbb{N}$ fractures $\gamma_k \subset \Omega$. Each of the fractures γ_k are open and bounded and are such that $\Gamma = \cup_{k=1}^{N_\Gamma} \gamma_k$. We assume that fractures can only intersect at their endpoints, and we assume throughout that the fracture network is completely immersed in the domain, i.e., $\overline{\Gamma} \cap \partial\Omega = \emptyset$. Consequently, the boundary $\partial\gamma_k$ of a one–dimensional fracture has one of three possible forms: two intersection points, a single intersection point and an immersed fracture tip, or two immersed fracture tips; the latter of which refers to an isolated fracture. Shown in Figure 4.1 are an example of a fractured domain and the possible boundary points of a fracture. We write $\Omega_\Gamma = \Omega \setminus \overline{\Gamma}$ to represent the bulk domain, i.e., the domain without the fracture network. Moreover, we denote with $\mathcal{I}$ the set of all fracture intersection points i. Indeed, more than two fractures can intersect at a single point. For example, two lines intersecting in the shape of an X would represent four fractures, sharing the intersection point in the middle. Given an intersection point $i \in \mathcal{I}$, we denote with S_i the set of fractures sharing this point; this is illustrated in Figure 4.2.

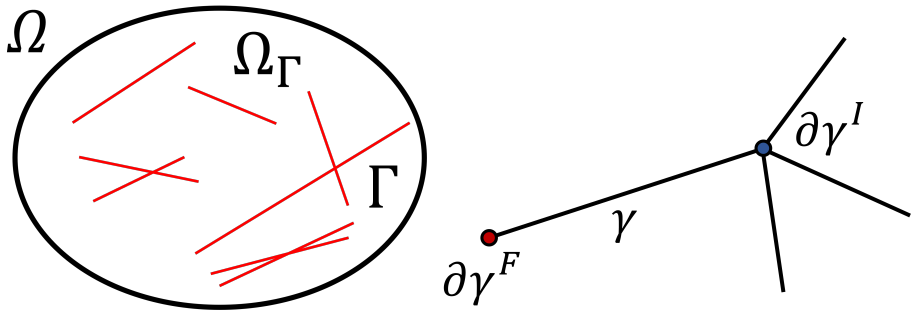

FIG. 4.1 – *Example fractured domain and fracture boundary labels.*

The unit outward normal vector to the fracture network is denoted by $\mathbf{n}_\Gamma$, whose definition is according to the unique fracture it can be restricted to, i.e., the normal vector $\mathbf{n}_k$ (or sometimes denoted by $\mathbf{n}_{\gamma_k}$). The network Γ can be arbitrarily extended to $\partial\Omega$ in order to partition Ω into a series of Lipschitz subdomains; the orientation of $\mathbf{n}_\Gamma$ is fixed and is defined according to which subdomain (after labelling) it should point into[1].

Although we consider a fully–immersed fracture network, in the case where the network touches the domain boundary, fracture boundaries $\partial\gamma_k$ are divided into $\partial\gamma_k^N$ and $\partial\gamma_k^D$, such that $\partial\gamma_k^N \cup \partial\gamma_k^D = \partial\gamma_k \cap \partial\Omega$, and boundary conditions can be imposed. Furthermore, by

[1] Cf. Figure 4.3 and Section 4.3.2.

defining the intersected part of a fracture boundary $\partial\gamma_k^I = \partial\gamma_k \cap \mathcal{I}$, an immersed fracture tip is thus $\partial\gamma_k^F = \partial\gamma_k \setminus \cup_{s=D,N,I}\partial\gamma_k^s$; cf. the right image in Figure 4.1. For $s = D, N, F$ define $I^s = \cup_{k=1}^{N_\Gamma}\partial\gamma_k^s$. Therefore, a completely immersed fracture network has $I^D = I^N = \emptyset$.

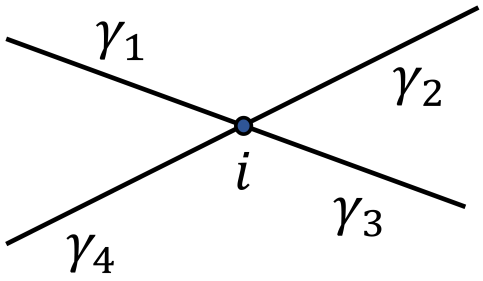

FIG. 4.2 – *Intersection point of fractures.*

4.2 The governing equations

4.2.1 Some more model notations

We consider here a single fluid of constant density, ignoring the effects of gravity. This model, taken from [55], assumes that flow in both the bulk (porous medium) and the fracture network are described via Darcy's law, and by conservation of mass. As mentioned previously, it is assumed that the fractures are partially filled with debris; we refer to [57] where this assumption is not considered, and a different set of equations for the flow in the fractures is used instead.

The macroscopic variables, $\mathbf{u}$ and p, represent the Darcy velocity and fluid pressure, respectively, in the bulk domain Ω_Γ. The permeability tensor $\mathbf{K}$, in the bulk, includes the dependence on the viscosity μ. Flow within a fracture is derived via a model reduction, whereby the governing equations are integrated over the fracture aperture. The reduced variables $\hat{\mathbf{u}}$ and $\hat{p}$ represent, respectively, the flux and average pressure in each fracture. These variables are composed as the product of the fracture variables $\hat{\mathbf{u}}_k$ and $\hat{p}_k$, for $k = 1, 2, \ldots, N_\Gamma$.

We make the assumption that the permeability (scaled by viscosity) in each fracture can be represented as a diagonal tensor in local (tangent and normal) coordinates; i.e. $\mathbf{K} = \hat{K}_n \mathbf{n}_\Gamma \otimes \mathbf{n}_\Gamma + \hat{\mathbf{K}}_{\boldsymbol{\tau}}$, where on each γ_k, $\hat{\mathbf{K}}_{\boldsymbol{\tau}}$ is a tensor acting only on the plane defined by γ_k. In our two dimensional setting, $\hat{\mathbf{K}}_{\boldsymbol{\tau}} = \hat{K}_{\boldsymbol{\tau}}\boldsymbol{\tau}$ for a scalar function $\hat{K}_{\boldsymbol{\tau}}$, where $\boldsymbol{\tau} = \prod_{k=1}^{N_\Gamma}\boldsymbol{\tau}_k$ is the projector onto the tangent plane of the fracture network ($\boldsymbol{\tau}_k = \mathbb{I} - \mathbf{n}_k \otimes \mathbf{n}_k$).

Of course, physically, fractures are not one–dimensional manifolds and have an aperture which may vary along their length. We denote by $w_k(\mathbf{x})$ the aperture of fracture γ_k and

assume that it is continuously differentiable; we assume also the existence of a constant $w_* > 0$ such that $w_k > w_*$ for all $k = 1, 2, \ldots, N_\Gamma$. That is, the fracture apertures are uniformly bounded below. We note that in the work [27], the limiting case where $w_k \to 0$, i.e. collapsing fractures, is allowed.

Moreover, we define the scaled quantities $\hat{\mathbf{K}} = w_\Gamma \hat{\mathbf{K}_{\boldsymbol{\tau}}}$ and $\eta = w_\Gamma / \hat{K}_n$. Here, w_Γ is the aperture of the fracture network, equal to w_k on γ_k. The quantity $\hat{\mathbf{K}}$ is an effective tangential permeability, while η represents an effective conductivity.

4.2.2 The strong form

Here we see the model problem for groundwater flow in a fractured porous medium. The following equations consist of a Darcy flow problem in the bulk domain Ω_Γ and a reduced Darcy flow problem on the fracture network Γ, given by (4.1) and (4.2), respectively. Each set of equations has also a set of coupling conditions: in (4.1) we see conditions for the bulk variables on Γ, while in (4.2) we see conditions imposed at the intersection points of fractures. The latter assumes flux conservation and pressure continuity at the intersection points. Moreover, we assume a homogeneous boundary condition for the bulk velocity on $\partial\Omega^u$ and impose no–flow out of the immersed fracture tips. Recall that the fracture network Γ is completely immersed in the domain.

We seek the solutions $(\mathbf{u}, p)$, defined on Ω_Γ, and $(\hat{\mathbf{u}}, \hat{p})$, defined on Γ, such that

$$
\begin{cases}
\mathbf{K}^{-1}\mathbf{u} + \nabla p = 0 & \text{in } \Omega_\Gamma, \\
\operatorname{div} \mathbf{u} = f & \text{in } \Omega_\Gamma, \\
p = g_D & \text{on } \partial\Omega^D, \\
\mathbf{u} \cdot \mathbf{n} = 0 & \text{on } \partial\Omega^N, \\
\eta\{\mathbf{u} \cdot \mathbf{n}_\Gamma\} = [\![p]\!] & \text{on } \Gamma, \\
\eta\xi_0 [\![\mathbf{u} \cdot \mathbf{n}_\Gamma]\!] = \{p\} - \hat{p} & \text{on } \Gamma,
\end{cases}
\tag{4.1}
$$

$$
\begin{cases}
\hat{\mathbf{K}}^{-1}\hat{\mathbf{u}} + \nabla_{\boldsymbol{\tau}} \hat{p} = 0 & \text{in } \Gamma, \\
\operatorname{div}_{\boldsymbol{\tau}} \hat{\mathbf{u}} = \hat{f} + [\![\mathbf{u} \cdot \mathbf{n}_\Gamma]\!] & \text{in } \Gamma, \\
\hat{\mathbf{u}} \cdot \boldsymbol{\tau} = 0 & \text{on } I^F, \\
\hat{p}_k = p_i & \text{in } i \quad \forall \gamma_k \in S_i \ \forall i \in \mathcal{I}, \\
\sum_{k:\gamma_k \in S_i} (\hat{\mathbf{u}}_k \cdot \boldsymbol{\tau}_k)|_i = 0 & \text{in } i \quad \forall i \in \mathcal{I}.
\end{cases}
\tag{4.2}
$$

In the above, $\boldsymbol{\tau}$ represents the unit outward vector on the tangent plane represented by a fracture γ_k. Similar to $\mathbf{n}_\Gamma$, the vector $\boldsymbol{\tau}$ is defined according to which fracture we are restricted to. The operators $\operatorname{div}_{\boldsymbol{\tau}}$ and $\nabla_{\boldsymbol{\tau}}$ are the associated tangential divergence and gradient operators, respectively; in the two dimensional setting, these are of course both equal to $\partial/\partial x_{\boldsymbol{\tau}}$, the tangential derivative along the fracture. We proceed using the same notation as would be encountered in higher dimensions, so as to retain some notion of

generality. Furthermore, the closure parameter ξ_0 is related to the usual parameter ξ, often encountered in the literature (e.g. [94]) via $\xi_0 = (2\xi - 1)/4$; a different choice of ξ_0 relates to a different assumption made on the pressure profile across the fracture aperture when deriving the equations for the reduced model on the fracture network.

We define the usual average and jump operators, respectively, for functions defined on Ω_Γ, as

$$\{v\} := \frac{v^+ + v^-}{2}, \quad [\![v]\!] := v^+ - v^-,$$

where $v^\pm$ is the trace of the function on Γ from either side; cf. Section 4.3.2 where this notion is established more generally for less regular functions.

Before introducing the functional setting for which a weak formulation of (4.1)–(4.2) can be established, we must first make some assumptions on the data; such assumptions are paramount in proving well–posedness of the resulting problem, in Section 4.3.4.

To this end, we require $f \in L^2(\Omega_\Gamma)$ and $\hat{f} \in L^2(\Gamma)$, and that the boundary data term $g_D \in H^{\frac{1}{2}}(\partial\Omega^D)$. We have assumed a fully immersed network, but in the case that $I^D \neq \emptyset$ we would require $\hat{p} = \hat{g}_D \in H^{\frac{1}{2}}(I^D)$.

The permeability tensors $\mathbf{K}$ and $\hat{\mathbf{K}}$ are each assumed to be uniformly elliptic. That is, we assume the existence of constants $0 < K_* < K^*$ and $0 < \hat{K}_* < \hat{K}^*$ such that

$$K_*\|\mathbf{z}\|^2 \leq \mathbf{z}^\top \mathbf{K}(\mathbf{x})\mathbf{z} \leq K^*\|\mathbf{z}\|^2 \text{ a.e. in } \Omega_\Gamma,$$
$$\hat{K}_*\|\hat{\mathbf{z}}\|^2 \leq \hat{\mathbf{z}}^\top \hat{\mathbf{K}}(\mathbf{x})\hat{\mathbf{z}} \leq \hat{K}^*\|\hat{\mathbf{z}}\|^2 \text{ a.e. in } \Gamma,$$

for all $\mathbf{z} \in \mathbb{R}^d$ and for all $\hat{\mathbf{z}} \in \mathbb{R}$ with $\hat{\mathbf{z}} \cdot \mathbf{n}_\Gamma = 0$; the norm $\|\cdot\|$ being the Euclidean 2–norm.

Furthermore, we impose an assumption on the effective conductivity η. That is, the existence of constants $0 < \eta_* < \eta^*$ such that

$$\eta_* \leq \eta(\mathbf{x}) \leq \eta^* \text{ a.e. in } \Gamma.$$

Lastly, we set $\gamma_* = \min_k |\gamma_k|$ and $\gamma^* = \max_k |\gamma_k|$ as the smallest and largest lengths of the fractures; an obvious, but needed, assumption is that $\gamma_* > 0$.

4.3 Well–posedness of the continuous problem

4.3.1 Functional setting

Within this section we lay the foundations for the functional setting required for a weak formulation of (4.1)–(4.2) to exist. The justification for the function spaces defined here should become apparent during the derivation of the weak formulation in Section 4.3.3.

We start by introducing the space $H(\mathrm{div}, \Omega_\Gamma)$, recalling that $\Omega_\Gamma = \Omega \setminus \overline{\Gamma}$. This space consists of those vector–valued functions in $[L^2(\Omega_\Gamma)]^2$ whose distributional divergence is in $L^2(\Sigma)$ for all measurable $\Sigma \subset \Omega_\Gamma$. We emphasise here that functions in $L^2(\Omega_\Gamma)$ may be identified with those in $L^2(\Omega)$ since Γ is a set of measure zero. Such definition of $H(\mathrm{div}, \Omega_\Gamma)$ means that with respect to a partition of the domain, for example, into triangles $\mathscr{T}_h = \{\kappa\}$, global conformity requirements for $\mathbf{v} \in H(\mathrm{div}, \Omega_\Gamma)$ are that $\mathbf{v}|_\kappa \in H(\mathrm{div}, \kappa)$ for all $\kappa \in \mathscr{T}_h$, and that the normal–trace of $\mathbf{v}$ across element interfaces is continuous, except for those intersecting Γ; such definition will allow for the physical assumption, or lack thereof, that the normal–component of the Darcy velocity $\mathbf{u}$ may be discontinuous across the fracture network. We note also that $H(\mathrm{div}, \Omega_\Gamma)$ may be a broken space if the fracture network splits Ω into disconnected parts.

Moreover, we define the function spaces

$$
\begin{aligned}
V^\Omega &= \{\mathbf{v} \in H(\mathrm{div}, \Omega_\Gamma) : [\![\mathbf{v} \cdot \mathbf{n}_\Gamma]\!], \{\mathbf{v} \cdot \mathbf{n}_\Gamma\} \in L^2(\Gamma), (\mathbf{v} \cdot \mathbf{n})|_{\partial\Omega^N} = 0\}, \\
M^\Omega &= L^2(\Omega_\Gamma), \\
V^\Gamma &= \left\{ \hat{\mathbf{v}} \in \prod_{k=1}^{N_\Gamma} H(\mathrm{div}, \gamma_k) : \sum_{k:\gamma_k \in S_i} (\hat{\mathbf{v}}_k \cdot \boldsymbol{\tau}_k)|_i = 0 \quad \forall i \in \mathcal{I}, \quad (\hat{\mathbf{v}} \cdot \boldsymbol{\tau})|_{I^F} = 0 \right\}, \\
M^\Gamma &= L^2(\Gamma).
\end{aligned}
$$

To make sense of the jump and average of normal–traces on the fracture network, we refer to the upcoming Section 4.3.2. Each of these function spaces are Hilbert, and can be equipped with the relevant inner–products and induced norms. To this end, we define more compactly the spaces

$$
\begin{aligned}
\mathbf{V} &= V^\Omega \times V^\Gamma, \\
\mathbf{M} &= M^\Omega \times M^\Gamma,
\end{aligned}
$$

with the norms[2]

$$
\begin{aligned}
\|(\mathbf{v}, \hat{\mathbf{v}})\|^2_{\mathbf{V}} &= \|\mathbf{v}\|^2_{V^\Omega} + \|\hat{\mathbf{v}}\|^2_{V^\Gamma}, \\
\|(q, \hat{q})\|^2_{\mathbf{M}} &= \|q\|^2_{L^2(\Omega)} + \|\hat{q}\|^2_{L^2(\Gamma)},
\end{aligned}
$$

where

$$
\begin{aligned}
\|\mathbf{v}\|^2_{V^\Omega} &= \|\mathbf{v}\|^2_{[L^2(\Omega)]^2} + \|\mathrm{div}\ \mathbf{v}\|^2_{L^2(\Omega)} + \|\{\mathbf{v} \cdot \mathbf{n}_\Gamma\}\|^2_{L^2(\Gamma)} + \|[\![\mathbf{v} \cdot \mathbf{n}_\Gamma]\!]\|^2_{L^2(\Gamma)}, \\
\|\hat{\mathbf{v}}\|_{V^\Gamma} &= \|\hat{\mathbf{v}}\|^2_{L^2(\Gamma)} + \|\mathrm{div}_{\boldsymbol{\tau}}\ \hat{\mathbf{v}}\|^2_{L^2(\Gamma)}.
\end{aligned}
$$

[2] In other works, for example [94] the norm on the velocity space $\mathbf{V}$ has instead the squared norms of the normal traces of the bulk velocity $\mathbf{v}$ on either side of Γ, instead of the norms of the jump and average operators. One can show however that these norms are in fact equivalent [55].

4.3.2 Trace theory on fractures

Before proceeding to the derivation of the weak formulation of (4.1)–(4.2), we need to consider traces. Indeed, the idea of a function (for example the bulk Darcy velocity $\mathbf{u}$ or bulk pressure p), or its normal–component, being restricted onto the fracture network Γ may not make sense if the function is not, in a loose sense, regular enough. Here, we briefly state some details concerning the trace of functions onto fractures, which is a simple extension of existing trace theory on Lipschitz domains. The main idea (illustrated in Figure 4.3) is that in the case where the fracture network, or part of it, is completely immersed in the domain, we can always extend the network in order to partition the domain Ω into several smaller Lipschitz domains; on these subdomains the usual trace theory applies, where part of the boundary of these subdomains indeed contain the fractures we are interested in.

Thus, we need only to investigate the trace of a function on a single fracture, and proceed as such. Consider an open and bounded Lipschitz domain $\Omega \subset \mathbb{R}^d$, and a single fracture γ. In general, this fracture either cuts the domain into two smaller Lipschitz subdomains $\Omega^{\pm}$, or it is either partially or fully immersed. In either of the latter cases, denote by $\tilde{\gamma} \supset \gamma$ the (arbitrary) extension[3] of γ to the boundary of the domain, such that $\tilde{\gamma}$ then partitions Ω into the two Lipschitz subdomains $\Omega^{\pm}$. Fix the normal vector $\mathbf{n}_\gamma = \mathbf{n}^+|_\gamma = -\mathbf{n}^-|_\gamma$ and the spatial dimension $d = 2$.

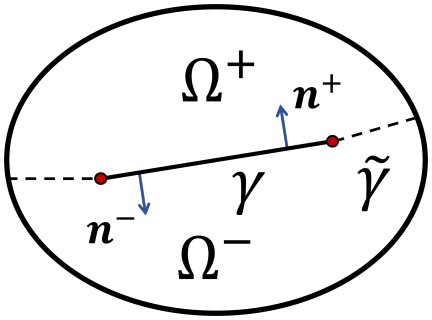

FIG. 4.3 – *The arbitrary extension of an immersed fracture to create partitioning Lipschitz subdomains.*

Building on the discussion in Section 2.1, for $s > 0$ and $p \in [1, \infty)$ we consider here the operators $T^{\pm} : W^{s,p}(\Omega^{\pm}) \to L^p(\partial\Omega^{\pm})$ extending the notion of trace such that

$$T^{\pm}[u] = u|_{\partial\Omega^{\pm}} \quad \forall u \in W^{s,p}(\Omega^{\pm}) \cap C^0(\overline{\Omega^{\pm}}).$$

Standard trace theory (see, for example, [51, Theorem 3.10]) says that for $s > \frac{1}{p}$, since $\Omega^{\pm}$ are Lipschitz, that $T^{\pm}$ are bounded. That is, there are constants $C^{\pm}$ (depending on s, p and

[3] Cf. Figure 4.3.

$\Omega^{\pm}$) such that

$$\|T^{\pm}[u]\|_{L^p(\partial\Omega^{\pm})} \leq C^{\pm}\|u\|_{W^{s,p}(\Omega^{\pm})}.$$

For example, $s = 1$ and $p = 2$ tells us that

$$\|T^{\pm}[u]\|_{L^2(\partial\Omega^{\pm})} \leq C^{\pm}\|u\|_{H^1(\Omega^{\pm})}. \tag{4.3}$$

Since $\gamma \subset \partial\Omega^{\pm}$ in either case, we know that

$$\|T^{\pm}[u]\|_{L^p(\gamma)} \leq C^{\pm}\|u\|_{W^{s,p}(\Omega^{\pm})} \leq C^{\pm}\|u\|_{W^{s,p}(\Omega)}.$$

If u is defined only on $\Omega_\gamma = \Omega \setminus \overline{\gamma}$, then the right–hand–side can be replaced with the norm taken on the (possibly) broken space $W^{s,p}(\Omega_\gamma)$, and the same is true throughout. We emphasise that traces may not always be continuous across the fracture γ, which is why we require the two separate trace operators on either side. Using the above however, we can derive bounds on both the jumps of functions across the fracture, and for averages. For the average of a function, we have

$$\begin{aligned}\|\{u\}\|_{L^p(\gamma)} &= \left\| \frac{1}{2}(T^+[u] + T^-[u]) \right\|_{L^p(\gamma)} \\ &\leq \frac{1}{2}\left(\|T^+[u]\|_{L^p(\gamma)} + \|T^-[u]\|_{L^p(\gamma)}\right) \\ &\leq \max\{C^+, C^-\}\|u\|_{W^{s,p}(\Omega)}.\end{aligned}$$

For the jump of the function u across the fracture, an added factor of two appears in the bound as

$$\|[\![u]\!]\|_{L^p(\gamma)} \leq 2\max\{C^+, C^-\}\|u\|_{W^{s,p}(\Omega)}.$$

Remark 4.1. *For particular choices of s and p we can consider the surjectivity of the trace operators $T^{\pm}$. Indeed, if $s = 1$ and $p = 1$; $1/2 < s < 3/2$ and $p = 2$; or $1/p < s \leq 1$ and $p \neq \{1, 2\}$, then $T^{\pm} : W^{s,p}(\Omega^{\pm}) \to W^{s-\frac{1}{p},p}(\partial\Omega^{\pm})$ are bounded and surjective.*

While still considering the single fracture γ, we consider normal–traces; here, we refer to [51, Theorem 4.15]. Indeed, from Section 2.1 we know that for Lipschitz domains, vector–valued functions in $H(\mathrm{div}, \Omega)$ have normal–traces $(\mathbf{v} \cdot \mathbf{n})|_{\partial\Omega}$ defined only in the space $H^{-\frac{1}{2}}(\partial\Omega)$. That is, as linear functionals acting on $H^{\frac{1}{2}}(\partial\Omega)$. This is a particular case of the normal–trace operator defined between the spaces

$$W^{\mathrm{div},p}(\Omega) = \{\mathbf{v} \in [L^p(\Omega)]^2 : \mathrm{div}\ \mathbf{v} \in L^p(\Omega)\}$$

and $W^{-\frac{1}{p},p}(\partial\Omega)$. As such, we define the following normal–trace operators

$$T^{d,\pm} : H(\mathrm{div}, \Omega^{\pm}) \to H^{-\frac{1}{2}}(\partial\Omega^{\pm}).$$

The quantity $T^{d,\pm}[\mathbf{u}]$ is defined via the Divergence Theorem by

$$\langle T^{d,\pm}[\mathbf{u}],\phi\rangle_{H^{-\frac{1}{2}}(\partial\Omega^\pm),H^{\frac{1}{2}}(\partial\Omega^\pm)} = \int_{\Omega^\pm} \mathfrak{E}^\pm[\phi]\text{div }\mathbf{u} + \int_{\Omega^\pm} \nabla\mathfrak{E}^\pm[\phi]\cdot\mathbf{u} \quad \forall\phi\in H^{\frac{1}{2}}(\partial\Omega^\pm),$$

and whose definition is independent of the choice of right–hand inverse (or extension operator) $T^\pm[\mathfrak{E}^\pm[\phi]]=\phi$. These operators extend the idea of normal–trace such that

$$T^{d,\pm}[\mathbf{u}] = \mathbf{u}|_{\partial\Omega^\pm}\cdot\mathbf{n}^\pm \quad \forall\mathbf{u}\in[C^\infty(\overline{\Omega^\pm})]^2,$$

and are, in fact, surjective onto $H^{-\frac{1}{2}}(\partial\Omega^\pm)$.

More often than not, we must use the definition $T^{d,\pm}[\mathbf{u}]$ when considering the normal–trace of $\mathbf{u}$, unless we assume some more regularity. Indeed, with $\Omega^\pm$ still only assumed to be Lipschitz, and assuming $\mathbf{u}\in[H^1(\Omega^\pm)]^2$ instead of $H(\text{div},\Omega^\pm)$, one can obtain the normal–trace of $\mathbf{u}$ in $L^2(\partial\Omega^\pm)$.

With $\Omega^\pm$ Lipschitz (e.g. polygonal), we know that the unit outward normal vector $\mathbf{n}^\pm\in L^\infty(\partial\Omega^\pm)$. We discuss here how we can consider the quantity $T^\pm[\mathbf{u}]\cdot\mathbf{n}^\pm$ as an extension of $T^{d,\pm}[\mathbf{u}]$ for $\mathbf{u}\in[H^1(\Omega^\pm)]^2$, interpreting the trace of a vector as taking traces component–wise. We shall see in Lemma 4.2 that $T^\pm[\mathbf{u}]\cdot\mathbf{n}^\pm\in L^2(\partial\Omega^\pm)$; therefore, identifying $L^2(\partial\Omega^\pm)$ with its own dual–space, we can view $T^\pm[\mathbf{u}]\cdot\mathbf{n}^\pm$ as a member of $H^{-\frac{1}{2}}(\partial\Omega^\pm)$ (this is since $[L^2(\partial\Omega^\pm)]^*\subset H^{-\frac{1}{2}}(\partial\Omega^\pm)$ and $H^{\frac{1}{2}}(\partial\Omega^\pm)\subset L^2(\partial\Omega^\pm)$).

Therefore,

$$\begin{aligned}\langle T^\pm[\mathbf{u}]\cdot\mathbf{n}^\pm,\phi\rangle_{H^{-\frac{1}{2}}(\partial\Omega^\pm),H^{\frac{1}{2}}(\partial\Omega^\pm)} &= \langle T^\pm[\mathbf{u}]\cdot\mathbf{n}^\pm,\phi\rangle_{L^2(\partial\Omega^\pm)^*,L^2(\partial\Omega^\pm)}\\ &= \int_{\partial\Omega^\pm}(T^\pm[\mathbf{u}]\cdot\mathbf{n}^\pm)\phi\\ &= \int_{\Omega^\pm}\mathfrak{E}^\pm[\phi]\text{div }\mathbf{u} + \int_{\Omega^\pm}\nabla\mathfrak{E}^\pm[\phi]\cdot\mathbf{u} \quad \forall\phi\in H^{\frac{1}{2}}(\partial\Omega^\pm).\end{aligned}$$

This shows that $T^\pm[\mathbf{u}]\cdot\mathbf{n}^\pm = T^{d,\pm}[\mathbf{u}]$ in $H^{-\frac{1}{2}}(\partial\Omega^\pm)$, i.e., the former is an extension of the latter for the more regular $\mathbf{u}\in[H^1(\Omega^\pm)]^2$.

Lemma 4.2. *Under the foregoing notation, let $\mathbf{u}\in[H^1(\Omega^\pm)]^2$. Then, there are constants $D^\pm>0$, depending only on $\Omega^\pm$, such that*

$$\|T^\pm[\mathbf{u}]\cdot\mathbf{n}^\pm\|_{L^2(\partial\Omega^\pm)} \le D^\pm\|\mathbf{u}\|_{[H^1(\Omega^\pm)]^2}.$$

Proof. Denote $\mathbf{u} = (u_1, u_2)^\top$ where $u_i \in H^1(\Omega^\pm)$, $i = 1, 2$ and $\mathbf{n}^\pm = (n_1^\pm, n_2^\pm)$. We have

$$\begin{aligned}
\|T^\pm[\mathbf{u}] \cdot \mathbf{n}^\pm\|^2_{L^2(\partial\Omega^\pm)} &= \int_{\partial\Omega} (T^\pm[\mathbf{u}] \cdot \mathbf{n}^\pm)^2 \\
&= \int_{\partial\Omega^\pm} (T^\pm[u_1] n_1^\pm + T^\pm[u_2] n_2^\pm)^2 \\
&\leq \|\mathbf{n}^\pm\|^2_{L^\infty(\partial\Omega^\pm)} \int_{\partial\Omega^\pm} (T^\pm[u_1] + T^\pm[u_2])^2 \\
&= \|\mathbf{n}^\pm\|^2_{L^\infty(\partial\Omega^\pm)} \|T^\pm[u_1] + T^\pm[u_2]\|^2_{L^2(\partial\Omega^\pm)}.
\end{aligned}$$

The triangle inequality, followed by Cauchy's inequality thus tells us that

$$\begin{aligned}
\|\mathbf{n}^\pm\|^2_{L^\infty(\partial\Omega)} \|T^\pm[u_1] + T^\pm[u_2]\|^2_{L^2(\partial\Omega^\pm)} &\leq \|\mathbf{n}^\pm\|^2_{L^\infty(\partial\Omega^\pm)} (\|T^\pm[u_1]\|^2_{L^2(\partial\Omega^\pm)} + \|T^\pm[u_2]\|^2_{L^2(\partial\Omega^\pm)} \\
&\quad + 2\|T^\pm[u_1]\|_{L^2(\partial\Omega^\pm)} \|T^\pm[u_2]\|_{L^2(\partial\Omega^\pm)}) \\
&\leq 2\|\mathbf{n}^\pm\|^2_{L^\infty(\partial\Omega^\pm)} \|T^\pm[\mathbf{u}]\|^2_{L^2(\partial\Omega^\pm)}.
\end{aligned}$$

The trace operator $T^\pm : [H^1(\Omega^\pm)]^2 \to L^2(\partial\Omega^\pm)$ is bounded (cf. (4.3)), giving the constants $C^\pm > 0$ such that

$$2\|\mathbf{n}^\pm\|^2_{L^\infty(\partial\Omega^\pm)} \|T^\pm[\mathbf{u}]\|^2_{L^2(\partial\Omega^\pm)} \leq 2\|\mathbf{n}^\pm\|^2_{L^\infty(\partial\Omega^\pm)} (C^\pm)^2 \|\mathbf{u}\|^2_{[H^1(\Omega^\pm)]^2}.$$

Thus, with $D^\pm = \sqrt{2}\|\mathbf{n}^\pm\|_{L^\infty(\partial\Omega^\pm)} C^\pm$ we see that

$$\|T^\pm[\mathbf{u}] \cdot \mathbf{n}^\pm\|_{L^2(\partial\Omega^\pm)} \leq D^\pm \|\mathbf{u}\|_{[H^1(\Omega^\pm)]^2},$$

as required. Of course, $\|\mathbf{n}^\pm\|_{L^\infty(\partial\Omega^\pm)} \leq 1$, so the same conclusions hold with the constants $D^\pm = \sqrt{2}C^\pm$ instead. □

This result shows that the normal–trace operator is in fact bounded in $L^2(\partial\Omega^\pm)$ when acting on the more regular space $[H^1(\Omega^\pm)]^2$.

Similar to before, we determine a bound on the average normal–trace across the fracture γ. We have, for $\mathbf{u} \in [H^1(\Omega)]^2$,

$$\begin{aligned}
\|\{\mathbf{u} \cdot \mathbf{n}_\gamma\}\|_{L^2(\gamma)} &= \left\| \frac{1}{2} \left(T^+[\mathbf{u}] \cdot \mathbf{n}_\gamma + T^-[\mathbf{u}] \cdot \mathbf{n}_\gamma \right) \right\|_{L^2(\gamma)} \\
&= \left\| \frac{1}{2} \left(T^+[\mathbf{u}] \cdot \mathbf{n}^+ - T^-[\mathbf{u}] \cdot \mathbf{n}^- \right) \right\|_{L^2(\gamma)} \\
&\leq \frac{1}{2} \left(\|T^+[\mathbf{u}] \cdot \mathbf{n}^+\|_{L^2(\gamma)} + \|T^-[\mathbf{u}] \cdot \mathbf{n}^-\|_{L^2(\gamma)} \right) \\
&\leq \frac{1}{2} \left(\|T^+[\mathbf{u}] \cdot \mathbf{n}^+\|_{L^2(\partial\Omega^+)} + \|T^-[\mathbf{u}] \cdot \mathbf{n}^-\|_{L^2(\partial\Omega^-)} \right) \\
&\leq \max\{D^+, D^-\} \|\mathbf{u}\|_{[H^1(\Omega)]^2}
\end{aligned}$$

i.e. with $D = \max\{D^+, D^-\}$, we have

$$\|\{\mathbf{u} \cdot \mathbf{n}_\gamma\}\|_{L^2(\gamma)} \leq D\|\mathbf{u}\|_{[H^1(\Omega)]^2}. \tag{4.4}$$

The same bounds hold for $\|[\![\mathbf{u}\cdot\mathbf{n}_\gamma]\!]\|_{L^2(\gamma)}$ as well, with a factor of two on the right–hand–side.

To conclude this section we state two more results that will be useful later on.

Lemma 4.3. *Suppose $\Omega \subset \mathbb{R}^2$ is an open and bounded Lipschitz domain that is also convex. Then, for $\varphi \in H^2(\Omega) \cap H^1_{0,D}(\Omega)$ we have the elliptic regularity result*

$$\|\varphi\|_{H^2(\Omega)} \leq C_{ER}(\Omega)\|\Delta\varphi\|_{L^2(\Omega)},$$

where $C_{ER}(\Omega) > 0$ is a constant depending only on the domain.

Proof. See, for example, [30, p. 139]. □

Lemma 4.4. *Suppose $\Omega \subset \mathbb{R}^2$ is an open and bounded Lipschitz domain that is also convex. Then, for $\phi \in H^2(\Omega) \cap H^1_{0,D}(\Omega)$ there is a constant $C > 0$ such that*

$$\|\{\nabla\phi \cdot \mathbf{n}_\gamma\}\|_{L^2(\gamma)} \leq C\|\Delta\phi\|_{L^2(\Omega)}.$$

Proof. The proof is a simple application of the estimate (4.4) and the elliptic regularity result given above as Lemma 4.3. Since $\phi \in H^2(\Omega)$ we know that $\nabla\phi \in [H^1(\Omega)]^2$; therefore,

$$\begin{aligned}\|\{\nabla\phi \cdot \mathbf{n}_\gamma\}\|_{L^2(\gamma)} &\leq \max\{D^+, D^-\}\|\nabla\phi\|_{[H^1(\Omega)]^2} \\ &\leq \max\{D^+, D^-\}\|\phi\|_{H^2(\Omega)} \\ &\leq C_{\mathrm{ER}}(\Omega)\max\{D^+, D^-\}\|\Delta\phi\|_{L^2(\Omega)},\end{aligned}$$

as required, with $C = C_{\mathrm{ER}}(\Omega)\max\{D^+, D^-\}$. □

Where it is obvious throughout, we drop the operator notation when referring to traces, and instead use the usual notation of restrictions. A full characterisation of traces on fractures, and more precise details than those stated here, can be found in the work [6].

4.3.3 Deriving the weak formulation

As is typical when defining a weak formulation for elliptic PDEs, we begin by multiplying the governing equations by test functions and integrating over the associated domains. Firstly, in (4.1) and (4.2) we multiply Darcy's law, in both the bulk and fracture network, by test functions $(\mathbf{v}, \hat{\mathbf{v}})$. We see that

$$\int_{\Omega_\Gamma} (\mathbf{K}^{-1}\mathbf{u}) \cdot \mathbf{v} + \int_\Gamma (\hat{\mathbf{K}}^{-1}\hat{\mathbf{u}}) \cdot \hat{\mathbf{v}} + \int_{\Omega_\Gamma} \mathbf{v} \cdot \nabla p + \int_\Gamma \hat{\mathbf{v}} \cdot \nabla_{\boldsymbol{\tau}} \hat{p} = 0. \tag{4.5}$$

Next, we look in particular at the third integral in (4.5). Here, we apply integration by parts, taking into account the fracture network as part of the boundary. Thus,

$$\int_{\Omega_\Gamma} \mathbf{v} \cdot \nabla p = -\int_{\Omega_\Gamma} p \operatorname{div} \mathbf{v} + \int_{\partial\Omega^D} g_D(\mathbf{v} \cdot \mathbf{n}) + \int_\Gamma [\![p(\mathbf{v} \cdot \mathbf{n}_\Gamma)]\!].$$

The fracture integral can be simplified via the jump–average relation: $[\![ab]\!] = \{a\}[\![b]\!]+[\![a]\!]\{b\}$, and hence we see that

$$\int_\Gamma [\![p(\mathbf{v}\cdot\mathbf{n}_\Gamma)]\!] = \int_\Gamma (\{p\}[\![\mathbf{v}\cdot\mathbf{n}_\Gamma]\!] + [\![p]\!]\{\mathbf{v}\cdot\mathbf{n}_\Gamma\}).$$

Using the bulk–fracture interface conditions in (4.1) we see that

$$\begin{aligned}\int_\Gamma (\{p\}[\![\mathbf{v}\cdot\mathbf{n}_\Gamma]\!] + [\![p]\!]\{\mathbf{v}\cdot\mathbf{n}_\Gamma\}) &= \int_\Gamma [(\hat{p} + \eta\xi_0[\![\mathbf{u}\cdot\mathbf{n}_\Gamma]\!])[\![\mathbf{v}\cdot\mathbf{n}_\Gamma]\!] + \eta\{\mathbf{u}\cdot\mathbf{n}_\Gamma\}\{\mathbf{v}\cdot\mathbf{n}_\Gamma\}] \\ &= \int_\Gamma \eta(\xi_0[\![\mathbf{u}\cdot\mathbf{n}_\Gamma]\!][\![\mathbf{v}\cdot\mathbf{n}_\Gamma]\!] + \{\mathbf{u}\cdot\mathbf{n}_\Gamma\}\{\mathbf{v}\cdot\mathbf{n}_\Gamma\}) + \int_\Gamma \hat{p}[\![\mathbf{v}\cdot\mathbf{n}_\Gamma]\!].\end{aligned}$$

Similarly, the fourth integral in (4.5) can be written as a sum over the individual fractures and then integrated by parts as

$$\begin{aligned}\int_\Gamma \hat{\mathbf{v}}\cdot\nabla_{\boldsymbol{\tau}}\hat{p} = \sum_{k=1}^{N_\Gamma}\int_{\gamma_k}\hat{\mathbf{v}}_k\cdot\nabla_{\boldsymbol{\tau}}\hat{p}_k = \sum_{k=1}^{N_\Gamma}\left(-\int_{\gamma_k}\hat{p}_k\mathrm{div}_{\boldsymbol{\tau}}\,\hat{\mathbf{v}}_k + \int_{\partial\gamma_k^F}\hat{p}_k(\hat{\mathbf{v}}_k\cdot\boldsymbol{\tau}_k)\right) \\ + \sum_{i\in\mathcal{I}}\sum_{k:\gamma_k\in S_i}\hat{p}_k(\hat{\mathbf{v}}_k\cdot\boldsymbol{\tau}_k)|_i.\end{aligned}$$

Indeed, since the fracture network is immersed the fracture boundaries $\partial\gamma_k$ consist of immersed tips and intersection points. We impose no–flow out of the immersed tips for the test function $\hat{\mathbf{v}}$, i.e., $\hat{\mathbf{v}}\in V^\Gamma$, and thus this contribution vanishes from the above. Moreover, the intersection conditions from (4.2) together imply that

$$\sum_{i\in\mathcal{I}}\sum_{k:\gamma_k\in S_i}\hat{p}_k(\hat{\mathbf{v}}_k\cdot\boldsymbol{\tau}_k)|_i = \sum_{i\in\mathcal{I}}p_i\sum_{k:\gamma_k\in S_i}(\hat{\mathbf{v}}_k\cdot\boldsymbol{\tau}_k)|_i = 0.$$

This means that simply, in our case of an immersed network,

$$\int_\Gamma \hat{\mathbf{v}}\cdot\nabla_{\boldsymbol{\tau}}\hat{p} = -\int_\Gamma \hat{p}\,\mathrm{div}_{\boldsymbol{\tau}}\,\hat{\mathbf{v}}.$$

Collecting these results brings us to the following statement

$$\begin{aligned}\int_{\Omega_\Gamma}(\mathbf{K}^{-1}\mathbf{u})\cdot\mathbf{v} + \int_\Gamma(\hat{\mathbf{K}}^{-1}\hat{\mathbf{u}})\cdot\hat{\mathbf{v}} - \int_{\Omega_\Gamma}p\,\mathrm{div}\,\mathbf{v} - \int_\Gamma\hat{p}\,\mathrm{div}_{\boldsymbol{\tau}}\,\hat{\mathbf{v}} \\ + \int_\Gamma\eta(\xi_0[\![\mathbf{u}\cdot\mathbf{n}_\Gamma]\!][\![\mathbf{v}\cdot\mathbf{n}_\Gamma]\!] + \{\mathbf{u}\cdot\mathbf{n}_\Gamma\}\{\mathbf{v}\cdot\mathbf{n}_\Gamma\}) + \int_\Gamma\hat{p}[\![\mathbf{v}\cdot\mathbf{n}_\Gamma]\!] = -\int_{\partial\Omega^D}g_D(\mathbf{v}\cdot\mathbf{n}).\end{aligned}$$

Define the bilinear form $A:\mathbf{V}\times\mathbf{V}\to\mathbb{R}$ as

$$A((\mathbf{u},\hat{\mathbf{u}}),(\mathbf{v},\hat{\mathbf{v}})) := a(\mathbf{u},\mathbf{v}) + \hat{a}(\hat{\mathbf{u}},\hat{\mathbf{v}}) \tag{4.6}$$

where

$$\begin{aligned}a(\mathbf{u},\mathbf{v}) &:= \int_{\Omega_\Gamma}(\mathbf{K}^{-1}\mathbf{u})\cdot\mathbf{v} + \int_\Gamma\eta(\xi_0[\![\mathbf{u}\cdot\mathbf{n}_\Gamma]\!][\![\mathbf{v}\cdot\mathbf{n}_\Gamma]\!] + \{\mathbf{u}\cdot\mathbf{n}_\Gamma\}\{\mathbf{v}\cdot\mathbf{n}_\Gamma\}), \\ \hat{a}(\hat{\mathbf{u}},\hat{\mathbf{v}}) &:= \int_\Gamma(\hat{\mathbf{K}}^{-1}\hat{\mathbf{u}})\cdot\hat{\mathbf{v}}.\end{aligned}$$

Furthermore, define the bilinear form $B : \mathbf{V} \times \mathbf{M} \to \mathbb{R}$ as

$$B((\mathbf{v}, \hat{\mathbf{v}}), (q, \hat{q})) := b(\mathbf{v}, q) + \hat{b}(\hat{\mathbf{v}}, \hat{q}) + d(\mathbf{v}, \hat{q}) \tag{4.7}$$

where

$$b(\mathbf{v}, q) := -\int_{\Omega_\Gamma} q \operatorname{div} \mathbf{v}, \quad \hat{b}(\hat{\mathbf{v}}, \hat{q}) := -\int_\Gamma \hat{q} \operatorname{div}_{\boldsymbol{\tau}} \hat{\mathbf{v}}, \quad d(\mathbf{v}, q) := \int_\Gamma \hat{q} [\![\mathbf{v} \cdot \mathbf{n}_\Gamma]\!].$$

Dealing with the conservation of mass equations in the model is straightforward, and just amounts to multiplying by test functions $(q, \hat{q}) \in \mathbf{M}$ and integrating over the domains. Thus, with the linear functionals $F^u : \mathbf{V} \to \mathbb{R}$ and $F^p : \mathbf{M} \to \mathbb{R}$ defined, respectively, by

$$F^u((\mathbf{v}, \hat{\mathbf{v}})) := -\int_{\partial\Omega^D} g_D(\mathbf{v} \cdot \mathbf{n}), \quad F^p((q, \hat{q})) := -\int_{\Omega_\Gamma} fq - \int_\Gamma \hat{f}\hat{q},$$

we can write down a weak formulation of the fractured porous medium model (4.1)–(4.2) as the standard saddle–point problem:

Find $(\mathbf{u}, \hat{\mathbf{u}}) \in \mathbf{V}$ and $(p, \hat{p}) \in \mathbf{M}$ such that

$$A((\mathbf{u}, \hat{\mathbf{u}}), (\mathbf{v}, \hat{\mathbf{v}})) + B((\mathbf{v}, \hat{\mathbf{v}}), (p, \hat{p})) = F^u((\mathbf{v}, \hat{\mathbf{v}})), \tag{4.8}$$

$$B((\mathbf{u}, \hat{\mathbf{u}}), (q, \hat{q})) = F^p((q, \hat{q})), \tag{4.9}$$

for all $(\mathbf{v}, \hat{\mathbf{v}}) \in \mathbf{V}$ and $(q, \hat{q}) \in \mathbf{M}$.

4.3.4 Establishing continuous well–posedness

Consider here the case where the fracture network Γ consists of a single fracture (also denoted by Γ) intersecting the boundary of the domain Ω at both ends, splitting it in two. Of course, this is different to the immersed fracture network model described previously, but the well–posedness result can, and has, been extended to cover these more complex cases, which we discuss in Remark 4.7. In this case, we adopt the notation $I^D = \partial\Gamma^D$ and $I^N = \partial\Gamma^N$ for the boundary of the fracture.

Since (4.8)–(4.9) has the structure of a typical saddle–point problem, standard theory for mixed problems can be employed with ease to establish well–posedness via Theorem 2.7. That is, assuming that the linear functionals F^u and F^p, and the bilinear forms A and B, are continuous, we require the following two criteria to be satisfied.

Firstly, it is sufficient that A is coercive on the null space $\mathbf{V}^0$, defined below as

$$\mathbf{V}^0 = \{(\mathbf{v}, \hat{\mathbf{v}}) \in \mathbf{V} : B((\mathbf{v}, \hat{\mathbf{v}}), (q, \hat{q})) = 0 \quad \forall (q, \hat{q}) \in \mathbf{M}\}. \tag{4.10}$$

This space is the same as the kernel of the associated operator $\mathfrak{B}$ to the bilinear form B, which we will define and discuss in Section 4.5.1. Next, inf–sup stability for the bilinear form

B must be satisfied; that is, the existence of a constant $\beta > 0$ such that for all $(q, \hat{q}) \in \mathbf{M}$

$$\sup_{(\mathbf{v},\hat{\mathbf{v}})\in\mathbf{V}} \frac{B((\mathbf{v},\hat{\mathbf{v}}),(q,\hat{q}))}{\|(\mathbf{v},\hat{\mathbf{v}})\|_{\mathbf{V}}} \geq \beta\|(q,\hat{q})\|_{\mathbf{M}}.$$

The continuity proofs are fairly trivial (see [55, 94], for example). Moreover, the statements, and proofs, of the coercivity of A and the inf–sup stability of B are given as the following two lemmas, respectively.

Lemma 4.5. *With $\xi_0 > 0$, the bilinear form $A : \mathbf{V} \times \mathbf{V} \to \mathbb{R}$ defined by (4.6) is coercive on the null space $\mathbf{V}^0$ defined by (4.10). That is, there is a constant $C_A > 0$, such that for all $(\mathbf{v}, \hat{\mathbf{v}}) \in \mathbf{V}^0$*

$$A((\mathbf{v},\hat{\mathbf{v}}),(\mathbf{v},\hat{\mathbf{v}})) \geq C_A\|(\mathbf{v},\hat{\mathbf{v}})\|^2_{\mathbf{V}},$$

and C_A is independent of $(\mathbf{v}, \hat{\mathbf{v}})$.

Proof. We notice first that if $(\mathbf{v}, \hat{\mathbf{v}}) \in \mathbf{V}^0$ then div $\mathbf{v} = 0$ in $L^2(\Omega_\Gamma)$ and $\mathrm{div}_{\boldsymbol{\tau}}\hat{\mathbf{v}} = [\![\mathbf{v}\cdot\mathbf{n}_\Gamma]\!]_\Gamma$ in $L^2(\Gamma)$. Therefore, looking at each of the terms in $A((\mathbf{v},\hat{\mathbf{v}}),(\mathbf{v},\hat{\mathbf{v}}))$ separately, we see that

$$\begin{aligned}\int_{\Omega_\Gamma}(\mathbf{K}^{-1}\mathbf{v})\cdot\mathbf{v} + \int_\Gamma(\hat{\mathbf{K}^{-1}}\hat{\mathbf{v}})\cdot\hat{\mathbf{v}} + \int_\Gamma \eta\xi_0[\![\mathbf{v}\cdot\mathbf{n}_\Gamma]\!]^2 + \int_\Gamma \eta\{\mathbf{v}\cdot\mathbf{n}_\Gamma\}^2 \\ \geq \frac{1}{K^*}\|\mathbf{v}\|^2_{[L^2(\Omega)]^2} + \frac{1}{\hat{K}^*}\|\hat{\mathbf{v}}\|^2_{L^2(\Gamma)} + \eta_*\xi_0\|[\![\mathbf{v}\cdot\mathbf{n}_\Gamma]\!]\|^2_{L^2(\Gamma)} + \eta_*\|\{\mathbf{v}\cdot\mathbf{n}_\Gamma\}\|^2_{L^2(\Gamma)},\end{aligned}$$

using the data assumptions outlined in Section 4.2.2. Now, since $(\mathbf{v}, \hat{\mathbf{v}}) \in \mathbf{V}^0$ we see that

$$\|(\mathbf{v},\hat{\mathbf{v}})\|^2_{\mathbf{W}} = \|\mathbf{v}\|^2_{[L^2(\Omega)]^2} + \|\hat{\mathbf{v}}\|^2_{L^2(\Gamma)} + 2\|[\![\mathbf{v}\cdot\mathbf{n}_\Gamma]\!]\|^2_{L^2(\Gamma)} + \|\{\mathbf{v}\cdot\mathbf{n}_\Gamma\}\|^2_{L^2(\Gamma)}.$$

Therefore,

$$A((\mathbf{v},\hat{\mathbf{v}}),(\mathbf{v},\hat{\mathbf{v}})) \geq \min\left\{\frac{1}{K^*}, \frac{1}{\hat{K}^*}, \frac{\eta_*\xi_0}{2}, \eta_*\right\}\|(\mathbf{v},\hat{\mathbf{v}})\|^2_{\mathbf{V}}.$$

With C_A as the above constant, noting that $C_A > 0$ is true only if $\xi_0 > 0$ (as this was not assumed in Section 4.2.2), we conclude the proof. □

Lemma 4.6. *Assume that Ω is convex. Then, for the bilinear form $B : \mathbf{V} \times \mathbf{M} \to \mathbb{R}$, defined by (4.7), there exists a constant $\beta > 0$ such that such that for all $(q, \hat{q}) \in \mathbf{M}$*

$$\sup_{(\mathbf{v},\hat{\mathbf{v}})\in\mathbf{V}} \frac{B((\mathbf{v},\hat{\mathbf{v}}),(q,\hat{q}))}{\|(\mathbf{v},\hat{\mathbf{v}})\|_{\mathbf{V}}} \geq \beta\|(q,\hat{q})\|_{\mathbf{M}}.$$

Proof. We prove the statement of inf–sup stability by proving an equivalent statement. That is, for a given $(q, \hat{q}) \in \mathbf{M}$, if there exists a $(\mathbf{v}, \hat{\mathbf{v}}) \in \mathbf{V}$ such that:

$$\begin{aligned}B((\mathbf{v},\hat{\mathbf{v}}),(q,\hat{q})) &= \|(q,\hat{q})\|^2_{\mathbf{M}}, \\ \|(\mathbf{v},\hat{\mathbf{v}})\|_{\mathbf{V}} &\leq C\|(q,\hat{q})\|_{\mathbf{M}},\end{aligned}$$

for a constant $C > 0$ independent of $(q, \hat{q})$ and $(\mathbf{v}, \hat{\mathbf{v}})$, then inf–sup stability is satisfied (see [30, 94], for example). Thus, for a given $(q, \hat{q}) \in \mathbf{M}$ we construct such a $(\mathbf{v}, \hat{\mathbf{v}}) \in \mathbf{V}$ as follows.

We consider two auxiliary problems, whose well–posedness is known thanks to a simple application of the Lax–Milgram theorem. We proceed also assuming that Ω is convex. Firstly, we consider the solution $\varphi \in H^2(\Omega)$ to

$$\begin{aligned} -\Delta\varphi &= q \text{ in } \Omega, \\ \varphi &= 0 \text{ on } \partial\Omega^D, \\ \frac{\partial\varphi}{\partial\mathbf{n}} &= 0 \text{ on } \partial\Omega^N, \end{aligned}$$

whose existence is guaranteed by the regularity of the domain, [55, p. 9] i.e., it is a convex polygon[4]. Furthermore, with $\Delta_{\boldsymbol{\tau}} = \mathrm{div}_{\boldsymbol{\tau}}(\nabla_{\boldsymbol{\tau}})$, we consider $\hat{\varphi} \in H^2(\Gamma)$ the solution of

$$\begin{aligned} -\Delta_{\boldsymbol{\tau}}\hat{\varphi} &= \hat{q} \text{ on } \Gamma, \\ \hat{\varphi} &= 0 \text{ on } \partial\Gamma^D, \\ \frac{\partial\hat{\varphi}}{\partial\boldsymbol{\tau}} &= 0 \text{ on } \partial\Gamma^N. \end{aligned}$$

We pose the velocities $\mathbf{v} = -\nabla\varphi$ and $\hat{\mathbf{v}} = -\nabla_{\boldsymbol{\tau}}\hat{\varphi}$, noting that $\mathrm{div}\ \mathbf{v} = -q \in L^2(\Omega_\Gamma)$ and $\mathrm{div}_{\boldsymbol{\tau}}\hat{\mathbf{v}} = -\hat{q} \in L^2(\Gamma)$. Moreover, since $\mathbf{v} \in [H^1(\Omega)]^2$ we know that $\mathbf{v} \cdot \mathbf{n}_\Gamma \in L^2(\Gamma)$, cf. Lemma 4.2, (therefore $(\mathbf{v}, \hat{\mathbf{v}})$ is indeed a member of $\mathbf{V}$ when restricting the domain of $\mathbf{v}$ to Ω_Γ) and in this case, since $\mathbf{v} \in [H^1(\Omega)]^2 \subset H(\mathrm{div}, \Omega)$, we know that $[\![\mathbf{v} \cdot \mathbf{n}_\Gamma]\!] = 0$.

We see that

$$\begin{aligned} B((\mathbf{v}, \hat{\mathbf{v}}), (q, \hat{q})) &= -\int_{\Omega_\Gamma} q\ \mathrm{div}\ \mathbf{v} - \int_\Gamma \hat{q}\ \mathrm{div}_{\boldsymbol{\tau}}\ \hat{\mathbf{v}} + \int_\Gamma \hat{q}[\![\mathbf{v} \cdot \mathbf{n}_\Gamma]\!] \\ &= \int_{\Omega_\Gamma} |q|^2 + \int_\Gamma |\hat{q}|^2 \\ &= \|q\|^2_{L^2(\Omega)} + \|\hat{q}\|^2_{L^2(\Gamma)} = \|(q, \hat{q})\|^2_{\mathbf{M}}. \end{aligned}$$

Since both φ and $\hat{\varphi}$ have zero trace on part of their domain boundaries, the following Poincaré–Friedrichs inequalities hold:

$$\begin{aligned} \|\varphi\|_{L^2(\Omega)} &\leq C_{\mathrm{PF}}(\Omega)\|\nabla\varphi\|_{[L^2(\Omega)]^2}, \\ \|\hat{\varphi}\|_{L^2(\Gamma)} &\leq C_{\mathrm{PF}}(\Gamma)\|\nabla_{\boldsymbol{\tau}}\hat{\varphi}\|_{L^2(\Gamma)}. \end{aligned}$$

Moreover, thanks to the Cauchy–Schwarz inequality and the (weak formulations of the)

[4]The same is true also if Ω is bounded and has a boundary of class C^1.

auxiliary problems, we see that

$$\begin{aligned}\|\mathbf{v}\|^2_{[L^2(\Omega)]^2} &= \|\nabla\varphi\|^2_{[L^2(\Omega)]^2}\\ &= (\nabla\varphi,\nabla\varphi)_{L^2(\Omega)}\\ &= (q,\varphi)_{L^2(\Omega)}\\ &\leq \|q\|_{L^2(\Omega)}\|\varphi\|_{L^2(\Omega)}\\ &\leq C_{\mathrm{PF}}(\Omega)\|q\|_{L^2(\Omega)}\|\nabla\varphi\|_{[L^2(\Omega)]^2},\end{aligned}$$

and so

$$\|\mathbf{v}\|_{L^2(\Omega)} \leq C_{\mathrm{PF}}(\Omega)\|q\|_{L^2(\Omega)}. \tag{4.11}$$

Similarly,

$$\|\hat{\mathbf{v}}\|_{L^2(\Gamma)} \leq C_{\mathrm{PF}}(\Gamma)\|\hat{q}\|_{L^2(\Gamma)}. \tag{4.12}$$

Finally, using (4.11)–(4.12), and letting $C_n > 0$ be the final constant from Lemma 4.4, noting that $\|\Delta\varphi\|_{L^2(\Omega)} = \|q\|_{L^2(\Omega)}$, we see that

$$\begin{aligned}\|(\mathbf{v},\hat{\mathbf{v}})\|^2_{\mathbf{V}} &= \|\mathbf{v}\|^2_{[L^2(\Omega)]^2} + \|\hat{\mathbf{v}}\|^2_{L^2(\Gamma)} + \|\mathrm{div}\ \mathbf{v}\|^2_{L^2(\Omega)} + \|\mathrm{div}_{\boldsymbol{\tau}}\hat{\mathbf{v}}\|^2_{L^2(\Gamma)} + \|\{\mathbf{v}\cdot\mathbf{n}_\Gamma\}\|^2_{L^2(\Gamma)}\\ &= \|\mathbf{v}\|^2_{[L^2(\Omega)]^2} + \|\hat{\mathbf{v}}\|^2_{L^2(\Gamma)} + \|q\|^2_{L^2(\Omega)} + \|\hat{q}\|^2_{L^2(\Gamma)} + \|\{\nabla\varphi\cdot\mathbf{n}_\Gamma\}\|^2_{L^2(\Gamma)}\\ &\leq (1 + C_{\mathrm{PF}}(\Omega)^2 + C_n^2)\|q\|^2_{L^2(\Omega)} + (1 + C_{\mathrm{PF}}(\Gamma)^2)\|\hat{q}\|^2_{L^2(\Gamma)}\\ &\leq \max\{1 + C_{\mathrm{PF}}(\Omega)^2 + C_n^2, 1 + C_{\mathrm{PF}}(\Gamma)^2\}\|(q,\hat{q})\|^2_{\mathbf{M}}\\ &\equiv C\|(q,\hat{q})\|^2_{\mathbf{M}}.\end{aligned}$$

□

Therefore, thanks to Lemma 4.5 and Lemma 4.6, we have well–posedness of the weak formulation (4.8)–(4.9).

Remark 4.7. *When considering the case of a fully immersed, or partially immersed, fracture network Γ, it is only the inf–sup stability proof that needs adjusting. Indeed, the proofs in these cases follow the exact same procedure, and conclude such stability in the same way; in these cases, the above stated auxiliary problems are not sufficient. For a network which touches the boundary of the domain such that $I^D \neq \emptyset$, it is possible to formulate a coercive Poisson problem similar to that used in Lemma 4.6. Its extension is fairly straightforward, and can be found in [54], for example.*

When the network is fully immersed, pressure cannot be imposed on part of the fracture boundary and so–called flux–carriers must be constructed [55]. Here, an arbitrary extension of the network partitioning the domain into several Lipschitz subdomains is used; a coercive problem utilising flux–carriers is defined on each domain, in order to construct a suitable velocity $\mathbf{v}$ required in the proof of inf–sup stability.

4.4 Mixed finite element approximations

The numerical method to be employed within this work will be a standard, conforming, mixed finite element method, approximating the solutions of the weak formulation (4.8)–(4.9) with functions from the finite–dimensional subspaces $\mathbf{V}_h \subset \mathbf{V}$ and $\mathbf{M}_h \subset \mathbf{M}$. Such approximation spaces will consist of piecewise polynomial functions, defined according to some shape–regular triangulation $\mathscr{T}_h = \{\kappa\}$ of the closed domain $\overline{\Omega}$. We denote by h the usual mesh–size parameter, defined as the length of the largest edge making up the triangulation, used as an index for the triangulation and subsequent approximation spaces.

We proceed under the simplifying assumption that the triangulation $\mathscr{T}_h$ respects the fracture network[5] Γ, i.e., Γ does not cut into the interior of any elements $\kappa \in \mathscr{T}_h$. We assume also that the network itself is made up of interfaces, or edges, between elements in $\mathscr{T}_h$. Under these assumptions, denote with $\mathscr{E}_h$ all of the edges in $\mathscr{T}_h$; we can subsequently write down

$$\Gamma_h = \{\mathcal{E} \in \mathscr{E}_h : \mathcal{E} \cap \Gamma \neq \emptyset\} \text{ such that } \overline{\Gamma} = \cup_{\mathcal{E}\in\Gamma_h} \overline{\mathcal{E}},$$

as the partitioning of the fracture network Γ into one–dimensional elements.

Recall that the use of a mixed finite element method allows for a simultaneous computation of the required pressures and fluxes in both the bulk and fracture network domains, retaining a notion of mass conservation at a local level. Such a notion is paramount when paired with transport schemes, as in [4, 88, 60], as these schemes are typically quite sensitive to non–conservative flow fields [27]. Indeed, a mixed finite element approach allows us the usual tools from the literature for a rigorous analysis of the method employed.

Remark 4.8. *For a large proportion of numerical methods, the quality of the underlying computational meshes, or triangulations, has a huge impact on the accuracy of the solution. Indeed, a conforming mesh as assumed here can lead to small elements of low quality (for example those with high aspect ratios and small angles), often breaking the shape–regularity assumption we establish first and foremost. It is, of course, possible to define a partition of* Γ *that is independent of the triangulation* $\mathscr{T}_h$ *as, for example, described in [56], but this can still lead to the aforementioned problem. However, going one step further, the fracture network may even cut elements from* $\mathscr{T}_h$*, not respecting the triangulation at all. In this case, extended finite elements [45, 54], among other methods such as mortar methods [26], mimetic finite difference [55], discontinuous Galerkin and virtual element methods [47], and finite volume approaches [6] may be utilised instead of a standard mixed finite element method. We emphasise that this list of references is by no means exhaustive, and point*

[5] In the presence of general fractures, the approximation with straight lines would incur a modelling error penalty, leading to a maximum second order accuracy under subsequent uniform mesh refinement.

further to the expansive literature.

4.4.1 Approximation spaces

Here, we build up the definitions of the approximation spaces $\mathbf{V}_h$ and M_h to be used in the mixed finite element approximation of the fracture flow problem. Starting locally on elements $\kappa \in \mathscr{T}_h$ with the usual RT and BDM spaces, we construct two configurations of approximation spaces to be utilised. To this end, we define first a reference interval and polynomial spaces on fracture edges.

Definition 4.9. *The reference interval I_{REF} is the interval $[-1, 1]$ in ζ–space.*

Definition 4.10. *Consider a one–dimensional element $\mathcal{E}$ given by the straight line connecting the points $\mathbf{X}_1$ $\mathbf{X}_2 \in \mathbb{R}^2$. Define the affine mapping $F_{\mathcal{E}} : I_{REF} \to \mathcal{E}$ via*

$$F_{\mathcal{E}}(\zeta) = \mathbf{X}_1 \ell_0(\zeta) + \mathbf{X}_2 \ell_1(\zeta),$$

where $\ell_0(\zeta) = \frac{(1-\zeta)}{2}$ and $\ell_1(\zeta) = \frac{(1+\zeta)}{2}$ are the lowest–order Lobatto shape functions on I_{REF}. The Jacobian of such mapping is given by

$$\mathcal{J}_{\mathcal{E}} := DF_{\mathcal{E}} = \frac{1}{2} \begin{bmatrix} x_2 - x_1 \\ y_2 - y_2 \end{bmatrix},$$

with length $|\mathcal{J}_{\mathcal{E}}| = \frac{|\mathcal{E}|}{2}$.

We aim to construct conforming finite–dimensional subspaces for each of the function spaces outlined in Section 4.3.1. That is, we require the four subspaces $V_h^\Omega \subset V^\Omega$, $V_h^\Gamma \subset V^\Gamma$, $M_h^\Omega \subset M^\Omega$, and $M_h^\Gamma \subset M^\Gamma$.

Since we are restricting ourselves to the case of two spatial dimensions for the bulk domain, the tangential divergence on the fracture network is the same as the tangential derivative. Moreover, in this case, the spaces $H^1(\Gamma)$ and $H(\mathrm{div}_{\boldsymbol{\tau}}, \Gamma)$ are the same; therefore, global conformity requirements for functions in V^Γ imply that the approximation space V_h^Γ will need to consist of continuous piecewise polynomials, with respect to Γ_h.

The following definitions build towards the definitions of our approximation spaces.

Definition 4.11. *For $D \subset \mathbb{R}^d$, $d = 1, 2$, and $k \geq 0$ an integer, let $\mathbb{P}_k(D)$ denote the set of polynomials of degree at most k, on D. Moreover, let $\mathcal{E}$ be a one–dimensional manifold (e.g. a line) embedded in a two–dimensional domain. Define polynomials on $\mathcal{E}$ as*

$$\mathbb{P}_k(\mathcal{E}) = \{q : \mathcal{E} \to \mathbb{R} : \tilde{q} = q \circ F_{\mathcal{E}} \in \mathbb{P}_k(I_{REF})\},$$

that is, those functions that when mapped to the reference interval I_{REF} are polynomials in the variable ζ, of degree at most k.

Definition 4.12. *For $k \geq 0$ an integer, and $\kappa \in \mathscr{T}_h$ some triangular element, define the following spaces, where $\mathbf{n}_\kappa \in L^\infty(\partial\kappa)$ denotes the unit outward normal vector to κ, and $\mathcal{E}_i$ are its three edges.*

$$\begin{aligned} R_k(\partial\kappa) &= \{\phi \in L^2(\kappa) : \phi|_{\mathcal{E}_i} \in \mathbb{P}_k(\mathcal{E}_i)\ \forall i = 1,2,3\}, \\ RT_k(\kappa) &= \{\mathbf{v}_h \in [\mathbb{P}_k(\kappa)]^2 + \mathbf{x}\mathbb{P}_k(\kappa) : \mathbf{v}_h \cdot \mathbf{n}_\kappa \in R_k(\partial\kappa)\}, \\ BDM_k(\kappa) &= \{\mathbf{v}_h \in [\mathbb{P}_k(\kappa)]^2 : \mathbf{v}_h \cdot \mathbf{n}_\kappa \in R_k(\partial\kappa)\}, \end{aligned}$$

with $k > 0$ for the space $BDM_k(\kappa)$.

Definition 4.13. *For $k \geq 0$ an integer, define*

$$\begin{aligned} RT_k(\Omega_\Gamma, \mathscr{T}_h) &= \{\mathbf{v}_h \in H(\mathrm{div}, \Omega_\Gamma) : \mathbf{v}_h|_\kappa \in RT_k(\kappa)\ \forall \kappa \in \mathscr{T}_h\}, \\ BDM_k(\Omega_\Gamma, \mathscr{T}_h) &= \{\mathbf{v}_h \in H(\mathrm{div}, \Omega_\Gamma) : \mathbf{v}_h|_\kappa \in BDM_k(\kappa)\ \forall \kappa \in \mathscr{T}_h\}, \\ \mathbb{P}_k(\Omega_\Gamma, \mathscr{T}_h) &= \{q_h \in L^2(\Omega_\Gamma) : q_h|_\kappa \in \mathbb{P}_k(\kappa)\ \forall \kappa \in \mathscr{T}_h\}, \\ \mathbb{P}^c_k(\Gamma, \Gamma_h) &= \{\hat{\mathbf{v}}_h \in C^0(\Gamma) : \hat{\mathbf{v}}_h|_{\mathcal{E}} \in \mathbb{P}_k(\mathcal{E})\ \forall \mathcal{E} \in \Gamma_h\}, \\ \mathbb{P}_k(\Gamma, \Gamma_h) &= \{\hat{q}_h \in L^2(\Gamma) : \hat{q}_h|_{\mathcal{E}} \in \mathbb{P}_k(\mathcal{E})\ \forall \mathcal{E} \in \Gamma_h\}, \end{aligned}$$

with $k > 0$ for the space $BDM_k(\Omega_\Gamma, \mathscr{T}_h)$.

We reiterate that the requirement $\mathbf{v}_h \in H(\mathrm{div}, \Omega_\Gamma)$ allows for discontinuous normal–traces across the fracture network; a degree of freedom doubling will occur on the edges making up the fracture network, reminiscent of DG methods, for example.

Moreover, we now define two configurations of approximation spaces that we will refer to in the remainder of this chapter, utilising either RT or BDM spaces for the bulk Darcy velocity approximation. We define firstly, for $k \geq 0$, the spaces

$$\begin{cases} V^\Omega_{h,k} & = \{\mathbf{v}_h \in RT_k(\Omega_\Gamma, \mathscr{T}_h) : (\mathbf{v}_h \cdot \mathbf{n})|_{\partial\Omega^N} = 0\}, \\ M^\Omega_{h,k} & = \{q \in \mathbb{P}_k(\Omega_\Gamma, \mathscr{T}_h)\}, \\ V^\Gamma_{h,k} & = \{\hat{\mathbf{v}}_h \in \mathbb{P}^c_{k+1}(\Gamma, \Gamma_h) : \textstyle\sum_{l \in S_i} (\hat{\mathbf{v}}_h|_{\gamma_l} \cdot \boldsymbol{\tau}_l)|_i = 0\ \forall i \in \mathcal{I},\ (\hat{\mathbf{v}} \cdot \boldsymbol{\tau})|_{I^F} = 0\}, \\ M^\Gamma_{h,k} & = \{\hat{q} \in \mathbb{P}_k(\Gamma, \Gamma_h)\}. \end{cases} \tag{I}$$

Moreover, define for $k \geq 1$, the spaces

$$\begin{cases} V^\Omega_{h,k} & = \{\mathbf{v}_h \in BDM_k(\Omega_\Gamma, \mathscr{T}_h) : (\mathbf{v}_h \cdot \mathbf{n})|_{\partial\Omega^N} = 0\}, \\ M^\Omega_{h,k} & = \{q \in \mathbb{P}_{k-1}(\Omega_\Gamma, \mathscr{T}_h)\}, \\ V^\Gamma_{h,k} & = \{\hat{\mathbf{v}}_h \in \mathbb{P}^c_{k+1}(\Gamma, \Gamma_h) : \textstyle\sum_{l \in S_i} (\hat{\mathbf{v}}_h|_{\gamma_l} \cdot \boldsymbol{\tau}_l)|_i = 0\ \forall i \in \mathcal{I},\ (\hat{\mathbf{v}} \cdot \boldsymbol{\tau})|_{I^F} = 0\}, \\ M^\Gamma_{h,k} & = \{\hat{q} \in \mathbb{P}_k(\Gamma, \Gamma_h)\}. \end{cases} \tag{II}$$

One may notice from configuration (II), that we increase the polynomial degree of the discrete velocity space when moving down a dimension onto the fracture network. In essence, this is so that the polynomial degree of normal–traces of functions from V_h^Ω match that of M_h^Γ. We refer to [27], which deals with each of these configurations also, referring to them as families of spaces of the first and second kind, respectively, looking at them from the more abstract view within exterior calculus.

4.5 Well–posedness of the discrete problem

With either configuration of spaces (I) or (II), the discrete problem is to:

Find $(\mathbf{u}_h, \hat{\mathbf{u}}_h) \in \mathbf{V}_{h,k} = V_{h,k}^\Omega \times V_{h,k}^\Gamma$ and $(p_h, \hat{p}_h) \in \mathbf{M}_{h,k} = M_{h,k}^\Omega \times M_{h,k}^\Gamma$ such that

$$A((\mathbf{u}_h, \hat{\mathbf{u}}_h), (\mathbf{v}_h, \hat{\mathbf{v}}_h)) + B((\mathbf{v}_h, \hat{\mathbf{v}}_h), (p_h, \hat{p}_h)) = F^u((\mathbf{v}_h, \hat{\mathbf{v}}_h)), \tag{4.13}$$

$$B((\mathbf{u}_h, \hat{\mathbf{u}}_h), (q_h, \hat{q}_h)) = F^p((q_h, \hat{q}_h)), \tag{4.14}$$

for all $(\mathbf{v}_h, \hat{\mathbf{v}}_h) \in \mathbf{V}_{h,k}$ and $(q_h, \hat{q}_h) \in \mathbf{M}_{h,k}$.

For the discrete problem (4.13)–(4.14), we of course would like to show the existence of a unique solution, and that this solution converges to the exact solutions of the continuous problem (4.8)–(4.9) under mesh refinement (i.e. as $h \to 0$). Since the numerical method employed is conforming, the continuity of the bilinear forms A and B, as well as the continuity of the linear functionals F^u and F^p, transfer directly onto the discrete subspaces. Therefore, in order to show well–posedness for (4.13)–(4.14), similar to that presented in Section 4.3.4, we need to show that two key criteria are satisfied.

To this end, define the discrete null space

$$\mathbf{V}_h^0 = \{(\mathbf{v}_h, \hat{\mathbf{v}}_h) \in \mathbf{V}_h : B((\mathbf{v}_h, \hat{\mathbf{v}}_h), (q_h, \hat{q}_h)) = 0 \ \forall (q_h, \hat{q}_h) \in \mathbf{M}_h\},$$

noting that, in general, $\mathbf{V}_h^0 \not\subset \mathbf{V}^0$, defined in (4.10). Exactly the same as in the continuous case, it is sufficient that the bilinear form A is coercive on the discrete null space $\mathbf{V}_h^0$. Secondly, the bilinear form B must satisfy a discrete inf–sup condition; i.e. we require the existence of a constant $\beta_* > 0$, which is independent of h, such that

$$\sup_{(\mathbf{v}_h, \hat{\mathbf{v}}_h) \in \mathbf{V}_h} \frac{B((\mathbf{v}_h, \hat{\mathbf{v}}_h), (q_h, \hat{q}_h))}{\|(\mathbf{v}_h, \hat{\mathbf{v}}_h)\|_{\mathbf{V}}} \geq \beta_* \|(q_h, \hat{q}_h)\|_{\mathbf{M}} \quad \forall (q_h, \hat{q}_h) \in \mathbf{M}_h.$$

For the remainder of this chapter, we consider only the spaces in configuration (I) with $k = 0$; such can be referred to as a lowest order RT approximation. To approach the discrete well–posedness in this setting, some interpolation theory is a necessary prerequisite.

4.5.1 Interpolation in a lowest order approximation

Proceeding with a lowest–order RT approximation, we firstly associate with the discrete space $\mathbf{M}_{h,0} = M^{\Omega}_{h,0} \times M^{\Gamma}_{h,0}$ the L^2–projection operator $\pi_{h,0} = (\pi^{\Omega}_{h,0}, \pi^{\Gamma}_{h,0}) : \mathbf{M} \to \mathbf{M}_{h,0}$. These individual operators are each defined by

$$\int_{\Omega_\Gamma} (q - \pi^{\Omega}_{h,0}[q])\varphi_h = 0 \quad \forall \varphi_h \in M^{\Omega}_{h,0},$$
$$\int_{\Gamma} (\hat{q} - \pi^{\Gamma}_{h,0}[\hat{q}])\hat{\varphi}_h = 0 \quad \forall \hat{\varphi}_h \in M^{\Gamma}_{h,0}.$$

Furthermore, we have the following well–known interpolation estimates, (see [71, 56], for example), where C may differ in each case, but is independent of h and $(q, \hat{q})$.

$$\|q - \pi^{\Omega}_{h,0}[q]\|_{L^2(\Omega_\Gamma)} \leq Ch\|q\|_{H^1(\Omega_\Gamma)}, \tag{4.15}$$
$$\|\hat{q} - \pi^{\Gamma}_{h,0}[\hat{q}]\|_{L^2(\Gamma)} \leq Ch\|\hat{q}\|_{H^1(\Gamma)}. \tag{4.16}$$

The projection, or interpolation, operator associated with the space $\mathbf{V}$ requires some extra regularity, so that normal–traces of the functions we interpolate are square–integrable. To this end, we define for a fixed $s > 2$ the space

$$\mathbf{W}^{(s)} := \mathbf{V} \cap ([L^s(\Omega_\Gamma)]^2 \times [L^s(\Gamma)]^2).$$

Within standard literature, for example [25], the usual, lowest–order, $H(\mathrm{div})$–interpolation operator simply enforces that the integral average of the normal–traces across element edges match, for both the function $\mathbf{v}$ and its interpolant. However, since continuity of normal–traces are not required across those edges forming the fracture network Γ, we double the degrees of freedom associated to the edges making up the fracture network and interpolate from either side. To this end, we partition the edges $\mathcal{E}_h$ into those intersecting Γ and those that do not; i.e., $\mathcal{E}_h = \mathcal{E}^o_h \cup \Gamma_h$. We then define the interpolation operator $\Pi_{h,0} = (\Pi^{\Omega}_{h,0}, \Pi^{\Gamma}_{h,0}) : \mathbf{V}^{(s)} \to \mathbf{V}_{h,0}$ using the following degrees of freedom

$$\int_{\mathcal{E}} (\mathbf{v} - \Pi^{\Omega}_{h,0}[\mathbf{v}]) \cdot \mathbf{n}_{\mathcal{E}} = 0 \quad \forall \mathcal{E} \in \mathscr{E}^o_h,$$
$$\int_{\mathcal{E}} (\mathbf{v}^{\pm} - \Pi^{\Omega}_{h,0}[\mathbf{v}^{\pm}]) \cdot \mathbf{n}^{\pm}_{\mathcal{E}} = 0 \quad \forall \mathcal{E} \in \Gamma_h.$$

Alternatively, insisting both the jump and average of the function and its interpolant are equal across the edges $\mathcal{E} \in \Gamma_h$ is equivalent to the second stated condition. These degrees of freedom come from the definition of the local interpolation operators $\rho_\kappa : \mathbf{W}^s(\kappa) := H(\mathrm{div}, \kappa) \cap [L^s(\kappa)]^2 \to RT_0(\kappa)$, defined for each element $\kappa \in \mathscr{T}_h$, by

$$\int_{\partial\kappa} p_0(\mathbf{v} - \rho_\kappa[\mathbf{v}]) \cdot \mathbf{n}_\kappa = 0 \quad \forall p_0 \in R_0(\partial\kappa), \tag{4.17}$$

see, for example, [25] or Section 3.3.3.

In three spatial dimensions, i.e. the case where the network of fractures consists of planes, the degrees of freedom associated with $\Pi^{\Gamma}_{h,0}$ are similar to the usual interpolant for lowest–order RT approximations. That is,

$$\int_e (\hat{\mathbf{v}} - \Pi^{\Gamma}_{h,0}[\hat{\mathbf{v}}]) \cdot \mathbf{n}_e = 0 \quad \forall e \in \Gamma_h^{\mathscr{E}},$$

where $\Gamma_h^{\mathscr{E}}$ is the set of interfaces in the partition Γ_h. However, when in two spatial dimensions, as is the case for this work, the fracture network is one–dimensional and so the interpolation operator looks different. Indeed, in this case $\Pi^{\Gamma}_{h,0}$ is just the standard Lagrange interpolation operator, where the function $\hat{\mathbf{v}}$ and its interpolant agree at the nodal points of the one–dimensional elements in Γ_h [56].

Moreover, let $\mathscr{Y} : RT_0(\kappa) \to R_0(\partial\kappa)$ be the discrete normal–trace mapping defined by $\mathbf{v}_h \mapsto (\mathbf{v}_h \cdot \mathbf{n}_\kappa)|_{\partial\kappa}$. According to (4.17) we have

$$\int_{\partial\kappa} p_0(\mathbf{v} - \rho_\kappa[\mathbf{v}]) \cdot \mathbf{n}_\kappa = 0 \quad \forall p_0 \in \mathrm{Im}(\mathscr{Y}),$$

or equivalently,

$$\int_{\partial\kappa} [(\mathbf{v} - \rho_\kappa[\mathbf{v}]) \cdot \mathbf{n}_\kappa](\mathbf{w}_h \cdot \mathbf{n}_\kappa) = 0 \quad \forall \mathbf{w}_h \in RT_0(\kappa).$$

It should be clear that the quantity $\rho_\kappa[\mathbf{v}] \cdot \mathbf{n}_\kappa$ is nothing more than the L^2–projection of $\mathbf{v} \cdot \mathbf{n}_\kappa$ from $L^2(\partial\kappa)$ onto $\mathrm{Im}(\mathscr{Y}) \subset R_0(\partial\kappa)$[6]. Consequently, usual bounds for L^2–projections imply that, on either side of an edge $\mathcal{E} \in \mathscr{E}_h$, we have

$$\|([\mathbf{v} - \rho_{\kappa^\pm}[\mathbf{v}]) \cdot \mathbf{n}_\mathcal{E}]^\pm\|_{L^2(\mathcal{E})} \leq C^\pm h_\mathcal{E} \|[\mathbf{v} \cdot \mathbf{n}_\mathcal{E}]^\pm\|_{H^1(\mathcal{E})},$$

for some constant $C > 0$, independent of h and $\mathbf{v} \in [H^1(\Omega_\Gamma)]^2$; from which we can infer

$$\|[(\mathbf{v} - \Pi_{h,0}[\mathbf{v}]) \cdot \mathbf{n}_\Gamma]^\pm\|_{L^2(\Gamma)} \leq \tilde{C}^\pm h \|[\mathbf{v} \cdot \mathbf{n}_\Gamma]^\pm\|_{H^1(\Gamma)}.$$

Furthermore, there are constants C_A, $C_J > 0$ such that

$$\|\{(\mathbf{v} - \Pi^{\Omega}_{h,0}[\mathbf{v}]) \cdot \mathbf{n}_\Gamma\}\|_{L^2(\Gamma)} \leq C_A h \|\{\mathbf{v} \cdot \mathbf{n}_\Gamma\}\|_{H^1(\Gamma)}, \tag{4.18}$$

$$\|[\![(\mathbf{v} - \Pi^{\Omega}_{h,0}[\mathbf{v}]) \cdot \mathbf{n}_\Gamma]\!]\|_{L^2(\Gamma)} \leq C_J h \|[\![\mathbf{v} \cdot \mathbf{n}_\Gamma]\!]\|_{H^1(\Gamma)}. \tag{4.19}$$

We have also the usual interpolation estimates, referring again to [71, 56].

$$\|\mathbf{v} - \Pi^{\Omega}_{h,0}[\mathbf{v}]\|_{[L^2(\Omega)]^2} \leq Ch \|\mathbf{v}\|_{[H^1(\Omega)]^2}, \tag{4.20}$$

$$\|\mathrm{div}(\mathbf{v} - \Pi^{\Omega}_{h,0}[\mathbf{v}])\|_{L^2(\Omega)} \leq Ch \|\mathrm{div}\ \mathbf{v}\|_{H^1(\Omega)}, \tag{4.21}$$

$$\|\hat{\mathbf{v}} - \Pi^{\Gamma}_{h,0}[\hat{\mathbf{v}}]\|_{L^2(\Gamma)} \leq Ch \|\hat{\mathbf{v}}\|_{H^1(\Gamma)}, \tag{4.22}$$

$$\|\mathrm{div}_{\boldsymbol{\tau}}(\hat{\mathbf{v}} - \Pi^{\Gamma}_{h,0}[\hat{\mathbf{v}}])\|_{L^2(\Gamma)} \leq Ch \|\mathrm{div}_{\boldsymbol{\tau}} \hat{\mathbf{v}}\|_{H^1(\Gamma)}. \tag{4.23}$$

[6] Since L^2–projection is unique and $\rho_\kappa[\mathbf{v}] \cdot \mathbf{n}_\kappa \in R_0(\partial\kappa)$.

Note that the estimates on the divergences are also a consequence of L^2–projection.

Furthermore, an extremely useful property we have is that each of the interpolation operators $\pi_{h,0}$ and $\Pi_{h,0}$ are uniformly continuous (see [56], for example[7]); that is,

$$\|\pi_{h,0}[(q,\hat{q})]\|_{\mathbf{M}} \leq \|(q,\hat{q})\|_{\mathbf{M}} \quad \forall (q,\hat{q}) \in \mathbf{M}, \tag{4.24}$$

$$\|\Pi_{h,0}[(\mathbf{v},\hat{\mathbf{v}})]\|_{\mathbf{V}} \leq C\|(\mathbf{v},\hat{\mathbf{v}})\|_{\mathbf{H}} \quad \forall (\mathbf{v},\hat{\mathbf{v}}) \in \mathbf{H}, \tag{4.25}$$

where $\mathbf{H} = [H^1(\Omega_\Gamma)]^2 \times H^1(\Gamma) \subset \mathbf{V}$, and the inclusion $\mathbf{H} \hookrightarrow \mathbf{V}$ is continuous and dense; this space is equipped with the product norm

$$\|(\mathbf{v},\hat{\mathbf{v}})\|^2_{\mathbf{H}} := \|\mathbf{v}\|^2_{[H^1(\Omega_\Gamma)]^2} + \|\hat{\mathbf{v}}\|^2_{H^1(\Gamma)}.$$

The operators $\Pi_{h,0}$ and $\pi_{h,0}$ play an important role in proving well–posedness for the discrete problem; in particular, they satisfy a commuting property with the divergence operators defined on the bulk and the fracture network. Indeed, to this end we define the operator $\mathrm{DIV} : \mathbf{V} \to \mathbf{M}$ via the usual divergence operators, by

$$\mathrm{DIV}(\mathbf{v},\hat{\mathbf{v}}) := (\mathrm{div}\ \mathbf{v}, \mathrm{div}_{\boldsymbol{\tau}}\ \hat{\mathbf{v}} - [\![\mathbf{v}\cdot\mathbf{n}_\Gamma]\!]_\Gamma) \quad \forall (\mathbf{v},\hat{\mathbf{v}}) \in \mathbf{V}.$$

The following commuting property is well known for this lowest order configuration of spaces:

$$\mathrm{DIV}(\Pi_{h,0}[(\mathbf{v},\hat{\mathbf{v}})]) = \pi_{h,0}[\mathrm{DIV}(\mathbf{v},\hat{\mathbf{v}})],$$

and this implies, thanks to properties of commuting diagrams, that

$$\mathrm{DIV}(\mathbf{W}_{h,0}) = \mathbf{M}_{h,0}.$$

Remark 4.14. *From [56] we gain insight into the case where the grids are non–matching, i.e. Γ_h is a mesh independent of $\mathscr{T}_h$. Here, we must introduce the discrete divergence $\mathrm{DIV}_h : \mathbf{V}_h \to \mathbf{M}_h$ defined as $\mathrm{DIV}_h(\mathbf{v}_h,\hat{\mathbf{v}}_h) = (\mathrm{div}\ \mathbf{v}_h, \mathrm{div}_{\boldsymbol{\tau}}\ \hat{\mathbf{v}}_h - \pi^\Gamma_{h,0}[[\![\mathbf{v}_h\cdot\mathbf{n}_\Gamma]\!]])$, since the trace–space of the bulk velocity space V_h^Ω is not, in general, a subset of the fracture pressure space M_h^Γ. Indeed, here we have, in general, that $\mathrm{DIV}_h\Pi_{h,0}[\mathbf{v},\hat{\mathbf{v}}] \neq \pi_{h,0}\mathrm{DIV}(\mathbf{v},\hat{\mathbf{v}})$. However, we still do have the commuting properties for the individual interpolation operators:*

$$\mathrm{div}\ \Pi^\Omega_{h,0}[\mathbf{v}] = \pi^\Omega_{h,0}[\mathrm{div}\ \mathbf{v}],$$
$$\mathrm{div}_{\boldsymbol{\tau}}\ \Pi^\Gamma_{h,0}[\hat{\mathbf{v}}] = \pi^\Gamma_{h,0}[\mathrm{div}_{\boldsymbol{\tau}}\ \hat{\mathbf{v}}].$$

Indeed, in this setting, in general,

$$\pi^\Gamma_{h,0}[\mathbf{v}\cdot\mathbf{n}] \neq \pi^\Gamma_{h,0}[\Pi^\Omega_{h,0}[\mathbf{v}]\cdot\mathbf{n}].$$

[7] Who also reiterates that, indeed, (4.24) without a constant is well known for L^2–projections.

4.5.2 Verification of discrete well–posedness

We can now address the well–posedness of (4.13)–(4.14) using a lowest–order RT approximation. The satisfaction of the two criteria discussed in Section 4.5 can now be shown.

We first notice a link between the bilinear form B and the DIV operator; that is,

$$B((\mathbf{v},\hat{\mathbf{v}}),(q,\hat{q})) = -(\mathrm{DIV}(\mathbf{v},\hat{\mathbf{v}}),(q,\hat{q}))_{\mathbf{M}},$$

for all $(\mathbf{v},\hat{\mathbf{v}}) \in \mathbf{V}$ and $(q,\hat{q}) \in \mathbf{M}$. This means that the null space $\mathbf{V}^0$ is equal to the kernel of DIV. We have already seen in Section 4.5.1 that $\mathrm{DIV}(\mathbf{V}_{h,0}) = \mathbf{M}_{h,0}$, and this automatically implies that

$$\mathbf{V}^0_{h,0} \subset \mathbf{V}^0.$$

Indeed, this is because the operator associated with B when defined on $\mathbf{V}_{h,0} \times \mathbf{M}_{h,0}$ is nothing more than the divergence operator DIV restricted to $\mathbf{V}_{h,0}$. With such an inclusion, the proof of coercivity of the bilinear form A on $\mathbf{V}^0$, given by Lemma 4.5, transfers directly onto $\mathbf{V}^0_{h,0}$.

Although the surjectivity of DIV from $\mathbf{V}_{h,0}$ onto $\mathbf{M}_{h,0}$ is an equivalent condition for the discrete inf–sup condition to hold (since both $L^2(\Omega_\Gamma)$ and $L^2(\Gamma)$ can be identified with their respective dual spaces), it does not guarantee that the obtained inf–sup constant is independent of the mesh size parameter h. As in Chapter 3, we appeal to Proposition 3.20, restated below as Proposition 4.15 using the notations of this chapter.

Proposition 4.15. *Assume there is the Banach space $\mathbf{H} \hookrightarrow \mathbf{V}$, with norm $\|\cdot\|_{\mathbf{H}}$ and a linear subspace $\mathbf{Q}_h \subset \mathbf{M}_h$, with a semi–norm $|\cdot|_{\mathbf{Q}}$. Suppose that, for some $\beta_{\mathbf{H}} > 0$ we have*

$$\sup_{(\mathbf{v},\hat{\mathbf{v}})\in\mathbf{H}} \frac{B((\mathbf{v},\hat{\mathbf{v}}),(q_h,\hat{q}_h))}{\|(\mathbf{v},\hat{\mathbf{v}})\|_{\mathbf{H}}} \geq \beta_{\mathbf{H}}|(q_h,\hat{q}_h)|_{\mathbf{Q}} \quad \forall (q_h,\hat{q}_h) \in \mathbf{Q}_h, \tag{4.26}$$

and assume that there exists a linear operator $\Pi_h : \mathbf{H} \to \mathbf{V}$ such that

$$\begin{cases} B((\Pi_h[(\mathbf{v},\hat{\mathbf{v}})] - (\mathbf{v},\hat{\mathbf{v}}),(q_h,\hat{q}_h)) = 0 \quad \forall (\mathbf{v},\hat{\mathbf{v}}) \in \mathbf{H},\ \forall (q_h,\hat{q}_h) \in \mathbf{Q}_h, \\ \|\Pi_h[\mathbf{v},\hat{\mathbf{v}}]\|_{\mathbf{V}} \leq C_{\mathbf{H}}\|(\mathbf{v},\hat{\mathbf{v}})\|_{\mathbf{H}}, \end{cases} \tag{4.27}$$

with $C_{\mathbf{H}} > 0$ independent of h. Then, we have

$$\sup_{(\mathbf{v}_h,\hat{\mathbf{v}}_h)\in\mathbf{V}_h} \frac{B((\mathbf{v}_h,\hat{\mathbf{v}}_h),(q_h,\hat{q}_h))}{\|(\mathbf{v}_h,\hat{\mathbf{v}}_h)\|_{\mathbf{V}}} \geq \beta_*|(q_h,\hat{q}_h)|_{\mathbf{Q}} \quad \forall (q_h,\hat{q}_h) \in \mathbf{Q}_h,$$

with $\beta_* = \frac{\beta_{\mathbf{H}}}{C_{\mathbf{H}}}$.

Proof. See [25, Proposition 5.4.3]. □

Under the foregoing notation of this chapter, along with $\mathbf{Q}_h = \mathbf{M}_{h,0}$, Proposition 4.15 is indeed satisfied for a lowest order RT approximation and we have discrete inf–sup stability with a constant independent of h, for reasons precisely the same as in Section 3.4: commuting properties of the DIV operator with Π_h, and the uniform continuity of Π_h from $\mathbf{H}$ onto $\mathbf{V}$[8]. We note also that the proof of Lemma 4.6 showed that continuous inf–sup holds also on the subspace $\mathbf{H} \subset \mathbf{W}$, since the solutions φ and $\hat{\varphi}$, of the stated auxiliary problems, are in $H^2(\Omega)$ and $H^2(\Gamma)$, respectively[9].

We refer the reader to the works [27, 26] for details concerning the interpolation, discrete well–posedness, and subsequent convergence, when considering the spaces in both configurations (I) and (II) with arbitrary order. These works utilise a dimensional hierarchy approach much different from that presented here, along with elements of exterior calculus to describe reduced fracture models in a unified fashion; standard literature concerning finite element approximations for flow in fractured media is typically only done in lowest order RT, or a different method is used entirely. The choice here to remain in lowest order RT is one made in light of ease of presentation.

4.5.3 Convergence of the discrete solutions

We conclude this chapter by very briefly addressing the topic of convergence. As we saw in the absence of fractures, discrete well–posedness with constants independent of the mesh parameter h imply the quasi–optimality result given in Theorem 2.8. We have that here also, restated with the relevant notations of this chapter.

Proposition 4.16. *Let $[(\mathbf{u}, \hat{\mathbf{u}}), (p, \hat{p})] \in \mathbf{V} \times \mathbf{M}$ be the solution of the problem (4.8, 4.9), and $[(\mathbf{u}_h, \hat{\mathbf{u}}_h), (p_h, \hat{p}_h)] \in \mathbf{V}_h \times \mathbf{M}_h$ be the solution of the discrete problem (4.13, 4.14); assume each of these problems are well–posed according to Theorem 2.7. Letting β_* be an inf–sup constant for the discrete pair $(\mathbf{V}_h, \mathbf{Q}_h)$ and C_A the coercivity constant for $A(\cdot,\cdot)$ on $\mathbf{W}_h^0$, one has the following estimate, with a constant C depending on $\|A\|$, $\|B\|$, β_*, and C_A, but independent of h:*

$$\|(\mathbf{u} - \mathbf{u}_h, \hat{\mathbf{u}} - \hat{\mathbf{u}}_h)\|_{\mathbf{V}} + \|(p - p_h, \hat{p} - \hat{p}_h)\|_{\mathbf{M}} \leq C \left(\inf_{(\mathbf{v}_h, \hat{\mathbf{v}}_h) \in \mathbf{V}_h} \|(\mathbf{u} - \mathbf{v}_h, \hat{\mathbf{u}} - \hat{\mathbf{v}}_h)\|_{\mathbf{V}} + \inf_{(q_h, \hat{q}_h) \in \mathbf{M}_h} \|(p - q_h, \hat{p} - \hat{q}_h)\|_{\mathbf{M}} \right).$$

Moreover, when we have the inclusion of the null spaces $\mathbf{V}_h^0 \subset \mathbf{V}^0$, we have

$$\|(\mathbf{u} - \mathbf{u}_h, \hat{\mathbf{u}} - \hat{\mathbf{u}}_h)\|_{\mathbf{V}} \leq C \inf_{(\mathbf{v}_h, \hat{\mathbf{v}}_h) \in \mathbf{V}_h} \|(\mathbf{u} - \mathbf{v}_h, \hat{\mathbf{u}} - \hat{\mathbf{v}}_h)\|_{\mathbf{V}}.$$

[8] Throughout, we have used $\mathbf{H}$ instead of the less regular space $\mathbf{W}^{(s)}$ since the former is required so that the interpolation estimates can indeed be used.

[9] As is the case also when considering networks of fractures, see [55] for details.

We then arrive at the following *a priori* convergence result.

Theorem 4.17. *Under the notations of this section, we have the following a priori error estimate, where the constant $C > 0$ is independent of h:*

$$\begin{aligned}\|(\mathbf{u}-\mathbf{u}_h, \hat{\mathbf{u}}-\hat{\mathbf{u}}_h)\|_{\mathbf{V}} + \|(p-p_h, \hat{p}-\hat{p}_h)\|_{\mathbf{M}} \\ \leq Ch(\|(p,\hat{p})\|_{\mathbf{M}} + \|(\mathbf{u},\hat{\mathbf{u}})\|_{\mathbf{H}} + \|(\operatorname{div}\mathbf{u}, \operatorname{div}_{\boldsymbol{\tau}}\hat{\mathbf{u}})\|_{\mathbf{M}} \\ + \|\{\mathbf{u}\cdot\mathbf{n}_\Gamma\}\|_{H^1(\Gamma)} + \|[\![\mathbf{u}\cdot\mathbf{n}_\Gamma]\!]\|_{H^1(\Gamma)}),\end{aligned}$$

assuming the exact solutions are regular enough so that the right–hand–side is defined.

Proof. Using the interpolation operators $\pi_{h,0}$ and $\Pi_{h,0}$, defined in Section 4.5.1, we see that

$$\inf_{(\mathbf{v}_h,\hat{\mathbf{v}}_h)\in\mathbf{V}_h} \|(\mathbf{u}-\mathbf{v}_h, \hat{\mathbf{u}}-\hat{\mathbf{v}}_h)\|_{\mathbf{V}} \leq \|(\mathbf{u}-\Pi^{\Omega}_{h,0}[\mathbf{u}], \hat{\mathbf{u}}-\Pi^{\Gamma}_{h,0}[\hat{\mathbf{u}}])\|_{\mathbf{V}},$$

$$\inf_{(q_h,\hat{q}_h)\in\mathbf{M}_h} \|(p-q_h, \hat{p}-\hat{q}_h)\|_{\mathbf{M}} \leq \|(p-\pi^{\Omega}_{h,0}[p], \hat{p}-\pi^{\Gamma}_{h,0}[\hat{p}])\|_{\mathbf{M}}.$$

The proof follows by applying Proposition 4.16 and the estimates (4.15, 4.16, 4.18, 4.19, 4.20, 4.23). □

Remark 4.18. *To end, we note that [94] obtains the same convergence result except taking care to handle how the fracture width might be involved in the constant C. Indeed, here it is shown that $C = \max\{w_\Gamma, h\}$. Moreover, [27] has a convergence result for any k in configurations (I) or (II); here it is shown that the convergence is of order h^{k+1}, where k is the order of the polynomials in the bulk pressure space.*

Chapter 5

Streamlines through fractured porous media

Previously, Chapter 4 presented the model and numerical approximation, via a mixed finite element method, of the bulk–fracture flow equations. Our attention turns now to streamline tracing within this same setting.

Furthermore, in this chapter we describe the procedure where streamlines can be traced through a porous medium that contains fractures. Recall that in our setting, the bulk porous medium is represented by a two–dimensional Lipschitz domain, but the fractures, as described in Chapter 4, are one–dimensional manifolds embedded in the domain. Indeed in the case where a streamline intersects a fracture, there is a lack of transversal flow information across its width; hence we cannot determine its trajectory after this intersection has occurred.

This chapter is organised as follows. First, we re–cap the governing equations of the bulk–fracture flow model, under the simplifying case of a single one–dimensional immersed fracture embedded in some two–dimensional domain; we then discuss the fracture expansion procedure and introduce an interpolant, or ansatz, for the definition of the continuous and discrete velocity fields inside the expanded fracture; we conclude by showing that weak forms of conversation of mass and Darcy's law are still satisfied in this expanded fracture with the defined velocity field, as well as discussing the lack of satisfaction of the strong form of Darcy's law even when it is true for the non–expanded variables.

5.1 Expansion of fractures

Given that a particle trajectory intersects a fracture, the only current option, following the work presented thus far in this thesis, is to interpret the trajectory as moving along the fracture, along its tangent direction[1]. However, recalling the model (4.1, 4.2), we see that no–flow conditions are also imposed in and out of the fracture tips, and therefore there is no way for the trajectory to exit the fracture in some reasonable sense. Our approach to this problem is inspired by the work by Hægland, et al. in the works [66, 64], as example papers from the thesis [63] (and the other papers and references therein), where the same problem was faced in the finite volume setting. Hægland details a procedure in which the one–dimensional fracture is expanded back into two dimensions; here, Pollock's method is employed to interpolate constant velocity fluxes into and inside the fracture in order to satisfy conservation of mass and an integrated form of Darcy's law. Then, the streamline can be traced through the now two–dimensional fracture until it intersects the bulk domain again; this exit-point is mapped back onto the one-dimensional fracture and is taken as the exit-point in the original bulk–fracture setting, where streamline tracing can then resume at this point[2]. A cartoon example, showing what such streamline tracing may look like in fractured domains can be seen in Figure 5.1.

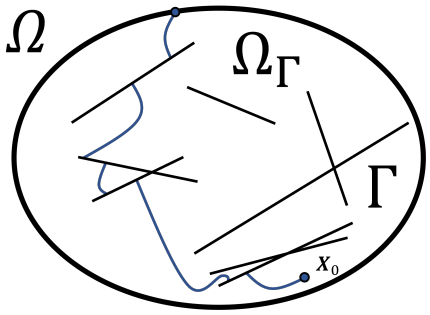

FIG. 5.1 – *Cartoon example of what streamline tracing might look like through a fracture network.*

5.1.1 The governing equations

Here, we briefly recall the governing equations for flow in fractured porous media, used previously in this thesis. For the sake of simplicity, we consider here only the case where a single fracture is fully embedded in the domain. To this end, let $\Omega \subset \mathbb{R}^2$ be an open and

[1] The direction according to the velocity $\hat{u}$, here a scalar and defined according to the governing equations (5.1, 5.2).

[2] Cf. Figure 5.4 and Section 5.2.

bounded domain with Lipschitz, or polygonal, boundary[3] $\partial\Omega$. Assume further the boundary is partitioned by the non-empty sets $\partial\Omega^N$ and $\partial\Omega^D$. As usual, $\mathbf{n}$ denotes the unit outward normal vector to $\partial\Omega$.

We denote here a single fracture $\gamma \subset \Omega$ and assume that it is fully immersed in the domain. Indeed, here we do not consider the intersection of different fractures within some network, nor the intersection of a fracture with the domain boundary; we refer the reader to [66] for these details. Moving forward, with the fracture tips $\partial\gamma = \{X_0, X_1\} \cap \partial\Omega = \emptyset$, we apply this setting to (4.1, 4.2) with $I^F = \partial\gamma$. Recall the notation $\Omega_\gamma = \Omega \setminus \overline{\gamma}$ denoting the bulk part of the porous medium and $\mathbf{n}_\gamma$ the unit outward normal vector to the fracture. Assuming the fracture is filled with debris, the governing equations are, again, given as the below coupled problem.

$$\begin{cases} \mathbf{K}^{-1}\mathbf{u} + \nabla p = 0 & \text{in } \Omega_\gamma, \\ \operatorname{div} \mathbf{u} = f & \text{in } \Omega_\gamma, \\ p = g_D & \text{on } \partial\Omega^D, \\ \mathbf{u} \cdot \mathbf{n} = 0 & \text{on } \partial\Omega^N, \\ \eta\{\mathbf{u} \cdot \mathbf{n}_\Gamma\} = [\![p]\!] & \text{on } \gamma, \\ \eta\xi_0[\![\mathbf{u} \cdot \mathbf{n}_\Gamma]\!] = \{p\} - \hat{p} & \text{on } \gamma, \end{cases} \tag{5.1}$$

$$\begin{cases} \hat{K}^{-1}\hat{u} + \partial_{\hat{x}}\hat{p} = 0 & \text{in } \gamma, \\ \partial_{\hat{x}}\hat{u} = \hat{f} + [\![\mathbf{u} \cdot \mathbf{n}_\gamma]\!] & \text{in } \gamma, \\ \hat{u} = 0 & \text{on } \partial\gamma. \end{cases} \tag{5.2}$$

The coordinate system on γ is given by $(\hat{x}, \hat{y})$ where the $\hat{x}$ direction points in the direction of the fixed, unit tangent vector $\boldsymbol{\tau}$ to γ, and $\hat{y}$ the unit normal vector $\mathbf{n}_\gamma$. Our fracture is assumed a straight line embedded in the domain and so these vectors are indeed fixed and constant along the fracture length and aperture; cf. Figure 5.2.

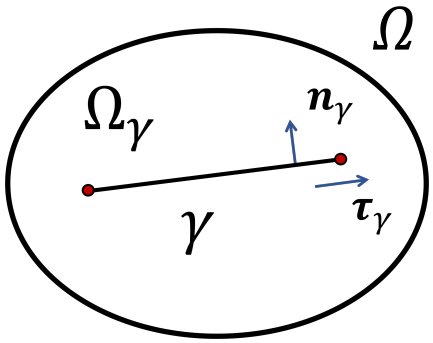

FIG. 5.2 – *A single fracture in the domain, with associated unit normal and tangent vectors.*

[3]For well–posedness we may also assume it is a convex polygon or Lipschitz with a C^1 boundary.

We recall also the scaled quantities $\hat{K} = w_\gamma \hat{K}_{\boldsymbol{\tau}} \boldsymbol{\tau}$ and $\eta = w_\gamma / \hat{K}_{\mathbf{n}}$ as the effective permeability and effective conductivity, respectively, where w_γ is the aperture, or width, of the fracture and $\hat{K}_{\boldsymbol{\tau}}$ and $\hat{K}_{\mathbf{n}}$ are the tangential and normal components of the fracture permeability. We assume the fracture width is constant along all of its length.

The weak formulation of this system of equations, and their numerical approximation by a mixed finite element method was covered in Chapter 4. For example, we can employ a lowest order approximation using the spaces in configuration (II) to obtain the numerical solutions $(\mathbf{u}_h, p_h)$ and $(\hat{u}_h, \hat{p}_h)$ on some triangulation $\mathscr{T}_h$ of the domain Ω. Recall that the fracture γ will be represented by mesh edges in the triangulation of the bulk, denoted by $\gamma_h = \{\mathcal{E} \in \mathscr{E}_h : \mathcal{E} \cap \gamma \neq \emptyset\}$, where $\mathscr{E}_h$ is the set of all interfaces in $\mathscr{T}_h$. In this example setting, $\mathbf{u}_h$ is piecewise linear on the triangles; p_h is piecewise constant on the triangles; $\hat{u}_h$ is piecewise quadratic and continuous on the edges in γ_h; and $\hat{p}$ is piecewise linear on the edges in γ_h.

5.2 Streamline tracing

Suppose $\mathbf{x}_0 \in \Omega_\gamma$. We are interested in the particle trajectory starting at $\mathbf{x}_0$ due to the Darcy velocity $\mathbf{u}$; denoted by $\mathbf{X}_\mathbf{u} : [0, \infty) \to \mathbb{R}^2$, the trajectory satisfies the usual initial value problem given by

$$\frac{d\mathbf{X}_\mathbf{u}}{dt} = \frac{\mathbf{u}}{\psi},$$

where ψ is a scalar field representing the porosity of the rock making up the bulk domain.

Suppose at some time $t^* > 0$ we have, for the first time, an intersection of the particle trajectory with the fracture, i.e.,

$$\mathbf{X}_\mathbf{u}(t^*) \in \gamma.$$

Indeed, it is not possible to proceed with the streamline tracing under the current regime. Since γ is a one–dimensional manifold embedded in Ω, there is no transversal flow information available due to the averaging process undergone to derive the modelling equations in the first place. Furthermore, there is no flow out of the fracture tips either, meaning $\mathbf{X}_\mathbf{u}$ will be trapped inside of the fracture, stagnating. Following the work by [66], we proceed similarly by expanding and re–imagining the fracture γ in two spatial dimensions, denoting this expanded fracture by γ^*.

First, however, we will introduce some notation moving forward. As per the diagram shown in Figure 5.3, γ is expanded so that it has a physical width w_γ; the original position of the fracture corresponding to $\hat{y} = 0$ (i.e. so that for notational convenience, $\gamma = \{(\hat{x}, 0) \in \gamma^*\} \subset \gamma^*$) in this coordinate system. As discussed in Section 5.1, we follow the procedure as

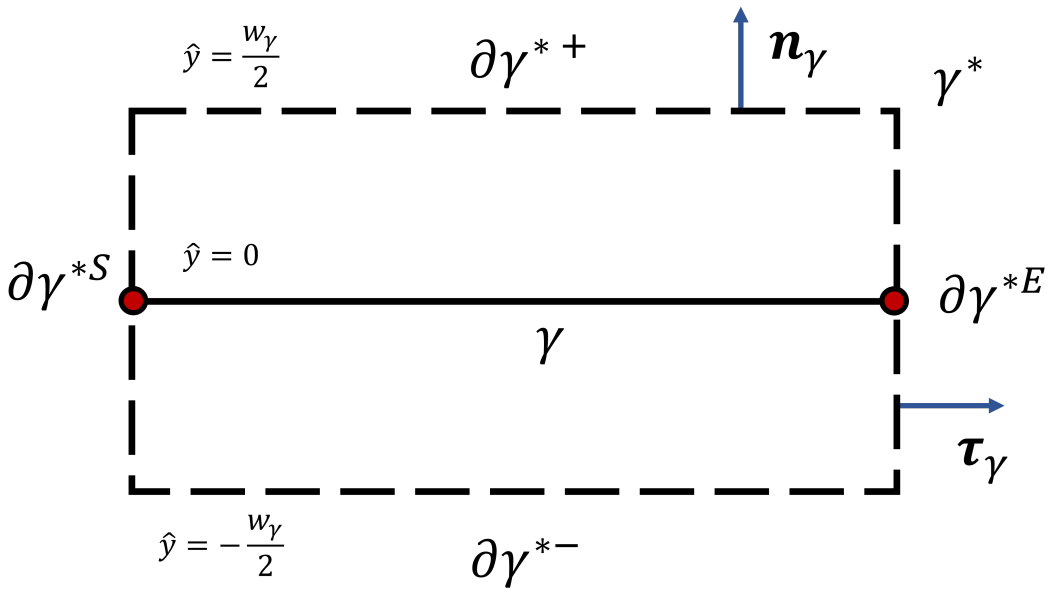

FIG. 5.3 – *Expansion process for a single fracture.*

pictured: the streamline intersects γ; the entry point $\mathbf{A} = \mathbf{X}_\mathbf{u}(t^*)$ is mapped to a point $\mathbf{B}$ on the boundary of γ^* based on the direction of entry; the streamline is, somehow, traced within γ^* until it exits; this exit point $\mathbf{C}$ is mapped back onto the one–dimensional fracture γ at the point $\mathbf{D}$; tracing of the particle trajectory then resumes in the bulk domain. Such process is sketched in Figure 5.4.

The aim moving forward is to determine how to trace the streamline within γ^*, i.e., how to define a suitable velocity in the expanded fracture that allows for physical streamlines to be traced, that make sense. Indeed, one could solve the paired Darcy's law and conservation of mass equations in the expanded fracture itself, as an option, to obtain a velocity field to trace the streamlines. However, when in realistic applications the number of fractures occupying the domain (and hence the number of possible intersections with the traced streamline) is often in the thousands[4], this does not seem very computationally feasible. Instead, we present a computationally simpler approach, that is, one of a post–processing nature involving an interpolant, or ansatz, of the bulk and fracture velocities $\mathbf{u}$ and $\hat{u}$, respectively, solving (5.1, 5.2) (or indeed, as we shall see, their approximations).

Furthermore, we denote the boundary of the expanded fracture as $\partial\gamma^* \equiv \partial\gamma^{*+} \cup \partial\gamma^{*-} \cup \partial\gamma^{*S} \cup \partial\gamma^{*E}$, the partition into the segments making up the top, bottom, start, and end of this two–dimensional object, respectively.

To this end, we propose the following velocity field to be employed when tracing streamlines

[4]See [55], for example.

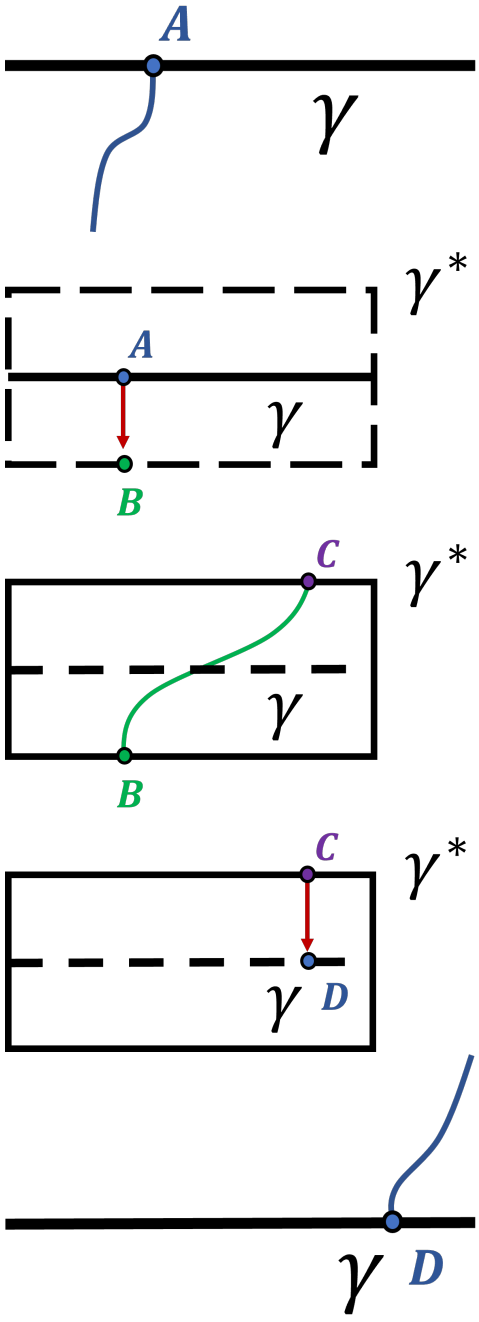

FIG. 5.4 – *Streamline tracing utilising the expansion procedure.*

through the expanded fracture γ^*:

$$\mathbf{u}^* := \frac{\hat{u}}{w_\gamma}\boldsymbol{\tau}_\gamma + \phi(\hat{x},\hat{y})\mathbf{n}_\gamma, \tag{5.3}$$

where the scalar function ϕ is yet to be determined.

In the discrete setting, recall that the fracture γ is already partitioned by $\gamma_h = \{(\ell_{i-1},\ell_i) : i = 1,2,\ldots,N\}$. The one dimensional elements (originally mesh edges in $\mathscr{T}_h$) are expanded into rectangular elements in γ^*. We write

$$\gamma_h^* = \{V_i : i = 1,2,\cdots N\},$$

where V_i is the rectangle of dimensions $w_\gamma \times (\ell_i - \ell_{i-1})$, w_γ is the constant (parameter) width of γ, and now the constant, physical, width of γ^*. The expansion of the fracture mesh into these elements is illustrated in Figure 5.5.

For a given V_i we describe its boundary in sections, similar to the boundary of γ^*; those corresponding to the bulk–fracture interface are labelled as $\partial V_i^{\pm}$ while the side boundaries, corresponding to the fracture element interfaces, as labelled as $\partial V_i^{\mathrm{S/E}}$; S/E meaning start/end, in line with the direction of the tangent vector $\boldsymbol{\tau}_\gamma$, to γ and γ^*; cf. Figure 5.6. Furthermore, we will utilise the following characteristic functions defined on these rectangular elements.

$$\chi_i(\hat{x},\hat{y}) = \begin{cases} 1 & (\hat{x},\hat{y}) \in V_i, \\ 0 & \text{otherwise.} \end{cases}$$

In this discrete setting, we propose the following interpolant approximation to be employed when tracing streamlines through the expanded fracture γ^*:

$$\mathbf{u}_h^* := \frac{\hat{u}_h}{w_\gamma}\boldsymbol{\tau}_\gamma + \sum_{i=1}^{N} \phi_i(\hat{x},\hat{y})\chi_i(\hat{x},\hat{y})\mathbf{n}_\gamma, \tag{5.4}$$

where the scalar functions ϕ_i, $i = 1,2,\ldots,N$, are to be determined, and indeed, their sum (multiplied by characteristic functions) corresponding to an approximation of the scalar field ϕ, in the continuous ansatz (5.3).

5.3 Weak conservation of mass

Moving forward, a choice must be made for the normal component ϕ. A sensible choice is to enforce flux–continuity between the interface of the bulk domain and the expanded fracture, hence having ϕ match the incoming normal–flux here. We choose to impose this flux–continuity so that the streamlines traced into the expanded fracture remain continuous, and hence physical. In the discrete setting, we will show a possible choice for the ϕ_i that

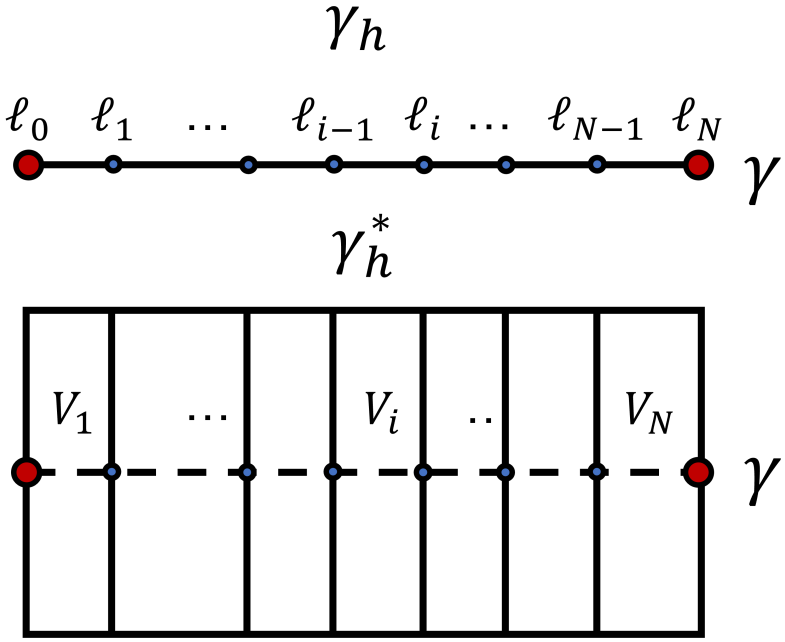

FIG. 5.5 – *Mesh transformation on the expanded fracture.*

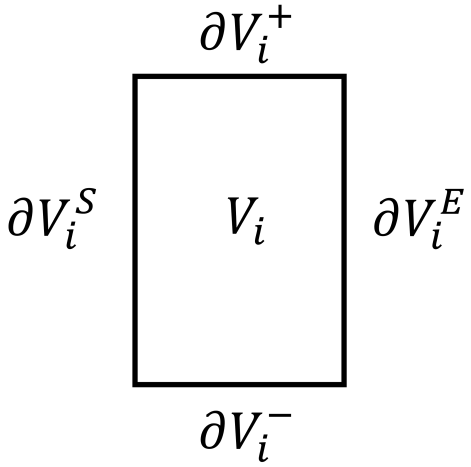

FIG. 5.6 – *Boundary notations for an element in the expanded fracture mesh.*

match the number of degrees of freedom present on the interface, in the bulk; for example, using the spaces in configuration (II) to obtain $\mathbf{u}_h$ and $\hat{u}_h$, the bulk normal–flux is piecewise linear on the edges making up γ (and hence the boundary of γ^*). Here, ϕ_i being chosen as a bilinear function in the element V_i means it has enough degrees of freedom to match the linear functions from either side of the fracture, and this, of course, can be extended to reasonable interpolants for higher–order bulk velocities.

Indeed, following the above discussion, along $\partial\gamma^*$ we should have $\mathbf{u}^* \cdot \boldsymbol{\eta} + \mathbf{u} \cdot \boldsymbol{\eta} = 0$, where $\boldsymbol{\eta}$ is the (not fixed) unit outward normal vector to to $\partial\gamma^*$, and where $\mathbf{u}$ is the Darcy velocity in the bulk domain. From the definition of $\mathbf{u}^*$, i.e., (5.3), we see that along $\partial\gamma^*$

$$\mathbf{u}^* \cdot \boldsymbol{\eta} = \mathbf{u}^* \cdot (\pm\boldsymbol{\tau}_\gamma) = \pm\frac{\hat{u}}{w_\gamma} = 0 \text{ on } \partial\gamma^*_\pm,$$

and hence, the flux–continuity condition becomes

$$\phi(\hat{x}, \pm w_\gamma/2) = -T^\pm[\mathbf{u} \cdot \mathbf{n}_\gamma]^5. \tag{5.5}$$

With the flux–continuity (5.5) we obtain a full definition for the ansatz $\mathbf{u}^*$; with this, we have the following proposition showing a satisfaction of conservation of mass, in a weak sense.

Proposition 5.1. *With the interpolated velocity field $\mathbf{u}^*$, given by (5.3), such that ϕ is chosen according to (5.5), we have*

$$\int_{\gamma^*} \hat{q}\text{div}\,\mathbf{u}^* = \int_{\gamma^*} \hat{q}\frac{\hat{f}}{w_\gamma} \;\; \forall \hat{q} \in L^2(\gamma).$$

Proof. Firstly, according to Green's formula (Proposition 2.3), we have for a fixed $\hat{q} \in L^2(\gamma)$,

$$\int_{\gamma^*} \hat{q}\text{div }\mathbf{u}^* = \int_{\partial\gamma^*} \hat{q}(\mathbf{u}^* \cdot \boldsymbol{\eta}) - \int_{\gamma^*} \hat{\nabla}\hat{q} \cdot \mathbf{u}^*,$$

where $\boldsymbol{\eta}$ is the unit outward normal to $\partial\gamma^*$. We see that since

$$\hat{\nabla}\hat{q} \cdot \mathbf{u}^* = \begin{pmatrix} \partial_{\hat{x}}\hat{q} \\ 0 \end{pmatrix} \cdot \begin{pmatrix} \hat{u}/w_\gamma \\ \phi \end{pmatrix} = \partial_{\hat{x}}\hat{q}\hat{u}/w_\gamma,$$

then

$$\int_{\gamma^*} \hat{q}\text{div }\mathbf{u}^* = \int_{\partial\gamma^*} \hat{q}(\mathbf{u}^* \cdot \boldsymbol{\eta}) - \int_{\gamma^*} \partial_{\hat{x}}\hat{q}\frac{\hat{u}}{w_\gamma}.$$

Moving forward, we can split the boundary integral into contributions over each part of the boundary, i.e.,

$$\int_{\partial\gamma^*} \hat{q}(\mathbf{u}^* \cdot \boldsymbol{\eta}) = \int_{\partial\gamma^*_+} \hat{q}(\mathbf{u}^* \cdot \mathbf{n}_\gamma) + \int_{\partial\gamma^*_-} \hat{q}(\mathbf{u}^* \cdot (-\mathbf{n}_\gamma)) + \int_{\partial\gamma^*_S} \hat{q}(\mathbf{u}^* \cdot (-\boldsymbol{\tau})) + \int_{\partial\gamma^*_E} \hat{q}(\mathbf{u}^* \cdot \boldsymbol{\tau}).$$

[5] We have abused notation here to emphasise needing the fixed normal vector $\mathbf{n}_\gamma$, instead of using the normal–trace operator $\pm T^{d,\pm}[\mathbf{u}]$, with a sign adjustment since $\mathbf{n}_\gamma = \mathbf{n}^+ = -\mathbf{n}^-$.

Furthermore, we know the integrand on each part of these boundary components. Therefore,

$$\begin{aligned}\int_{\gamma^*} \hat{q}(\mathbf{u}^* \cdot \boldsymbol{\eta}) &= \int_{\partial\gamma_+^*} \hat{q}\phi(\hat{x}, w_\gamma/2) - \int_{\partial\gamma_-^*} \hat{q}\phi(\hat{x}, -w_\gamma/2) - \int_{\partial\gamma_S^*} \hat{q}\frac{\hat{u}}{w_\gamma} + \int_{\partial\gamma_E^*} \hat{q}\frac{\hat{u}}{w_\gamma} \\ &= \int_\gamma \hat{q}(\phi(\hat{x}, w_\gamma/2) - \phi(\hat{x}, -w_\gamma/2)) + w_\gamma \left(\hat{q}(\ell_E)\frac{\hat{u}(\ell_E)}{w_\gamma} - \hat{q}(\ell_S)\frac{\hat{u}(\ell_S)}{w_\gamma}\right) \\ &= \int_\gamma -\hat{q}[\![\mathbf{u} \cdot \mathbf{n}_\gamma]\!] + \hat{q}(\ell_E)\hat{u}(\ell_E) - \hat{q}(\ell_S)\hat{u}(\ell_S) \\ &= \int_\gamma \hat{q}(-\partial_{\hat{x}}\hat{u} + \hat{f}) + \hat{q}(\ell_E)\hat{u}(\ell_E) - \hat{q}(\ell_S)\hat{u}(\ell_S),\end{aligned}$$

where the final equality follows from (4.8, 4.9), the weak formulation for the continuous solution $\hat{u}$. Now,

$$-\int_\gamma \hat{q}\partial_{\hat{x}}\hat{u} = \int_\gamma \hat{u}\partial_{\hat{x}}\hat{q} - (\hat{q}(\ell_E)\hat{u}(\ell_E) - \hat{q}(\ell_S)\hat{u}(\ell_S)),$$

due to integration by parts. With this, we see that

$$\begin{aligned}\int_{\gamma^*} \hat{q}\operatorname{div}\mathbf{u}^* &= \int_\gamma \hat{u}\partial_{\hat{x}}\hat{q} - (\hat{q}(\ell_E)\hat{u}(\ell_E) - \hat{q}(\ell_S)\hat{u}(\ell_S)) + \int_\gamma \hat{q}\hat{f} \\ &\quad + \hat{q}(\ell_E)\hat{u}(\ell_E) - \hat{q}(\ell_S)\hat{u}(\ell_S) - \int_{\gamma^*} \partial_{\hat{x}}\hat{q}\frac{\hat{u}}{w_\gamma} \\ &= \int_{-w\gamma/2}^{w_\gamma/2}\int_\gamma \frac{\hat{u}}{w_\gamma}\partial_{\hat{x}}\hat{q} - \int_{\gamma^*} \frac{\hat{u}}{w_\gamma}\partial_{\hat{x}}\hat{q} + \int_\gamma \hat{q}\hat{f} \\ &= \int_{\gamma^*} \frac{\hat{u}}{w_\gamma}\partial_{\hat{x}}\hat{q} - \int_{\gamma^*} \frac{\hat{u}}{w_\gamma}\partial_{\hat{x}}\hat{q} + \int_\gamma \hat{q}\hat{f} \\ &= \int_\gamma \hat{q}\hat{f} = \int_{-w_\gamma/2}^{w_\gamma/2}\int_\gamma \hat{q}\frac{\hat{f}}{w_\gamma} \\ &= \int_{\gamma^*} \hat{q}\frac{\hat{f}}{w_\gamma}.\end{aligned}$$

□

Hence, the flux–continuity assumption (5.5) is reasonable to assume for sensible streamline computation since it implies that conservation of mass is retained within this setting.

Let us consider the discrete setting with a single expanded element V_i. In this setting, it is, due to the expansion, neighboured by two triangular elements from the underlying bulk mesh $\mathscr{T}_h$. Let us consider the restriction, or trace, of the bulk-velocity $\mathbf{u}_h$ to the top and bottom boundary components $\partial V_i^\pm$. Recall that the expanded element V_i corresponds to the one-dimensional element (ℓ_{i-1}, ℓ_i); hence, we can interpret the flow of $\mathbf{u}_h$ into $\partial V_i^\pm$ as the same as the flow into either side of the one-dimensional element, conceptually, as

$$(\mathbf{u}_h \cdot \mathbf{n}_\gamma)|_{\partial V_i^\pm} := T^\pm_{(\ell_{i-1},\ell_i)}[\mathbf{u}_h \cdot \mathbf{n}_\gamma].$$

Furthermore, in the interpolated discrete velocity

$$\mathbf{u}_h^* := \frac{\hat{u}_h}{w_\gamma}\boldsymbol{\tau}_\gamma + \sum_{i=1}^N \phi_i(\hat{x}, \hat{y})\chi_i(\hat{x}, \hat{y})\mathbf{n}_\gamma, \tag{5.6}$$

the ϕ_i are selected so as to satisfy the flux–continuity property, normal to the expanded fracture:

$$\phi_i(\hat{x}, \pm w_\gamma/2) \equiv -(\mathbf{u}_h \cdot \mathbf{n}_\gamma)|_{\partial V_i^\pm}(\hat{x}) \ \ \forall \hat{x} \in (\ell_{i-1}, \ell_i). \tag{5.7}$$

Suppose the adjacent triangular elements to V_i are labelled $\kappa_i^\pm$. Within the discrete setting, the bulk $\mathbf{u}_h|_{\kappa_i^\pm} \in BDM_{k+1}(\kappa_i^\pm)$, where the lowest order case corresponds to $k = 0$. The condition (5.7) can indeed be satisfied given that

$$\phi_i|_{\partial V_i^\pm} \in T^d[BDM_{k+1}(\kappa_i^\pm)] \equiv \mathbb{P}_k((\ell_{i-1}, \ell_i)).$$

For example, in the lowest order case, ϕ_i being chosen as a bilinear function means flux–continuity between the bulk–fracture interface can be enforced. More explicitly, suppose

$$\begin{aligned}(\mathbf{u}_h \cdot \mathbf{n}_\gamma)|_{\partial V_i^\pm} &\equiv A_i^\pm + B_i^\pm \hat{x}, \\ \phi_i(\hat{x}, \hat{y}) &\equiv a_i + b_i\hat{x} + c_i\hat{y} + d_i\hat{x}\hat{y}.\end{aligned}$$

Then, (5.7), along with some simple linear algebra, leads to

$$a_i = -(A_i^+ + A_i^-)/2, \tag{5.8}$$

$$b_i = -(B_i^+ + B_i^-)/2, \tag{5.9}$$

$$c_i = -(A_i^+ - A_i^-)/w_\gamma, \tag{5.10}$$

$$d_i = -(B_i^+ - B_i^-)/w_\gamma. \tag{5.11}$$

Moreover, the same mass conservation holds true when considering the discrete interpolated velocity field $\mathbf{u}_h^*$. We see in the above proof to Proposition 5.1, that it is the consequence of basic calculus paired with the flux–continuity requirement on ϕ and the weak formulation of the original fracture-bulk Darcy problem; the same weak formulation holds in the discrete setting, i.e., (4.13, 4.14), and thus we may arrive at the following result.

Corollary 5.2. *With the interpolated, discrete, velocity field $\mathbf{u}_h^*$ given by (5.6) such that the ϕ is chosen according to (5.7), we have*

$$\int_{V_i} \operatorname{div} \mathbf{u}_h^* = \int_{V_i} \frac{\hat{f}}{w_\gamma} \ \ \forall i = 1, 2, \ldots, N.$$

Proof. As detailed before, we have the discrete version of Proposition 5.1

$$\int_{\gamma^*} \hat{q}_h \operatorname{div} \mathbf{u}_h^* = \int_{\gamma^*} \hat{q}_h \frac{\hat{f}}{w_\gamma} \ \ \forall \hat{q}_h \in M_{h,k}^\gamma,$$

recalling from configuration (II) the discrete spaces $\hat{u} \in V_{h,k}^\gamma \equiv \{\hat{v}_h \in \mathbb{P}_{k+1}^c(\gamma, \gamma_h) : \hat{v}|_{I^F} = 0\}$ and $\hat{q}_h \in M_{h,k}^\gamma = \mathbb{P}_k(\gamma, \gamma_h)$ taken for a single fracture in the network. Let $\hat{q}_h = \chi_i$ be the characteristic function on V_i, then the result follows immediately. □

Something that has not been addressed yet is the continuity of flux between the elements V_i in the expanded fracture. When tracing a streamline within V_i there is no guarantee it will enter the fracture and leave without entering a neighbouring expanded element. Therefore, it is vital that we have tangential continuity of the flux, $\mathbf{u}_h^* \cdot \boldsymbol{\tau}$ across the interfaces between the V_i; this will ensure the streamline stays continuous when being traced from one V_i to the next. Fortunately, with the interpolant (5.3), this continuity is achieved automatically since $\hat{u}_h$ is continuous across this interface and w_γ is constant; recall that

$$\hat{u}_h \in \{\mathbb{P}_k^c(\gamma, \gamma_h) : \hat{u}_h|_{I^F} = 0\}.$$

Being the only tangential part of the expanded velocity field means no further work needs to be done in order to achieve this flux–continuity.

The full choice, or definition, of ϕ in the continuous setting is still an open question, since the only restriction required is the condition (5.5). For example, one choice is to interpolate the continuous velocities $\mathbf{u}$ and $\hat{u}$ onto some mesh of the bulk domain and fracture, such that their normal–trace is respected, and then apply the aforementioned discussion in the discrete setting to define ϕ via the sum of discrete ϕ_i.

Alternatively, ϕ could yet be determined by other physical laws on the expanded fracture. One may consider Darcy's law to be the answer, however, we shall see in the following section that a weak formulation of Darcy's law is automatically satisfied in this setting and that a strong form cannot hold true even if the bulk and fracture velocities each satisfy their respective strong forms of Darcy's law as well.

5.4 Weak Darcy's law

Let $\mathbf{K}^*$ be the permeability tensor in the expanded fracture, which matches the permeability of the one–dimensional fracture via

$$\mathbf{K}^* = \begin{pmatrix} K_{\boldsymbol{\tau}_\gamma} & 0 \\ 0 & K_{\mathbf{n}_\gamma} \end{pmatrix}.$$

Just as we have defined an interpolated velocity field, representing the Darcy velocity within the expanded fracture γ^*, it is useful to think about the pressure as well. We define such a pressure by

$$p^*(\hat{x}, \hat{y}) = \hat{p}(\hat{x}) + q^*(\hat{x}, \hat{y}),$$

where $\hat{p}$ is the pressure solution on the one–dimensional fracture, satisfying (5.1, 5.2). This follows the ansatz–style approach we have taken thus far; indeed, $\hat{p}$, and more so its discrete approximation $\hat{p}_h$, will be known to us, and are already stored when it comes round to

streamline computation. With these in place, we have already the weak satisfaction of Darcy's law in the expanded fracture, given in the below proposition.

Proposition 5.3. *Under the foregoing notations, we have the following formulation of Darcy's law in the expanded fracture γ^*:*

$$\int_{\gamma^*} (\mathbf{K}^{*-1}\mathbf{u}^*)\hat{v}\boldsymbol{\tau}_\gamma = \int_{\gamma^*} p^* \partial_{\hat{x}}\hat{v} \ \ \forall \hat{v} \in V^\gamma,$$

recalling the function space $V^\gamma = \{\hat{v} \in H^1(\gamma) : \hat{v}|_{I^F} = 0\}$. Furthermore, the interpolated pressure field is such that $q^*(\hat{x}, \hat{y}) \equiv 0$, i.e., $p^* = \hat{p}$.

Proof. We begin by noting that due to its diagonal nature,

$$\mathbf{K}^{*-1} = \begin{pmatrix} 1/K_{\boldsymbol{\tau}_\gamma} & 0 \\ 0 & 1/K_{\mathbf{n}_\gamma} \end{pmatrix}.$$

Furthermore,

$$\mathbf{K}^{*-1}\mathbf{u}^* = K_{\boldsymbol{\tau}_\gamma}^{-1} \frac{\hat{u}}{w_\gamma} \boldsymbol{\tau}_\gamma + K_{\mathbf{n}_\gamma}^{-1} \phi \mathbf{n}_\gamma.$$

Recall the definition: $\hat{K} := w_\gamma K_{\boldsymbol{\tau}_\gamma}$ to see that

$$(\mathbf{K}^{*-1}\mathbf{u}^*) \cdot \hat{v}\boldsymbol{\tau}_\gamma = \hat{K}^{-1}\hat{u}\hat{v}$$

for some given, fixed, $\hat{v} \in V^\gamma$. The weak formulation (4.8, 4.9) tells us that

$$\int_\gamma \hat{K}^{-1}\hat{u}\hat{v} = \int_\gamma \hat{p}\partial_{\hat{x}}\hat{v} \ \ \forall \hat{v} \in V^\gamma.$$

Therefore,

$$\int_{\gamma^*} (\mathbf{K}^{*-1}\mathbf{u}^*) \cdot \hat{v}\boldsymbol{\tau}_\gamma = \int_{\gamma^*} \hat{K}^{-1}\hat{u}\hat{v} = w_\gamma \int_\gamma \hat{K}^{-1}\hat{u}\hat{v} = w_\gamma \int_\gamma \hat{p}\partial_{\hat{x}}\hat{v} = \int_{\gamma^*} \hat{p}\partial_{\hat{x}}\hat{v}.$$

With $p^* = \hat{p} + q^*$, we would require

$$\int_{\gamma^*} q^* \partial_{\hat{x}}\hat{v} = 0 \ \ \forall \hat{v} \in V^\gamma,$$

which, of course, implies $q^* = 0$ (a.e.) in γ^*. □

The fact that the quantity q^* vanishes is only required because of the diagonal form of the permeability field $\mathbf{K}^*$. Indeed, if $\boldsymbol{\tau}_\gamma \cdot \mathbf{K}^{*-1}\mathbf{n}_\gamma \neq 0$, which may happen, for example, if $\mathbf{K}^*$ has a non–zero entry (2, 1), then the term

$$\int_{\gamma^*} \hat{v}\boldsymbol{\tau}_\gamma \cdot \mathbf{K}^{*-1}\mathbf{n}_\gamma \phi \neq 0.$$

In this case, we will see that the relation

$$\int_{\gamma^*} \hat{v}\boldsymbol{\tau}_\gamma \cdot \mathbf{K}^{*-1}\mathbf{n}_\gamma \phi = \int_{\gamma^*} q^* \partial_{\hat{x}}\hat{v} \ \ \forall \hat{v} \in V^\gamma \tag{5.12}$$

is required. This expression relates together q^* in the interpolated pressure field with ϕ, which, up to this point is otherwise undetermined in the interior of the expanded fracture. If we use again an interpolant for ϕ, (5.12) may imply a suitable choice for $\hat{q}$ so that Darcy's law is satisfied. Or alternatively, some interpolant for q will imply a choice for ϕ in the interior of the fracture.

We note that with p^* interpreted as the pressure inside the expanded fracture, we do not have pressure continuity between the interface of bulk and fracture, otherwise assumed in the original model (in [94], for example) before averaging takes place. This however will not have an effect on the physicality of streamline tracing in this context.

Lastly, we remark that Proposition 5.3 holds also in the discrete setting with interpolated velocity field $\mathbf{u}_h^*$, test functions $\hat{v}_h \in V_{h,k}^{\gamma}$ and interpolated pressure $p_h^* = \hat{p}_h$[6].

5.4.1 Strong Darcy's law

To conclude this chapter we look briefly at an interesting property of our interpolated velocity $\mathbf{u}^*$ in the expanded fracture. That is, that even if we are in the fortunate circumstance where our bulk and (one–dimensional) fracture variables satisfy their physical laws in their strong form, that the same cannot be said for our choice of interpolated velocity field in the expanded fracture; we show this in two ways.

Firstly, suppose that $\mathbf{u}^*$ satisfies Darcy's law in γ^*. That is,

$$\mathbf{u}^* = -\mathbf{K}^* \hat{\nabla} p^*, \tag{5.13}$$

where $p^* = \hat{p}(\hat{x}) + q^*(\hat{x}, \hat{y})$ is the pressure in γ^*; q^* is to be determined; and $\hat{\nabla}$ is the gradient operator in the expanded fracture, i.e., $(\partial_{\hat{x}}, \partial_{\hat{y}})^\top$. Explicitly, we have

$$\begin{pmatrix} \hat{u}/w_\gamma \\ \phi \end{pmatrix} = -\mathbf{K}^* \begin{pmatrix} \partial_{\hat{x}} \hat{p} + \partial_{\hat{x}} q^* \\ \partial_{\hat{y}} q^* \end{pmatrix}.$$

In the direction of $\hat{x}$ we have

$$\frac{\hat{u}}{w_\gamma} = -K_{\boldsymbol{\tau}_\gamma} (\partial_{\hat{x}} \hat{p} + \partial_{\hat{x}} q^*).$$

Since (5.13) tells us that $w_\gamma K_{\boldsymbol{\tau}_\gamma} = \hat{K}$ and $\hat{u} + \hat{K} \partial_{\hat{x}} \hat{p} = 0$, the above becomes

$$\hat{K} \partial_{\hat{x}} q^* = 0,$$

which, since $\hat{K} \neq 0$ is a scalar in this setting, simply states that

$$\partial_{\hat{x}} q^* = 0.$$

[6]Indeed, the bulk–fracture problem has Galerkin orthogonality: the continuous and discrete solutions satisfy the same weak formulation.

This lack of $\hat{x}$ dependence in q^* causes an immediate issue, since in the $\hat{y}$ direction we have

$$-\frac{\phi}{K_{\mathbf{n}_\gamma}} = \partial_{\hat{y}} q^*,$$

i.e., q^* must have $\hat{x}$ dependence. This is indeed a contradiction, and therefore Darcy's law cannot be imposed this way.

Alternatively, let us suppose instead that p^* might take a different form. Given that $\mathbf{u}^* = -\mathbf{K}^* \hat{\nabla} p^*$, we consider the curve ζ_i obtained by tracing the boundary of some arbitrary element V_i anti-clockwise. Since the permeability tensor is constant, and since the curl of a gradient is always zero, we must have that the path integral

$$\int_{\zeta_i} \mathbf{u}^* \cdot d\mathbf{s} = 0. \tag{5.14}$$

Recall that $\partial V_i = \partial V_i^+ \cup \partial V_i^- \cup \partial V_i^S \cup \partial V_i^E$. The contributions of (5.14) along the top and bottom of γ^* (i.e. $\partial V_i^{\pm}$) will cancel each other out since $\hat{u}$ does not depend on $\hat{y}$. Furthermore, we then would require

$$\int_{-w\gamma/2}^{w_\gamma/2} (\phi_i(\ell_{i-1}, \hat{y}) - \phi_i(\ell_i, \hat{y}))\, d\hat{y} = 0.$$

For example, if using the lowest order projection $\mathbf{u}_h = \Pi_{h,0}[\mathbf{u}]$ to define the ϕ_i, we would require

$$w_\gamma b_i (\ell_{i-1} - \ell_i) = 0,$$

with b_i defined according to (5.9), which is clearly not possible. Hence, within this context, $\mathbf{u}^*$ cannot satisfy (5.13) with any possible choice of scalar field p^*.

Chapter 6

Goal–oriented estimation for Darcy's equations

Within this chapter, our focus is on the error estimation for quantities of interest involving the solutions to Darcy's equations. We first present the standard dual–weighted–residual (DWR) theory employed in order to derive *a posteriori* error estimates for such quantities. Subsequently, these estimates are decomposed over the triangulation of the domain used to define the discrete approximations, in order to drive a standard adaptive algorithm for accurate computation of the quantities of interest. We briefly cover some alternative choices for this decomposition, as well as addressing the convergence of quantities of interest in the context of Darcy's equations, before finishing the chapter with some numerical examples. These examples highlight some interesting features of the chosen decomposition of the *a posteriori* error estimate, namely their so–called sharpness. We conclude with an example where the adaptive routine not only recovers the optimal rate of convergence for an irregular solution, but showcases superconvergence of the quantity of interest, in some cases.

6.1 The dual–weighted–residual method

This section aims to apply the standard theory of dual–weighted–residual error estimation for quantities of interest for the so–called *primal problem* given by the variational form of Darcy's equations (3.8, 3.9)[1]. It is not precisely the solutions (that is, the Darcy velocity **u**

[1]We do not consider fractures in this chapter, but aim towards extending the theory presented here and in the subsequent Travel Time chapter for porous domains with networks of fractures.

and the pressure p) that we are interested in; we are instead concerned with some quantity involving the solutions, often referred to as the quantity of interest (QoI). We seek to be able to control and minimise the error in the QoI, when the exact solutions are replaced by a discrete approximation, e.g., the solutions of (3.19, 3.20), to within some user–defined tolerance.

The theory presented here is standard DWR theory, following for example [18, 69]; most literature on the topic covers the following analysis and is often self–contained.

We assume the QoI can be expressed as the potentially nonlinear functional $Q([\mathbf{u}, p])$ of the solutions $\mathbf{u}$ and p. In brief, the selection of such a QoI readily defines a problem considered adjoint to (3.8, 3.9); this problem is exploited in order to derive an estimate for the error in the QoI when evaluated at the discrete solutions $(\mathbf{u}_h, p_h)$, i.e. an estimate for $Q([\mathbf{u}, p]) - Q([\mathbf{u}_h, p_h])$. In the case of a nonlinear functional, also referred to as the goal functional, some notion of its derivative is required, which we present below.

Definition 6.1. *Let X be a vector space, Y a normed space and $F : X \to Y$ a function. Then, given $x \in X$, if the limit*

$$F'[x](w) := \lim_{\varepsilon \to 0} \frac{F(x + \varepsilon w) - F(x)}{\varepsilon}$$

exists, for all $w \in X$, and the mapping $w \mapsto F'[x](w)$ is linear and continuous, then F is said to be Gâteaux differentiable at x. Moreover, in this case we refer to the quantity $F'[x](\cdot) : X \to Y$ as the Gâteaux derivative, of F, evaluated at x.

Definition 6.2. *Let X and Y be normed spaces, and let $F : X \to Y$ be a function. For $x \in X$, if a continuous linear operator $F'[x](\cdot) : X \to Y$ exists such that*

$$\lim_{\|h\|_X \to 0} \frac{\|F(x + h) - F(x) - F'[x](h)\|_Y}{\|h\|_X} = 0,$$

then F is said to be Fréchet differentiable at x and $F'[x](\cdot)$ is referred to as the Fréchet derivative of F, evaluated at x. It is also true that if F is Fréchet differentiable at x then it is Gâteaux differentiable at x as well, and these derivatives coincide.

We proceed with the error estimation in a general setting. To this end, let H be a Hilbert space and let $\mathcal{N}(\cdot, \cdot) : H \times H \to \mathbb{R}$ be a semi–linear form (in its second argument) such that the *abstract primal problem* has the form:

Find $u \in H$ such that

$$\mathcal{N}(u, v) = 0 \quad \forall v \in H. \tag{6.1}$$

Let $H_h \subset H$ be a finite dimensional subspace defining the *abstract discrete primal problem*:

Find $u_h \in H_h$ such that

$$\mathcal{N}(u_h, v_h) = 0 \quad \forall v_h \in H_h. \tag{6.2}$$

Of course, since $v_h \in H_h$ implies $v_h \in H$, we have the Galerkin orthogonality property

$$\mathcal{N}(u, v_h) - \mathcal{N}(u_h, v_h) = 0 \quad \forall v_h \in H_h. \tag{6.3}$$

Let $Q(\cdot) : H \to \mathbb{R}$ be the functional representing the quantity of interest (that is, we are interested in the value of $Q(u)$). We allow for the case that $Q(\cdot)$ is nonlinear, but insist that it is Fréchet differentiable, according to Definition 6.2. To this end, the mean–value–linearisation of $Q(\cdot)$ is defined by

$$\overline{Q}(u, u_h; u - u_h) := \int_0^1 Q'[\theta u + (1-\theta)u_h](u - u_h)\, d\theta = Q(u) - Q(u_h).$$

Furthermore, consider the mapping $u \mapsto \mathcal{N}(u, v)$; for a fixed $v \in H$, denote by $\mathcal{N}'_u[w](\cdot, v)$ the Fréchet derivative of this mapping, evaluated at some $w \in H$. The mean–value–linearisation of $\mathcal{N}(\cdot, v)$ is then

$$\mathscr{M}(u, u_h; u - u_h, v) := \int_0^1 \mathcal{N}'_u[\theta u + (1-\theta)u_h](u - u_h, v)\, d\theta = \mathcal{N}(u, v) - \mathcal{N}(u_h, v).$$

With the above notation, we define the *abstract adjoint problem I* as:

Find $z \in H$ such that

$$\mathscr{M}(u, u_h; w, z) = \overline{Q}(u, u_h; w) \quad \forall w \in H. \tag{6.4}$$

Moreover, define the residual by

$$\mathscr{R}(u_h, w) := -\mathcal{N}(u_h, w) \quad \forall w \in H.$$

Then, given below in Theorem 6.3, we have an error representation formula for the QoI.

Theorem 6.3. *Under the foregoing notation, let u be the solution of the continuous problem (6.1) with discrete approximation u_h solving (6.2). Then, for the goal functional $Q(\cdot) : H \to \mathbb{R}$ we have*

$$Q(u) - Q(u_h) = \mathscr{R}(u_h, z - z_I) \quad \forall z_I \in H_h,$$

where z is the solution to the adjoint problem (6.4).

Proof. We have, $\forall z_I \in H_h$,

$$\begin{aligned} Q(u) - Q(u_h) &= \overline{Q}(u, u_h, u - u_h) && (6.5)\\ &= \mathscr{M}(u, u_h; u - u_h, z) && (6.6)\\ &= \mathscr{M}(u, u_h; u - u_h, z) + \mathcal{N}(u_h, z_I) - \mathcal{N}(u, z_I) && (6.7)\\ &= \mathscr{M}(u, u_h; u - u_h, z) - \mathscr{M}(u, u_h; u - u_h, z_I) && (6.8)\\ &= \mathscr{M}(u, u_h; u - u_h, z - z_I) && (6.9)\\ &= \mathcal{N}(u, z - z_I) - \mathcal{N}(u_h, z - z_I) && (6.10)\\ &= -\mathcal{N}(u_h, z - z_I) && (6.11)\\ &= \mathscr{R}(u_h, z - z_I). && (6.12) \end{aligned}$$

□

In view of estimating the error $Q(u) - Q(u_h)$, Theorem 6.3 is an excellent start. Here, we removed an explicit dependence of the error on the solution u to the primal problem (6.1), although the adjoint solution z still depends on u. Therefore, unless we know the solution z solving the adjoint problem (6.4), which we very rarely do, the expression given by the error representation formula is not computable and cannot be used in practice.

In order to proceed, and obtain a computable estimate for the error $Q(u) - Q(u_h)$, the general approach in the DWR method is to approximate the problem (6.4). To this end, we need to introduce two further problems. Firstly consider a linearised version of the *abstract adjoint problem I*, which is obtained by putting $u = u_h$ in (6.4):

Find $z_\star \in H$ such that

$$\mathcal{N}'[u_h](w, z_\star) = Q'[u_h](w) \quad \forall w \in H. \tag{6.13}$$

We refer to the above problem as the *abstract adjoint problem II*. Again, one cannot solve (6.13) in general; moreover, its use is that it readily, and more easily, allows us to define a suitable discrete problem. To this end, let $W_h \subset H$ be a finite–dimensional subspace such that $W_h \not\subset H_h$. Then, we wish to:

Find $z_h \in W_h$ such that

$$\mathcal{N}'[u_h](w_h, z_h) = Q'[u_h](w_h) \quad \forall w_h \in W_h. \tag{6.14}$$

We refer to (6.14) as the *abstract discrete adjoint problem II*, which can be solved using similar finite element methods used to obtain the solution approximation u_h. The condition that $W_h \not\subset H_h$ is essential due to the aforementioned Galerkin orthogonality property (6.3). If $W_h \subset H_h$, then we see that replacing z with z_h in Theorem 6.3 tells us that

$$Q(u) - Q(u_h) \approx \mathscr{R}(u_h, z_h - z_I) = -\mathcal{N}(u_h, z_h - z_I) = 0$$

since $z_h - z_I \in H_h$ and since u_h solves the discrete problem (6.2); this statement is clearly not very useful in practice. Examples of a suitable W_h include using the same triangulation of the domain as the space H_h but with a higher polynomial degree of approximation, or using the same polynomial degree but on some finer mesh; we employ the former in this chapter. Using all of the adjoint problems (6.4, 6.13, 6.14), we see that the residual may be decomposed into the three parts

$$Q(u) - Q(u_h) = \mathscr{R}(u_h, z - z_\star) + \mathscr{R}(u_h, z_\star - z_h) + \mathscr{R}(u_h, z_h - z_I). \tag{6.15}$$

The first term $\mathscr{R}(u_h, z - z_\star)$ represents the error induced by the approximate linearisation of *adjoint problem I*, and the second term $\mathscr{R}(u_h, z_\star - z_h)$ represents the error induced by discretising *adjoint problem II*. The last term, $\mathscr{R}(u_h, z_h - z_I)$, is most useful since it is computable. If we assume that the other, noncomputable, residual terms converge to zero with an asymptotic rate faster than this latter term, we can estimate the error in the QoI with the computable part directly via

$$Q(u) - Q(u_h) \approx \mathscr{R}(u_h, z_h - z_I) \quad \forall z_I \in H_h, \tag{6.16}$$

which we refer to as the *computable error estimate*[2]. Typically, $z_I \in H_h$ is chosen to be a projection of the discrete linearised adjoint solution z_h. The importance of this projection is essential to ensure that the double rate of convergence expected in optimal goal–oriented adaptive regimes is retained when elementwise error indicators are defined based on (6.16), cf. Section 6.3.

Moving forward, (6.1) may define a residual $\mathscr{R}(u_h, z_h - z_I)$ that can be localised, or decomposed, into a sum of elementwise contributions on a triangulation $\mathscr{T}_h$ of the domain, defining the space H_h. Doing so would give us the error estimate, and *stopping criterion* $\mathcal{S}$ such that

$$|Q(u) - Q(u_h)| \approx \left| \sum_{\kappa \in \mathscr{T}_h} \eta_\kappa \right| \leq \sum_{\kappa \in \mathscr{T}_h} |\eta_\kappa| =: \mathcal{S}.$$

Indeed, we would like the bounded sum

$$\mathcal{S} := \sum_{\kappa \in \mathscr{T}_h} |\eta_\kappa|$$

to converge with the same rate as the goal error $Q(u) - Q(u_h)$ on a sequence of meshes obtained via refinement. In practice, this can be checked by considering the *bounded effectivity index* $\theta_{\geq}$; that is, if

$$\theta_{\geq} := \frac{\mathcal{S}}{|Q(u) - Q(u_h)|} \to \Upsilon \in \mathbb{R}, \tag{6.17}$$

[2]Cf. [73].

then $\mathcal{S}$ remains representative of the error under mesh refinement and could be a viable choice as the stopping criterion for the refinement algorithm, as long as it also remains an upper bound. If this is the case, the local indicators η_κ are referred to as being *sharp*. The bounded sum $\mathcal{S}$ being used as a stopping criterion means that the adaptive refinement algorithm should be terminated when

$$\mathcal{S} \leq \texttt{TOL}$$

for a user–defined tolerance $\texttt{TOL} > 0$. If the indicators are sharp then $\mathcal{S} \leq \texttt{TOL}$ should mean that the error is below this tolerance as well[3]. If $\mathcal{S}$ remains an upper bound then using it as a stopping criterion will give an extra level of security, and certainty, in practical applications.

Furthermore, as we shall see in Section 6.6, it is the absolute values of the indicators η_κ that are considered when marking elements for refinement when considering an adaptive refinement algorithm. If the indicators are not sharp then we cannot possibly hope to obtain optimal meshes for the given quantity of interest, since the bounded sum $\mathcal{S}$ no longer represents the goal error $Q(u) - Q(u_h)$.

6.2 DWR formulation of Darcy's equations

Here, we will briefly contextualise the *a posteriori* error analysis presented in Section 6.1 for the case of (the variational form of) Darcy's equations (3.8, 3.9). Furthermore, we decompose the error estimate (6.16), in the context of Darcy's equations into element–based indicators on a mesh $\mathscr{T}_h$ based on the usual integration–by–parts approach.

To this end, we recall some notation from Chapter 3. Let Ω be the usual open, bounded, Lipschitz domain in $\mathbb{R}^2$ whose polygonal boundary is partitioned into $\partial\Omega = \partial\Omega^D \cup \partial\Omega^N$. Define the spaces $\mathbf{V} := H_{0,N}(\mathrm{div}, \Omega)$ and $Q := L^2(\Omega)$, according to Section 2.1. We define, on the shape–regular triangulation $\mathscr{T}_h$ the approximation spaces $\mathbf{V}_h^k$ and Q_h^k according to Section 3.4, for k an integer; that is,

$$\mathcal{M}_k(\Omega, \mathscr{T}_h) := \{\mathbf{v}_h \in H(\mathrm{div}, \Omega) : \mathbf{v}_h|_\kappa \in \mathcal{M}_k(\kappa)\ \forall \kappa \in \mathscr{T}_h\}, \tag{6.18}$$

$$V_h^k := \{\mathbf{v}_h \in \mathcal{M}_k(\Omega, \mathscr{T}_h) : (\mathbf{v}_h \cdot \mathbf{n})|_{\partial\Omega^N} = 0\}, \tag{6.19}$$

moreover,

$$D_k(\kappa) = \mathrm{div}(\mathcal{M}_k(\kappa)) = \begin{cases} \mathbb{P}_k(\kappa) & (\mathcal{M}_k(\kappa) = RT_k(\kappa)), \\ \mathbb{P}_{k-1}(\kappa) & (\mathcal{M}_k(\kappa) = BDM_k(\kappa)), \end{cases}$$

[3]Although as noted in [92], we are not even guaranteed the upper bound $Q(u) - Q(u_h) \leq \mathcal{S}$ employing these standard DWR techniques, and more sophisticated techniques should be employed instead.

and

$$Q_h^k := \mathcal{L}^0(D_k, \mathscr{T}_h) = \{q_h \in L^2(\Omega) : Q_h|_\kappa \in D_k(\kappa),\ \forall \kappa \in \mathscr{T}_h\}. \tag{6.20}$$

We proceed by rewriting the variational formulation of Darcy's equations (3.8, 3.9), and its finite element approximation (3.19, 3.20), in a form such that the theory from Section 6.1 can be readily applied. To this end, recall the bilinear forms $a(\cdot,\cdot) : V \times V \to \mathbb{R}$ and $b(\cdot,\cdot) : V \times Q \to \mathbb{R}$ and the linear functionals $G \in V^*$ and $F \in Q^*$, defined in (3.6) and (3.7), respectively, and define the following spaces:

$$\mathscr{W} := V \times Q,$$
$$\mathscr{W}_h^k := V_h^k \times Q_h^k.$$

Define the bilinear form $\mathscr{A}(\cdot,\cdot) : \mathscr{W} \times \mathscr{W} \to \mathbb{R}$ as

$$\mathscr{A}([\mathbf{v}, q], [\mathbf{v}', q']) := a(\mathbf{v}, \mathbf{v}') + b(\mathbf{v}', q) + b(\mathbf{v}, q'),$$

and the linear functional $\mathscr{L}(\cdot) : \mathscr{W} \to \mathbb{R}$ by

$$\mathscr{L}([\mathbf{v}, q]) := G(\mathbf{v}) + F(q).$$

Thereby, the *(continuous) primal problem* can be stated as:

Find $[\mathbf{u}, p] \in \mathscr{W}$ such that

$$\mathscr{A}([\mathbf{u}, p], [\mathbf{v}, q]) = \mathscr{L}([\mathbf{v}, q]) \quad \forall [\mathbf{v}, q] \in \mathscr{W}.$$

The appropriate semi–linear form $\mathcal{N}(\cdot,\cdot) : \mathscr{W} \times \mathscr{W} \to \mathbb{R}$ is thus

$$\mathcal{N}([\mathbf{v}, q], [\mathbf{v}', q']) := \mathscr{A}([\mathbf{v}, q], [\mathbf{v}', q']) - \mathscr{L}([\mathbf{v}', q']),$$

so that the *primal problem* is equivalent to:

Find $[\mathbf{u}, p] \in \mathscr{W}$ such that

$$\mathcal{N}([\mathbf{u}, p], [\mathbf{v}, q]) = 0 \quad \forall [\mathbf{v}, q] \in \mathscr{W}. \tag{6.21}$$

Furthermore, the *discrete primal problem* is:

Find $[\mathbf{u}_h, p_h] \in \mathscr{W}_h^k$ such that

$$\mathcal{N}([\mathbf{u}_h, p_h], [\mathbf{v}_h, q_h]) = 0 \quad \forall [\mathbf{v}_h, q_h] \in \mathscr{W}_h^k. \tag{6.22}$$

For a given QoI functional $Q(\cdot) : \mathscr{W} \to \mathbb{R}$, *adjoint problem I* is to:

Find $[\mathbf{z}, r] \in \mathscr{W}$ such that

$$\mathscr{A}([\mathbf{v}, q], [\mathbf{z}, r]) = \overline{Q}([\mathbf{u}, p], [\mathbf{u}_h, p_h]; [\mathbf{v}, q]) \quad \forall [\mathbf{v}, q] \in \mathscr{W}. \tag{6.23}$$

The adjoint solutions $[\mathbf{z}, r]$ to (6.23) will be referred to as being the adjoint velocity and adjoint pressure, respectively.

Subsequently, the *(linearised) adjoint problem II* is to:

Find $[\mathbf{z}_\star, r_\star] \in \mathscr{W}$ such that

$$\mathscr{A}([\mathbf{v}, q], [\mathbf{z}_\star, r_\star]) = Q'[[\mathbf{u}_h, p_h]]([\mathbf{v}, q]) \quad \forall [\mathbf{v}, q] \in \mathscr{W}. \tag{6.24}$$

Moreover, we define the *discrete adjoint problem II* on the same mesh as the *discrete primal problem*, but with an increased polynomial degree of approximation; i.e.,

Find $[\mathbf{z}_h, r_h] \in \mathscr{W}_h^{k+1}$ such that

$$\mathscr{A}([\mathbf{v}_h, q_h], [\mathbf{z}_h, r_h]) = Q'[[\mathbf{u}_h, p_h]]([\mathbf{v}_h, q_h]) \quad \forall [\mathbf{v}_h, q_h] \in \mathscr{W}_h^{k+1}. \tag{6.25}$$

For ease of language we will refer to the solutions $[\mathbf{z}_h, r_h]$ as being the discrete adjoint velocity and discrete adjoint pressure, respectively, although they are technically the discrete approximations to the solutions of *adjoint problem II*. With these problems in mind, applying Theorem 6.3 and looking again at the decomposition of the residual term, we arrive with ease at the *computable error estimate* for Darcy's equations, for a generic QoI $Q([\mathbf{u}, p])$:

$$Q([\mathbf{u}, p]) - Q([\mathbf{u}_h, p_h]) \approx \mathscr{R}([\mathbf{u}_h, p_h], [\mathbf{z}_h - \mathbf{z}_I, r_h - r_I]) \tag{6.26}$$

$$= \mathscr{L}([\mathbf{z}_h - \mathbf{z}_I, r_h - r_I] - \mathscr{A}([\mathbf{u}_h, p_h], [\mathbf{z}_h - \mathbf{z}_I, r_h - r_I]). \tag{6.27}$$

Again, (cf. Section 6.1) $\mathbf{z}_I$ and r_I are typically chosen to be projections of the discrete linearised adjoint solutions $\mathbf{z}_h$ and r_h, respectively, so that the double rate of convergence in the error of the QoI is retained when defining elementwise error indicators, defined next as part of Section 6.3.

6.3 Decomposition of the computable error estimate

In this section, we decompose the computable error estimate (6.27) into element–based indicators on the mesh $\mathscr{T}_h$, based on the usual, integration–by–parts approach[4], this decomposition and subsequent indicator description is taken from [73].

To this end, writing the right–hand–side of (6.27) as a sum over the mesh $\mathscr{T}_h$, we get

$$\begin{aligned} Q([\mathbf{u}, p]) - Q([\mathbf{u}_h, p_h]) \approx \sum_{\kappa \in \mathscr{T}_h} \Big(& - \langle (\mathbf{z}_h - \mathbf{z}_I) \cdot \mathbf{n}_\kappa, g_D \rangle_{\partial\kappa \cap \partial\Omega^D} - \int_\kappa (r_h - r_I) f \\ & - \int_\kappa \mathbf{K}^{-1} \mathbf{u}_h \cdot (\mathbf{z}_h - \mathbf{z}_I) + \int_\kappa p_h \nabla \cdot (\mathbf{z}_h - \mathbf{z}_I) + \int_\kappa (r_h - r_I) \nabla \cdot \mathbf{u}_h \Big), \end{aligned} \tag{6.28}$$

[4] A technique commonly used and similar to the standard integration–by–parts decomposition employed for Poisson's equation, see [86, pp. 105–107] for example.

where $\mathbf{n}_\kappa$ denotes the unit outward normal vector to element $\kappa \in \mathscr{T}_h$. Employing the Green's formula stated in Proposition 2.3, we see that in particular

$$\int_\kappa p_h \nabla \cdot (\mathbf{z}_h - \mathbf{z}_I) = -\int_\kappa (\mathbf{z}_h - \mathbf{z}_I) \cdot \nabla p_h + \langle (\mathbf{z}_h - \mathbf{z}_I) \cdot \mathbf{n}_\kappa, p_h \rangle_{\partial\kappa}.$$

Therefore, summing over the elements in the mesh, gives

$$\sum_{\kappa \in \mathscr{T}_h} \int_\kappa p_h \nabla \cdot (\mathbf{z}_h - \mathbf{z}_I) = \sum_{\kappa \in \mathscr{T}_h} \Big(-\int_\kappa (\mathbf{z}_h - \mathbf{z}_I) \cdot \nabla p_h + \frac{1}{2} \langle (\mathbf{z}_h - \mathbf{z}_I) \cdot \mathbf{n}_\kappa, [\![p_h]\!] \rangle_{\partial\kappa \setminus \partial\Omega} + \langle (\mathbf{z}_h - \mathbf{z}_I) \cdot \mathbf{n}_\kappa, p_h \rangle_{\partial\kappa \cap \partial\Omega^D} \Big), \tag{6.29}$$

where $[\![\cdot]\!]$ denotes the jump operator across an element face. Inserting (6.29) into (6.28) gives the following result.

Theorem 6.4. *Under the foregoing notation, we have the (approximate) a posteriori error estimate*

$$|Q([\mathbf{u}, p]) - Q([\mathbf{u}_h, p_h])| \approx \Big| \sum_{\kappa \in \mathscr{T}_h} \eta_\kappa \Big| \leq \sum_{\kappa \in \mathscr{T}_h} |\eta_\kappa|$$

where the element indicator η_κ is split into the four contributions

$$\eta_\kappa \equiv \eta_\kappa^{BC} + \eta_\kappa^{DL} + \eta_\kappa^{CM} + \eta_\kappa^{PR},$$

each given by:

$$\eta_\kappa^{BC} = \langle (\mathbf{z}_h - \mathbf{z}_I) \cdot \mathbf{n}_\kappa, p_h - g_D \rangle_{\partial\kappa \cap \partial\Omega^D}, \tag{6.30}$$

$$\eta_\kappa^{DL} = -\int_\kappa (\mathbf{K}^{-1} \mathbf{u}_h + \nabla p_h) \cdot (\mathbf{z}_h - \mathbf{z}_I), \tag{6.31}$$

$$\eta_\kappa^{CM} = \int_\kappa (r_h - r_I)(\nabla \cdot \mathbf{u}_h - f), \tag{6.32}$$

$$\eta_\kappa^{PR} = \frac{1}{2} \langle (\mathbf{z}_h - \mathbf{z}_I) \cdot \mathbf{n}_\kappa, [\![p_h]\!] \rangle_{\partial\kappa \setminus \partial\Omega}. \tag{6.33}$$

Each of the indicator contributions (6.30)–(6.33) is *adjoint–weighted* and may be interpreted as the following: η_κ^{BC} measures how well the boundary condition (3.3) is satisfied; η_κ^{DL} measures how well Darcy's Law (3.1) is satisfied; η_κ^{CM} measures how well the conservation of mass equation (3.2) is satisfied; and finally, η_κ^{PR} is a measure of the interior pressure residual across element interfaces.

To conclude this section we briefly discuss a triviality which occurs when a lowest–order approximation is used for the discrete problem (6.22). Here, the discrete pressure p_h is a piecewise–constant function on the elements in the mesh. Therefore, wherever the jump term $[\![p_h]\!]$ appears (which is in the contribution $\eta_\kappa^{\mathrm{PR}}$), it is piecewise–constant per element, on its edges. If $\mathbf{z}_I$ is selected as being $\Pi_h \mathbf{z}_h$, with the interpolation operator defined by

(3.13), then we have

$$\frac{1}{2}\langle(\mathbf{z}_h - \Pi_h\mathbf{z}_h)\cdot\mathbf{n}_\kappa, [\![p_h]\!]\rangle_{\partial\kappa\setminus\partial\Omega} \equiv \frac{1}{2}\int_{\partial\kappa\setminus\partial\Omega}(\mathbf{z}_h - \rho_\kappa\mathbf{z}_h)\cdot\mathbf{n}_\kappa[\![p_h]\!] = 0,$$

since the boundary integral is computed as sum of internal edge integrals, and recalling the definition of ρ_κ in either Definition 3.13 or Definition 3.14. The same behaviour occurs within the contribution η_κ^{BC}, here we see that

$$\langle(\mathbf{z}_h - \Pi_h\mathbf{z}_h)\cdot\mathbf{n}, p_h\rangle_{\partial\kappa\cap\partial\Omega} \equiv \int_{\partial\kappa\cap\partial\Omega}(\mathbf{z}_h - \rho_\kappa\mathbf{z}_h)\cdot\mathbf{n}p_h = 0. \tag{6.34}$$

This tells us is that $\eta_\kappa^{\mathrm{PR}} = 0$ for all $\kappa \in \mathscr{T}_h$; furthermore, combined with (6.34), this shows that the element–based indicators defined in Theorem 6.4 are precisely the same as those appearing in (6.28) where the integrals over the domain are simply taken over the elements instead, and no integration–by–parts has taken place.

6.4 Alternative decompositions

As a brief aside, while not being implemented in the work of this thesis, here we discuss a couple of interesting, alternative choices for decomposing the error estimate (6.27). Indeed, the integration–by–parts approach presented in Theorem 6.4 is not the only way to decompose the residual; different definitions for the indicators η_κ may have different properties relating to sharpness and the optimality of adaptive mesh refinement. The two approaches below were investigated when trying to seek indicators that are sharp under an RT implementation. A simple variational approach defines different indicators than those presented before, however in practice the same problems were encountered concerning sharpness for RT velocity approximations. The second approach utilises a partition of unity (PU) and here the defined indicators can be proven sharp under a BDM implementation, the implementation of these was not carried out during this research due to the apparent added complexity compared to those defined under the integration–by–parts approach; it is still unclear how these would behave under an RT approximation.

6.4.1 A simple variational localisation

The first, of two, alternative decompositions we consider is obtained easily exploiting the fact that, in practice, the approximate solutions $(\mathbf{z}_h, r_h)$, obtained via (6.25), are found in the space $\mathscr{W}_h^{k+1}$. Thereby, the discrete adjoint solutions employed in the error estimate are defined on the same mesh as the discrete primal solution, but with a higher polynomial degree. Using hierarchical bases to build the space $\mathscr{W}_h^{k+1}$ allows for the following construction of element–based indicators.

Indeed, since $[\mathbf{z}_h, r_h] \in \mathscr{W}_h^{k+1}$, there are coefficients z_i and r_i such that

$$\mathbf{z}_\star \equiv \sum_{i=1}^{N} z_i \mathbf{w}_i, \qquad r_\star \equiv \sum_{j=1}^{M} r_j \varphi_j,$$

where $\mathbf{w}_i$ and φ_i are basis functions spanning V_h^{k+1} and Q_h^{k+1}, respectively. We see that

$$\begin{aligned} Q([\mathbf{u}, p]) - Q([\mathbf{u}_h, p_h]) &\approx \mathscr{L}([\mathbf{z}_h, r_h]) - \mathscr{A}([\mathbf{u}_h, p_h], [\mathbf{z}_h, r_h]) \\ &= G(\mathbf{z}_h) + F(r_h) - a(\mathbf{u}_h, \mathbf{z}_h) - b(\mathbf{u}_h, r_h) - b(\mathbf{z}_h, p_h) \\ &= \sum_{i=1}^{N} z_i (G(\mathbf{w}_i) - a(\mathbf{u}_h, \mathbf{w}_i) - b(\mathbf{w}_i, p_h)) + \sum_{j=1}^{M} r_j (F(\varphi_j) - b(\mathbf{u}_h, \varphi_j)). \end{aligned}$$

We first define indicators that are associated to each of the basis functions, given by

$$\eta_i^z := z_i (G(\mathbf{w}_i) - a(\mathbf{u}_h, \mathbf{w}_i) - b(\mathbf{w}_i, p_h)),$$

and

$$\eta_j^r := r_j (F(\varphi_j) - b(\mathbf{u}_h, \varphi_j)),$$

which allows us to write

$$Q([\mathbf{u}, p]) - Q([\mathbf{u}_h, p_h]) \approx \sum_{i=1}^{N} \eta_i^z + \sum_{j=1}^{M} \eta_j^r.$$

If we re–index via

$$\overline{\eta}_i := \begin{cases} \eta_i^z & i = 1, 2, \ldots N, \\ \eta_{i-N}^r & i = N+1, \ldots N+M, \end{cases}$$

then we can write more simply the decomposition of the error estimate (6.27) as

$$Q([\mathbf{u}, p]) - Q([\mathbf{u}_h, p_h]) \approx \sum_{i=1}^{N+M} \overline{\eta}_i.$$

We could choose to stop here: when considering element marking for adaptive refinement, the indicators $\overline{\eta}_i$ chosen then correspond to a particular basis function in the space $\mathscr{W}_h^{k+1}$; those elements occupying the support of the selected basis functions are those selected for refinement.

Alternatively, we could instead redistribute the basis–dependent indicators among the elements in the mesh. This is achieved, for example, by defining for $\kappa \in \mathscr{T}_h$

$$\eta_\kappa := \sum_{i \in I} \frac{\overline{\eta}_i}{c_{i,\kappa}},$$

where I is the index set of basis functions having support on element κ. The constant $c_{i,\kappa}$ serves to distribute $\overline{\eta}_i$ across the elements intersecting the support of its corresponding basis function. For example, if $\overline{\eta}_i$ is the indicator for a basis function with two elements

intersecting its support (those sharing the edge it is associated to, for example), then $c_{i,\kappa} = 2$. These element–based indicators[5] are used as usual in terms of marking and refining since

$$Q([\mathbf{u}, p]) - Q([\mathbf{u}_h, p_h]) \approx \sum_{\kappa \in \mathscr{T}_h} \eta_\kappa.$$

6.4.2 A partition of unity decomposition

Decomposition by a partition of unity is a more well studied type of decomposition, particularly by the authors Wick et al. in, for example, [116, 131]. Here, instead of the basis–dependent indicators being defined by the discrete adjoint solutions $(\mathbf{z}_h, r_h)$, they are defined by a partition of unity (PU). Usually using the standard continuous, linear, hat functions, consider the partition of unity

$$1 = \sum_i \varphi_i,$$

such that $\|\nabla \varphi_i\|_{L^\infty(\Omega)} = \mathcal{O}(h^{-1})$ as $h \to 0$.

Going back to the full, *noncomputable* error representation formula[6], given by

$$\begin{aligned} Q([\mathbf{u}, p]) - Q([\mathbf{u}_h, p_h]) = &- \langle (\mathbf{z} - \mathbf{z}_I) \cdot \mathbf{n}, g \rangle_{\partial\Omega} - \int_\Omega \mathbf{K}^{-1} \mathbf{u}_h \cdot (\mathbf{z} - \mathbf{z}_I) \\ &+ \int_\Omega p_h \nabla \cdot (\mathbf{z} - \mathbf{z}_I) - \int_\Omega f(r - r_I) + \int_\Omega (r - r_I) \nabla \cdot \mathbf{u}_h, \end{aligned}$$

we define the PU indicator $\hat{\eta}_i$ by

$$\hat{\eta}_i := - \langle \varphi_i (\mathbf{z} - \mathbf{z}_I) \cdot \mathbf{n}, g \rangle_{\partial\Omega} - \int_\Omega \mathbf{K}^{-1} \mathbf{u}_h \cdot \varphi_i (\mathbf{z} - \mathbf{z}_I) \tag{6.35}$$

$$+ \int_\Omega p_h \nabla \cdot (\varphi_i (\mathbf{z} - \mathbf{z}_I)) - \int_\Omega f \varphi_i (r - r_I) + \int_\Omega \varphi_i (r - r_I) \nabla \cdot \mathbf{u}_h. \tag{6.36}$$

Clearly,

$$Q([\mathbf{u}, p]) - Q([\mathbf{u}_h, p_h]) = \sum_i \hat{\eta}_i,$$

and these indicators can be redistributed among the elements in a similar way to the decomposition presented in Section 6.4.1; that is, split across the elements in the mesh supporting the function φ_i. Moreover, these indicators are indeed sharp when using a BDM_k implementation, when we set $\mathbf{z}_I$ and r_I as the usual projections, or interpolants; this result is presented below as Theorem 6.5.

[5] These indicators were in fact implemented alongside those given by Theorem 6.4; similar results were found in the examples showcased in Section 6.6, especially concerning the sharpness of the indicators under an RT_0 implementation. Furthermore, there is empirical evidence that these indicators are also sharp for a BDM_1 implementation.

[6] Stated as part of Theorem 6.3.

Theorem 6.5. *Suppose* $[\mathbf{u}, p]$ *is the solution of (6.21),* $[\mathbf{u}_h, p_h]$ *is the solution of (6.22), and for a given QoI with functional* $Q(\cdot) : \mathscr{W} \to \mathbb{R}$, $[\mathbf{z}, r]$ *is the solution of (6.23). Assume the solutions* $[\mathbf{u}, p]$ *and* $[\mathbf{z}, r]$ *are smooth enough so that they achieve the optimal bounds in Theorem 3.21, Proposition 3.17, and Proposition 3.18. Then, there is a constant* $C = C(\mathbf{u}, \nabla \cdot \mathbf{u}, \mathbf{z}, \nabla \cdot \mathbf{z}, p, r)$ *such that*

$$\sum_i |\hat{\eta}_i| \leq Ch^{2k},$$

with the PU indicators $\hat{\eta}_i$ *defined by (6.35, 6.36) and* $\mathbf{z}_I = \Pi_h \mathbf{z}$, $r_I = P_h r$.

Proof. Since, for all i, we have $\varphi_i(\mathbf{z} - \mathbf{z}_I) \in H_{0,N}(\mathrm{div}, \Omega)$, then (3.8) tells us that

$$-\langle \varphi_i(\mathbf{z} - \mathbf{z}_I) \cdot \mathbf{n}, g \rangle_{\partial\Omega} = \int_\Omega \mathbf{K}^{-1}\mathbf{u} \cdot \varphi_i(\mathbf{z} - \mathbf{z}_I) - \int_\Omega p \nabla \cdot (\varphi_i(\mathbf{z} - \mathbf{z}_I)).$$

Thus,

$$\begin{aligned}\hat{\eta}_i = &- \int_\Omega (p - p_h)\nabla \cdot (\varphi_i(\mathbf{z} - \mathbf{z}_I)) + \int_\Omega \mathbf{K}^{-1}(\mathbf{u} - \mathbf{u}_h) \cdot \varphi_i(\mathbf{z} - \mathbf{z}_I) \\ &- \int_\Omega f\varphi_i(r - r_I) + \int_\Omega \varphi_i(r - r_I)\nabla \cdot \mathbf{u}_h.\end{aligned}$$

Furthermore, since for all i, we have $\varphi_i(r - r_I) \in L^2(\Omega)$ then

$$-\int_\Omega f\varphi_i(r - r_I) = -\int_\Omega \varphi_i(r - r_I)\nabla \cdot \mathbf{u}.$$

This tells us that

$$\hat{\eta}_i = -\int_\Omega (p - p_h)\nabla \cdot (\varphi_i(\mathbf{z} - \mathbf{z}_I)) + \int_\Omega \mathbf{K}^{-1}(\mathbf{u} - \mathbf{u}_h) \cdot \varphi_i(\mathbf{z} - \mathbf{z}_I) - \int_\Omega \varphi_i(r - r_I)\nabla \cdot (\mathbf{u} - \mathbf{u}_h).$$

Next, since we have the following product rule for divergence

$$\nabla \cdot (\varphi_i(\mathbf{z} - \mathbf{z}_I)) = \nabla\varphi_i \cdot (\mathbf{z} - \mathbf{z}_I) + \varphi_i \nabla \cdot (\mathbf{z} - \mathbf{z}_I),$$

we know that

$$\hat{\eta}_i = -\int_\Omega (p - p_h)\varphi_i \nabla \cdot (\mathbf{z} - \mathbf{z}_I) - \int_\Omega (p - p_h)\nabla\varphi_i \cdot (\mathbf{z} - \mathbf{z}_I) \tag{6.37}$$

$$+ \int_\Omega \mathbf{K}^{-1}(\mathbf{u} - \mathbf{u}_h) \cdot \varphi_i(\mathbf{z} - \mathbf{z}_I) - \int_\Omega \varphi_i(r - r_I)\nabla \cdot (\mathbf{u} - \mathbf{u}_h). \tag{6.38}$$

The integrals over Ω in (6.37, 6.38) can instead be replaced with the patch of elements $\mathrm{supp}(\varphi_i) \subset P_i = \cup\kappa$. By applying the triangle inequality, and pulling out the supremums of the functions φ_i and $\nabla\varphi_i$, we see that

$$|\hat{\eta}_i| \leq \|\varphi_i\|_{L^\infty(P_i)}\|p - p_h\|_{L^2(P_i)}\|\nabla \cdot (\mathbf{z} - \mathbf{z}_I)\|_{L^2(P_i)} \tag{6.39}$$

$$+ \|\nabla\varphi_i\|_{L^\infty(P_i)}\|p - p_h\|_{L^2(P_i)}\|\mathbf{z} - \mathbf{z}_I\|_{[L^2(P_i)]^2} \tag{6.40}$$

$$+ \frac{1}{\lambda_-}\|\varphi_i\|_{L^\infty(P_i)}\|\mathbf{u} - \mathbf{u}_h\|_{[L^2(P_i)]^2}\|\mathbf{z} - \mathbf{z}_I\|_{[L^2(P_i)]^2} \tag{6.41}$$

$$+ \|\varphi_i\|_{L^\infty(P_i)}\|\nabla \cdot (\mathbf{u} - \mathbf{u}_h)\|_{L^2(P_i)}\|r - r_I\|_{L^2(P_i)}, \tag{6.42}$$

where, in particular, the term (6.41) follows by the triangle inequality paired with the condition (3.5).

The result is readily seen, noting that $\|\varphi\|_{L^2(P_i)} = \mathcal{O}(1)$, $\|\nabla\varphi\|_{L^2(P_i)} = \mathcal{O}(h^{-1})$ and by application of the bounds from Theorem 3.21, Proposition 3.17, and Proposition 3.18. □

Although we have a proof of sharpness for these indicators, their implementation is slightly more tricky than those used in Theorem 6.4, which (cf. Section 6.6) already show evidence of being sharp, and so are not implemented within this work. A PU application, and proof of sharpness, under a Raviart–Thomas approximation requires further research.

6.5 Convergence of quantities of interest

Before looking at some numerical examples in Section 6.6, we should address the convergence of the approximation of the quantity of interest. This section aims to provide at least a sufficient condition, under uniform mesh refinement, for us to see

$$Q([\mathbf{u}, p]) - Q([\mathbf{u}_h, p_h]) \to 0$$

given that the finite element approximations $\mathbf{u}_h$ and p_h converge[7]. Such a proof of convergence is readily achieved by starting from (6.5), and applying the convergence results from Theorem 3.21, Proposition 3.17, and Proposition 3.18. This *a priori* convergence result is presented below as Theorem 6.6.

Theorem 6.6. *Under the notation of Section 6.2, suppose* $[\mathbf{u}, p]$ *is the solution of (6.21),* $[\mathbf{u}_h, p_h]$ *is the solution of (6.22), and for a given QoI with functional* $Q(\cdot) : \mathscr{W} \to \mathbb{R}$, $[\mathbf{z}, r]$ *is the solution of (6.23). Assume the solutions* $[\mathbf{u}, p]$ *and* $[\mathbf{z}, r]$ *are smooth enough to achieve the optimal bounds in Theorem 3.21, Proposition 3.17, and Proposition 3.18. Then, there exists a constant* $C = C(\mathbf{u}, \nabla\cdot\mathbf{u}, \mathbf{z}, \nabla\cdot\mathbf{z}, p, r)$, *independent of* h, *such that*

$$|Q([\mathbf{u}, p]) - Q([\mathbf{u}_h, p_h])| \leq Ch^{2\varphi(k)},$$

where $\varphi(k) = k$ *if* $\mathcal{M}_k(\kappa) = BDM_k$ *in* V_h, *and* $\varphi(k) = k+1$ *if* $\mathcal{M}_k(\kappa) = RT_k$ *in* V_h.

Proof. We begin by applying (6.5) with the appropriate notations for this context, and by setting $\mathbf{z}_I = \Pi_h\mathbf{z}$ and $r_I = P_h r$, where the interpolants are as they appear in Proposition

[7] To the exact solutions $\mathbf{u} \in \mathbf{V}$ and $p \in Q$ measured in their respective norms.

3.17 and Proposition 3.18, respectively. Here, we see that

$$\begin{aligned} Q([\mathbf{u},p]) - Q([\mathbf{u}_h,p_h]) &= \overline{Q}([\mathbf{u},p],[\mathbf{u}_h,p_h];[\mathbf{u}-\mathbf{u}_h,p-p_h]) \\ &= \mathscr{M}([\mathbf{u},p],[\mathbf{u}_h,p_h];[\mathbf{u}-\mathbf{u}_h,p-p_h],[\mathbf{z}-\Pi_h\mathbf{z},r-P_hr]) \\ &= \mathscr{A}([\mathbf{u}-\mathbf{u}_h,p-p_h],[\mathbf{z}-\Pi_h\mathbf{z},r-P_hr]). \end{aligned}$$

Therefore, since the bilinear form $a(\cdot,\cdot)$ is continuous on $[H(\mathrm{div},\Omega)]^2$ and since the bilinear form $b(\cdot,\cdot)$ is continuous on $H(\mathrm{div},\Omega)\times L^2(\Omega)$, there are constants $\|a\| =: c_a > 0$ and $\|b\| =: c_b > 0$ such that

$$\begin{aligned} |Q([\mathbf{u},p]) - Q([\mathbf{u}_h,p_h])| &= |\mathscr{A}([\mathbf{u}-\mathbf{u}_h,p-p_h],[\mathbf{z}-\Pi_h\mathbf{z},r-P_hr])| \\ &= |a(\mathbf{u}-\mathbf{u}_h,\mathbf{z}-\Pi_h\mathbf{z}) + b(\mathbf{u}-\mathbf{u}_h,r-P_hr) + b(\mathbf{z}-\Pi_h\mathbf{z},p-p_h)| \\ &\le |a(\mathbf{u}-\mathbf{u}_h,\mathbf{z}-\Pi_h\mathbf{z})| + |b(\mathbf{u}-\mathbf{u}_h,r-P_hr)| \\ &+ |b(\mathbf{z}-\Pi_h\mathbf{z},p-p_h)| \\ &\le c_a\|\mathbf{u}-\mathbf{u}_h\|_{H(\mathrm{div},\Omega)}\|\mathbf{z}-\Pi_h\mathbf{z}\|_{H(\mathrm{div},\Omega)} \\ &+ c_b\|\mathbf{u}-\mathbf{u}_h\|_{H(\mathrm{div},\Omega)}\|r-P_hr\|_{L^2(\Omega)} \\ &+ c_b\|\mathbf{z}-\Pi_h\mathbf{z}\|_{H(\mathrm{div},\Omega)}\|p-p_h\|_{L^2(\Omega)}. \end{aligned}$$

The result follows immediately applying the *a priori* estimates: Theorem 3.21, Proposition 3.17, and Proposition 3.18. □

6.6 Numerical experiments

Before we begin this section we address some nomenclature: by referring to either a BDM_1 or RT_0 implementation we mean that in the definition of the spaces (6.19) and (6.20), we set $\mathcal{M}_k(\kappa) = BDM_1(\kappa)$ or $RT_0(\kappa)$. In either case we have $D_k(\kappa) = \mathbb{P}_0(\kappa)$ and the approximation space Q_h^k has piecewise–constant functions.

Moving forward, we investigate the performance of an adaptive regime employing the local error indicators defined in Theorem 6.4, for a couple of quantities of interest that are described by linear functionals. The first example highlights an intriguing empirical observation: that is, the indicators are not sharp when an RT_0 implementation is used. The second experiment looks at an irregular primal solution on an L–shaped domain; here we witness superconvergence in the (QoI) error when a BDM_1 implementation is used. The obtained results are compared with an RT_0 implementation. In each case the quantity of interest only depends on the pressure, p.

The adaptive regime is based on the loop

$$\texttt{SOLVE} \to \texttt{ESTIMATE} \to \texttt{MARK} \to \texttt{REFINE} \to \texttt{SOLVE} \to \ldots$$

There exist a variety of different marking strategies that can used to select suitable elements for refinement. Here, we employ a marking strategy of Dörfler–type[8]. That is, a *refinement parameter* $\omega \in (0,1)$ is selected, by the user, and a minimal set of elements $\mathscr{T}' \subset \mathscr{T}_h$ are marked, such that

$$\sum_{\kappa' \in \mathscr{T}'} |\eta_{\kappa'}| \geq \omega \sum_{\kappa \in \mathscr{T}_h} |\eta_\kappa| \equiv \omega \mathcal{S}. \tag{6.43}$$

The strategy (6.43) reiterates the need for *sharp* indicators: it is indeed the bounded sum $\mathcal{S}$ that is used to select elements for refinement.

In the interpretation of the obtained results, and often throughout this section, we will refer to rates of convergence as being optimal, or not. For uniform mesh refinement we refer to Theorem 6.6 in which, since the *a priori* error bounds, and interpolation error bounds, are each optimal, has the optimal rate of convergence for the error in the approximate QoI. Applying Theorem 6.6 for a BDM_1 or RT_0 implementation means that if the error in the QoI is $\mathcal{O}(h^2)$ as $h \to 0$, then this convergence is indeed optimal.

Of course, it does not make sense to talk about the mesh parameter h on an adaptively refined mesh. With $\mathfrak{N}$ denoting the number of degrees of freedom in the primal discrete spaces (that is, the dimension of the space $\mathscr{W}_h^k$ in (6.22)), in two dimensions, we know that $\mathfrak{N}^{-1} \sim h^2$ on quasi-uniform meshes [123, pp. 31–34]. This means that for an RT_k implementation, the optimal rate of convergence, for the error in the QoI, using adaptively refined meshes is $\mathcal{O}(\mathfrak{N}^{-(k+1)})$, while for a BDM_k implementation the optimal rate is $\mathcal{O}(\mathfrak{N}^{-k})$. Therefore, when looking at the subsequent loglog plots for the errors involved in the upcoming experiments, we plot $\mathfrak{N}$ on the x–axis; a line of slope -1 will therefore show the optimal rate for uniform and adaptive refinements, of the error in the QoI, under both an RT_0 and BDM_1 implementation.

6.6.1 Experiment I: Sharpness of indicators

In this first experiment we set $\Omega = (0,1)^2$ to be the unit square, and let the entire boundary be made up of the Dirichlet part, i.e., $\partial\Omega = \partial\Omega^D$ and $\partial\Omega^N = \emptyset$. By setting $f = 2\pi^2 \sin(\pi x)\sin(\pi y)$, $g_D = 0$ and $K = \mathbb{I}_2$ in (3.8, 3.9), one obtains the solution

$$p = \sin(\pi x)\sin(\pi y),$$

[8]Introduced by Dörfler in [49], this marking strategy can be used in proving theoretical results for the convergence of adaptive methods; see [37], for example.

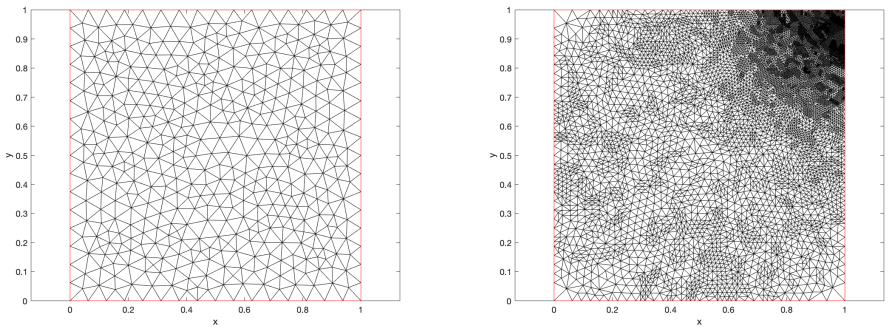

FIG. 6.1 – *Initial and final adaptive meshes using a BDM_1 implementation.*

with associated Darcy velocity $\mathbf{u} = -\nabla p$. Here, we consider the quantity of interest

$$Q([\mathbf{u}, p]) := \int_\Omega x^{10} y^{10} p = \frac{(-7257600 + 1814400\pi^2 - 151200\pi^4 + 5040\pi^6 - 90\pi^8 + \pi^{10})^2}{\pi^{22}}$$
$$\approx 0.000508986\ldots$$

The primal solutions $(\mathbf{u}, p)$ are clearly very smooth, therefore we should not expect adaptive refinement to give approximations that outperform uniform refinement. Despite this, we expect to see adaptive refinement in the top right corner of the domain, due to the adjoint weighting.

As well as testing the indicators for sharpness via the *bounded effectivity index* (6.17), we would like to test the effectiveness of the proposed *a posteriori* error estimator; i.e., gain insight into the extent in which the computable error representation (6.27) approximates the true goal error. For this, we look at the *effectivity index*

$$\theta_h := \frac{\sum_\kappa \eta_\kappa}{Q([\mathbf{u}, p]) - Q([\mathbf{u}_h, p_h])}. \tag{6.44}$$

Indeed, if effectivity indices of 1 are witnessed then (6.27) can be deemed a reliable estimator.

In this experiment, a Dörfler marking parameter of $\omega = 1/3$ is chosen. Table 6.1 shows the results under a uniform refinement for a BDM_1 implementation: we see effectivity indices close to 1 on all meshes, showing that (6.27) is reliably predicting the size of the error; we can also see from the same table that the bounded effectivity indices look to converge to some constant, showing evidence that the indicators are sharp under uniform mesh refinement. Moreover, under adaptive mesh refinement we witness the same behaviour, as concurred by Table 6.2.

Furthermore, this example shows that the adaptive algorithm outperforms uniform mesh refinements. However, a quick glance at the loglog plots in Figure 6.2 reveals that the error, under uniform and adaptive refinements, eventually looks to converge with the same, optimal

TABLE 6.1 – *Results obtained under uniform refinement using a BDM_1 implementation.*

Number of DOF	**Error**	**Est. Error**	$\mathcal{S}$	θ_h	$\theta_{\geq}$
3552	1.7140×10^{-5}	1.7236×10^{-5}	1.8163×10^{-5}	1.0056	1.0596
14080	4.2854×10^{-6}	4.2913×10^{-5}	4.5240×10^{-6}	1.0014	1.0557
56064	1.0715×10^{-6}	1.0718×10^{-6}	1.1300×10^{-6}	1.0003	1.0547

TABLE 6.2 – *Results obtained under adaptive refinement using a BDM_1 implementation.*

Number of DOF	**Error**	**Est. Error**	$\mathcal{S}$	θ_h	$\theta_{\geq}$
3552	1.7140×10^{-5}	1.7236×10^{-5}	1.8163×10^{-5}	1.0056	1.0596
3697	1.0871×10^{-5}	1.0903×10^{-6}	1.1829×10^{-5}	1.0029	1.0882
4028	6.6938×10^{-6}	6.7021×10^{-6}	7.6420×10^{-6}	1.0012	1.1416
4823	3.5798×10^{-6}	3.5828×10^{-6}	4.5373×10^{-6}	1.0008	1.2675
6252	1.9656×10^{-6}	1.9667×10^{-6}	2.9207×10^{-6}	1.0004	1.4856
8714	1.0316×10^{-6}	1.0319×10^{-6}	1.9546×10^{-6}	1.0003	1.8947
12856	6.1087×10^{-7}	6.1108×10^{-7}	1.3447×10^{-6}	1.0004	2.2013
19723	3.6458×10^{-7}	3.6469×10^{-7}	9.1105×10^{-7}	1.0003	2.4989
29833	2.8492×10^{-7}	2.8496×10^{-7}	6.0713×10^{-7}	1.0002	2.1309
44717	1.7964×10^{-7}	1.7967×10^{-7}	4.1597×10^{-7}	1.0001	2.3155
68226	1.1671×10^{-7}	1.1673×10^{-7}	2.8178×10^{-7}	1.0001	2.4143

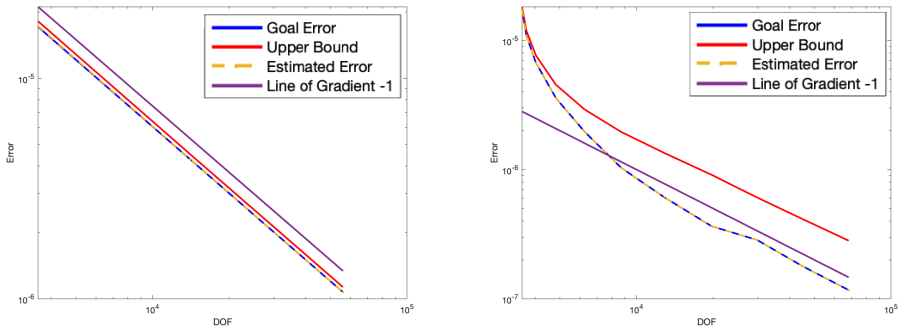

FIG. 6.2 – *Loglog plots for BDM_1: left has uniform refinement; right has adaptive refinement.*

rate: $\mathcal{O}(h^2)$ or $\mathcal{O}(\mathfrak{N}^{-1})$. The results for adaptive refinement could be pre–asymptotic; that is, under further refinement we might expect to see a continuation of the optimal rate of convergence.

However, different behaviour is witnessed when an RT_0 implementation is used instead. While we still seem to have a convergent algorithm for the adaptive regime, the loglog plots in Figure 6.3, as well as the data in Tables 6.3 and 6.4, reveal a very obvious lack of sharpness for the indicators, under both uniform and adaptive refinement; here a blow–up

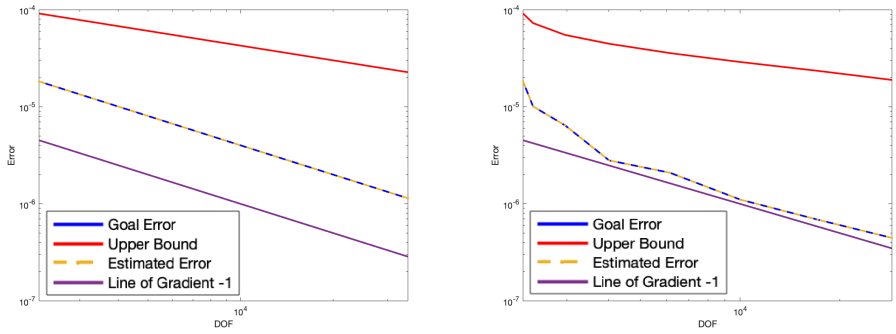

FIG. 6.3 – *Loglog plots for RT_0: left has uniform refinement; right has adaptive refinement.*

TABLE 6.3 – *Effectivity indices obtained under uniform refinement using an RT_0 implementation.*

Number of DOF	θ_h	$\theta_{\geq}$
2212	1.0050	5.0338
8784	1.0013	9.9951
35008	1.0003	19.925

TABLE 6.4 – *Effectivity indices obtained under adaptive refinement using an RT_0 implementation.*

Number of DOF	θ_h	$\theta_{\geq}$
2212	1.0050	5.0338
2371	1.0016	7.2314
2961	1.0006	8.5513
4024	1.0004	15.9371
6149	1.0001	17.1098
10012	1.0001	26.1620
17140	1.0001	34.1628
28754	1.0000	42.4481

in the bounded effectivity indices is witnessed since the rate of convergence of the bounded sum $\mathcal{S}$ (labelled as the upper bound) is no longer matching the rate of convergence witnessed for the error itself. However, we still see effectivity indices close to 1 on all of the employed meshes, and therefore the error estimate (6.27) is still a reliable error estimator in this example.

We re–iterate that if the user were to use the bounded sum $\mathcal{S}$, even in this example, as the stopping criterion in the program utilising this adaptive regime, then the entire process will have to run for a much longer time under an RT_0 implementation, compared with BDM_1, since here $\mathcal{S}$ converges at a slower rate.

A proposed conjecture for the lack of sharpness for an RT_0 implementation, using the indicators in Theorem 6.4, is that the resulting velocity space V_h^k in (6.19) is not a complete polynomial space[9]. In a numerical investigation the term

$$\eta_\kappa^{\mathrm{DL}} = -\int_\kappa (K^{-1}\mathbf{u}_h + \nabla p_h)\cdot(\mathbf{z}_h - \rho_\kappa \mathbf{z}_h)$$

seems to be the issue. Applying the Cauchy–Schwarz inequality we see that

$$\mathcal{S} = \sum_\kappa |\eta_\kappa| \leq \sum_\kappa \Big| \int_\kappa (K^{-1}\mathbf{u}_h + \nabla p_h)\cdot(\mathbf{z}_h - \rho_\kappa \mathbf{z}_h)\Big| + \sum_\kappa \Big|\eta_\kappa^{\mathrm{PR}} + \eta_\kappa^{\mathrm{CM}} + \eta_\kappa^{\mathrm{BC}}\Big|.$$

The latter term converges like $\mathcal{O}(h^2)$, while

$$\sum_\kappa \Big| \int_\kappa (K^{-1}\mathbf{u}_h + \nabla p_h)\cdot(\mathbf{z}_h - \rho_\kappa \mathbf{z}_h)\Big| \leq \|\mathbf{z}_h - \Pi \mathbf{z}_h\|_{[L^2(\Omega)]} \sqrt{\sum_\kappa \|K^{-1}\mathbf{u}_h + \nabla p_h\|^2_{L^2(\kappa)}} = \mathcal{O}(h),$$

and this was concurred by the obtained numerics[10].

This lower rate of convergence seems to pollute the bounded sum $\mathcal{S}$, and we witnessed $\mathcal{S} = \mathcal{O}(h)$ as well. The investigation further revealed that the indicators η_κ are often similar in size but of opposite sign: i.e., there is significant cancellation happening in the error estimate $\sum_\kappa \eta_\kappa$, so when we look at $\mathcal{S}$, those terms that originally cancel no longer do, resulting in a loss of rate of convergence. A similar phenomenon occurs in [101, p. 142] where here, the authors witness large cancellations in their error estimate.

6.6.2 Experiment II: Superconvergence in an L–shaped domain

In this second experiment, the irregular primal solutions $(\mathbf{u}, p)$ and the chosen quantity of interest $Q([\mathbf{u}, p])$ will not be able to induce the optimal rate of convergence for the goal error under uniform mesh refinement. We will see that not only, under adaptive refinement, that the optimal rate is recovered for RT_0 and BDM_1 implementations, but a superconvergence is witnessed in the BDM_1 implementation as well. This superconvergence is not witnessed in the RT_0 implementation, and again we see here a lack of sharpness for the indicators η_κ.

The domain for this problem is given by the L–shaped $\Omega = [-1,1]^2 \setminus [-1,0]$, and the data f and g_D are chosen in (3.8, 3.9) so that, in standard polar coordinates, the pressure solution is given by

$$p = \rho^{2/3}\sin\left(\frac{2(\pi-\theta)}{3}\right), \tag{6.45}$$

with $x = \rho\sin(\theta)$ and $y = \rho\cos(\theta)$. The gradient of p in the radial direction

$$\nabla_{(\rho,\theta)} p \cdot \hat{\rho} = \frac{2}{3\rho^{\frac{1}{3}}}\sin\left(\frac{2(\pi-\theta)}{3}\right)$$

[9] Indeed, this space consists of vector–valued linear functions, but does not have all of the linear functions that we have if a BDM_1 implementation is used instead.

[10] These numerics are not presented in this thesis.

is clearly singular at the origin, where $\rho = 0$; although p is analytic in $\overline{\Omega} \setminus \{\mathbf{0}\}$ we have $p \notin H^2(\Omega)$ [74, p. 20]. Hence, we might expect to witness a goal error convergence which differs from the rate predicted by Theorem 6.6.

The quantity of interest is given by

$$Q([\mathbf{u}, p]) := \frac{1}{|\mathcal{R}|} \int_{\mathcal{R}} p,$$

where $\mathcal{R} \subset \Omega$ is the triangular region pictured in Figure 6.4, and $|\mathcal{R}| = 1/2$ is the area of the region. This QoI represents an integral average of the pressure over the region $\mathcal{R}$. The exact quantity of interest is approximately computed via quadrature on very fine, uniformly refined, meshes until the absolute error between successive approximations is sufficiently small[11].

Before proceeding to the results of this experiment, we recall the error representation (6.15) now decomposed into the two[12] parts:

$$Q([\mathbf{u}, p]) - Q([\mathbf{u}_h, p_h]) = \mathscr{R}([\mathbf{u}_h, p_h], [\mathbf{z} - \mathbf{z}_h, r - r_h]) + \mathscr{R}([\mathbf{u}_h, p_h], [\mathbf{z}_h - \mathbf{z}_I, r_h - r_I]), \quad (6.46)$$

for all $[\mathbf{z}_I, r_I] \in \mathscr{W}_h$. Rearranging (6.46), we see

$$\theta_h = 1 - \frac{\mathscr{R}([\mathbf{u}_h, p_h], [\mathbf{z} - \mathbf{z}_h, r - r_h])}{Q([\mathbf{u}, p]) - Q([\mathbf{u}_h, p_h])}, \quad (6.47)$$

with the effectivity index (6.44) defined in the usual way.

It is clear in (6.47) that if the residual term $\mathscr{R}([\mathbf{u}_h, p_h], [\mathbf{z} - \mathbf{z}_h, r - r_h])$ decays to zero at a rate that is faster than the rate at which the goal error decays, then we should see the effectivity index converge to 1 under mesh refinement; this was true in the first experiment. However, if $\mathscr{R}([\mathbf{u}_h, p_h], [\mathbf{z} - \mathbf{z}_h, r - r_h])$ decays at the same rate as $Q([\mathbf{u}, p]) - Q([\mathbf{u}_h, p_h])$ then the ratio of the terms will converge to some constant $\alpha \in \mathbb{R}$ and the effectivity index will see the convergence $\theta_h \to 1 - \alpha$. Under uniform mesh refinement, as observed by the plots in Figure 6.5, we see precisely this. The effectivity θ_h seems to converge to a number around 0.6, while the bounded effectivity $\theta_{\geq}$ seems to converge to a number around 0.65. Here, the error estimate (6.27) is not doing a great job, and while the indicators are still sharp, we notice that $\mathcal{S}$ as an *upper bound* is in fact not guaranteed.

Moreover, we consider here two types of adaptive refinement, which we will give the nicknames *greedy* and *not–greedy*. Greedy refinement has Dörfler marking with parameter $\omega = 4/5$ while not–greedy refinement has $\omega = 1/3$ instead. Looking at the loglog plots

[11] The final mesh, which we deem *fine enough*, and accept the approximate computation of the QoI in place of its exact value, is often referred to as an overkill mesh.

[12] Since the QoI is given by a linear functional, and since the Darcy problem is fully linear, there is no linearisation step.

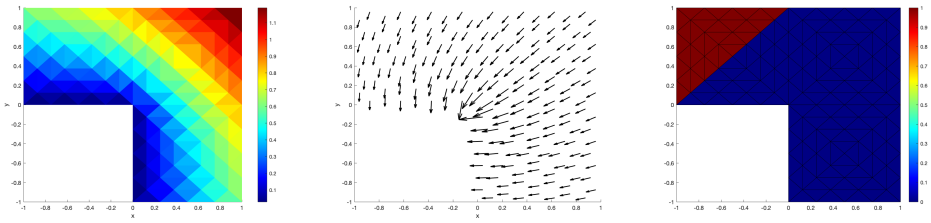

FIG. 6.4 – *Example pressure and velocity approximations, and the region of interest.*

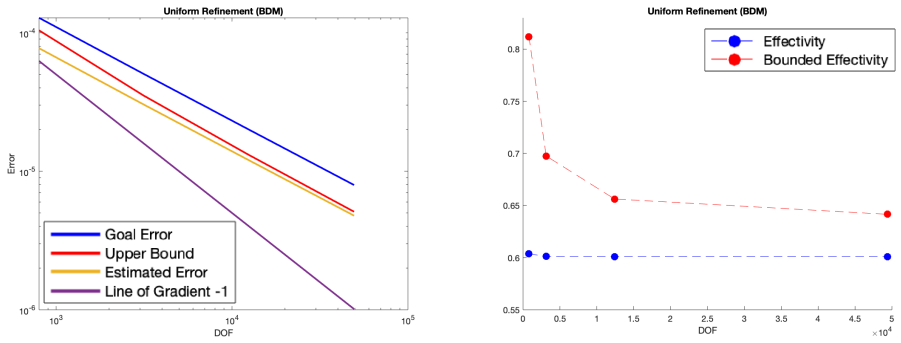

FIG. 6.5 – *Results under uniform refinement for a BDM_1 implementation.*

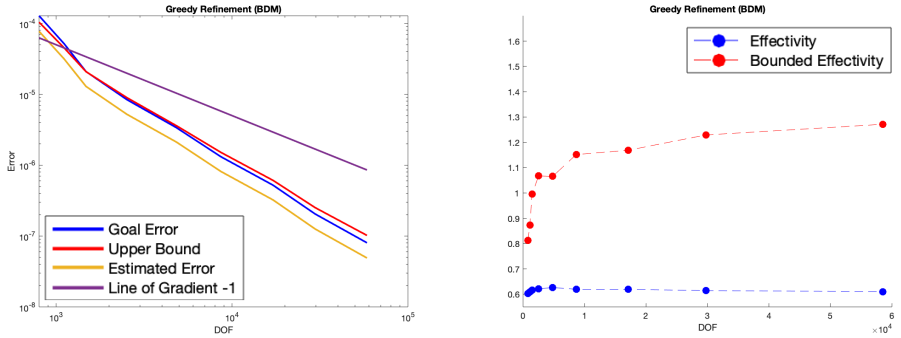

FIG. 6.6 – *Results under a greedy adaptive refinement for a BDM_1 implementation.*

in Figures 6.6 and 6.7 we notice that for both adaptive refinements, the error looks to converge to zero faster than the optimal rate. Moreover, for a greedy refinement the indicators remain sharp and show a similar effectivity convergence that is exhibited by uniform refinement in Figure 6.5.

However, for a not–greedy refinement, we see a loss of sharpness in the indicators but a convergence of the effectivity θ_h to 1. Indeed, this loss of sharpness seems to be down to the superconvergence exhibited under the adaptive regime: the bounded sum $\mathcal{S}$ also looks to converge faster than the optimal rate, but does not seem to see as much of this *added* rate that the error itself enjoys.

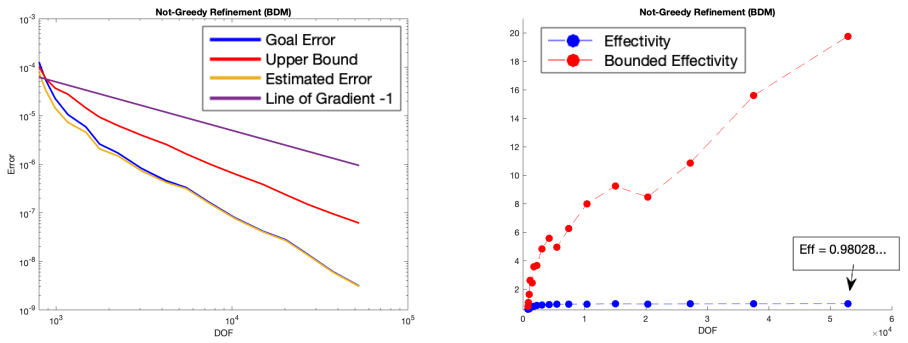

FIG. 6.7 – *Results under a not-greedy adaptive refinement for a BDM_1 implementation.*

The superconvergence seems to occur from the problem setup. We know that the solution (6.45) satisfies Laplace's equation: $-\Delta p = 0$, which of course means the velocity $\mathbf{u}$ is divergence–free[13]: $\nabla \cdot \mathbf{u} = 0$. Numerics, not shown here, reveal that both $\|\nabla \cdot (\mathbf{u} - \mathbf{u}_h)\|_{L^2(\Omega)}$ and $\|\nabla \cdot (\mathbf{z}_h - \Pi_h \mathbf{z}_h)\|_{L^2(\Omega)}$ are negligibly small, giving evidence that, in this experiment, the divergence $\nabla \cdot \mathbf{u}$ is computed exactly, and we even seem to have $\nabla \cdot \mathbf{z}_h = \nabla \cdot (\Pi_h \mathbf{z}_h)$ as well. With this in mind, the convergence result from Theorem 6.6 relies on the bound

$$|Q([\mathbf{u}, p]) - Q([\mathbf{u}_h, p_h])| \leq c_a \|\mathbf{u} - \mathbf{u}_h\|_{H(\mathrm{div},\Omega)} \|\mathbf{z} - \Pi_h \mathbf{z}\|_{H(\mathrm{div},\Omega)} \tag{6.48}$$

$$+ c_b \|\mathbf{u} - \mathbf{u}_h\|_{H(\mathrm{div},\Omega)} \|r - P_h r\|_{L^2(\Omega)} \tag{6.49}$$

$$+ c_b \|\mathbf{z} - \Pi_h \mathbf{z}\|_{H(\mathrm{div},\Omega)} \|p - p_h\|_{L^2(\Omega)}. \tag{6.50}$$

By replacing $\mathbf{z}$ with $\mathbf{z}_h$ in the above, due to $\|\nabla \cdot (\mathbf{u} - \mathbf{u}_h)\|_{L^2(\Omega)}$ and $\|\nabla \cdot (\mathbf{z}_h - \Pi_h \mathbf{z}_h)\|_{L^2(\Omega)}$ both vanishing, the $H(\mathrm{div}, \Omega)$–norms appearing in (6.48) - (6.50) are replaced with the $L^2(\Omega)$–norm instead; this shows a convergence rate *faster than optimal*. Indeed, in a BDM_1 implementation, the $L^2(\Omega)$ error of the velocity approximations converge with a rate faster than that when measured in the $H(\mathrm{div}, \Omega)$–norm. This is not seen in an RT_0 implementation since here, convergence under the $L^2(\Omega)$ and $H(\mathrm{div}, \Omega)$ norms are given by the same, slower rate. This superconvergence is not witnessed under a uniform refinement as there is a loss in the rate of convergence measured in the $L^2(\Omega)$–norm that is only recovered under an adaptive regime, since the primal solutions are irregular.

The final adaptively refined meshes, in the BDM_1 implementation, are shown in Figure 6.8. In these we see the expected refinements occurring within the region of interest and at the singularity. More attention is given to the re–entrant corner where the singularity occurs, which is the opposite of what an RT_0 implementation shows next.

Again, as previously witnessed in the first numerical experiment, the indicators are never

[13] One has $f = 0$ in (3.2).

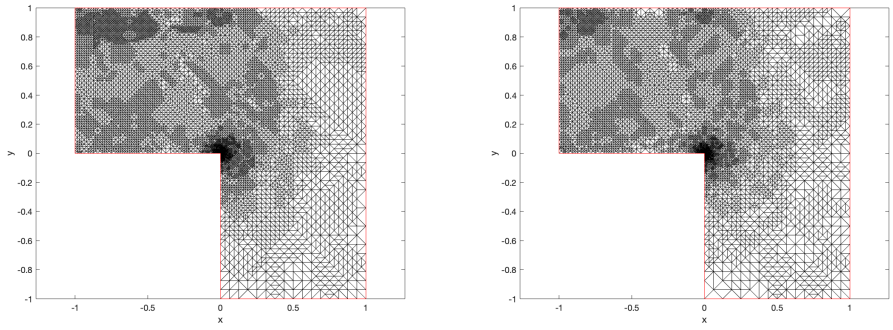

FIG. 6.8 – *Final meshes for BDM_1. Left: greedy, right: not-greedy.*

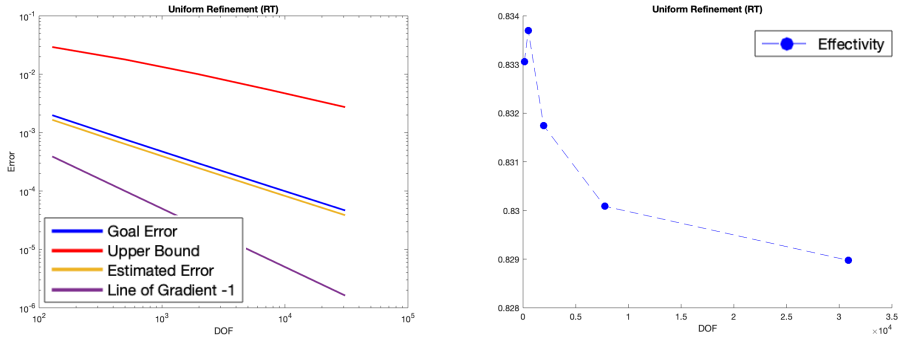

FIG. 6.9 – *Results under uniform refinement for an RT_0 implementation.*

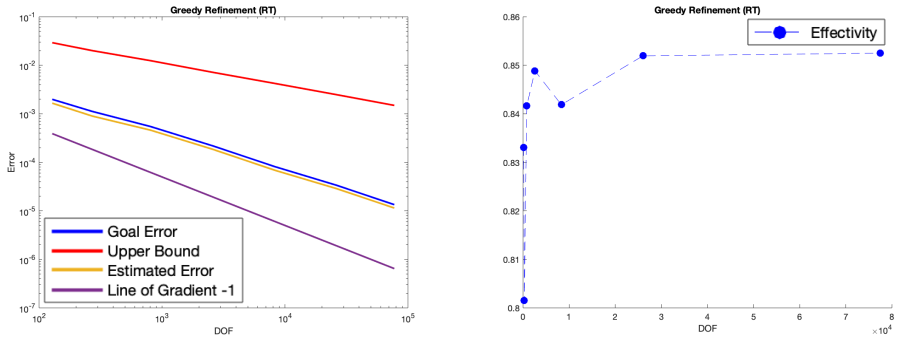

FIG. 6.10 – *Results under a greedy adaptive refinement for an RT_0 implementation.*

sharp using an RT_0 implementation; this is evident from the loglog plots in Figures 6.9, 6.10 and 6.11 where we can see the bounded sum $\mathcal{S}$ converging at a slower rate to the error, in each case. Because of this, the bounded effectivity indices are not shown on the effectivity plots since these blow–up.

Showcasing similar phenomena as the BDM_1 implementation, in Figures 6.9 and 6.10 we see the convergence of the effectivity θ_h to a number less than 1 for a uniform and greedy

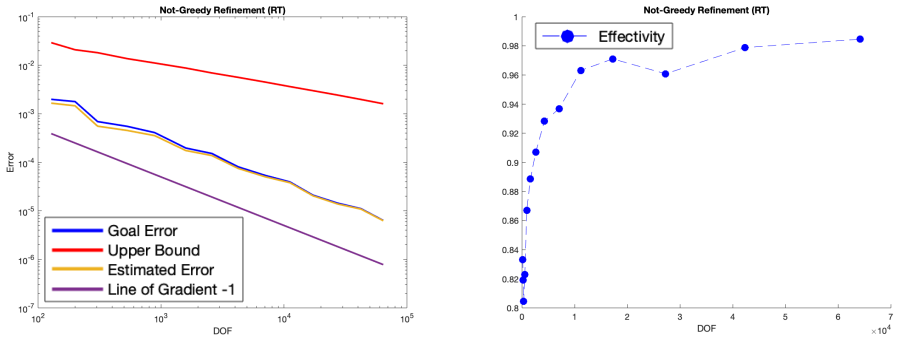

FIG. 6.11 – *Results under a not-greedy adaptive refinement for an RT_0 implementation.*

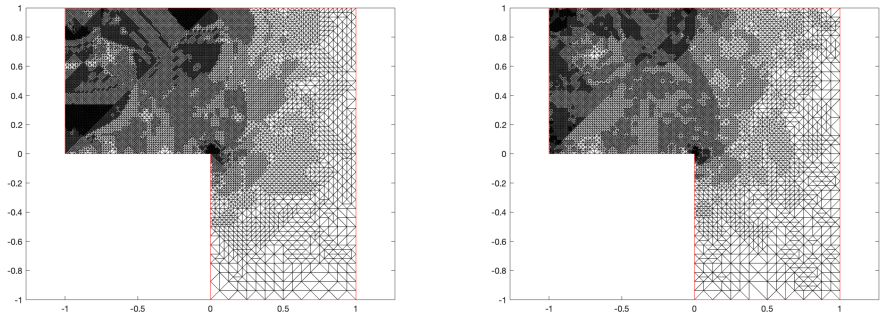

FIG. 6.12 – *Final meshes for RT_0. Left: greedy, right: not-greedy.*

refinement, although in this case θ_h is closer to 1 than in the BDM_1 implementation. Again, when a not–greedy refinement is considered, we see in Figure 6.11 what looks to be the convergence $\theta_h \to 1$, and as predicted, for each adaptive refinement we no longer see the superconvergence exhibited previously. What we do see however is a recovery of the optimal rate of convergence for the not–greedy refinement, and almost the same recovery for the greedy refinement; perhaps $\omega = 4/5$ is too close to 1 in this case, since the slope of the goal error in Figure 6.10 looks to sit in between those in Figures 6.11 and 6.9.

Figure 6.12 shows the final adaptively refined meshes for the RT_0 implementation. Here, we seem to witness more heavy refinement taking place in the region of interest $\mathcal{R}$ than at the re–entrant corner, when compared to those in Figure 6.8. This could be predicted by looking at the indicator contribution

$$\eta_\kappa^{\mathrm{DL}} = -\int_\kappa \mathbf{K}^{-1}\mathbf{u}_h \cdot (\mathbf{z}_h - \Pi_h \mathbf{z}_h).$$

These terms (summed with absolute values inside the sum) in the bounded sum $\mathcal{S}$ look to converge with a rate slower than the others, and thus their contribution to $\mathcal{S}$ will remain the largest under long–term mesh refinement. This will highlight elements in which $\mathbf{z}_h - \Pi_h \mathbf{z}_h$

has most contribution, which would certainly be mostly within the region of interest or on its perimeter. The other terms in the indicators η_κ, for example the contribution η_κ^{BC}, will highlight elements around the re–entrant corner since here we expect the error between the approximation p_h and the boundary data g_D, on the boundary, to be largest. Indeed, in a BDM_1 implementation, each indicator contribution decays at the same rate, which is why we do not see as much refinement in the region $\mathcal{R}$ when compared with an RT_0 implementation.

While an interesting example to investigate, the exhibited superconvergence definitely makes this problem a special case, and does not wholly reflect the behaviour we would expect to see for other irregular Darcy problems undergoing this goal–adaptive treatment[14]. However it does seem to highlight certain nuances associated with the implementation of Darcy's equations that are not present, in say, a typical Poisson's equation application.

[14]This example is usually a good benchmark problem, since it reflects typical behaviour that elliptic PDE problems exhibit near the re—entrant corner of an L—shaped domain [74, p. 20].

Chapter 7

The travel time functional

The structure of this chapter[1] is as follows. First, we define the travel time functional and derive a computable, exact, expression for its derivative; we then apply this theory in the context of Darcy's equations, groundwater flow, and the burial of high–level radioactive waste, before concluding with some numerical examples. The first of these examples acts as a preliminary, or cautionary, example concerning convergence and sharpness of element–based indicators for the travel time functional. The second and third examples are academic–style examples which aim to build confidence in the proposed *a posteriori* error estimate; while the final example adaptively simulates the leakage of radioactive waste within a domain inspired by (albeit greatly simplified) the Sellafield site, located in Cumbria, UK. This final, physically motivated example matches the experiment conducted in [42] but uses the new linearisation result instead.

7.1 Travel time as the quantity of interest

Quantities of interest and their approximate error estimation were considered in Chapter 6; while the dual–weighted–residual theory presented, as part of Section 6.1, considered the case of nonlinear functionals representing the QoI, the examples showcased in Section 6.6 had each an example of a linear functional, for the purposes of investigating the sharpness of element–based indicators, and the general performance of the proposed *a posteriori* error estimate (6.16).

[1] This Chapter has sections taken from the published article [73] by the same author; indeed, the research and contributions presented within were attained through the study of this PhD.

Within this chapter, we consider a single example of a functional that is not only nonlinear, but also unbounded. This functional, referred to as the travel time functional, represents the time–of–flight of leaked radioactive waste, modelled as nonsorbing, nondispersive, purely advective transport–based, particles, reaching the boundary of the domain; vital in the postclosure safety assessment of potential burial sites, this waste can possibly be transported by the surrounding groundwater back up to the surface of the site [105, 43, 42].

Error estimation for this novel functional via the DWR method, in particular the linearised *adjoint problem II* (i.e. the problems (6.13) or (6.24)), requires evaluation of its Gâteaux derivative, given by Definition 6.1. Such evaluation encompasses the main result of this chapter; indeed, we provide an exact expression for the derivative of the travel time functional, considering both the case where the underlying velocity field representing the fluid flow is continuous or discontinuous on the domain.

7.2 Linearisation of the travel time functional

Within this section, we define the travel time functional for generic velocity fields and address briefly the difficulties involved with its linearisation. To this end, consider an open and bounded Lipschitz domain[2] $\Omega \subset \mathbb{R}^d$, $d = 2, 3$, with polygonal boundary $\partial\Omega$, and the semi–infinite time interval $\mathcal{I} = [0, \infty)$. Let us suppose we have a generic velocity field $\mathbf{u} = \mathbf{u}(\mathbf{x}, t) : \overline{\Omega} \times \mathcal{I} \to \mathbb{R}^d$. For a user–defined initial position $\mathbf{x}_0 \in \Omega$, the particle trajectory $\mathbf{X} \equiv \mathbf{X}_\mathbf{u}$, due to $\mathbf{u}$, is given by the solution of the following IVP:

$$\frac{d\mathbf{X}}{dt}(t) = \mathbf{u}(\mathbf{X}(t), t) \quad \forall t \in \mathcal{I}, \tag{7.1}$$

$$\mathbf{X}(0) = \mathbf{x}_0. \tag{7.2}$$

The so–called travel time of the velocity field, $T(\mathbf{u}; \mathbf{x}_0)$, is defined to be the time–of–flight of the particle trajectory $\mathbf{X}_\mathbf{u}$ from its initial position $\mathbf{x}_0$ to, if ever, its first exit point out of the domain Ω. Thereby, the functional[3] $T(\mathbf{u}; \mathbf{x}_0)$ is defined by

$$T(\mathbf{u}; \mathbf{x}_0) = \inf\{t \in \mathcal{I} : \mathbf{X}_\mathbf{u}(t) \notin \Omega\}. \tag{7.3}$$

Alternatively, we can write this in the equivalent form:

$$T(\mathbf{u}; \mathbf{x}_0) = \int_{P(\mathbf{u}; \mathbf{x}_0)} \frac{ds}{\|\mathbf{u}\|_2},$$

[2] We do not consider fractures in this Chapter.

[3] Not to be confused with the notation used in Chapter 2 and Chapter 4 for the trace of $H^1(\Omega)$ functions.

where $\|\cdot\|_2$ denotes the standard Euclidean 2–norm and $P(\mathbf{u};\mathbf{x}_0)$ is the curve[4] traced by the particle trajectory from its initial position to the first boundary contact:

$$P(\mathbf{u};\mathbf{x}_0) = \{\mathbf{X}_\mathbf{u}(t) \in \overline{\Omega} : t \in [0, T(\mathbf{u};\mathbf{x}_0)]\}.$$

The integral version of the functional clearly highlights the difficulty concerning the demonstration of its differentiability. Indeed, the nonlinearity occurs within the integrand and the curve in which the integral is taken over depends itself on the velocity field. The travel time functional cannot clearly be globally continuous and therefore not globally Fréchet differentiable. We shall see, however, that it is possible to evaluate its Gâteaux derivative (Theorem 7.2). The regularity of the functional itself will not be addressed within this work.

Additionally, evaluating the travel time functional itself involves the computation of the velocity streamlines, or particle trajectories $\mathbf{X}_\mathbf{u}(t)$. Within this work, we follow the techniques outlined in [82] for streamline computation; furthermore, a streamfunction approach can indeed be employed when the considered fluid flow approximations are divergence–free [95], and it is even possible for high–order velocity approximations, when also divergence–free, to have accurate streamline tracing [81].

7.2.1 Linearisation in the continuous case

A preliminary result for the linearisation of the travel time functional involves assuming that the velocity field $\mathbf{u}$ satisfying the underlying flow problem is continuous on Ω. When this is the case, then the Gâteaux derivative of the travel time functional may be evaluated and computed as an integral, in time, weighted by a variable $\mathbf{Z}$ which may be considered as being *adjoint* to the particle trajectory $\mathbf{X}_\mathbf{u}$. The theorem below presents such a preliminary version of the main result of this chapter.

Theorem 7.1. *Suppose that the velocity field $\mathbf{u}(\mathbf{x},t)$ is continuous on Ω. Let $\mathbf{n} = \mathbf{n}(\mathbf{x})$ be the unit outward normal vector to $\partial\Omega$. Assume $\partial\Omega$ is flat in some neighbourhood of the exit point $\mathbf{X}_\mathbf{u}(T(\mathbf{u};\mathbf{x}_0))$, and that the particle trajectory is such that $\mathbf{u}(\mathbf{X}_\mathbf{u}(T(\mathbf{u};\mathbf{x}_0)), T(\mathbf{u};\mathbf{x}_0)) \cdot \mathbf{n}(\mathbf{X}_\mathbf{u}(T(\mathbf{u};\mathbf{x}_0))) \neq 0$. Let $\mathbf{Z}$ be the solution of the IVP:*

$$-\frac{d\mathbf{Z}}{dt}(t) - [\nabla\mathbf{u}(\mathbf{X}(t),t)]^\top \mathbf{Z}(t) = \mathbf{0} \quad \forall t \in [0, T(\mathbf{u};\mathbf{x}_0)),$$
$$\mathbf{Z}(T(\mathbf{u};\mathbf{x}_0)) = -\frac{\mathbf{n}}{\mathbf{u}(\mathbf{X}(T(\mathbf{u};\mathbf{x}_0)), T(\mathbf{u};\mathbf{x}_0)) \cdot \mathbf{n}}.$$

Then, the Gâteaux derivative of the travel time functional may be evaluated as

$$T'[\mathbf{u}](\mathbf{v}) = \int_0^{T(\mathbf{u};\mathbf{x}_0)} \mathbf{Z}(t) \cdot \mathbf{v}(\mathbf{X}(t),t)\, dt.$$

[4] We will often use the term *streamline* interchangeably to refer to either the particle trajectory $\mathbf{X}(t)$ or the curve that it traces.

The above result can be used to evaluate the derivative required for the implementation of DWR *a posteriori* error estimators, where here the velocity field $\mathbf{u}$ is replaced with its discrete approximation $\mathbf{u}_h$. However, such approximations are usually obtained via finite element methods, and the continuity of $\mathbf{u}_h$ at element interfaces is not always guaranteed. In this case, Theorem 7.1 must be generalised to allow for such discontinuity; this is addressed in the following sub–section, where Theorem 7.2 is derived without such a continuity assumption. Moreover, Theorem 7.2 presents a more general result in which Theorem 7.1 may be recovered easily by setting the resulting jump terms equal to zero.

7.2.2 Linearisation in the discontinuous case

We emphasise that the main result (i.e. evaluating the Gâteaux derivative of the travel time functional) is independent of where the velocity field $\mathbf{u}$ has come from; for now we are concerned only about the continuity of $\mathbf{u}$. Indeed, computing an approximation to the travel time functional via an approximation of the velocity field $\mathbf{u}$ may or may not lead to a continuous velocity field; this depends on the fluid model and the type of approximation that is employed.

More explicitly: suppose our problem was not in groundwater flow and the disposal of radioactive waste, but instead that we are interested in $T(\mathbf{u};\mathbf{x}_0)$ where $\mathbf{u}$ is a flow governed by Stokes equations. In this situation, typically vector–valued H^1–conforming elements are employed (cf. [30]), on some mesh $\mathscr{T}_h$, to obtain an approximation (at least in two spatial dimensions) $\mathbf{u}_h$ that is continuous across the element interfaces. Here, Theorem 7.1 can be applied to evaluate the derivative $T'[\mathbf{u}_h](\cdot)$ (to, for example, drive an adaptive mesh refinement algorithm). However, in the context of this work, an $H(\mathrm{div})$–conforming approximation of a flow governed by Darcy's equations is used and as such, this conformity does not guarantee continuity of the velocity field across element interfaces. Thereby, in the following discussion we derive a more general result stated in Theorem 7.2.

The main result is stated below in Theorem 7.2, which provides the evaluation of the Gâteaux derivative $T'[\mathbf{v}](\cdot)$, of the travel time functional $T(\cdot)$.

Theorem 7.2. *Let $\mathbf{n}=\mathbf{n}(\mathbf{x})$ be the unit outward normal vector to the boundary $\partial\Omega$. Assume firstly that $\partial\Omega$ is flat in some neighbourhood of the exit point $\mathbf{X}_\mathbf{v}(T_\mathbf{v})$, in particular, this means that the unit outward normal vector $\mathbf{n}=\mathbf{n}(\mathbf{X}_\mathbf{v}(T_\mathbf{v}))$ is unique. Assume also that the particle trajectory is such that $\mathbf{v}(\mathbf{X}_\mathbf{v}(T_\mathbf{v}),T_\mathbf{v})\cdot\mathbf{n}(\mathbf{X}_\mathbf{v}(T_\mathbf{v}))\neq 0$. Suppose that $\mathscr{T}_h$ is a simplicial partition of Ω and that $\mathbf{v}$ is discontinuous across the faces $\{\mathcal{F}_i\}$ that intersect the path $t\mapsto\mathbf{X}_\mathbf{v}(t)$, defined by (7.1) at the times $\{t_i=t_{i,\mathbf{v}}\}$. Lastly, assume that the particle trajectory is such that $\mathbf{v}|_{\partial\kappa}\cdot\mathbf{n}_\kappa\neq 0$ on any of the boundaries $\partial\kappa$ of the elements $\kappa\in\mathscr{T}_h$,*

where $\mathbf{n}_\kappa$ *is the unit outward normal vector to* $\partial\kappa$*, and assume also that it does not exit through the boundary of any of the element faces, except possibly at the exit–point where here the domain boundary is flat. With the above notation described, let* $\mathbf{Z} : [0, T_\mathbf{v}] \to \mathbb{R}^d$ *be the solution to the adjoint, or dual (linearised–adjoint, backward–in–time) IVP:*

$$\begin{cases} \mathcal{L}^*_\mathbf{v}(\mathbf{Z}(t)) \equiv -\frac{d\mathbf{Z}}{dt} - [\nabla \mathbf{v}(\mathbf{X}_\mathbf{v}(t), t)]^\top \mathbf{Z} = \mathbf{0} \qquad \forall t \in [0, T_\mathbf{v}) \setminus \{t_{i,\mathbf{v}}\}, \\ \mathbf{Z}(T_\mathbf{v}) = -\frac{\mathbf{n}(\mathbf{X}_\mathbf{v}(T_\mathbf{v}))}{\mathbf{v}(\mathbf{X}_\mathbf{v}(T_\mathbf{v}), T_\mathbf{v}) \cdot \mathbf{n}(\mathbf{X}_\mathbf{v}(T_\mathbf{v}))}, \\ [\![\mathbf{Z}(t_{i,\mathbf{v}})]\!] = -\frac{\mathbf{Z}(t^+_{i,\mathbf{v}}) \cdot [\![\mathbf{v}(t_{i,\mathbf{v}})]\!] \mathbf{n}^-_i}{\mathbf{v}(\mathbf{X}_\mathbf{v}(t^-_{i,\mathbf{v}}), t^-_{i,\mathbf{v}}) \cdot \mathbf{n}^-_i} \qquad \forall i, \end{cases} \tag{7.4}$$

where $\mathbf{n}^-_i$ *is the unit outward normal vector to the faces* $\{\mathcal{F}_i\}$*, pointing in the same direction as the particle trajectory* $\mathbf{X}_\mathbf{v}(t)$ *at the time of intersection* $t = t_i$*, and where* $[\![\mathbf{Z}(t_{i,\mathbf{v}})]\!] = \mathbf{Z}(t^+_{i,\mathbf{v}}) - \mathbf{Z}(t^-_{i,\mathbf{v}})$ *and* $[\![\mathbf{v}(t_{i,\mathbf{v}})]\!] = \mathbf{v}(\mathbf{X}_\mathbf{v}(t^+_{i,\mathbf{v}}), t^+_{i,\mathbf{v}}) - \mathbf{v}(\mathbf{X}_\mathbf{v}(t^-_{i,\mathbf{v}}), t^-_{i,\mathbf{v}})$ *denote jump operators. Then, the Gâteaux derivative of* $T(\cdot)$*, evaluated at* $\mathbf{v}$*, is given by*

$$T'[\mathbf{v}](\mathbf{w}) = \int_0^{T_\mathbf{v}} \mathbf{Z}(t) \cdot \mathbf{w}(\mathbf{X}_\mathbf{v}(t), t)\, dt.$$

The plus/minus notation refers to the times after/before, respectively, the trajectory $\mathbf{X}_\mathbf{v}$ intersects the element interface, forwards in time. We may also index $\mathbf{Z}_\mathbf{v} \equiv \mathbf{Z}$ to indicate that $\mathbf{Z}_\mathbf{v}$ solves the IVP (7.4) induced by the velocity field $\mathbf{v}$. Also, we note that if the velocity field driving the trajectory is in fact continuous across the element interfaces, then the jump terms vanish and Theorem 7.1 is recovered.

We now proceed to prove Theorem 7.2. To this end, we require two lemmas which are given below. Firstly, consider the so–called trajectory derivative, corresponding to the change in the particle path as a result of a change in velocity:

$$\mathbf{X}' \equiv \partial_\mathbf{v} \mathbf{X}_\mathbf{v}[\mathbf{w}] := \lim_{\varepsilon \to 0^+} \frac{\mathbf{X}_{\mathbf{v}+\varepsilon\mathbf{w}} - \mathbf{X}_\mathbf{v}}{\varepsilon},$$

recalling the notation that $\mathbf{X}_\mathbf{v}$ is the trajectory induced by the velocity field $\mathbf{v}$.

Lemma 7.3. *Let* $\mathbf{v}$ *be as before, discontinuous across the faces* $\{\mathcal{F}_i\}$ *intersecting the path* $t \mapsto \mathbf{X}_\mathbf{v}(t)$ *at the times* $\{t_i = t_{i,\mathbf{v}}\}$*. Then, the trajectory derivative* $\mathbf{X}' : \mathcal{I} \to \mathbb{R}^d$ *satisfies the IVP:*

$$\begin{cases} \mathcal{L}_\mathbf{v}(\mathbf{X}'(t)) \equiv \frac{d\mathbf{X}'}{dt} - \nabla \mathbf{v}(\mathbf{X}_\mathbf{v}(t), t)\mathbf{X}' = \mathbf{w}(\mathbf{X}_\mathbf{v}(t), t) \qquad \forall t \in \mathcal{I} \setminus \{t_i\}, \\ \mathbf{X}'(0) = \mathbf{0}, \\ [\![\mathbf{X}'(t_i)]\!] = -[\![\mathbf{v}(t_i)]\!] t'_i \qquad \forall i, \end{cases} \tag{7.5}$$

where

$$t'_i = -\frac{\mathbf{X}'(t^-_i) \cdot \mathbf{n}^-_i}{\mathbf{v}(\mathbf{X}_\mathbf{v}(t^-_i), t^-_i) \cdot \mathbf{n}^-_i}. \tag{7.6}$$

Proof. The time derivative of $\mathbf{X}'$ is given by

$$\frac{d\mathbf{X}'}{dt} = \frac{d}{dt}\lim_{\varepsilon\to 0^+}\frac{\mathbf{X}_{\mathbf{v}+\varepsilon\mathbf{w}}-\mathbf{X}_{\mathbf{v}}}{\varepsilon} = \lim_{\varepsilon\to 0^+}\frac{(\mathbf{v}+\varepsilon\mathbf{w})(\mathbf{X}_{\mathbf{v}+\varepsilon\mathbf{w}},t)-\mathbf{v}(\mathbf{X}_{\mathbf{v}}(t),t)}{\varepsilon},$$

where we recall the pathline equations the trajectories satisfy. Thus,

$$\begin{aligned}
\frac{d\mathbf{X}'}{dt} &= \lim_{\varepsilon\to 0^+}\frac{(\mathbf{v}+\varepsilon\mathbf{w})(\mathbf{X}_{\mathbf{v}+\varepsilon\mathbf{w}},t)-\mathbf{v}(\mathbf{X}_{\mathbf{v}}(t),t)}{\varepsilon}\\
&= \lim_{\varepsilon\to 0^+}\frac{\mathbf{v}(\mathbf{X}_{\mathbf{v}+\varepsilon\mathbf{w}}(t),t)-\mathbf{v}(\mathbf{X}_{\mathbf{v}}(t),t)}{\varepsilon}+\mathbf{w}(\mathbf{X}_{\mathbf{v}}(t),t)\\
&= \lim_{\varepsilon\to 0^+}\frac{\mathbf{v}(\mathbf{X}_{\mathbf{v}}(t)+\varepsilon\mathbf{X}'(t)+o(\varepsilon),t)-\mathbf{v}(\mathbf{X}_{\mathbf{v}}(t),t)}{\varepsilon}+\mathbf{w}(\mathbf{X}_{\mathbf{v}}(t),t)\\
&= \lim_{\varepsilon\to 0^+}\frac{[\nabla\mathbf{v}(\mathbf{X}_{\mathbf{v}}(t),t)](\varepsilon\mathbf{X}'(t)+o(\varepsilon))}{\varepsilon}+\mathbf{w}(\mathbf{X}_{\mathbf{v}}(t),t)\\
&= [\nabla\mathbf{v}(\mathbf{X}_{\mathbf{v}}(t),t)]\mathbf{X}'(t)+\lim_{\varepsilon\to 0^+}\frac{\nabla\mathbf{v}(\mathbf{X}_{\mathbf{v}}(t),t)o(\varepsilon)}{\varepsilon}+\mathbf{w}(\mathbf{X}_{\mathbf{v}}(t),t)\\
&= [\nabla\mathbf{v}(\mathbf{X}_{\mathbf{v}}(t),t)]\mathbf{X}'(t)+\mathbf{w}(\mathbf{X}_{\mathbf{v}}(t),t),
\end{aligned}$$

i.e., for all $t\in\mathcal{I}\setminus\{t_i\}$ (so that $\nabla\mathbf{v}(\mathbf{X}_{\mathbf{v}}(t),t)$ exists away from the discontinuities),

$$\frac{d\mathbf{X}'}{dt}-[\nabla\mathbf{v}(\mathbf{X}_{\mathbf{v}}(t),t)]\mathbf{X}'(t)=\mathbf{w}(\mathbf{X}_{\mathbf{v}}(t),t).$$

The initial condition follows easily as

$$\mathbf{X}'(0)=\lim_{\varepsilon\to 0^+}\frac{\mathbf{X}_{\mathbf{v}+\varepsilon\mathbf{w}}(0)-\mathbf{X}_{\mathbf{v}}(0)}{\varepsilon}=\lim_{\varepsilon\to 0^+}\frac{\mathbf{x}_0-\mathbf{x}_0}{\varepsilon}=\mathbf{0}.$$

Although the velocity $\mathbf{v}$ has discontinuities, we still require that the trajectory $\mathbf{X}_{\mathbf{v}}$ is continuous. Hence, we have the coupling conditions between the two maps:

$$(\mathbf{v}\mapsto\mathbf{X}_{\mathbf{v}}(t_i^+))=(\mathbf{v}\mapsto\mathbf{X}_{\mathbf{v}}(t_i^-))\quad\forall i.$$

Taking the Gâteaux derivative of each side (i.e., $(d/d\varepsilon)(\cdot)(\mathbf{v}+\varepsilon\mathbf{w})$, as $\varepsilon\to 0$) gives

$$\mathbf{X}'(t_i^+)+\frac{d\mathbf{X}(t_i^+)}{dt}t_i'=\mathbf{X}'(t_i^-)+\frac{d\mathbf{X}(t_i^-)}{dt}t_i'\quad\forall i.$$

Thus,

$$\mathbf{X}'(t_i^+)+\mathbf{v}(\mathbf{X}_{\mathbf{v}}(t_i^+),t_i^+)t_i'=\mathbf{X}'(t_i^-)+\mathbf{v}(\mathbf{X}_{\mathbf{v}}(t_i^-),t_i^-)t_i'\quad\forall i;$$

rearranging gives

$$[\![\mathbf{X}'(t_i)]\!]=-[\![\mathbf{v}(t_i)]\!]t_i'.$$

The expression for $t_i'\equiv\partial_{\mathbf{v}}t_{i,\mathbf{v}}(\mathbf{w})$, given by (7.6), follows similarly to the proof given for the following Lemma 7.4. □

We note as well that a variational approach can be used instead to prove Lemma 7.3. For use in Lemma 7.4, consider the change in exit–time, or time–of–flight, due to a change in the velocity, given by

$$T'\equiv T'[\mathbf{v}](\mathbf{w})=\partial_{\mathbf{v}}T_{\mathbf{v}}(\mathbf{w}):=\lim_{\varepsilon\to 0^+}\frac{T_{\mathbf{v}+\varepsilon\mathbf{w}}-T_{\mathbf{v}}}{\varepsilon}.$$

Lemma 7.4. *Suppose that $\partial\Omega$ is flat in some neighbourhood of the exit point $\mathbf{X}_{\mathbf{v}}(T_{\mathbf{v}})$. Then, the derivative $\mathbf{X}'(T_{\mathbf{v}})$ satisfies*

$$\mathbf{X}'(T_{\mathbf{v}}) \cdot \mathbf{n} = -T'\mathbf{v}(\mathbf{X}_{\mathbf{v}}(T_{\mathbf{v}}), T_{\mathbf{v}}) \cdot \mathbf{n},$$

with $\mathbf{n} \equiv \mathbf{n}(\mathbf{X}_{\mathbf{v}}(T_{\mathbf{v}}))$.

Proof. Since $\partial\Omega$ is flat in some neighbourhood of the exit–point $\mathbf{X}_{\mathbf{v}}(T_{\mathbf{v}})$, for sufficiently small ε we have $(\mathbf{X}_{\mathbf{v}+\varepsilon\mathbf{w}}(T_{\mathbf{v}+\varepsilon\mathbf{w}}) - \mathbf{X}_{\mathbf{v}}(T_{\mathbf{v}})) \cdot \mathbf{n} = 0$, so that

$$\begin{aligned}
\mathbf{X}'(T_{\mathbf{v}}) \cdot \mathbf{n} &= \lim_{\varepsilon \to 0^+} \frac{\mathbf{X}_{\mathbf{v}+\varepsilon\mathbf{w}}(T_{\mathbf{v}}) - \mathbf{X}_{\mathbf{v}}(T_{\mathbf{v}})}{\varepsilon} \cdot \mathbf{n} \\
&= \lim_{\varepsilon \to 0^+} \frac{\mathbf{X}_{\mathbf{v}+\varepsilon\mathbf{w}}(T_{\mathbf{v}}) - \mathbf{X}_{\mathbf{v}+\varepsilon\mathbf{w}}(T_{\mathbf{v}+\varepsilon\mathbf{w}})}{\varepsilon} \cdot \mathbf{n} \\
&= \lim_{\varepsilon \to 0^+} \frac{\mathbf{X}_{\mathbf{v}+\varepsilon\mathbf{w}}(T_{\mathbf{v}}) - \mathbf{X}_{\mathbf{v}+\varepsilon\mathbf{w}}(T_{\mathbf{v}} + \varepsilon T' + o(\varepsilon))}{\varepsilon} \cdot \mathbf{n} \\
&= \lim_{\varepsilon \to 0^+} \frac{-\frac{d\mathbf{X}_{\mathbf{v}+\varepsilon\mathbf{w}}}{dt}(T_{\mathbf{v}})(\varepsilon T' + o(\varepsilon))}{\varepsilon} \cdot \mathbf{n} \\
&= \lim_{\varepsilon \to 0^+} \frac{-(\mathbf{v} + \varepsilon\mathbf{w})(\mathbf{X}_{\mathbf{v}+\varepsilon\mathbf{w}}(T_{\mathbf{v}}), T_{\mathbf{v}})(\varepsilon T' + o(\varepsilon))}{\varepsilon} \cdot \mathbf{n} \\
&= -T'\mathbf{v}(\mathbf{X}_{\mathbf{v}}(T_{\mathbf{v}}), T_{\mathbf{v}})) \cdot \mathbf{n}.
\end{aligned}$$

□

Remark 7.5. *The first step in the proof of Lemma 7.4 requires that the boundary $\partial\Omega$ is flat in a neighbourhood of the exit–point $\mathbf{X}_{\mathbf{v}}(T_{\mathbf{v}})$. Indeed, the statement $(\mathbf{X}_{\mathbf{v}+\varepsilon\mathbf{w}}(T_{\mathbf{v}+\varepsilon\mathbf{w}}) - \mathbf{X}_{\mathbf{v}}(T_{\mathbf{v}})) \cdot \mathbf{n} = 0$ is not true for any ε in the case of a curved boundary. Here, a contribution from the curvature at the exit–point would be present in both the result from Lemma 7.4 and would alter the adjoint–IVP in Theorem 7.2; as a brief sketch, Lemma 7.4 would state that $\mathbf{X}'(T_{\mathbf{v}}) \cdot \mathbf{n} = -(T' + \kappa_c \frac{\mathbf{X}'(T_{\mathbf{v}}) \cdot \boldsymbol{\tau}}{\|\mathbf{v}\|})(\mathbf{v}(\mathbf{X}_{\mathbf{v}}(T_{\mathbf{v}}), T_{\mathbf{v}}) \cdot \mathbf{n})$, where κ_c is the curvature of the boundary at the exit–point, and $\boldsymbol{\tau}$ is the unit tangent vector to $\partial\Omega$ at the exit–point.*

Thus, we are now able to prove the main result of this chapter.

Proof of Theorem 7.2

Proof. From Lemma 7.4 and (7.4) we have

$$T' = -\frac{\mathbf{X}'(T_{\mathbf{v}}) \cdot \mathbf{n}}{\mathbf{v}(\mathbf{X}_{\mathbf{v}}(T_{\mathbf{v}}), T_{\mathbf{v}}) \cdot \mathbf{n}} = \mathbf{X}'(T_{\mathbf{v}}) \cdot \mathbf{Z}(T_{\mathbf{v}}).$$

Since from (7.4) we know that $\mathcal{L}^*_{\mathbf{v}}(\mathbf{Z}(t)) = 0$ away from the jump times $\{t_i\}$, we have

$$T' \equiv \mathbf{X}'(T_{\mathbf{v}}) \cdot \mathbf{Z}(T_{\mathbf{v}}) = \mathbf{X}'(T_{\mathbf{v}}) \cdot \mathbf{Z}(T_{\mathbf{v}}) + \sum_i \int_{t_{i-1}}^{t_i} \mathcal{L}^*_{\mathbf{v}}(\mathbf{Z}(t)) \cdot \mathbf{X}'(t)\, dt.$$

Integrating by parts reveals that

$$\begin{aligned} T' &\equiv \sum_i \int_{t_{i-1}}^{t_i} \mathbf{Z}(t) \cdot \mathcal{L}_{\mathbf{v}}(\mathbf{X}'(t))\, dt \\ &\quad + \sum_i (\mathbf{Z}(t_i^+) \cdot \mathbf{X}'(t_i^+) - \mathbf{Z}(t_i^-) \cdot \mathbf{X}'(t_i^-)) + \mathbf{Z}(0) \cdot \mathbf{X}'(0) \\ &= \sum_i \int_{t_{i-1}}^{t_i} \mathbf{Z}(t) \cdot \mathbf{w}(\mathbf{X}_{\mathbf{v}}(t), t)\, dt + \sum_i (\mathbf{Z}(t_i^+) \cdot \mathbf{X}'(t_i^+) - \mathbf{Z}(t_i^-) \cdot \mathbf{X}'(t_i^-)), \end{aligned}$$

since from (7.5) in Lemma 7.3 we have that $\mathcal{L}_{\mathbf{v}}(\mathbf{X}'(t)) = \mathbf{w}(\mathbf{X}_{\mathbf{v}}(t), t)$ and $\mathbf{X}'(0) = \mathbf{0}$. The jump condition in (7.5) for $\mathbf{X}'$ can be rearranged to obtain the expression

$$\mathbf{X}'(t_i^+) = \mathbf{X}'(t_i^-) + [\![\mathbf{v}(t_i)]\!] \frac{\mathbf{X}'(t_i^-) \cdot \mathbf{n}_i^-}{\mathbf{v}(\mathbf{X}_{\mathbf{v}}(t_i^-), t_i^-) \cdot \mathbf{n}_i^-}.$$

Thereby,

$$\begin{aligned} T' \equiv & \sum_i \int_{t_{i-1}}^{t_i} \mathbf{Z}(t) \cdot \mathbf{w}(\mathbf{X}_{\mathbf{v}}(t), t)\, dt \\ & + \sum_i \left(\mathbf{Z}(t_i^+) \cdot \left(\mathbf{X}'(t_i^-) + [\![\mathbf{v}(t_i)]\!] \frac{\mathbf{X}'(t_i^-) \cdot \mathbf{n}_i^-}{\mathbf{v}(\mathbf{X}_{\mathbf{v}}(t_i^-), t_i^-) \cdot \mathbf{n}_i^-} \right) - \mathbf{Z}(t_i^-) \cdot \mathbf{X}'(t_i^-) \right). \end{aligned}$$

Notice that

$$\begin{aligned} & \mathbf{Z}(t_i^+) \cdot \left(\mathbf{X}'(t_i^-) + [\![\mathbf{v}(t_i)]\!] \frac{\mathbf{X}'(t_i^-) \cdot \mathbf{n}_i^-}{\mathbf{v}(\mathbf{X}_{\mathbf{v}}(t_i^-), t_i^-) \cdot \mathbf{n}_i^-} \right) - \mathbf{Z}(t_i^-) \cdot \mathbf{X}'(t_i^-) \\ &= \left(\mathbf{Z}(t_i^+) - \mathbf{Z}(t_i^-) + \frac{\mathbf{Z}(t_i^+)[\![\mathbf{v}(t_i)]\!]}{\mathbf{v}(\mathbf{X}_{\mathbf{v}}(t_i^-), t_i^-) \cdot \mathbf{n}_i^-} \cdot \mathbf{n}_i^- \right) \cdot \mathbf{X}'(t_i^-) \\ &= ([\![\mathbf{Z}(t_i)]\!] - [\![\mathbf{Z}(t_i)]\!]) \cdot \mathbf{X}'(t_i^-) = \mathbf{0}, \end{aligned}$$

due to the jump condition for $\mathbf{Z}(t_i)$ in (7.4) for all i. This implies that

$$T' \equiv \sum_i \int_{t_{i-1}}^{t_i} \mathbf{Z}(t) \cdot \mathbf{w}(\mathbf{X}_{\mathbf{v}}(t), t)\, dt = \int_0^{T_{\mathbf{v}}} \mathbf{Z}(t) \cdot \mathbf{w}(\mathbf{X}_{\mathbf{v}}(t), t)\, dt,$$

thus completing the proof. □

7.3 Application to Darcy flow

For a groundwater flow model governed by Darcy's equations (3.1)–(3.4), physical (non-sorbing, nondispersive, purely advective transport–based) particle trajectories are due to a velocity field known as the transport velocity, which relates the Darcy velocity $\mathbf{u}$ and the porosity, ϕ, of the surrounding rock via $\mathbf{u}_T = \mathbf{u}/\phi$. Indeed, the travel time along particle trajectories driven by this velocity field are those that should be considered in the travel time functional (7.3). With $\mathbf{x}_0$ the initial burial point, our quantity of interest can be expressed either by the functionals $\mathfrak{T}(\cdot\,; \mathbf{x}_0)$ or $T(\cdot\,; \mathbf{x}_0)$, where, in particular, the former is given by

$$\mathfrak{T}(\mathbf{u}; \mathbf{x}_0) = T(\mathbf{u}_T; \mathbf{x}_0) = \inf\{t > 0 : \mathbf{X}_{\mathbf{u}_T}(t) \notin \Omega\}, \tag{7.7}$$

and it is indeed the trajectory $\mathbf{X}_{\mathbf{u}_T}$ that should be considered ($\mathbf{v} \leftrightarrow \mathbf{u}_T$) in Theorem 7.2, and the functional $T(\mathbf{u}_T; \mathbf{x}_0)$ should be considered in the context of the *a posteriori* error estimation presented in Section 6.1 and Section 6.2.

Furthermore, a simple application of a generalised chain rule allows us to deduce an expression for the Gâteaux derivative of the functional $\mathfrak{T}(\cdot\,; \mathbf{x}_0)$, given by

$$\mathfrak{T}'[\mathbf{v}](\mathbf{w}) = T'[\mathbf{v}_T](\mathbf{w}_T). \tag{7.8}$$

7.3.1 Streamline computation

[5]Since the Darcy velocity $\mathbf{u}$ is approximated by the finite element solution $\mathbf{u}_h$ from (6.22), the streamline $P(\mathbf{u}; \mathbf{x}_0)$ will be approximated by $P(\mathbf{u}_h; \mathbf{x}_0)$. Under a BDM_1 and RT_0 implementation we can calculate these approximate streamlines exactly, following the techniques outlined in [43, 82]. In the case of higher–order approximations, streamline computations become non–trivial and other techniques, such as time-stepping methods, must be employed instead. It has been shown however, that for divergence–free flows, the streamlines may be evaluated via a streamfunction approach to a high accuracy, for both low and high-order implementations [95, 81].

We assume that the porosity ϕ is a piecewise–constant function with respect to the triangulation $\mathscr{T}_h$, of $\overline{\Omega}$; recall that the discrete solutions $\mathbf{u}_h$ and p_h are sought in the spaces (6.19) and (6.20), respectively, using such mesh. Having this assumption allows for an easy computation of the discrete streamlines using an element–by–element approach. Moreover, a key tool in this computational procedure is the so–called *contravariant Piola mapping*, which we discuss next.

The general technique employed for the computation of the streamline $P(\mathbf{u}_h; \mathbf{x}_0)$ is to map the IVP (7.1), per element, onto a reference element $\hat{\kappa}$. Then, evaluation of the streamline and subsequent travel time takes place there instead; the exit point on the reference element is mapped back to the physical mesh as a new starting point, and so on. Indeed, this requires a mapping (in this case an isomorphism) for $\mathbf{v} \in H(\mathrm{div}, \kappa)$ to and from $H(\mathrm{div}, \hat{\kappa})$. The preservation of normal traces is paramount in computing physical streamlines, and is also used in defining the basis functions for the space (6.19). Furthermore, employing the standard affine map $F_\kappa : \hat{\kappa} \to \kappa$, by composing it with the velocities, does not preserve normal traces and thus does not provide the isomorphism we need [43, p. 59]; the contravariant Piola mapping must be used instead, which we see defined below as Definition 7.8.

[5]This sub–section, as well as the first showcased numerical experiment (Section 7.4) were the only content within this chapter to not feature in the published article [73].

Definition 7.6. *The reference element $\hat{\kappa}$ is the triangle in (ξ, η) space with the anti-clockwise labelled vertices $\nu_1 = (-1, -1)$, $\nu_2 = (1, -1)$ and $\nu_3 = (-1, 1)$. The edges of $\hat{\kappa}$ are labelled such that edge $\mathcal{E}_i$ is the edge opposite to the vertex ν_i for $i = 1, 2, 3$.*

Definition 7.7. *Let $\psi_j(\xi, \eta)$ be the linear shape functions on $\hat{\kappa}$. i.e. they are such that $\psi_j(\nu_i) = \delta_{ij}$ for $i, j = 1, 2, 3$. Let $\kappa \in \mathscr{T}_h$ be a generic physical element from a triangulation with vertices $\mathbf{x}_i$, $i = 1, 2, 3$. The affine mapping $F_\kappa : \hat{\kappa} \to \kappa$ is defined such that*

$$F_\kappa(\xi, \eta) = \sum_{i=1}^{3} \mathbf{x}_i \psi_i(\xi, \eta) \equiv (x, y).$$

It is clear that $F_\kappa(\nu_i) = \mathbf{x}_i$ for $i = 1, 2, 3$.

Definition 7.8. *For $\kappa \in \mathscr{T}_h$ let J_κ be the Jacobi matrix of the affine mapping F_κ; denote its determinant by $|J_\kappa|$. Then, for $\hat{\mathbf{v}} \in [L^2(\kappa)]^2$, the contravariant Piola mapping is defined by*

$$\mathscr{F}_\kappa(\hat{\mathbf{v}}) := \frac{1}{|J_\kappa|} J_\kappa \hat{\mathbf{v}} \circ F_\kappa^{-1}.$$

Indeed, the contravariant Piola mapping preserves normal traces up to edge lengths. Denote by $\mathbf{n}_\kappa$ the unit outward normal vector to $\partial\kappa$, and $\mathbf{n}_{\hat{\kappa}}$ the unit outward normal vector to $\partial\hat{\kappa}$. For $\mathbf{n}_\kappa$ on the edge $\mathcal{E} = F_\kappa(\hat{\mathcal{E}})$, corresponding to $\mathbf{n}_{\hat{\kappa}}$ being on the edge $\hat{\mathcal{E}} \subset \partial\hat{\kappa}$, [43, pp. 60–61] shows that for $\hat{\mathbf{v}} \in H(\mathrm{div}, \hat{\kappa})$ and $\mathbf{v} := \mathscr{F}_\kappa(\hat{\mathbf{v}})$ we have

$$\mathbf{v} \cdot \mathbf{n}_\kappa = \frac{\|\hat{\mathcal{E}}\|}{\|\mathcal{E}\|} (\hat{\mathbf{v}} \cdot \mathbf{n}_{\hat{\kappa}}),$$

where $\|\cdot\|$ denotes edge length. Furthermore, it can be shown that $\mathscr{F}_\kappa$ is indeed an isomorphism between $H(\mathrm{div}, \hat{\kappa})$ and $H(\mathrm{div}, \kappa)$, for each element $\kappa \in \mathscr{T}_h$; see [43, p. 62] again, for example.

With the above in mind, we now consider the computation of streamlines on a single element $\kappa \in \mathscr{T}_h$. We set $t = 0$ at the entry point $\mathbf{x}_{\mathrm{IN}}$; our aim is to compute an expression for the particle trajectory $\mathbf{X}(t)$ on this element so that we can calculate the exit point $\mathbf{x}_{\mathrm{OUT}}$ and the total time spent within, referred to as the residence time. For the subsequent element, we set its entry point as the previous exit point, and the total travel time is calculated by summing up all of the residence times for each element the streamline intersects.

For the approximate Darcy velocity $\mathbf{u}_h$, the equation for the streamline $\mathbf{X}(t)$ on the element $\kappa \in \mathscr{T}_h$ is given by

$$\frac{d\mathbf{X}}{dt} = \mathbf{u}_{h,T}|_\kappa = \frac{\mathbf{u}_h|_\kappa}{\phi}, \ : \ \mathbf{X}(0) = \mathbf{x}_{\mathrm{IN}}. \tag{7.9}$$

If $\mathbf{u}_h$ is an RT_0 or BDM_1 velocity then so is the transport velocity $\mathbf{u}_{h,T}$ since the porosity ϕ is constant on the element κ. By employing the inverse of the contravariant Piola mapping

we consider (7.9) on the reference element $\hat{\kappa}$ instead; cf. Figure 7.1. Writing[6] $\hat{\mathbf{u}}_{h,T} = \mathscr{F}_{\kappa}^{-1}(\mathbf{u}_{h,T}|_{\kappa})$ we have the following IVP on the reference element:

$$\frac{d\hat{\mathbf{X}}}{d\hat{t}} = \hat{\mathbf{u}}_{h,T} \ : \ \hat{\mathbf{X}}(0) = \hat{\mathbf{x}}_{\text{IN}}. \tag{7.10}$$

In (7.10), $\hat{\mathbf{X}}(\hat{t}) = [\xi(\hat{t}), \eta(\hat{t})]^{\top}$ is the particle position on the reference element, and $\hat{\mathbf{x}}_{\text{IN}} = F_{\kappa}^{-1}(\mathbf{x}_{\text{IN}})$; furthermore, the reference time $\hat{t}$ is related to the physical time t by $t = |J_{\kappa}|\hat{t}$.

Firstly, suppose that $\mathbf{u}_h$ is an RT_0 velocity. Then, due to the Piola mapping, so is $\hat{\mathbf{u}}_{h,T}$ and there are constants α, β and γ such that

$$\hat{\mathbf{u}}_{h,T}(\xi, \eta) \equiv \begin{bmatrix} \alpha \\ \beta \end{bmatrix} + \gamma \begin{bmatrix} \xi \\ \eta \end{bmatrix}.$$

It can be shown, for example in [82] or [43, p. 71], that the solution to (7.10) is given by

$$\hat{\mathbf{X}}(\hat{t}) = \begin{cases} e^{\gamma\hat{t}}\hat{\mathbf{x}}_{\text{IN}} + \frac{(e^{\gamma\hat{t}}-1)}{\gamma} \begin{bmatrix} \alpha \\ \beta \end{bmatrix}, & \gamma \neq 0, \\ \hat{\mathbf{x}}_{\text{IN}} + \hat{t} \begin{bmatrix} \alpha \\ \beta \end{bmatrix}, & \gamma = 0. \end{cases} \tag{7.11}$$

With the solution (7.11), one can calculate, by hand, the intersection points with the three edges of the reference element $\hat{\kappa}$; the intersection point with the smallest positive reference time $\hat{t} = \hat{t}_I$ is the edge intersected within the element. The physical exit point is calculated via the affine map F_{κ}. Meanwhile, the residence time in κ is given by $t = |J_{\kappa}|\hat{t}_I$, which is subsequently stored and added to the total travel time.

When the velocity approximation $\mathbf{u}_h$ is a BDM_1 velocity, the analytical solution to the streamline IVP is obtained in a different way. Here, there are the constants $\alpha_{\xi,\eta}, \beta_{\xi,\eta}$ and $\gamma_{\xi,\eta}$ such that

$$\hat{\mathbf{u}}_{h,T}(\xi, \eta) \equiv \begin{bmatrix} \alpha_{\xi} + \beta_{\xi}\xi + \gamma_{\xi}\eta \\ \alpha_{\eta} + \beta_{\eta}\xi + \gamma_{\eta}\eta \end{bmatrix}, \tag{7.12}$$

and thus (7.10) becomes

$$\frac{d\hat{\mathbf{X}}}{d\hat{t}} = \begin{bmatrix} \alpha_{\xi} + \beta_{\xi}\xi + \gamma_{\xi}\eta \\ \alpha_{\eta} + \beta_{\eta}\xi + \gamma_{\eta}\eta \end{bmatrix} \ : \ \hat{\mathbf{X}}(0) = \hat{\mathbf{x}}_{\text{IN}}. \tag{7.13}$$

Indeed, (7.13) has many cases to consider; it is a linear differential equation and can thus be solved quite easily by re–writing as a single second–order, constant coefficient, ordinary differential equation for one of the solution components. However, since there are quite a few

[6] Hat notation was used previously in Chapter 4 and Chapter 5 to denote functions defined on fracture networks, but since fractures are not considered here, we proceed with this notation without confusion.

cases to consider, that depend on the parameters in (7.12), this becomes quite cumbersome very quickly. In light of this, we proceed by solving (7.13) utilising matrix exponentials, leading to a more succinct solution statement.

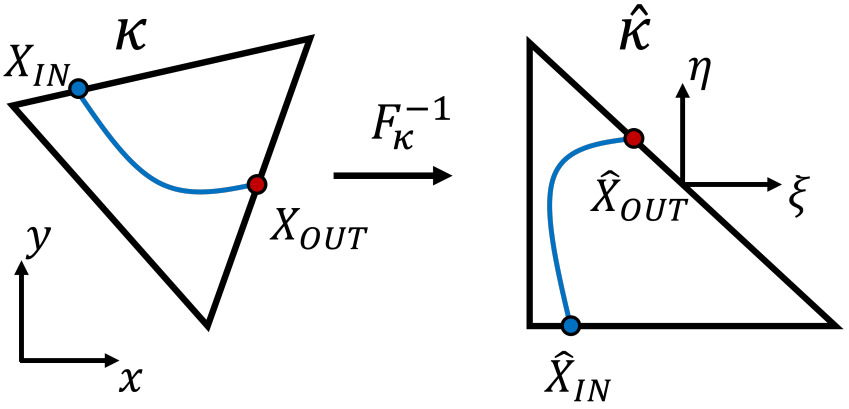

FIG. 7.1 – *Streamline tracing takes place on the reference element $\hat{\kappa}$.*

Recall the definition of a matrix exponential, given below in Definition 7.9.

Definition 7.9. *For any $n \in \mathbb{N}$ and any matrix $M \in \mathbb{R}^{n\times n}$, the power series*

$$e^M \equiv \texttt{exp}(M) := \sum_{i=0}^{\infty} \frac{M^i}{i!}$$

converges, and is called the matrix exponential of the matrix M.

Matrix exponentials enjoy many shared properties with the usual exponential for real numbers; while not all of them, enough of these properties are satisfied to be able to solve (7.13). To this end, define the following matrix and vector:

$$A := \begin{bmatrix} \beta_\xi & \gamma_\xi \\ \beta_\eta & \gamma_\eta \end{bmatrix}, \quad \mathbf{b} := \begin{bmatrix} \alpha_\xi \\ \alpha_\eta \end{bmatrix}. \tag{7.14}$$

With (7.14) we see that (7.13) may be rewritten as

$$\frac{d\hat{\mathbf{X}}}{d\hat{t}} - A\hat{\mathbf{X}} = \mathbf{b} \ : \ \hat{\mathbf{X}}(0) = \mathbf{x}_{\text{IN}}. \tag{7.15}$$

It is fairly easy to prove that the solution to (7.15) is given by

$$\hat{\mathbf{X}}(\hat{t}) = \begin{cases} e^{A\hat{t}}(\hat{\mathbf{x}}_{\text{IN}} + A^{-1}\mathbf{b}) - A^{-1}\mathbf{b}, & |A| \neq 0, \\ e^{A\hat{t}}(\hat{\mathbf{x}}_{\text{IN}} + \varphi(\hat{t})), & |A| = 0, \end{cases}$$

where $|A| = \beta_\xi\gamma_\eta - \gamma_\xi\beta_\eta$ is the determinant of A and

$$\varphi(\hat{t}) := \int_0^{\hat{t}} e^{-A\tau}\mathbf{b}\, d\tau$$

can be computed numerically, using quadrature techniques, in the case where A is singular.

In this case, root finding algorithms[7] for nonlinear equations must be employed to find the intersection times $\hat{t} = \hat{t}_I$ of the edges of $\hat{\kappa}$ with $\hat{\mathbf{X}}(\hat{t})$.

7.3.2 Implementation details for Theorem 7.2

In this section, let $\mathbf{u}_h \in \mathbf{V}_h$ and $\mathbf{v} \in \mathbf{V}$ be generic velocity fields. For example, $\mathbf{u}_h$ could be a discrete transport velocity, while $\mathbf{v}$ could be a basis function of $\mathbf{W}_h \subset \mathbf{V}$, $\mathbf{W}_h \not\subset \mathbf{V}_h$, so that the derivative

$$T'[\mathbf{u}_h](\mathbf{v}) = \int_0^{T(\mathbf{u}_h)} \mathbf{Z}(t) \cdot \mathbf{v}(\mathbf{X}_{\mathbf{u}_h}(t))\, dt \tag{7.16}$$

is required for computing the numerical solution to the approximate linearised adjoint problem (6.25). Of course, if $\mathbf{u}_h$ is the discrete Darcy velocity satisfying (6.22) then the derivative $\mathfrak{T}'[\mathbf{u}_h](\mathbf{v})$ can be evaluated combining this section with (7.8).

For simplicity of presentation, we restrict this discussion to $d = 2$, but we stress that the generalisation to $d = 3$ follows directly. In this setting, we recall that $\mathscr{T}_h$ is a shape-regular triangulation of $\overline{\Omega}$ for which $\mathbf{u}_h$ is discontinuous across the element interfaces intersected by the particle trajectory $\mathbf{X}_{\mathbf{u}_h}(t)$ at the times $\{t_i\}_{i=1}^N$; proceed with the assumptions stated in Theorem 7.2. Denote by $\mathbb{T}_h = \{\kappa_i\}_{i=1}^N \subset \mathscr{T}_h$ the ordered list of elements intersected by the particle trajectory. Here, we allow for repetitions if the trajectory re–enters the same element, where it will appear multiple times in $\mathbb{T}_h$ with different labels. In order to obtain the adjoint variable $\mathbf{Z}_{\mathbf{u}_h} \equiv \mathbf{Z}$, we can solve the IVP (7.4) in an element–by–element manner. That is, starting from the intersection point with the boundary of $\mathbf{X}_{\mathbf{u}_h}(t)$, we trace the particle trajectory backwards through its intersected elements, and solve for $\mathbf{Z}$ on each time interval that the trajectory is residing in that element. More precisely, consider the final element κ_N. The trajectory $\mathbf{X}_{\mathbf{u}_h}(t)$ occupies this element for $t \in (t_{N-1}, t_N)$, where $t_N \equiv T(\mathbf{u}_h; \mathbf{x}_0)$ is the travel time. Restricting to this time interval, the adjoint variable $\mathbf{Z}(t)$ solves the IVP

$$-\frac{d\mathbf{Z}(t)}{dt} - [\nabla \mathbf{u}_h(\mathbf{X}_{\mathbf{u}_h}(t))]^\top \mathbf{Z}(t) = \mathbf{0}.$$

For times $t \in (t_{N-1}, t_N)$, we have $\mathbf{X}_{\mathbf{u}_h}(t) \in \kappa_N$ and within this element $\mathbf{u}_h$ is a polynomial function. This means that together with the given final–time condition

$$\mathbf{Z}(t_N) = -\frac{\mathbf{n}}{\mathbf{u}_h(\mathbf{X}(t_N)) \cdot \mathbf{n}},$$

we can solve for $\mathbf{Z}$ within this time interval, via an exact method or using some approximate time–stepping technique for ODEs. For example, if $\mathbf{u}_h$ is a piecewise linear function on the

[7] For example, for the examples shown in Section 7.4 and Section 7.5, Matlab's `expm` and `fsolve` functions were employed in order to trace streamlines of BDM_1 velocities.

triangulation $\mathscr{T}_h$ (e.g. a lowest order RT or BDM function) then we may solve for $\mathbf{Z}$ directly via matrix exponentials. Indeed, the gradient of such a function will be piecewise constant on the same triangulation.

In such a case, denote by $\mathbf{a} = (\alpha_x, \alpha_y)^\top$, $\mathbf{b} = (\beta_x, \beta_y)^\top$ and $\mathbf{c} = (\gamma_x, \gamma_y)^\top$ the real coefficients such that on $\kappa_i \in \mathbb{T}_h$

$$\mathbf{u}_h|_{\kappa_i} \equiv \begin{bmatrix} \alpha_x + \beta_x x + \gamma_x y \\ \alpha_y + \beta_y x + \gamma_y y \end{bmatrix}.$$

Then, $\mathbf{a} = \mathbf{u}_h|_{\kappa_i}(0,0)$, $\mathbf{b} = \mathbf{u}_h|_{\kappa_i}(1,0) - \mathbf{a}$, $\mathbf{c} = \mathbf{u}_h|_{\kappa_i}(0,1) - \mathbf{a}$, and the gradient of $\mathbf{u}_h$ restricted to κ_i is given by

$$\nabla \mathbf{u}_h|_{\kappa_i} = \begin{bmatrix} \mathbf{b} & \mathbf{c} \end{bmatrix} = \begin{bmatrix} \beta_x & \gamma_x \\ \beta_y & \gamma_y \end{bmatrix}.$$

Denoting by $\Upsilon_i = [\nabla \mathbf{u}_h(\mathbf{X}_{\mathbf{u}_h}(t))]^\top|_{\kappa_i}$ the gradient transposed for each i, we then have

$$\mathbf{Z}(t) = \mathtt{exp}(\Upsilon_N(t_N - t))\mathbf{Z}(t_N) \quad \forall t \in (t_{N-1}, t_N]. \tag{7.17}$$

By putting $t = t_{N-1}$ in (7.17), we can evaluate $\mathbf{Z}(t_{N-1}^+)$. The jump condition in (7.4) can be rearranged for the value of $\mathbf{Z}$ at this time before the particle trajectory $\mathbf{X}_{\mathbf{u}_h}(t)$ crosses into the element κ_N, forwards in time, which is given by

$$\mathbf{Z}(t_{N-1}^-) = \mathbf{Z}(t_{N-1}^+) + \frac{\mathbf{Z}(t_{N-1}^+) \cdot [\![\mathbf{u}_h(t_{N-1})]\!]\mathbf{n}_{N-1}}{\mathbf{u}_h(\mathbf{X}(t_{N-1}^-)) \cdot \mathbf{n}_{N-1}}. \tag{7.18}$$

We see that all of the terms on the right–hand–side of the equality in (7.18) are known (also, the orientation of the normal vector $\mathbf{n}_{N-1}$ to the element interface does not matter since it appears both in the numerator and denominator). On the next (or previous, from the perspective of the particle trajectory) element, κ_{N-1}, we restrict to the time interval (t_{N-2}, t_{N-1}) and solve similarly. Now, using $\mathbf{Z}(t_{N-1}^-)$ as the final–time condition to obtain

$$\mathbf{Z}(t) = \mathtt{exp}(\Upsilon_{N-1}(t_{N-1} - t))\mathbf{Z}(t_{N-1}^-) \quad \forall t \in (t_{N-2}, t_{N-1}).$$

One then follows this procedure for all time intervals up to and including $(0, t_1)$. In general, for a piecewise linear velocity field $\mathbf{u}_h$, we may hence write

$$\mathbf{Z}(t) = \mathtt{exp}(\Upsilon_i(t_i - t))\mathbf{Z}(t_i^-) \quad \forall t \in (t_{i-1}, t_i). \tag{7.19}$$

When $\mathbf{u}_h$ is, for example, piecewise polynomial with a higher degree, or some other general function, then (7.19) does not apply since the matrices Υ_i will not be constant. Instead, one could employ a time–stepping technique within each time interval to solve for the adjoint solution $\mathbf{Z}(t)$; time–stepping from $\mathbf{Z}(t_i^-)$ until $\mathbf{Z}(t_{i-1}^+)$, using this to generate the next starting position $\mathbf{Z}(t_{i-1}^-)$, and so forth.

We note as well that the integral (7.16) can be reduced to a sum of integrals over these time–intervals for which the trajectory intersects the support of the function $\mathbf{v}$. This is especially useful when $\mathbf{v}$ is, for example, a finite element basis function, which has support on only a few elements of which either all or just one might intersect the trajectory. Because of this, and the need to compute $\mathbf{Z}(t)$ in the fashion stated above, the right–hand–side vector in (6.25) can easily be assembled by looping over these intersected elements in the same backwards fashion as described here.

7.4 A cautionary numerical experiment

For a couple of choices of simple, linear functionals, numerical experiments in Section 6.6 revealed a lack of sharpness for the indicators η_κ, defined in Theorem 6.4, under an RT_0 implementation. With this in mind, we present here an experiment for the travel time functional, in which the velocity approximation is considered only in BDM_1. The approximate adjoint solutions are sought in spaces defined on the same mesh as the primal discrete solutions, with polynomial degree one higher (cf. problems (6.22) and (6.25), with $k = 1$).

The purpose of the following examples is to utilise the linearisation result stated in Theorem 7.2 within the context of goal–oriented adaptivity of Darcy's equations. We are interested in the accurate estimation of the discretisation error induced by numerically approximating the travel time $\mathfrak{T}(\mathbf{u}; \mathbf{x}_0)$, for a given burial point $\mathbf{x}_0 \in \Omega$.

To this end, on the unit square $\Omega = (0, 1)^2$, we set up the primal problem (6.21), or (3.8, 3.9), so that the pressure solution is given exactly by

$$p = \cos(x)\cos(y) + x^4 y^3,$$

with associated Darcy velocity $\mathbf{u} = -\nabla p$. The initial position of the particle is set at the point $\mathbf{x}_0 = (0.23, 0.36)$; the exact travel time, $\mathfrak{T}([\mathbf{u}, p])$, is computed using Matlab's `ode45` function, whose adaptive time–stepping is employed to approximate the exact travel time to a high precision.

In Section 6.6 a Dörfler marking strategy was used to identify those elements suitable for adaptive mesh refinement. Here, we require a marking strategy that is less picky with its element selection, and instead choose to employ a fixed-fraction marking strategy. The refinement percentage is set to 10%; that is, elements corresponding to the top 10% largest values of $|\eta_\kappa|$ are those that are selected for refinement. A change in the marking strategy is a heuristic choice: in this example, using a Dörfler strategy, it appeared that most of the contribution to $\mathcal{S} = \sum_\kappa |\eta_\kappa|$ came from a few elements near the start of the particle

path; subsequent refinements were around the path, as expected, but occurred in patches. To avoid, in subsequent refinements, small elements being placed next to large ones, we switch to a fixed–fraction marking strategy; in this experiment, such marking leads to most elements on the travel path being marked for refinement, per loop of the adaptive routine.

Figure 7.2 shows the streamline $P(\mathbf{u}_h; \mathbf{x}_0)$ computed on the initial mesh, and the final mesh obtained under the adaptive regime[8]; refinement looks to take place on and around the travel path of the particle, which is completely expected. Indeed, Table 7.2 and the right loglog plot in Figure 7.3 shows that the adaptive algorithm looks to be convergent. We see for adaptive refinement effectivity indices very close to 1, showing that the error estimate (6.27) is reliably predicting the error in travel time approximation.

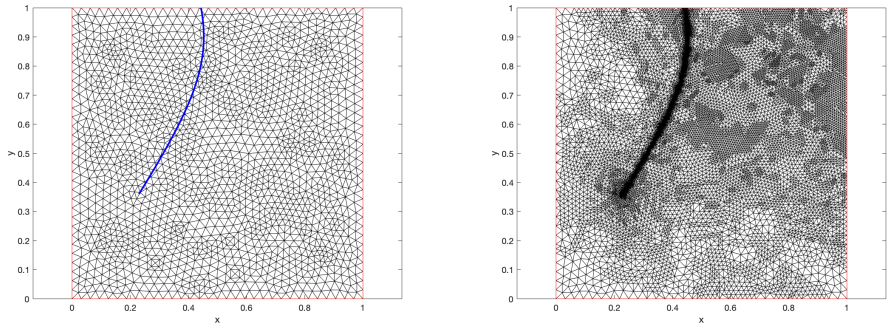

FIG. 7.2 – *Initial mesh and streamline, and the final adaptive mesh.*

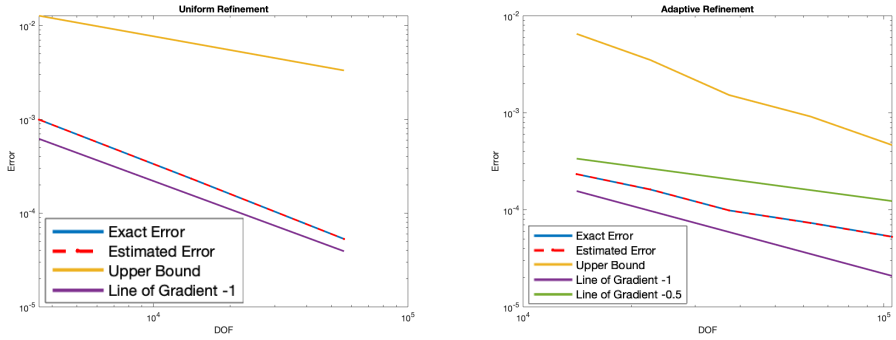

FIG. 7.3 – *Loglog plots: left has uniform refinement; right has adaptive refinement.*

Looking at the left loglog plot in Figure 7.3, it looks like the error converges optimally with order $\mathcal{O}(h^2)$, under uniform refinement. One would perhaps not expect this considering the apparent irregularity of the adjoint solution approximations shown in Figure 7.4. We also notice, according to the same loglog plot and in Table 7.1, that the indicators η_κ are no

[8]We apply the same adaptive loop as described in Section 6.6, but now using a fixed–fraction marking strategy in place of the Dörfler strategy employed previously.

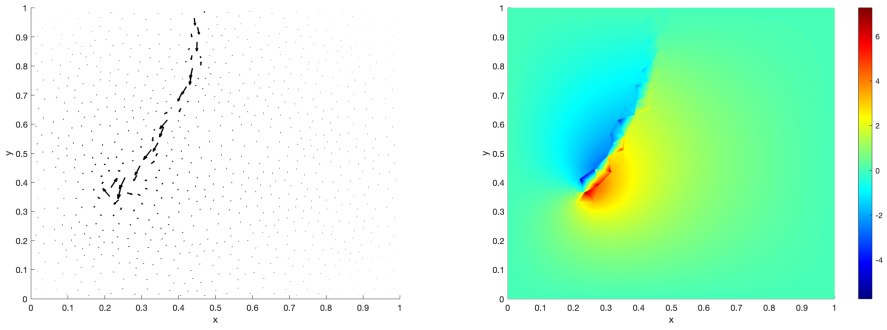

FIG. 7.4 – *Coarse approximations of the adjoint solutions.*

TABLE 7.1 – *Results obtained under uniform refinement.*

Number of DOF	**Error**	**Est. Error**	$\mathcal{S}$	θ_h	$\theta_{\geq}$
3552	-9.9260×10^{-4}	-9.9931×10^{-4}	1.2725×10^{-2}	1.0005	12.8200
14080	-2.3335×10^{-4}	-2.3346×10^{-4}	6.5011×10^{-3}	1.0005	27.9010
56064	-5.3057×10^{-5}	-5.3025×10^{-5}	3.3324×10^{-3}	0.9994	62.6570

longer sharp; indeed, it looks like the bounded sum $\mathcal{S}$ converges like $\mathcal{O}(h)$. This is evidenced by the bounded effectivity indices $\theta_{\geq}$ which seem to blow–up in this case.

Looking at the right loglog plot in Figure 7.3, we see what looks to be a decrease in the rate of convergence of the error under adaptive refinement. This rate looks somewhere between $\mathcal{O}(\mathfrak{N}^{-1})$ and $\mathcal{O}(\mathfrak{N}^{-1/2})$; the latter of which corresponds to $\mathcal{O}(h)$ on quasi–uniform meshes. It is difficult to tell in this case whether or not the indicators are sharp. Indeed, the bounded effectivities in Table 7.2 look like they may be converging to some fixed value, but more refinements are required to be able to say for sure. We note also the slope of the bounded sum $\mathcal{S}$ in the right loglog plot of Figure 7.3 looks steeper than that of the error; either this is pre–asymptotic and the slopes will eventually match, or with subsequent refinements $\mathcal{S}$ may fail as an upper bound for the error.

A convergence study in [95] shows this same, optimal, rate of convergence, under uniform refinement, but for divergence–free velocities. However, we note that it is not completely clear which rate of convergence we should even expect to see for the travel time functional in the first place, and it may well be problem sensitive. Indeed, the travel time functional is nonlinear and unbounded, so the theory presented in Section 6.1 may not completely hold true for this choice of functional. Moreover, as noted by [43, p. 94], the well–posedness of the adjoint problems (6.22), (6.24) and (6.25) still need addressing and, in particular, the regularity of the adjoint solutions themselves requires more investigation.

In Figure 7.4 is shown (coarse) approximations of the adjoint solutions, $\mathbf{z}_h$ and r_h, respec-

TABLE 7.2 – *Results obtained under adaptive refinement.*

Number of DOF	**Error**	**Est. Error**	$\mathcal{S}$	θ_h	$\theta_{\geq}$
14080	-2.3335×10^{-4}	-2.3346×10^{-4}	6.5107×10^{-3}	1.0005	27.9010
22542	-1.6199×10^{-4}	-1.6232×10^{-4}	3.4993×10^{-3}	1.0020	21.6020
37277	-9.8650×10^{-5}	-9.8554×10^{-5}	1.5234×10^{-3}	0.9990	15.4330
62627	-7.3444×10^{-5}	-7.3230×10^{-5}	9.1654×10^{-4}	0.9971	12.4790
105346	-5.2956×10^{-5}	-5.2749×10^{-5}	4.6569×10^{-4}	0.9961	8.7939

tively. There looks to be a discontinuity along the path for the adjoint pressure; we also notice that both solutions pretty much vanish away from the travel path. These solutions can be interpreted as generalised Green's functions for the travel time functional and Darcy's equations: [43, p. 85] agrees that we might expect to see a δ–type source or sink along the travel path.

Regarding the regularity of the adjoint solutions, some work has been undertaken on an experimental basis. Pictured in Figure 7.5, are the measurements of the norms $\|\mathbf{z}_h - \Pi_h \mathbf{z}_h\|_{H(\mathrm{div},\Omega)}$ and $\|r_h - P_h r_h\|_{L^2(\Omega)}$. A first, interesting observation to make is that the approximate adjoint pressure r_h behaves quite well: the error $\|r_h - P_h r_h\|_{L^2(\Omega)}$ decays with its optimal rate under adaptive refinement, and while losing some rate under uniform refinement, still converges. However, the same cannot be said for the approximate adjoint velocity $\mathbf{z}_h$. We see here that $\|\mathbf{z}_h - \Pi_h \mathbf{z}_h\|_{H(\mathrm{div},\Omega)}$ grows as the mesh refines; upon further investigation, and pictured in Figure 7.6, we see also a growth in $\|\mathbf{z}_h\|_{H(\mathrm{div},\Omega)}$ under mesh refinement, both uniform and adaptive.

The slow growth of $\|\mathbf{z}_h - \Pi_h \mathbf{z}_h\|_{H(\mathrm{div},\Omega)}$ does not seem to have a devastating effect on the error estimate (6.27) but might be responsible for the lack of sharpness witnessed under uniform refinement, as well as the loss of rate witnessed in an adaptive refinement. If this term instead decayed under mesh refinement, then we might expect to witness results more along the lines of Experiment I in Section 6.6.

A conjecture for this apparent convergence issue with the adjoint velocity $\mathbf{z}_h$ is that there is an *adjoint inconsistency*. The adjoint velocities $\mathbf{z}$ and $\mathbf{z}_\star$ might not be functions in $H(\mathrm{div}, \Omega)$ to begin with; moreover, we should seek the solution to the adjoint problems (6.23) and (6.24) in a different, less regular, function space (perhaps in $[H^{-1}(\Omega)]^2$, for example). While not pictured, the same terms shown in Figures 7.5 and 7.6, were measured in the $[L^2(\Omega)]^2$–norm and divergence was witnessed here as well.

We re–iterate that despite the above discussion, the proposed error estimator (6.27) still reliably predicts the error in the quantity of interest, in the case of the travel time functional,

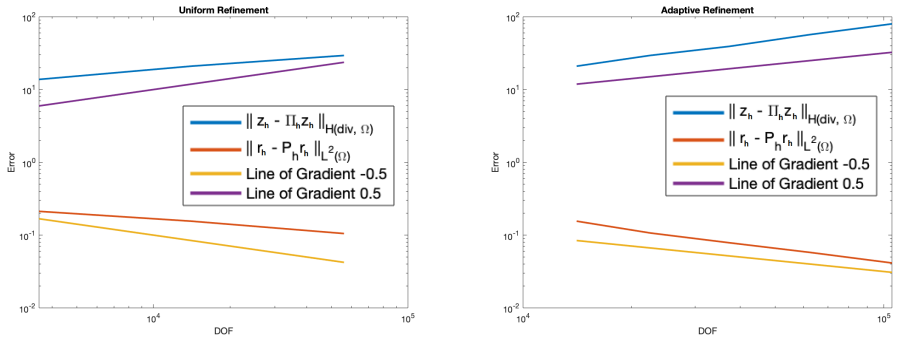

FIG. 7.5 – *Convergence of adjoint error terms.*

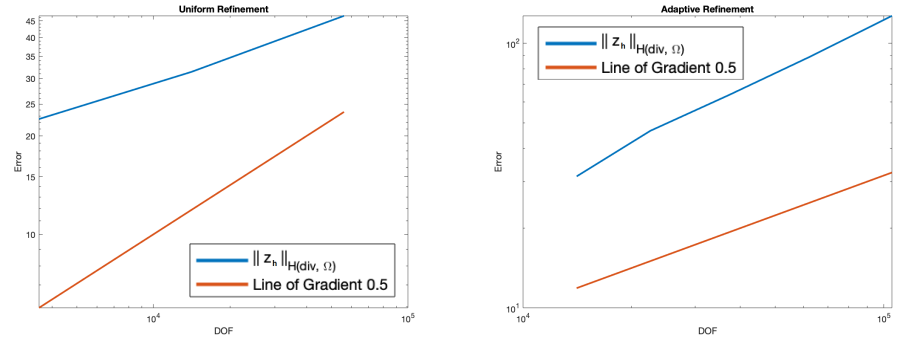

FIG. 7.6 – *Evaluation of the $H(div, \Omega)$ norm of the adjoint approximation $\mathbf{z}_h$.*

on every mesh employed in this example. The irregularity of the adjoint velocity, and its approximations, seems to have influence only for the indicators η_κ and their sharpness; therefore, the particulars of obtaining optimal meshes and the *correct* choice of adaptive routine remains an open problem.

7.5 Main numerical examples

The following numerical examples comprise those showcased in the published article [73]. As was the case in the previous example, in Section 7.4, fixed–fraction marking is utilised in Example III with a refinement selection of `REF` $= 10\%$, together with the standard red–green, regular, refinement strategy for triangular elements.

Again, we set $k = 1$ in problems (6.22) and (6.25) to obtain the approximate solutions to the primal and (linearised) adjoint problems; moreover, we still set $\mathbf{z}_I$ and r_I as the usual (interpolated) projections of $\mathbf{z}_h$ and r_h into the primal discrete space $\mathscr{W}_h^k$, under a BDM_k approximation.

In practice, we have observed that an RT_k approximation gives rise to quantitatively similar

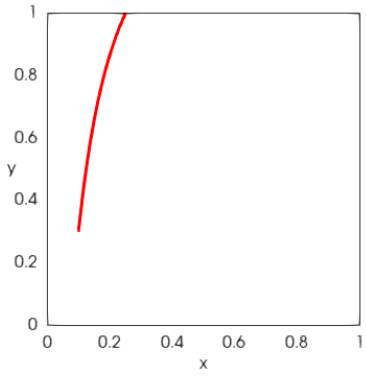

FIG. 7.7 – *Example I: Approximate particle trajectory on the final mesh. Cf. [73].*

results to those attained in our chosen BDM_k setting. Indeed, due to the property that $RT_k(\kappa) \subset BDM_{k+1}(\kappa) \subset RT_{k+1}(\kappa)$ for all $k \geq 0$ the vector–valued space constructed with $RT_k(\kappa)$ elements (vs. using $BDM_{k+1}(\kappa)$ elements) will have fewer degrees of freedom on a fixed triangulation of the domain. Moreover, the difference in the quality of approximation is only really seen in $[L^2(\Omega)]^2$; with the choice of $BDM_{k+1}(\kappa)$ elements, the error converges at higher–order, as the mesh is refined, compared with their $RT_k(\kappa)$ counterparts. The rate of convergence of the error, when measured in the $H(\mathrm{div}, \Omega)$ norm, is identical for both spaces.

7.5.1 Example I: A simple test case

This first example considers a very simple problem for which we know the value of the exact travel time $\mathfrak{T}(\mathbf{u}; \mathbf{x}_0)$. The travel time is approximated on a series of uniformly refined triangulations, in order to validate the proposed error estimate (6.27). To this end, let $\Omega = (0, 1)^2$; we impose appropriate boundary conditions, so that the exact Darcy velocity is given by $\mathbf{u} = [\sin(x)\cos(y)]^\top$. The porosity is set to be $\phi = 1$ everywhere so that the Darcy and transport velocities coincide. Furthermore, the de–coupling of the IVP for the particle trajectory $\mathbf{X}_\mathbf{u}(t)$ means that we can evaluate exactly the travel time for some choice of $\mathbf{x}_0 \in \Omega$. Selecting $\mathbf{x}_0 = (0.1,\ 0.3)$ gives

$$\mathfrak{T}(\mathbf{u}; \mathbf{x}_0) = \log\left(\frac{\tan(1) + \sec(1)}{\tan(0.3) + \sec(0.3)}\right) \approx 0.9216\ldots,$$

cf. Figure 7.7 which depicts the particle trajectory.

The results featured in Table 7.3 show the exact travel time error, the error estimate, and the resulting effectivity index on each of the uniform meshes employed for this example. Indeed, here we observe that the effectivity indices are extremely close to unity on each of the meshes, thereby demonstrating that the error estimate accurately predicts the travel

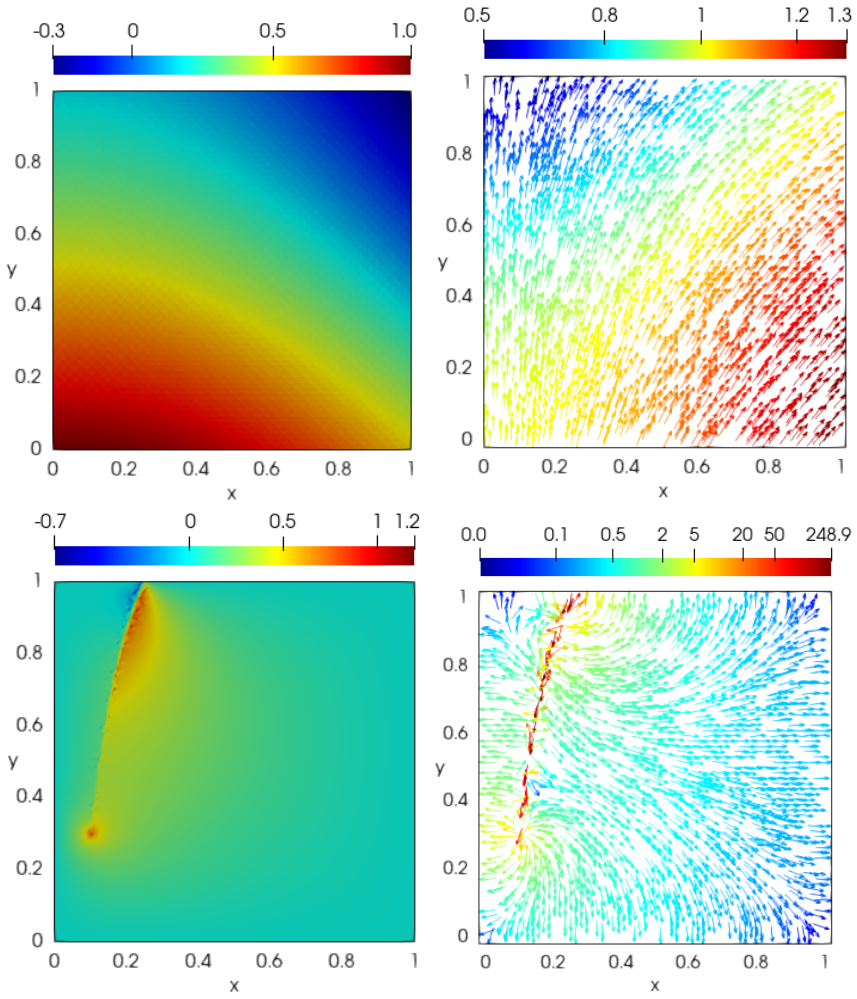

FIG. 7.8 – *Example I: Primal (top) and adjoint (bottom) pressure and velocity approximations on the final mesh. Cf. [73].*

TABLE 7.3 – *Example I: Results employing the BDM_1 finite element space.*

Number of DOFs	**Error**	**Est. Error**	θ_h
20	-8.274×10^{-3}	-8.476×10^{-3}	0.976
72	1.358×10^{-3}	1.360×10^{-3}	0.998
272	-3.155×10^{-5}	-2.818×10^{-5}	1.120
1056	-1.894×10^{-5}	-1.899×10^{-5}	0.997
4160	-2.085×10^{-6}	-2.084×10^{-6}	1.001
16512	-9.310×10^{-7}	-9.308×10^{-7}	1.000

time error in this simple example, even on particularly coarse meshes with less than 50 degrees of freedom.

The primal and adjoint pressure and velocity approximations on the final mesh are depicted

TABLE 7.4 – *Example II: Results employing the BDM_1 finite element space.*

Number of DOFs	**Error**	**Est. Error**	θ_h
198	1.188×10^{-3}	1.719×10^{-3}	0.691
764	4.773×10^{-4}	4.534×10^{-4}	1.053
3000	7.891×10^{-5}	8.178×10^{-5}	0.965
11888	1.255×10^{-5}	1.294×10^{-5}	0.970
47328	4.261×10^{-6}	4.460×10^{-6}	0.955
188864	-2.694×10^{-7}	-2.694×10^{-7}	1.000

in Figure 7.8. In particular, the adjoint solution approximations are highly discontinuous along, and near, the path $P(\mathbf{u}_h; \mathbf{x}_0)$. Indeed, close to $\mathbf{x}_0$ is a source–like feature, where the adjoint velocity travels backwards along the path to the initial position. Close to $P(\mathbf{u}_h; \mathbf{x}_0)$ we see that part of the adjoint velocity is pointing in the same direction as the primal Darcy velocity. These adjoint solutions vanish away from the path and may be interpreted as generalised Green's functions; in particular, the adjoint pressure looks to be bounded, while the adjoint velocity resembles more a Dirac–type measure.

7.5.2 Example II: A two–layered geometry

Similar to Example I, this numerical experiment considers a simple geometry and problem set–up in order to further validate the proposed error estimate (6.27) under uniform refinement. Here, the domain Ω, pictured in Figure 7.9, is defined by $\Omega = \{(x, y) \in \mathbb{R}^2 : 0 < x < 1,\ 0 < y < 1 - \frac{x}{10}\}$. Along the line $y = 1/2$ the domain is partitioned into the two sub–domains Ω_i, $i = 1, 2$, representing different types of rock. That is, the top layer consists solely of Calder Sandstone, while the bottom contains St. Bees Sandstone. To each of the sub–domains we assign a fixed, constant, permeability and porosity (cf. Example III), given by the dataset used in [42]. Furthermore, we assume that the triangulation $\mathscr{T}_h$ is aligned with the interface between Ω_1 and Ω_2. If this were not the case, then additional sub–partitions of the elements intersected by the interface would be required in order to allow for the use of standard quadrature and streamline tracing techniques (on this sub–partition) which are employed in these examples.

This example can be considered to be a simpler version of Example III, in which we apply the same boundary conditions. Along the top of the domain we impose atmospheric pressure, and no–flow out of the rest of the boundary. The burial point is chosen to be $\mathbf{x}_0 = (0.1,\ 0.1)$ and we set $f = 0$ in Darcy's equations (3.1)–(3.4). Unlike the previous example, the exact travel time $\mathfrak{T}(\mathbf{u}; \mathbf{x}_0)$ is not known in this case; instead, we use an approximation on the final mesh.

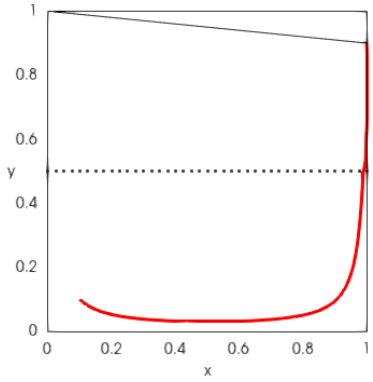

FIG. 7.9 – *Example II: Approximate particle trajectory on the final mesh.*

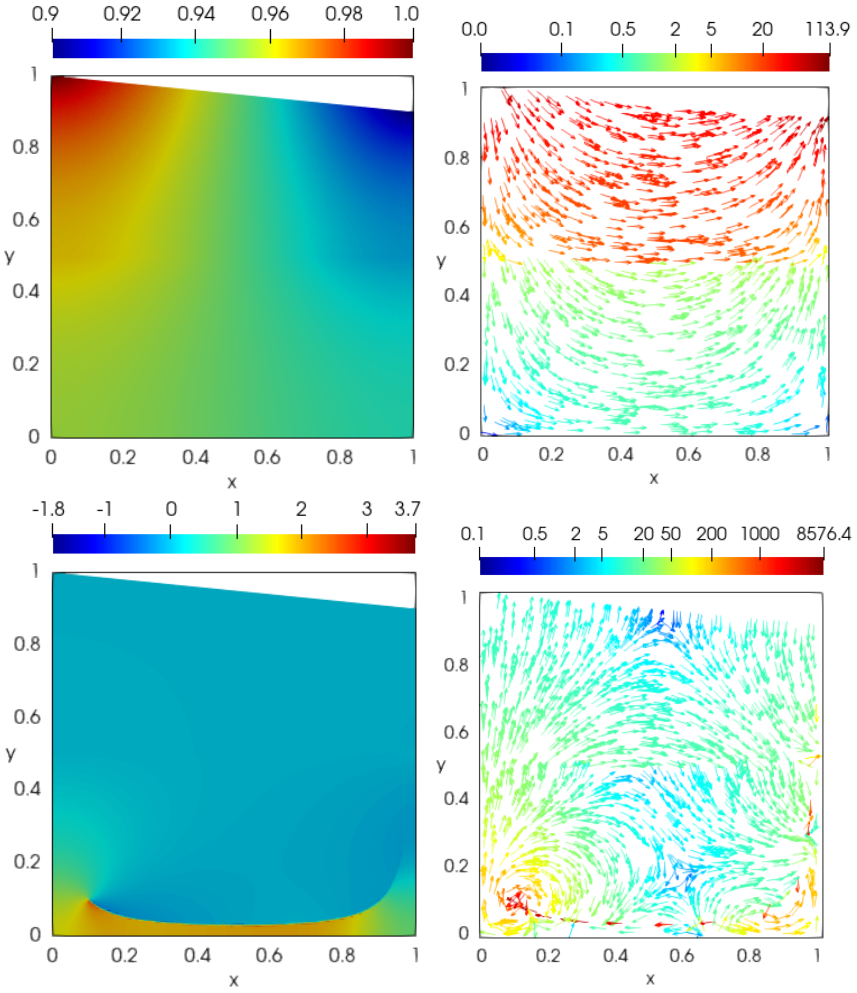

FIG. 7.10 – *Example II: Primal (top) and adjoint (bottom) pressure and velocity approximations on the final mesh. Cf. [73].*

The results presented in Table 7.4 again show that the proposed error estimate reliably predicts the size of the error, with effectivity indices close to unity on each of the meshes

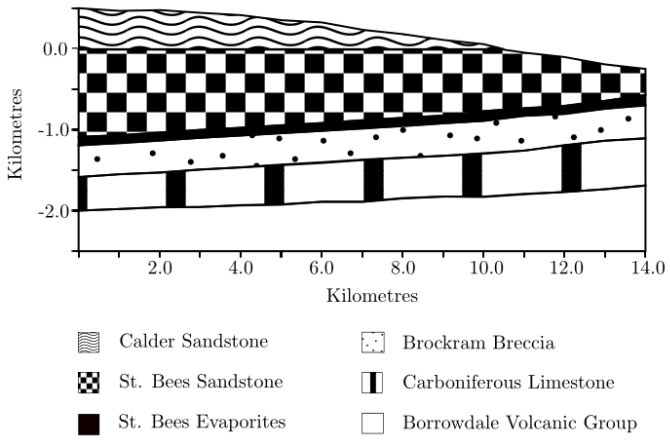

FIG. 7.11 – *Example III: The domain* Ω*, inspired by Sellafield; Cf. [42].*

employed. Although it looks as if the trajectory is exiting the domain parallel to the boundary (cf. Figure 7.9), the performance of the error estimator does not deteriorate in this setting.

The behaviour of the adjoint solution approximations, pictured in Figure 7.10, is similar to that witnessed in the adjoint approximations in Example I. Here, the sink, or source–like feature at $\mathbf{x}_0$ appears to be more noticeable.

7.5.3 Example III: Inspired by the Sellafield site

In this example, the domain Ω is defined as being the union of six sub–domains Ω_i, $i = 1, 2, \ldots, 6$, each representing a different type of rock. Each of these layers is assumed to have a given fixed, constant, porosity ϕ and permeability $\mathbf{k}$ related to the hydraulic conductivity $\mathbf{K}$ (cf. Section 7.3 and Chapter 3, respectively) by $\mathbf{K} = \rho g/\mu \mathbf{k}$, where ρ, g, and μ are the density of water, acceleration due to gravity, and kinematic velocity of water, respectively; the data for each of these is taken from [42]. As in Example II, we assume here that the triangulation $\mathscr{T}_h$ is aligned with each of the interfaces between all of the sub–domains.

We briefly mention that the domain Ω is merely inspired by the geological units found at the Sellafield site and in no way is physically representative of it; therefore, we draw no conclusions of real–life consequence within this numerical example in the context of the post–closure safety assessments of potential radioactive waste burial sites. Furthermore, this experiment merely aims to reproduce similar results previously obtained in [42] in order to verify the main linearisation result presented in Theorem 7.2. More details concerning this problem, as well as a more complex version of this test case, can be found in [42] where the permeability per layer was considered variable, but still constant per element.

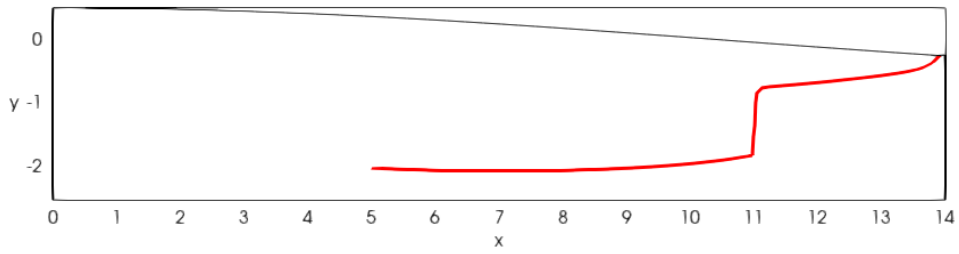

FIG. 7.12 – *Example III: Particle trajectory approximation on the initial mesh. Cf. [73].*

TABLE 7.5 – *Example III: Results employing the BDM_1 finite element space.*

Number of DOFs	Error	Est. Error	Eff. Index
22871	-8.905×10^{-5}	-5.970×10^{-5}	1.492
32624	-5.455×10^{-6}	-4.421×10^{-6}	1.234
47053	4.065×10^{-6}	4.382×10^{-6}	0.928
69887	-2.140×10^{-7}	-2.206×10^{-7}	0.970
1.0755×10^{5}	-4.216×10^{-8}	-4.326×10^{-8}	0.974
1.6796×10^{5}	-1.330×10^{-8}	-1.468×10^{-8}	0.906
2.6631×10^{5}	-8.280×10^{-9}	-8.280×10^{-9}	1.000

Here, we let $\partial\Omega^D$ be the top of the domain, representing the surface of the site, and let $\partial\Omega^N$ be the remainder of the boundary, as pictured in Figure 7.11. We make the same assumptions as [42]: the rock below the stratum consisting of Borrowdale Volcanic Group type is of much lower permeability than all of the other layers; there is a flow divide on the left and right edges of the domain; the pressure at the top of the domain is prescribed via $g_D = p_{\text{atm}}/\rho g + y$; the source term f is set equal to zero. The travel time path computed on the initial mesh is depicted in Figure 7.12.

Remark 7.10. *We note that for implementation purposes, and in the interest of reproducibility, atmospheric pressure $p_{atm} = 1.013 \times 10^5 Pa$ and other quantities entering the problem, are non–dimensionalised using the mass, length and time characteristic scales given by mass $= 1$, length $= 10^{-3}$, time $= 1/3155760000000$. Furthermore, the boundary condition is also translated to $g_D = p_{atm}/\rho g - (500 - 1000y)/1000$.*

In Table 7.5 we present the performance of the adaptive routine when approximating the travel time functional. The exact travel time $\mathfrak{T}(\mathbf{u}; \mathbf{x}_0)$ is based on the approximation computed on the final mesh and the computed error estimator; on this basis the exact travel time is approximately 0.49, which when written in the appropriate units corresponds to around 0.49×10^5 years. We can see from these results that the effectivity indices computed on all meshes are close to unity, indicating that the approximate error estimate (6.27) leads to reliable error estimation, similar to the previously undertaken work in [42]. We see that

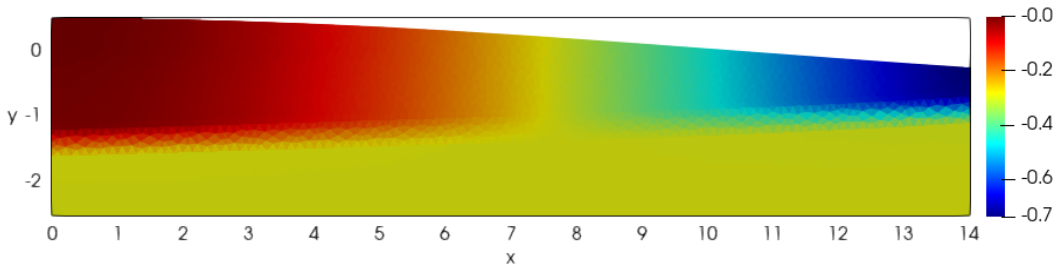

FIG. 7.13 – *Example III: Pressure approximation on the initial mesh. Cf. [73].*

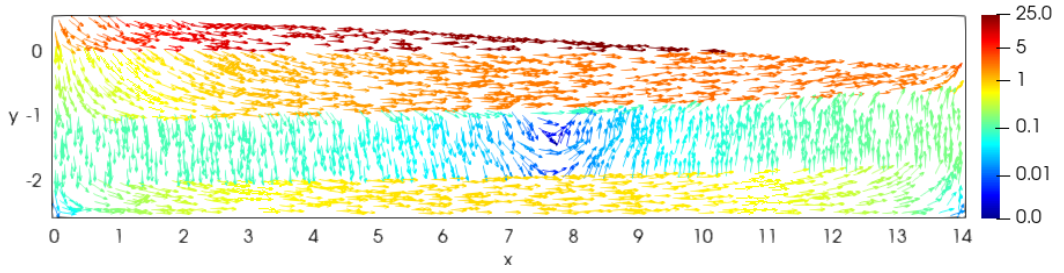

FIG. 7.14 – *Example III: Velocity approximation on the initial mesh. Cf. [73].*

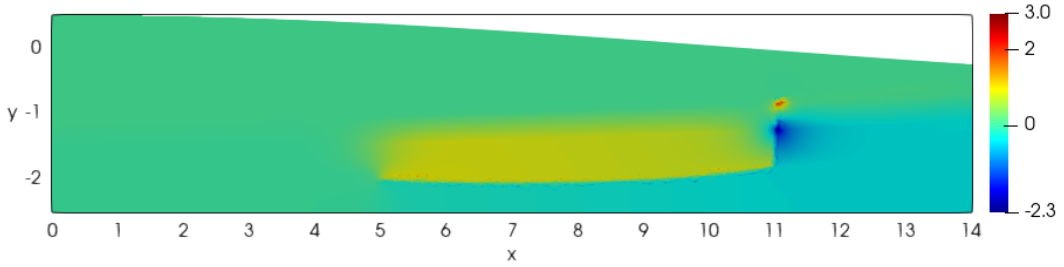

FIG. 7.15 – *Example III: Adjoint pressure approximation on the initial mesh. Cf. [73].*

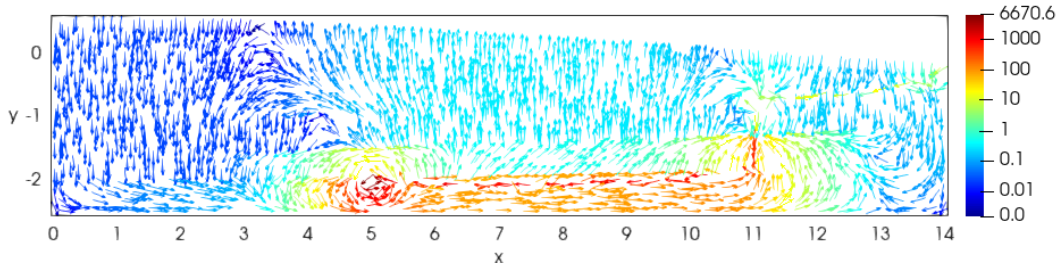

FIG. 7.16 – *Example III: Adjoint velocity approximation on the initial mesh. Cf. [73].*

for this physically motivated example we are able to estimate the error in the travel time functional very closely.

Figures 7.13 and 7.14 show the computed approximations $(\mathbf{u}_h, p_h) \in \mathscr{W}_h^1$ on the initial mesh. Again, here we observe discontinuities in the Darcy velocity across the rock layer interfaces, with the velocities differing by orders of magnitude within each of the strata. We also see a

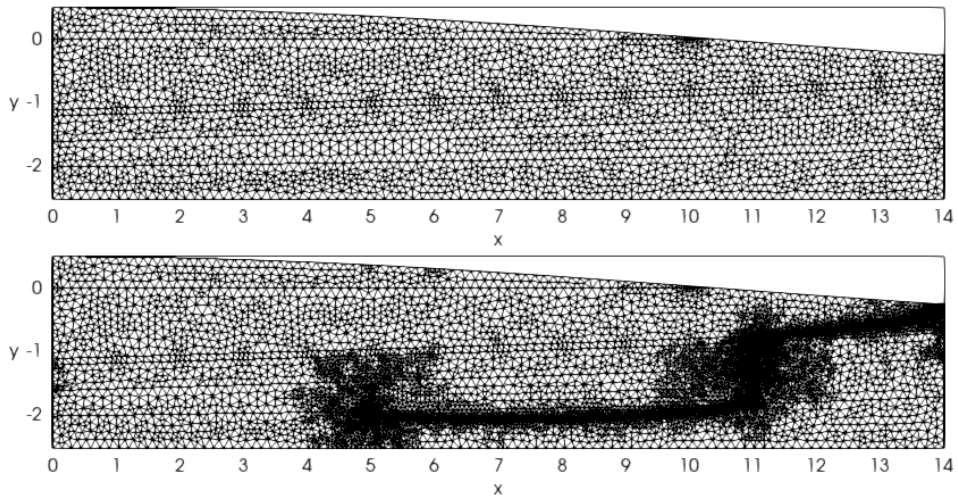

FIG. 7.17 – *Example III: Initial and final adaptively refined meshes. Cf. [73].*

local stationary point in the pressure near the center of the domain which accounts for the change in direction of the groundwater flow; indeed, in this region the flow moves upwards and thus could transport the buried nuclear waste back up to the surface of the site.

Figures 7.15 and 7.16 plot the computed adjoint approximations $(\mathbf{z}_h, r_h) \in \mathscr{W}_h^2$. As concurred by [42] we see a strong discontinuity along the direction of the trajectory $\mathbf{X}_{\mathbf{u}_h}$, and with both the adjoint velocity and pressure approximations vanishing away from the path $P(\mathbf{u}_h; \mathbf{x}_0)$. Close to the initial release point $\mathbf{x}_0$ we see what looks to be a source–like feature in the adjoint velocity approximation, and again, in agreement with [42], this velocity points in the same direction as the primal Darcy velocity (approximation) outside of, but close to, the path, but in the opposite direction along the path itself.

Finally, in Figure 7.17 we show the initial mesh and the final, adaptively refined, mesh. As expected, we observe mesh refinement taking place around the initial point $\mathbf{x}_0$, at the exit point, and along the trajectory itself. There is more significant refinement (compared with the rest of the path) where the trajectory changes direction; in these regions there are sharp discontinuities in the Darcy velocity approximation, which may lead to a large discretisation error of the primal Darcy problem. Such large errors contribute greatly to the error induced in the travel time functional and as such, is targeted more for refinement when compared with the regions containing long horizontal stretches of the trajectory; typically here, the velocity (especially when confined to a single rock layer) appears to be quite smooth.

Chapter 8

Conclusions

Summary

The summary of this thesis will be addressed chapter–by–chapter, skipping over Chapter 2 as a preliminary section of this work.

Chapter 3: Darcy's equations and discretisation

Chapter 3 saw the presentation of well established theory for Darcy's equations as a model for flow in porous media and their approximation by a mixed finite element method. The governing equations were described by a mixed system of elliptic PDEs that were translated into a weak, or variational, formulation in order to define its numerical approximation. The proof of well–posedness for the continuous problem was presented, giving the weak solutions $\mathbf{u} \in H_{0,N}(\mathrm{div}, \Omega)$ and $p \in L^2(\Omega)$. Furthermore, approximation by a mixed finite element method was described for both a Raviart–Thomas (RT) and Brezzi–Douglas–Marini (BDM) element used for the velocity space. We showed, as per standard theory on this topic, discrete well–posedness and convergence for an arbitrary polynomial degree of approximation, for both choice of spaces.

Chapter 4: Flow in fractured porous media

A shift of focus, Chapter 4 saw an extension and adaptation of the existing model for flow in porous media to incorporate fractures as explicit heterogeneities residing in the domain. The model that was presented is a popular choice within the literature since it considers

fractures as lower–dimensional embedded manifolds and, as such, allowed for easy treatment both analytically and numerically. Indeed, we saw the inclusion of networks of intersecting fractures sitting within the porous medium. As was the case in Chapter 3, in this chapter we considered the derivation of a weak formulation of the governing equations, and their subsequent well–posedness. Within this work, the simplifying case of a single fracture was presented, but it was discussed how the result could be extended to the more general case of a network of interesting fractures. Furthermore, in order to establish this rigorously, trace theory for Lipschitz domains with fractures was discussed at length. Moreover, numerical approximation via a mixed finite element method was presented, with the aim of again establishing discrete well–posedness and convergence for the method. This chapter considered only the simplest case of a lowest order RT approximation for the bulk velocity (and hence a continuous linear velocity on the fracture network) in order to clearly showcase the necessary details concerning degrees of freedom and the interpolation of functions into these discrete spaces. The chapter concluded with the statement of convergence in this case.

Chapter 5: Streamlines through fractured porous media

Under the model presented in Chapter 4, in Chapter 5 we presented the procedure in which streamlines can be traced through a porous medium containing fractures. This chapter utilised an existing approach in which the one–dimensional fractures are re–imagined, and expanded, as two–dimensional objects matching the dimension of the domain they reside in. An interpolant, or ansatz, for the velocity field inside the expanded fracture was stated, both in the continuous and discrete settings, which would then be used to trace the streamline through the fracture to give a suitable exit–point, something that was otherwise not possible in the one–dimensional setting. Here, we defined the interpolant such that physical laws were still retained in the expanded fracture: we saw that weak formulations of both Darcy's law and conservation of mass remained satisfied through this process. Concluding this chapter, it was briefly discussed that a limitation of this approach was the apparent dissatisfaction of the strong form of Darcy's law in the expanded setting, even when true in the bulk and one–dimensional fractures themselves. This approach could be implemented in order to trace streamlines in a fractured porous media setting; the retainment of physical laws and the continuity of fluxes on the fracture–bulk boundary means that streamlines through the expanded fracture would be continuous and physical, suitable for application in the travel time problem addressed later in the thesis in the non–fractured setting.

Chapter 6: Goal–oriented estimation for Darcy's equations

Quantities of interest of solutions to Darcy's equations was the focus in Chapter 6. Here, existing standard theory for the dual–weighted–residual (DWR) method was presented for an abstract problem that was then applied to the non–fractured Darcy model, discussed previously in Chapter 3 in this thesis. A computable error estimate for generic quantities of interest was derived and subsequently decomposed over the domain via the underlying mesh in order to define elementwise indicators for use in adaptive refinement. The approach utilised to define these indicators was a simple integration–by–parts of the error estimate, but alternative decompositions were also discussed: a simple approach via the variational localisation and one utilising a partition of unity (PU). A focus of this chapter was a property known as sharpness of the elementwise indicators, and this was investigated for linear quantities of interest in the context of Darcy's equations. Indeed, two numerical examples were presented to estimate the error in quantities of interest under both an RT and BDM velocity approximation and assess the sharpness of the indicators defined by the integration–by–parts approach. Based on the data presented as part of these examples, our recommendation is to only use these indicators with a BDM velocity approximation, since the property of sharpness is retained here but lost when an RT approximation is used instead. We saw this via the quantities defined as bounded effectivity indices, which should converge to some real number under mesh refinement. In all cases, such quantities looked to diverge when an RT velocity was considered. Retaining sharpness under mesh refinement is vital since without it you cannot expect to obtain optimal meshes, nor can you use the error estimate bounded by the triangle equality as a stopping criterion for the routine, something which adds an extra layer of security and certainty when wanting to refine to some user–defined tolerance. Indeed, the development of sharp RT–based indicators remains an open problem. As part of this chapter we gave a possible conjecture for the loss of sharpness under an RT approximation, but this has yet to be confirmed. Indeed, sharpness was proved for a BDM approximation for the PU indicators, and a similar proof holds for the indicators defined by the integration–by–parts. Moreover, the second example in this chapter showed a superconvergence of solution approximations, a consequence of the problem definition. Although sharpness is clearly a problem for indicators under an RT approximation, it was shown in both examples that the DWR error estimate performed very reliably at approximating the error in the quantities of interest, with effectivity indices close to one on all employed meshes.

Chapter 7: The travel time functional

Within Chapter 7, the travel time functional was defined and an exact expression for its derivative was derived. Such an expression was necessary in order to apply the DWR theory previously presented in Chapter 6. Indeed, the aim of this chapter was to accurately simulate the leakage of radioactive waste underground via the error estimation and adaptive treatment of the travel time functional. It was discussed also how streamlines may be computed exactly for a lowest order RT or BDM setting, the latter being the choice within this chapter as per the recommendations of the examples from Chapter 6. Such computations enabled the attainment of travel times for particles in porous media flow and the application of the linearisation result for the travel time functional; the expression for its derivative used an initial–value–problem considered adjoint to the particle trajectories, or streamlines, themselves.

Concluding this chapter was a handful of numerical examples. The first example, labelled as a cautionary numerical experiment, considered a simple domain and problem set–up with the aim of looking at the regularity and convergence of the adjoint solution approximations obtained via the DWR method, for the travel time functional. This example saw, even under a BDM approximation, a loss of sharpness again in the elementwise indicators used in the adaptive refinement. A closer investigation revealed that the adjoint velocity approximation in fact diverges in $[L^2(\Omega)]^2$, giving us an insight into its possible regularity in a space such as $[H^{-1}(\Omega)]^2$ or one even less regular than this. Despite this, the effect of this divergence did not alter the performance of the error estimate itself; indeed, here we still saw effectivity indices close to one on each of the employed meshes, showing that the DWR error estimate still reliably predicts the error in the travel time functional in this setting. Three more examples, each from the article [73], were then presented as well. The purpose of the first two of these was to assess the reliability of the DWR error estimate under uniform mesh refinement in academic–style problem set–ups, as concurred by the cautionary example, the estimate performs very well with effectivity indices close to one on all meshes. The last example within this chapter took place in a domain inspired by real–life units found at the Sellafield site, located in Cumbria in the United Kingdom. Comprised of many layers of rocks, each with differing material properties, this example saw the adaptive refinement of the underlying mesh in order to accurately compute the travel time. Despite this more complicated setting, we observed in this example that the DWR error estimate performs just as well as it did before, with effectivity indices close to one on each of the refined meshes. In each of the examples was visualised the adjoint solution approximations, in which we witnessed a source–like feature close to the initial position of the particle, with these solutions

looking to vanish away from the particle path, or streamline. Sharp discontinuities were observed in the adjoint velocity approximations, resembling Dirac–type measures. In spite of the apparent divergence in the adjoint velocity approximation, suggesting an alternative approach should be utilised for its approximation, the error estimate obtained from the DWR method performed very well even in the more complex setting of the Sellafield inspired example. Although a more suitable avenue would need investigating for the proper adaptive treatment of this problem, concerning the loss of sharpness in the indicators even in the BDM setting, and the regularity concerns of the adjoint velocity approximation, the approach showcased in this chapter clearly highlights the reliability of the error estimation for the travel time functional.

Future work

There are many avenues for continued research based on the work presented within this thesis; here we will state some of them. Firstly, extension of all the implementations within this thesis into three spatial dimensions should be carried out. Moreover, elementwise indicators for Darcy's equations in the DWR method should be defined such that they are sharp under an RT approximation. In doing so, cheaper computational implementations could be achieved compared with using a BDM approximation, with no loss of convergence measured in the H–div norm. Furthermore, the regularity of the adjoint problem associated with the travel time functional should be addressed; this would be very beneficial in understanding how to improve the DWR error estimate and give more insight into the expected rate of convergence of the travel time functional. The well–posedness of this adjoint problem still remains an open question.

In the case of fractured porous media flow, an extension of the work presented here should firstly be to generalise and implement the existing work without fractures up to and including the implementation and adaptive treatment of the travel time functional. Indeed, this would require a different DWR error estimate and definition of elementwise indicators. Adaptive refinement for a problem similar to the Sellafield inspired example incorporating fractures would be a good start on this road to more realistic applications of flow in porous media.

Furthermore, some other extensions of this work could be to, for example, consider other heterogeneities within the domain, such as caves or vugs. Utilising a Darcy–Stokes or Stokes–Brinkman model in these cases will require different analysis to that presented in this thesis, and a separate implementation in order to simulate these different types of domains. Of course, utilising any one of many other numerical methods to approximate flow in fractured porous media such that we are free of restrictions such as grid–inflexibility.

One could also consider an optimisation problem in the travel time setting: with a cost associated with drilling into rocks depending on their depth and material properties, where is a good location to potentially bury radioactive waste such that it is cost effective and either takes a given minimum time to reach the surface, or not at all?

Bibliography

[1] M. Ainsworth and J. Oden, *A posteriori error estimation in finite element analysis*, Computer Methods in Applied Mechanics and Engineering, 142 (1997), pp. 1–88.

[2] A. Al-Najem, E. Pirayesh, M. Y. Soliman, and S. Siddiqui, *Streamlines simulation of barrier fracture as a novel water shutoff technique*, Journal of petroleum exploration and production technology, 3 (2013), pp. 243–254.

[3] C. Alboin, J. Jaffré, J. E. Roberts, X. Wang, and C. Serres, *Domain decomposition for some transmission problems in flow in porous media*, in Numerical Treatment of Multiphase Flows in Porous Media, Berlin, Heidelberg, 2000, Springer Berlin Heidelberg, pp. 22–34.

[4] C. Alboin, J. Jaffré, J. Roberts, and C. Serres, *Modeling fractures as interfaces for flow and transport in porous media*, 295 (2001).

[5] Y. Amanbek, G. Singh, G. Pencheva, and M. F. Wheeler, *Error indicators for incompressible Darcy flow problems using enhanced velocity mixed finite element method*, Computer Methods in Applied Mechanics and Engineering, 363 (2020), p. 112884.

[6] P. Angot, F. Boyer, and F. Hubert, *Asymptotic and numerical modelling of flows in fractured porous media*, ESAIM: M2AN, 43 (2009), pp. 239–275.

[7] P. Antonietti, C. Facciolà, A. Russo, and M. Verani, *Discontinuous Galerkin approximation of flows in fractured porous media on polytopic grids*, SIAM Journal on Scientific Computing, 41 (2019), pp. A109–A138.

[8] P. F. Antonietti, L. Formaggia, A. Scotti, M. Verani, and N. Verzott, *Mimetic finite difference approximation of flows in fractured porous media*, ESAIM: M2AN, 50 (2016), pp. 809–832.

[9] T. Arbogast, L. Cowsar, M. Wheeler, and I. Yotov, *Mixed finite element methods on nonmatching multiblock grids*, SIAM Journal on Numerical Analysis, 37 (2000), pp. 1295–1315.

[10] T. Arbogast, J. Douglas, and U. Hornung, *Derivation of the double porosity model of single phase flow via homogenization theory*, SIAM Journal on Mathematical Analysis, 21 (1990), pp. 823–836.

[11] I. Babuška and T. Strouboulis, *The Finite Element Method and Its Reliability*, Numerical mathematics and Scientific Computation, Clarendon Press, Oxford University Press, New York, 2001.

[12] W. Bangerth and R. Rannacher, *Adaptive Finite Element Methods for Differential Equations*, Lectures in Mathematics. ETH Zürich, Birkhäuser Basel, 2003.

[13] T. P. Barrios and R. Bustinza, *An a posteriori error analysis of an augmented discontinuous Galerkin formulation for Darcy flow*, Numerische Mathematik, 120 (2012), pp. 231–269.

[14] T. P. Barrios, J. M. Cascón, and M. González, *A posteriori error analysis of an augmented mixed finite element method for Darcy flow*, Computer Methods in Applied Mechanics and Engineering, 283 (2015), pp. 909–922.

[15] T. P. Barrios, J. M. Cascón, and M. González, *A posteriori error estimation of a stabilized mixed finite element method for Darcy flow*, in Lecture Notes in Computational Science and Engineering, vol. 108, Springer Verlag, 2015, pp. 13–23.

[16] D. Batista, *Mesh-independent streamline tracing*, Journal of computational physics, 401 (2020), p. 108967.

[17] R. Becker and R. Rannacher, *A feed-back approach to error control in finite element methods: Basic analysis and examples*, East-West J. Numer. Math, 4 (1996), pp. 237–264.

[18] R. Becker and R. Rannacher, *An optimal control approach to a posteriori error estimation in finite element methods*, Acta Numerica, 10 (2001), p. 1–102.

[19] M. Benedetto, S. Berrone, S. Pieraccini, and S. Scialo, *The virtual element method for discrete fracture network simulations*, Computer Methods in Applied Mechanics and Engineering, 280 (2014), p. 135–156.

[20] F. Bengzon, A. Johansson, M. G. Larson, and R. Söderlund, *Simulation of multiphysics problems using adaptive finite elements*, in Applied Parallel Computing.

State of the Art in Scientific Computing, vol. 4699, Springer Berlin Heidelberg, 2007, pp. 733–743.

[21] B. Berkowitz, *Characterizing flow and transport in fractured geological media: A review*, Advances in Water Resources, 25 (2002), pp. 861–884.

[22] C. Bernardi, Y. Maday, and A. Patera, *A new nonconforming approach to domain decomposition : the mortar element method*, Nonlinear partial equations and their applications, (1994), pp. 13–51.

[23] C. Bernardi and A. Y. Orfi, *Finite element discretization of the time dependent axisymmetric Darcy problem*, SeMA Journal, 68 (2015), pp. 53–80.

[24] I. Berre, F. Doster, and E. Keilegavlen, *Flow in fractured porous media: A review of conceptual models and discretization approaches*, Transport in Porous Media, 130 (2019), pp. 215–236.

[25] D. Boffi, F. Brezzi, and M. Fortin, *Mixed Finite Element Methods and Applications*, Springer, Berlin, Heidelberg, 1 ed., 2013.

[26] W. M. Boon, *Conforming Discretizations of Mixed–Dimensional Partial Differential Equations*, PhD thesis, University of Bergen, 2018.

[27] W. M. Boon, J. M. Nordbotten, and I. Yotov, *Robust discretization of flow in fractured porous media*, SIAM Journal on Numerical Analysis, 56 (2018), pp. 2203–2233.

[28] D. Braess and R. Verfürth, *A posteriori error estimators for the Raviart–Thomas element*, SIAM Journal on Numerical Analysis, 33 (1996), pp. 2431–2444.

[29] K. Brenner, J. Hennicker, R. Masson, and P. Samier, *Gradient discretization of hybrid-dimensional Darcy flow in fractured porous media with discontinuous pressures at matrix–fracture interfaces*, IMA Journal of Numerical Analysis, 37 (2016), pp. 1551–1585.

[30] S. Brenner and R. Scott, *The Mathematical Theory of Finite Element Methods*, vol. 15 of Texts in Applied Mathematics, Springer-Verlag Berlin Heidelberg, 1 ed., 2008.

[31] F. Brezzi, J. Douglas, and L. D. Marini, *Two families of mixed finite elements for second order elliptic problems*, Numerische Mathematik, 47 (1985), pp. 217–235.

[32] E. Burman, P. Hansbo, and M. Larson, *A simple finite element method for elliptic bulk problems with embedded surfaces*, Computational Geosciences, 23 (2019).

[33] J. Cao and P. K. Kitanidis, *Adaptive-grid simulation of groundwater flow in heterogeneous aquifers*, Advances in Water Resources, 22 (1999), pp. 681–696.

[34] D. Capatina, R. Luce, H. El-Otmany, and N. Barrau, *Nitsche's extended finite element method for a fracture model in porous media*, Applicable Analysis, 95 (2016), pp. 2224–2242.

[35] T. Carraro and C. Goll, *A goal-oriented error estimator for a class of homogenization problems*, Journal of Scientific Computing, 71 (2017), pp. 1169–1196.

[36] C. Carstensen, *A posteriori error estimate for the mixed finite element method*, Mathematics of Computation, 66 (1997), pp. 465–476.

[37] J. M. Cascon, C. Kreuzer, R. H. Nochetto, and K. G. Siebert, *Quasi-optimal convergence rate for an adaptive finite element method*, SIAM Journal on Numerical Analysis, 46 (2008), pp. 2524–2550.

[38] H. Chen, T. Onishi, F. Olalotiti-Lawal, and A. Datta-Gupta, *Streamline tracing and applications in embedded discrete fracture models*, Journal of Petroleum Science & Engineering, 188 (2020), p. 106865.

[39] H. Chen, A. Salama, and S. Sun, *Adaptive mixed finite element methods for Darcy flow in fractured porous media*, Water Resources Research, 52 (2016), pp. 7851–7868.

[40] H. Chen and S. Sun, *A residual-based a posteriori error estimator for single-phase Darcy flow in fractured porous media*, Numerische Mathematik, 136 (2017), pp. 805–839.

[41] W. Chen and Y. Wang, *A posteriori error estimate for the H(div) conforming mixed finite element for the coupled Darcy–Stokes system*, Journal of Computational and Applied Mathematics, 255 (2014), pp. 502–516.

[42] K. A. Cliffe, J. Collis, and P. Houston, *Goal-oriented a posteriori error estimation for the travel time functional in porous media flows*, SIAM Journal on Scientific Computing, 37 (2015), pp. B127–B152.

[43] J. Collis, *Error estimation for PDEs with random inputs*, PhD thesis, University of Nottingham, December 2014.

[44] C. Cordes and W. Kinzelbach, *Comment on "application of the mixed hybrid finite element approximation in a groundwater flow model: Luxury or necessity?" by R. Mosé, P. Siegel, P. Ackerer, and G. Chavent*, Water Resources Research, 32 (1996), pp. 1905–1909.

[45] C. D´Angelo and A. Scotti, *A mixed finite element method for Darcy flow in fractured porous media with non-matching grids*, ESAIM: M2AN, 46 (2012), pp. 465–489.

[46] M. Del Pra, A. Fumagalli, and A. Scotti, *Well posedness of fully coupled fracture/bulk Darcy flow with xfem*, SIAM Journal on Numerical Analysis, 55 (2017), pp. 785–811.

[47] D. A. Di Pietro, L. Formaggia, and R. Masson, *Polyhedral Methods in Geosciences*, 27, Springer International Publishing, 1 ed., 2021.

[48] D. A. Di Pietro, M. Vohralík, and C. Widmer, *An a posteriori error estimator for a finite volume discretization of the two-phase flow*, in Finite Volumes for Complex Applications VI Problems & Perspectives, J. Fořt, J. Fürst, J. Halama, R. Herbin, and F. Hubert, eds., vol. 4 of Springer Proceedings in Mathematics, Springer, Berlin, Heidelberg, 2011, pp. 13–23.

[49] W. Dörfler, *A convergent adaptive algorithm for poisson's equation*, SIAM Journal on Numerical Analysis, 33 (1996), pp. 1106–1124.

[50] K. Eriksson, D. Estep, P. Hansbo, and C. Johnson, *Introduction to adaptive methods for differential equations*, Acta Numerica, 4 (1995), p. 105–158.

[51] A. Ern and J. Guermond, *Finite Elements I: Approximation and Interpolation*, Texts in Applied Mathematics, Springer International Publishing, 2021.

[52] I. Faille, A. Fumagalli, J. Jaffré, and J. E. Roberts, *Model reduction and discretization using hybrid finite volumes for flow in porous media containing faults*, Computational Geosciences, 20 (2016), pp. 317–339.

[53] E. Flauraud, F. Nataf, I. Faille, and M. Roland, *Domain decomposition for an asymptotic geological fault modeling*, Comptes Rendus Mecanique, 331 (2003), pp. 849–855.

[54] L. Formaggia, A. Fumagalli, A. Scotti, and P. Ruffo, *A reduced model for Darcy´s problem in networks of fractures*, ESAIM: M2AN, 48 (2014), pp. 1089–1116.

[55] L. Formaggia, A. Scotti, and F. Sottocasa, *Analysis of a mimetic finite difference approximation of flows in fractured porous media*, ESAIM: M2AN, 52 (2018), pp. 595–630.

[56] N. Frih, V. Martin, J. Roberts, and A. Saada, *Modeling fractures as interfaces with nonmatching grids*, Computational Geosciences, 16 (2012).

[57] N. Frih, J. Roberts, and A. Saada, *Modeling fractures as interfaces: A model for forchheimer fractures*, Computational Geosciences, 12 (2008).

[58] A. Fumagalli, E. Keilegavlen, and S. Scialò, *Conforming, non-conforming and non-matching discretization couplings in discrete fracture network simulations*, Journal of Computational Physics, 376 (2019), pp. 694–712.

[59] A. Fumagalli and A. Scotti, *A numerical method for two-phase flow in fractured porous media with non-matching grids*, Advances in Water Resources, 62 (2013), pp. 454–464. Computational Methods in Geologic CO2 Sequestration.

[60] A. Fumagalli and A. Scotti, *A reduced model for flow and transport in fractured porous media with non-matching grids*, Numerical Mathematics and Advanced Applications 2011, (2013), pp. 499–507.

[61] A. Fumagalli and A. Scotti, *A mathematical model for thermal single-phase flow and reactive transport in fractured porous media*, Journal of Computational Physics, 434 (2021), pp. 110–205.

[62] M. B. Giles and E. Süli, *Adjoint methods for pdes: a posteriori error analysis and postprocessing by duality*, Acta Numerica, 11 (2002), p. 145–236.

[63] H. Hægland, *Streamline methods with application to flow and transport in fractured media*, PhD thesis, University of Bergen, 2009.

[64] H. Hægland, A. Assteerawatt, H. Dahle, G. Eigestad, and R. Helmig, *Comparison of cell- and vertex-centered discretization methods for flow in a two-dimensional discrete-fracture–matrix system*, Advances in Water Resources, 32 (2009), pp. 1740–1755.

[65] H. Hægland, H. Dahle, G. Eigestad, K.-A. Lie, and I. Aavatsmark, *Improved streamlines and time-of-flight for streamline simulation on irregular grids*, Advances in Water Resources, 30 (2007), pp. 1027–1045.

[66] H. Hægland, H. K. Dahle, G. T. Eigestad, M. A. Celia, J. M. Nordbotten, and E. Øian, *Streamline methods on fault adapted grids for risk assessment of storage of CO2 in geological formations*, Zenodo, 2006.

[67] E. Hall, P. Houston, and S. Murphy, *hp-adaptive discontinuous Galerkin methods for neutron transport criticality problems*, SIAM Journal on Scientific Computing, 39 (2017), pp. B916–B942.

[68] R. Hartmann, *Lecture notes: Numerical analysis of higher order discontinuous Galerkin finite element methods*, Institute of Aerodynamics and Flow Technology, DLR (German Aerospace Center), (2008).

[69] R. Hartmann, *Multitarget error estimation and adaptivity in aerodynamic flow simulations*, SIAM Journal on Scientific Computing, 31 (2008), pp. 708–731.

[70] R. Hartmann and P. Houston, *Adaptive discontinuous Galerkin finite element methods for nonlinear hyperbolic conservation laws*, SIAM Journal on Scientific Computing, 24 (2003), pp. 979–1004.

[71] F. Hecht, Z. Mghazli, I. Naji, and J. E. Roberts, *A residual a posteriori error estimators for a model for flow in porous media with fractures*, Journal of Scientific Computing, 79 (2019), pp. 935—968.

[72] W. Hoitinga and E. H. van Brummelen, *Goal-oriented adaptive methods for a boltzmann-type equation*, AIP Conference Proceedings, 1333 (2011), pp. 81–86.

[73] P. Houston, F. Rourke, and K. G. van der Zee, *Linearization of the travel time functional in porous media flows*, SIAM Journal on Scientific Computing, 44 (2022), pp. B531–B557.

[74] P. Houston, D. Schötzau, and T. P. Wihler, *Energy norm a posteriori error estimation of hp-adaptive discontinuous Galerkin methods for elliptic problems*, Mathematical Models and Methods in Applied Sciences, 17 (2007), pp. 33–62.

[75] H. Huang, T. Long, J. Wan, and W. Brown, *On the use of enriched finite element method to model subsurface features in porous media flow problems*, Computational Geosciences, 15 (2011), pp. 721–736.

[76] L. C. Hull and K. N. Koslow, *Streamline routing through fracture junctions*, Water resources research, 22 (1986), pp. 1731–1734.

[77] M. Iding and P. Ringrose, *Evaluating the impact of fractures on the performance of the In Salah CO2 storage site*, International Journal of Greenhouse Gas Control, 4 (2010), pp. 242–248. The Ninth International Conference on Greenhouse Gas Control Technologies.

[78] J. Jaffré, M. Mnejja, and J. Roberts, *A discrete fracture model for two-phase flow with matrix-fracture interaction*, Procedia CS, 4 (2011), pp. 967–973.

[79] M. Jang, J. Lee, J. Choe, and J. M. Kang, *Modeling of solute transport in a single fracture using streamline simulation and experimental validation*, Journal of Hydrology (Amsterdam), 261 (2002), pp. 74–85.

[80] J. Jiang and R. M. Younis, *An improved projection-based embedded discrete fracture model (pedfm) for multiphase flow in fractured reservoirs*, Advances in Water Resources, 109 (2017), pp. 267–289.

[81] R. Juanes and S. F. Matringe, *Unified formulation for high-order streamline tracing on two-dimensional unstructured grids*, Journal of Scientific Computing, 38 (2009), pp. 50–73.

[82] E. Kaasschieter, *Mixed finite elements for accurate particle tracking in saturated groundwater flow*, Advances in Water Resources, 18 (1995), pp. 277–294.

[83] M. Karimi-Fard and L. Durlofsky, *A general gridding, discretization, and coarsening methodology for modeling flow in porous formations with discrete geological features*, Advances in Water Resources, 96 (2016), pp. 354–372.

[84] M. Karimi-Fard, L. Durlofsky, and K. Aziz, *An efficient discrete-fracture model applicable for general-purpose reservoir simulators*, SPE Journal, 9 (2004), pp. 227–236.

[85] R. A. Klausen, A. F. Rasmussen, and A. F. Stephansen, *Velocity interpolation and streamline tracing on irregular geometries*, Computational Geosciences, 16 (2012), pp. 261–276.

[86] M. G. Larson and F. Bengzon, *The Finite Element Method: Theory, Implementation, and Applications*, vol. 10 of Texts in Computational Science and Engineering, Springer-Verlag Berlin Heidelberg, 1 ed., 2013.

[87] M. G. Larson and A. Målqvist, *Goal oriented adaptivity for coupled flow and transport problems with applications in oil reservoir simulations*, Computer Methods in Applied Mechanics and Engineering, 196 (2007), pp. 3546–3561. Special Issue Honoring the 80th Birthday of Professor Ivo Babuška.

[88] M. G. Larson and A. Målqvist, *A posteriori error estimates for mixed finite element approximations of elliptic problems*, Journal of Scientific Computing, 108 (2008), pp. 487–500.

[89] R. J. LeVeque, *Finite Volume Methods for Hyperbolic Problems*, Cambridge Texts in Applied Mathematics, Cambridge University Press, 2002.

[90] L. Li and S. Lee, *Efficient field-scale simulation of black oil in a naturally fractured reservoir through discrete fracture networks and homogenized media*, SPE Reservoir Evaluation and Engineering, 11 (2008), pp. 750–758. cited By 362.

[91] Y. Luo, L. Zhang, Y. Feng, and Y. Zhao, *Three-dimensional streamline tracing method over tetrahedral domains*, Energies (Basel), 13 (2020), p. 6027.

[92] G. Mallik, M. Vohralík, and S. Yousef, *Goal-oriented a posteriori error estimation for conforming and nonconforming approximations with inexact solvers*, Journal of Computational and Applied Mathematics, 366 (2020), p. 112367.

[93] B. Mallison, M. Hui, and W. Narr, *Practical gridding algorithms for discrete fracture modeling workflows*, (2010).

[94] V. Martin, J. Jaffré, and J. E. Roberts, *Modeling fractures and barriers as interfaces for flow in porous media*, SIAM Journal on Scientific Computing, 26 (2005), pp. 1667–1691.

[95] S. F. Matringe, R. Juanes, and H. A. Tchelepi, *Robust streamline tracing for the simulation of porous media flow on general triangular and quadrilateral grids*, Journal of Computational Physics, 219 (2006), pp. 992–1012.

[96] C. McKeown, R. Haszeldine, and G. D. Couples, *Mathematical modelling of groundwater flow at Sellafield, UK*, Engineering Geology, 52 (1999), pp. 231–250.

[97] Z. Mghazli and I. Naji, *Guaranteed a posteriori error estimates for a fractured porous medium*, Mathematics and Computers in Simulation, 164 (2019), pp. 163–179. The 7th International Conference on Approximation Methods and Numerical Modelling in Environment and Natural Resources, held in Oujda, Morocco, May 17-20, 2017.

[98] Z. Mghazli and I. Naji, *Guaranteed a posteriori error estimates for a fractured porous medium*, Mathematics and Computers in Simulation, 164 (2019).

[99] A. Milne, A. Cliffe, D. Holton, P. Houston, C. Jackson, and S. Joyce, *A new method for conditioning stochastic groundwater flow models in fractured media*, Advances in Water Resources, (2010).

[100] F. Morales and R. Showalter, *The narrow fracture approximation by channeled flow*, Journal of Mathematical Analysis and Applications, 365 (2010), pp. 320–331.

[101] I. Mozolevski and S. Prudhomme, *Goal-oriented error estimation based on equilibrated-flux reconstruction for finite element approximations of elliptic problems*, Computer Methods in Applied Mechanics and Engineering, 288 (2015), pp. 127–145.

[102] H. Nick and S. Matthäi, *A hybrid finite-element finite-volume method with embedded discontinuities for solute transport in heterogeneous media*, Vadose Zone Journal, 10 (2011), pp. 299–312.

[103] NIREX, *Options for Radioactive Waste Management that have been Considered by NIREX*, no. N/049, 2002.

[104] J. M. Nordbotten, W. M. Boon, A. Fumagalli, and E. Keilegavlen, *Unified approach to discretization of flow in fractured porous media*, Computational Geosciences, 23 (2019), pp. 225–237.

[105] Nuclear Decommisioning Authority, *Geological Disposal: An Overview of the Generic Disposal System Safety Case*, 2010.

[106] J. Oden and S. Prudhomme, *Goal-oriented error estimation and adaptivity for the finite element method*, Computers & Mathematics with Applications, 41 (2001), pp. 735–756.

[107] A. Y. Orfi and D. Yakoubi, *A posteriori error estimates of finite element method for the time-dependent Darcy problem in an axisymmetric domain*, Computers & Mathematics with Applications, 77 (2019), pp. 2833–2853.

[108] S. L. Painter, C. W. Gable, and S. Kelkar, *Pathline tracing on fully unstructured control-volume grids*, Computational Geosciences, 16 (2012), pp. 1125–1134.

[109] M. Pal, *A unified approach to simulation and upscaling of single-phase flow through vuggy carbonates*, International Journal for Numerical Methods in Fluids, 69 (2012), pp. 1096–1123.

[110] P. Panfili, A. Cominelli, and A. Scotti, *Using embedded discrete fracture models (edfms) to simulate realistic fluid flow problems*, (2013).

[111] R. J. Pawar, G. S. Bromhal, J. W. Carey, W. Foxall, A. Korre, P. S. Ringrose, O. Tucker, M. N. Watson, and J. A. White, *Recent advances in risk assessment and risk management of geologic CO2 storage*, International Journal of Greenhouse Gas Control, 40 (2015), pp. 292–311.

[112] G. Pencheva and I. Yotov, *Balancing domain decomposition for mortar mixed finite element methods*, Numer. Linear Algebra Appl., 10 (2003), pp. 159–180.

[113] P. Popov, Y. Efendiev, and G. Qin, *Multiscale modeling and simulations of flows in naturally fractured karst reservoirs*, Communications in Computational Physics, 6 (2009), pp. 162–184.

[114] S. Prudhomme and J. Oden, *On goal-oriented error estimation for elliptic problems: application to the control of pointwise errors*, Computer Methods in Applied Mechanics and Engineering, 176 (1999), pp. 313–331.

[115] P. A. Raviart and J. M. Thomas, *A mixed finite element method for 2-nd order elliptic problems*, in Mathematical Aspects of Finite Element Methods, I. Galligani and E. Magenes, eds., Berlin, Heidelberg, 1977, Springer Berlin Heidelberg, pp. 292–315.

[116] T. Richter and T. Wick, *Variational localizations of the dual weighted residual estimator*, Journal of Computational and Applied Mathematics, 279 (2015), pp. 192–208.

[117] T. Sandve, I. Berre, and J. Nordbotten, *An efficient multi-point flux approximation method for discrete fracture–matrix simulations*, Journal of Computational Physics, 231 (2012), pp. 3784–3800.

[118] N. Schwenck, B. Flemisch, R. Helmig, and B. Wohlmuth, *Dimensionally reduced flow models in fractured porous media: crossings and boundaries*, Computational Geosciences, 19 (2015).

[119] J. Smith, S. Durucan, A. Korre, and J.-Q. Shi, *Carbon dioxide storage risk assessment: Analysis of caprock fracture network connectivity*, International Journal of Greenhouse Gas Control, 5 (2011), pp. 226–240.

[120] P. Solin, K. Segeth, and I. Dolezel, *Higher-Order Finite Element Methods*, Studies in Advanced Mathematics, CRC Press, 2003.

[121] C.-F. Tsang, I. Neretnieks, and Y. Tsang, *Hydrologic issues associated with nuclear waste repositories*, Water Resources Research, 51 (2015), pp. 6923–6972. cited By 76.

[122] X. Tunc, I. Faille, T. Gallouët, M. Cacas, and P. Havé, *A model for conductive faults with non-matching grids*, Computational Geosciences, 16 (2011), pp. 277–296.

[123] K. G. van der Zee, *Goal-Adaptive Discretization of Fluid-Structure Interaction*, PhD thesis, Delft University of Technology, 2009.

[124] K. G. van der Zee, E. H. van Brummelen, I. Akkerman, and R. de Borst, *Goal-oriented error estimation and adaptivity for fluid–structure interaction using exact linearized adjoints*, Computer Methods in Applied Mechanics and Engineering, 200 (2011), pp. 2738–2757. Special Issue on Modeling Error Estimation and Adaptive Modeling.

[125] J. Varela, E. Ahmed, E. Keilegavlen, J. M. Nordbotten, and F. A. Radu, *A posteriori error estimates for hierarchical mixed-dimensional elliptic equations*, Journal of Numerical Mathematics, (2022).

[126] R. Verfürth, *A Posteriori Error Estimation Techniques for Finite Element Methods*, Oxford University Press, 1 ed., 2013.

[127] M. Vohralík, *A posteriori error estimates for lowest-order mixed finite element discretizations of convection-diffusion-reaction equations*, SIAM Journal on Numerical Analysis, 45 (2007), pp. 1570–1599.

[128] M. Vohralík, *Unified primal formulation-based a priori and a posteriori error analysis of mixed finite element methods*, Mathematics of Computation, 79 (2010), pp. 2001–2032.

[129] G. Wang, Y. Wang, and Y. He, *A weak Galerkin finite element method based on H(div) virtual element for Darcy flow on polytopal meshes*, Journal of Computational and Applied Mathematics, 398 (2021), p. 113677.

[130] R. Weijermars and A. Khanal, *High-resolution streamline models of flow in fractured porous media using discrete fractures: Implications for upscaling of permeability anisotropy*, Earth-Science Reviews, 194 (2019), pp. 399–448.

[131] S. Weisser and T. Wick, *The dual-weighted residual estimator realized on polygonal meshes*, Computational Methods in Applied Mathematics, 18 (2018), pp. 753–776.

[132] K. Williamson, P. Burda, and B. Sousedík, *A posteriori error estimates and adaptive mesh refinement for the Stokes–Brinkman problem*, Mathematics and Computers in Simulation, 166 (2019), pp. 266–282.

[133] N. Zhang, J. Yao, S. Xue, and Z. Huang, *Multiscale mixed finite element, discrete fracture–vug model for fluid flow in fractured vuggy porous media*, International Journal of Heat and Mass Transfer, 96 (2016), pp. 396–405.

[134] L. Zuo, W. Yu, J. Miao, A. Varavei, and K. Sepehrnoori, *Streamline modeling of fluid transport in naturally fractured porous medium*, Petroleum Exploration and Development, 46 (2019), pp. 130–137.

[135] M. Ţene, S. B. Bosma, M. S. Al Kobaisi, and H. Hajibeygi, *Projection-based embedded discrete fracture model (pedfm)*, Advances in Water Resources, 105 (2017), pp. 205–216.